

DISSERTATION

ZUR ERLANGUNG DER DOKTORWÜRDE

DER NATURWISSENSCHAFTLICH-MATHEMATISCHEN GESAMTFAKULTÄT

DER RUPRECHT-KARLS UNIVERSITÄT HEIDELBERG

vorgelegt von

M.Sc. Massimo Leonardo Guglielmino

geboren in Heidelberg

Tag der mündlichen Prüfung:

17.07.2017

**Untersuchung von Ultrahochgeschwindigkeitseinschlägen von
mikro- und submikrometergroßen Partikeln auf
mineralischen Oberflächen mittels
konfokaler Lasermikroskopie**

–

**Investigation of hyper-velocity impacts of
micron- and submicron- sized particles on mineral targets by
confocal laser microscopy**

Gutachter:

Prof. Dr. rer. nat. Mario Trieloff

Priv.-Doz. Dr.-Ing. Ralf Srama

Kurzfassung:

Um die Oberflächenentwicklung von atmosphärelosen Monden und Asteroiden besser zu verstehen, wurden mit einem modifizierten Van de Graaff Beschleuniger Ultrahochgeschwindigkeitseinschläge auf mineralische Oberflächen durchgeführt. Diese Arbeit beschäftigt sich primär mit den Einschlagsdaten eines Olivintargets, das mit Cu-Partikeln beschossen wurden (Projektildurchmesser $D_p = 0,01\text{--}3,18 \mu\text{m}$; $v = 0,45\text{--}13 \text{ km/s}$ innerhalb 3σ). Darüber hinaus wurden auch Proben des kohligen Chondriten Allende CV3, einem basaltischen Achondrit (NWA 6966), Antigorit und Pyroxenen beschossen. Anstatt der konventionellen Rasterelektronenmikroskopie (REM) wurde erstmalig die konfokale Lasermikroskopie angewandt. Die Auswertung ist zerstörungsfrei und verzichtet dabei auch auf Beschichtungen. Das bildgebende Verfahren eines Lasermikroskops ermöglicht höher aufgelöste Visualisierungen der Topographie und 3D-Darstellungen der Einschlagstrukturen. Es konnte gezeigt werden, dass außer Kratern auch ein signifikanter Anteil an Projektilen in der Oberfläche stecken blieb oder sehr flache Vertiefungen hinterlassen hat. Krater im Olivin und auch Diopsid zeigen ausgedehnte radiale Frakturen und Spallationseffekte. Erst ab sehr hohen Einschlagsenergien kommt es zur Bildung von Kraterlippen, während gleichzeitig die Spallation abnimmt. Resultate am Olivintarget unterscheiden sich von anderen Materialien wie Kalknatron- oder Quarzgläsern oder metallischen Oberflächen. Mit dem Lasermikroskop konnten auf Olivinoberflächen auch ausgeprägte Vertiefungen mit einem Durchmesser-zu-Tiefe-Verhältnis (D/d) von bis zu $0,40 \pm 24 \%$ nachgewiesen werden. Es konnten sowohl tiefe als auch sehr flache Einschlagsstrukturen im Bereich weniger zehn Nanometer vermessen werden. Bei semi-transparenten Materialoberflächen ist es möglich, Schockeffekte in Mineralen aufgrund der Lichtbeugung zu erkennen. Auch wenn mit dem Lasermikroskop Strukturen im Submikrometer-Bereich erfasst werden können, liegt die Grenze der erkennbaren lateralen Kraterstrukturen bei Durchmessern von $D \sim 1 \mu\text{m}$.

Abstract

To understand the surface evolution of atmosphereless moons and asteroids, a modified van de Graaff accelerator was used to conduct hyper-velocity impacts on mineral surfaces. This study is primarily focusing on impact data of an olivine target, which was bombarded with Cu projectiles (Projectile diameter $D_p = 0.01\text{--}3.18\ \mu\text{m}$; $v = 0.45\text{--}13\ \text{km/s}$ within 3σ). In addition, also samples of the carbonaceous chondrite Allende CV3, a basaltic achondrite (NWA 6966), antigorite and pyroxenes were bombarded. Instead of conventional scanning electron microscopy (SEM) a confocal laser scanning microscope (LSM) was used for the first time. The LSM investigations are nondestructive and can be conducted without any coating. The imaging techniques of the LSM allow visualizing topographies and generating 3D-illustrations of impact structures. It could be demonstrated that besides cratering a significant proportion of projectiles remain stuck in the surface or produced flat indentations. Craters in olivine and diopside showed wide radial fractures and spallation effects. Only at high impact energies the formation of crater lips occurs, while spallation effects decrease. The results of the olivine target differ from other materials like soda lime glass (SLG) or fused quartz (FQ), or metal. The LSM is able to verify pronounced cavities on olivine surfaces, with a diameter to depth ratio (D/d) of $-0.40 \pm 24\ \%$. It was possible to measure both deep and also very shallow impact structures with a few 10 nm resolution. On semi-transparent surfaces it is possible to see shock effects in the mineral targets, as an effect of light diffraction. Even though the LSM is able to measure surface structures at the sub-micron scale, the limit of safe identification of crater-structures is at diameters of $D \sim 1\ \mu\text{m}$.

Für meine Frau Angelika

Table of content

1	Introduction.....	1
1.1	Meteorites and micrometeorites and the effects of space weathering.....	1
1.2	Aim and predictions.....	6
2	Samples, methods and experimental setup.....	8
2.1	Initial choice of samples.....	8
2.2	Methods of impact experiments.....	14
2.3	Dust accelerator.....	17
2.4	Laser microscopy for studying surface features of polished mineral surfaces ..	21
2.4.1	Laboratory situation and sample handling.....	22
2.4.2	Principles of confocal laser microscopy.....	23
2.4.3	Measuring procedure with a Keyence confocal laser microscope.....	28
3	Projectile properties.....	48
3.1	Shape and morphology of Copper projectiles.....	48
3.2	Bombardment flux rates and impact counts.....	52
3.3	Projectile statistics of the olivine target in the dust accelerator	55
3.3.1	Velocities of projectiles.....	55
3.3.2	Diameters of projectiles.....	56
3.3.3	Kinetic energies of projectiles.....	60
3.3.4	Energy densities of projectiles.....	62

4	Analysis of olivine targets	64
4.1	The chemical composition of olivine samples	64
4.2	Investigation of a non-bombarded target.....	66
4.3	Results of the non-bombarded target	68
4.4	Investigation of the bombarded olivine target.....	75
4.5	Comparison of LSM- and SEM-imaging	79
4.6	Results of the investigation of bombarded olivine	83
4.6.1	The determination of the impact center of the accelerator particle beam ..	85
4.6.2	Categorisation of features on olivine targets	89
4.6.3	Concentration of impact features.....	108
4.6.4	Size distributions on the bombarded target.....	109
4.6.5	Cu-track.....	114
4.6.6	Qualitative analysis using the SEM.....	120
4.7	Comparing categorised features on the non-bombarded and the bombarded olivine targets.....	123
4.7.1	Diameter to height diagrams: Positive features.....	125
4.7.2	Diameter/height to diameter diagrams: Positive features	133
4.7.3	Diameter to depth diagrams: Negative features	136
4.7.4	Diameter/depth to diameter diagrams: Negative features	141
4.8	Identification of submicron-scaled craters.....	144
4.9	The effect of carbon coating in laser microscopy measurements.....	147
4.10	Shadowing effects after carbon coating.....	154

5	Discussion.....	156
5.1	Interpretation of surface features	156
5.2	General interpretation of the bombarded olivine target.....	166
6	Conclusions	180
	Bibliography	184
	Appendix Appendix	196
	Appendix A: EMP measurements	196
	Appendix B: R-script.....	210
	Appendix C: Material properties.....	212
	Appendix D: Data	214

List of abbreviations

BSE	<u>B</u> ack <u>s</u> cattering <u>e</u> lectrons
DCL/BCL	<u>D</u> ark <u>C</u> ut <u>L</u> evel/ <u>B</u> right <u>C</u> ut <u>L</u> evel
C-Laser DIC	<u>C</u> ontrast <u>l</u> aser <u>d</u> ifferential <u>i</u> nterference <u>c</u> ontrast
CAI	<u>C</u> alcium and <u>A</u> luminium-rich <u>i</u> nclusions
EMP	<u>E</u> lectron <u>m</u> icroprobe
FIB	<u>F</u> ocused <u>i</u> on <u>b</u> eam
FQ	<u>F</u> used <u>q</u> uartz
GUI	<u>G</u> raphical <u>u</u> ser <u>i</u> nterface
HV	<u>H</u> yper- <u>v</u> elocity
ISD	<u>I</u> nterstellar <u>d</u> ust
IDP	<u>I</u> nterplanetary <u>d</u> ust <u>p</u> article
IRS	<u>I</u> nstitut für <u>R</u> aumfahr <u>s</u> ysteme (Institute for Space Systems at the University of Stuttgart)
LGG	<u>L</u> ight <u>g</u> as <u>g</u> un
LHB	<u>L</u> ate <u>h</u> eavy <u>b</u> ombardment
LSM	<u>L</u> aser <u>s</u> canning <u>m</u> icroscope
LHV	<u>L</u> ow <u>h</u> yper- <u>v</u> elocity
NIR	<u>N</u> ear <u>I</u> nfr <u>a</u> red spectroscopy
npFe ⁰	<u>n</u> ano- <u>p</u> hase reduced Iron (<u>F</u> e)

MPIK	<u>M</u> ax <u>P</u> lanck <u>I</u> nstitut für <u>K</u> ernphysik (Max Planck Institute for Nuclear Physics in Heidelberg)
SEM	<u>S</u> canning <u>e</u> lectron <u>m</u> icroscope
SE	<u>S</u> ecundary <u>e</u> lectrons
SIMS	<u>S</u> ecundary ion <u>m</u> ass <u>s</u> pectrometry
SLG	<u>S</u> oda <u>l</u> ime glass
SMFe	<u>s</u> ub-microscopic <u>m</u> etallic iron (<u>Fe</u>)
PSU	<u>P</u> article <u>s</u> election <u>u</u> nit
RGB	<u>R</u> ed <u>G</u> reen <u>B</u> lue color spectrum
TEM	<u>T</u> ransmission <u>e</u> lectron <u>m</u> icroscope

1 Introduction

1.1 Meteorites and micrometeorites and the effects of space weathering

By looking at the earth's natural satellite, the moon, by naked eye we can see different gray shades in visible light. Its appearance is determined by the variation in size and composition of the surface material and the topography, which is primarily altered by large meteorite impacts (Fig. 1.01).



Figure 1.01: Photo of full moon taken by a camera in Juarez, Chihuahua, Mexico. Credit: Anthony Lopez (space.com, 2014).

Moon itself is a result of a collision between the early Earth and a Mars-sized body (O'KEEFE, 1969; HARTMANN, *et al.* 1986). The dark lunar maria are impact basins that originated in the course of an increased impact activity 3.8–4.1 Ga ago, called the lunar of late heavy bombardment (LHB). After the late heavy bombardment the flux of extraterrestrial matter to the Earth-moon system decreased, but there is still a constant flux of dust in our solar system with millimeter to submicron sized particles, that impact on the moon and other atmosphereless solar system objects. The interstellar medium is a known dust source as well, and delivers submicron sized interstellar dust (ISD), $\sim 0.3 \mu\text{m}$, into our solar system. On the other hand interplanetary dust particles (IDPs) can have different sources in our solar system, e.g. comets, asteroids, the Edgeworth-Kuiper belt, atmosphereless planetary satellites and jet

streams from larger satellites and planets like Jupiter and Saturn (HILLIER *et al.*, 2009; APAI & LAURETTA, 2010; KEMPF *et al.*, 2010; HSU *et al.*, 2011). The flux of these dust particles is of enormous interest for space craft engineering and material vulnerability. It is important to understand the mechanics and effects of impacts on spacecraft relevant materials. Therefore many laboratory experiments have been conducted to test different projectiles on metals and alloys since the 1960s. Finding light, multifunctional and resistant materials is still of great motivation to space craft related laboratories. In addition to cosmic dust, there are 100 million space debris objects larger than 1 mm and even much smaller in near-Earth space, e.g. slag residues of rockets, paint flakes and fragments of explosions in the range of micron sized particles (KOBUSCH *et al.*, 2009) (Fig. 1.02 and 1.03).

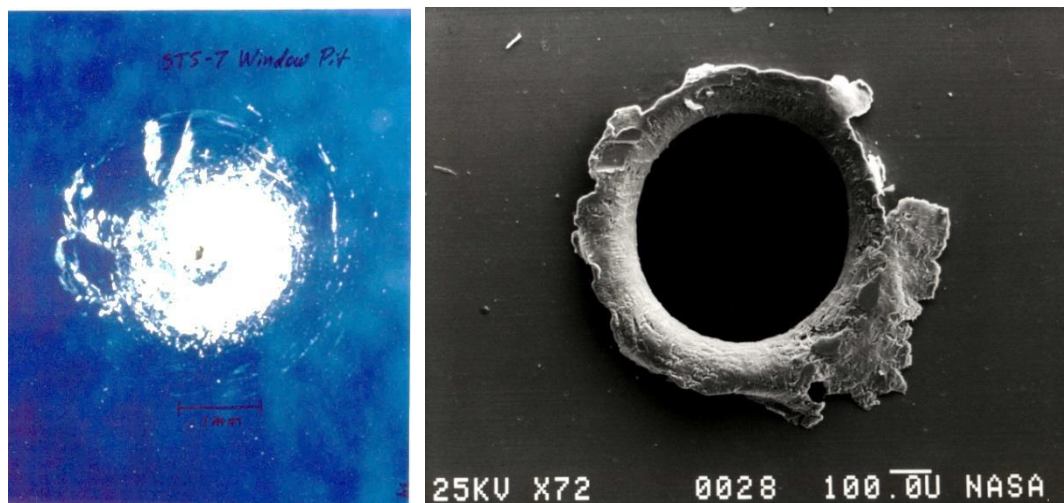


Figure 1.02: The left photograph shows an impact pit onto a window of a space craft caused by sub-millimeter orbital debris.

Figure 1.03: The right picture is a scanning electron microscopy image (SEM) of a solar panel hit by sub-micron sized orbital debris. Credit: NASA (orbitaldebris.jsc.nasa.gov).

Today the scientific community tested and is still testing projectiles (also referred to as impactors or impacting particles) and target combinations using impact simulation facilities. Data are established by these facilities, for various projectile size fractions, velocities, densities and targets. However, it is still difficult to understand how certain impact features are related to target and projectile properties, which is also discussed in this study. Whilst the major motivation and results are part of space craft evaluation, these findings are of great use to study the development of surfaces of natural

atmosphereless solar system bodies, because micrometeoroid bombardment is a major driver of surface alterations called “space weathering”. Understanding the evolution of their surfaces enables the interpretation of spectral data in terms of composition. It also gives a better comprehension of other physicochemical processes within our solar system.

First major insights to natural surface evolution in space were provided by microcrater analyses of lunar soil (Fig. 1.04) that started with Apollo 11 (NEUKUM *et al.*, 1970; VEDDER, 1971).

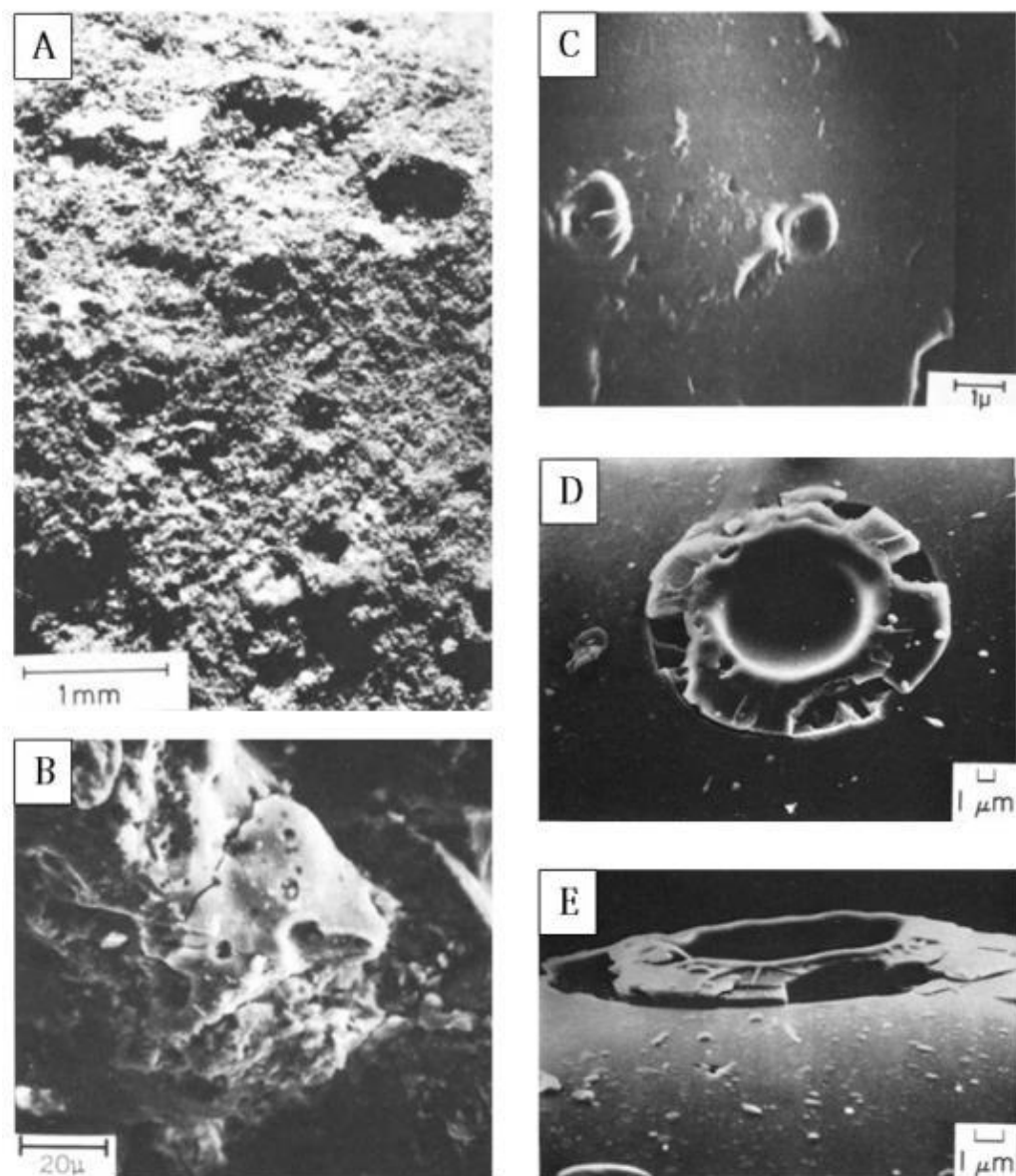


Figure 1.04: A: NASA-sample No. 10019 with millimeter-sized impact craters; B: NASA-sample No. 10019 with impact craters of $> 2\mu\text{m}$ diameter; C: NASA-sample No. 10084 glass spherule with micron-sized craters; D/F: Apollo 11 returned lunar soil sample glass spherules with micron-sized craters.

The analyses of sample material from different landing sites on the Moon showed large lateral heterogeneities, which are still not well explained. Subsurface magma oceans, giant impact during late accretion or heterogeneous accretion of chemically distinct sub-moon-sized bodies are discussed as reasons (HARTMANN *et al.*, 1986).

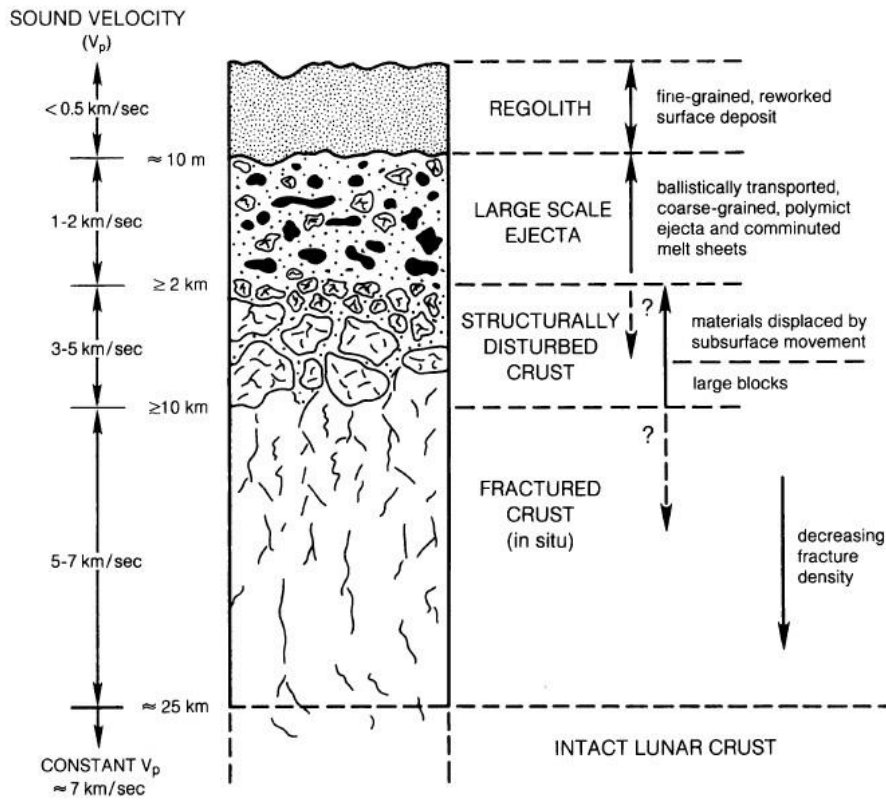


Figure 1.05: This figure is a tentative sketch interpreted from seismic velocities and somewhat speculative especially regarding the lower layers of lunar crust (HEIKEN *et al.*, 1991).

The moon is almost exclusively covered by powder like material, which is called lunar regolith. It is generated by micrometeorite bombardment, after fresh lunar bedrock is exposed by larger impacts or past lava eruptions. Large impacts can shatter and destroy the original bedrock and leave layers of broken, melted or altered debris behind and turnover the former regolith surface. This newly exposed material gets continuously covered by smaller impact craters.

The lunar regolith (Fig. 1.05) primarily consists of <math>< 1 \text{ cm}</math> sized particles accompanied by larger cobbles and boulders as a loose sediment or breccia, reaching downward to 10 m in depth – with rare exceptions down to 20 m (HEIKEN *et al.*, 1991). The physical

and optical effects of lunar space weathering were analysed in terrestrial laboratories using samples returned by the Apollo mission. Many processes are suspected to influence optical properties (CLARK *et al.*, 2002):

- Interplanetary dust and micrometeorite bombardment
- Electromagnetic radiation
- Solar wind ion implantation and sputtering
- Cosmic-ray bombardment
- Larger impacts by meteoroids, asteroids and comets

Those effects are not limited to the moon, and similarly affect other atmosphereless solar system bodies. However, applying results from lunar regolith to asteroids proved to be difficult. Asteroid studies show that other atmosphereless solar objects do not necessarily experience lunar-like space weathering (BLOCH *et al.*, 1971; HAPKE, 2001; CLARK *et al.*, 2002; VERNAZZA, *et al.*, 2009; BENNETT, *et al.*, 2013).

Besides X-ray, γ -ray, ultraviolet, infrared spectroscopy is by far the most frequently used method to illustrate and explain stages of surface evolution of atmosphereless solar system objects. It is expected that space weathering changes the surfaces in structure, chemical composition, mineralogy and its optical properties (CHAPMAN, 2004; CLARK *et al.*, 2002). The most discussed result of space weathering effects, is the formation of nanophase reduced iron (npFe⁰) or sub-microscopic metallic iron (SMFe), which seems also to have the most important influence in reflectance spectroscopy (CLARK *et al.*, 2002; NOGUCHI *et al.*, 2014).

Recent studies claim that solar wind is the major effect that cause the formation of npFe on S-Type asteroid 25143 Itokawa, but sputter deposits and/or impact deposits would also alter submicron grains (NOGUCHI *et al.*, 2014). Simulation suggests that impacts have a major role affecting an asteroid surface particle's size and shape (TSUCHIYAMA *et al.*, 2011). The Itokawa sample return mission by the Hayabusa spacecraft provided evidence of Fe-rich nanoparticles in surface layers of olivine, low-Ca pyroxene and plagioclase (NOGUCHI *et al.*, 2011).

In turn space weathering is not a linear process. It competes with effects of regolith turnover; or that to solar winds exposed surfaces are suggested to experience faster

weathering effects compared to others; or that there were changes of micrometeorite flux in the past; or that mineralogy and size of surface particle influence maturation of an atmosphereless solar system object: Olivine is more easily weathered than pyroxene and might cause variations of weathering degrees within in an asteroid class, which could be an effect of composition (BLOCH *et al.*, 1971; HÖRZ *et al.*, 1975; CLARK *et al.*, 2002; CHAPMAN, 2004; VERNAZZA *et al.*, 2009; NOGUCHI *et al.*, 2011; BENNETT, *et al.*, 2013).

Considering all these previous findings, high and hyper-velocity impact experiments using analogue silicate target materials could add further insights to the topic of space weathering. Moreover, it seems promising that identifying the surface mineralogy of an atmosphereless solar system object by understanding its degree or maturity of impact related space weathering, might help to make conclusions about its evolution or bulk chemical composition.

1.2 Aim and predictions

The aim of this study is to investigate hyper-velocity impacts of micron to submicron sized projectiles on mineral targets, using a dust accelerator facility. There are only two particle accelerators currently operating in cosmic dust research worldwide. Impact feature analyses are usually conducted with SEM stereoscopy. However, this study aimed at introducing a new method and used a confocal laser scanning microscope for mineral target investigation for the first time.

As the Heidelberg dust accelerator was planned to move to Stuttgart University, impact experiments were only possible at the very beginning of this study. Hence, a relatively large suite of targets were exposed to projectile impacts, independent of how time consuming subsequent laser microscope analyses turned to be out. The target suite consisted of different natural anhydrous minerals, which are known to be the basic components of solar system objects, a hydrous mineral, a carbonaceous chondrite and a basaltic achondrite.

After first analyses with the laser microscope, it became clear, that analyses were so time consuming that only one target could be studied in detail. The reason was that laser microscopy was so sensitive that numerous small scale features could be stud-

ied that are normally not accessible via SEM stereoscopy. Moreover, the mineral targets prepared from natural minerals had many small scale features not related to particle impacts which required a completely new effort to be distinguished.

Olivine is one of the most abundant minerals in chondrites and constituent of regolith. Hence, this study was focussed on an olivine target. Particular this specific olivine target experienced a high particle flux ensuring a high impact feature density, about 20 – 100 times higher than any other target from the accelerator experiments. Accordingly, the focus was to establish a basic method for impact evaluation on mineral targets with LSM.

Although this study only analysed olivine by LSM in detail, the impact experiments on the other minerals produced valuable sections containing impact features available for future studies.

2 Samples, methods and experimental setup

2.1 Initial choice of samples

Besides the introduction of the LSM technique for impact studies, it was endeavored to use natural mineral target material, which is more relevant for space weathering. Whilst quartz is an important material for space optics and windows (STRADLING *et al.*, 1993) it showed that soda lime glass is a good analogue target material for lunar glass, regarding density, softening temperature, viscosity and fracturing characteristics (VEDDER & MANDEVILLE, 1974). Previously both materials are well studied but were produced synthetically.

Asteroid Type	Meteorite Analogs	Mineralogy	Alteration Effects
S	H, L, LL chondrites; stony irons, IAB irons, lodranites; winonites, siderophiles, ureilites	Olivine, pyroxene, metal	Albedo: up to 50% decrease Red slope: weak to moderate increase Band suppression: 50% decrease
V	Basaltic achondrites	Pyroxene, feldspar	Band suppression: 20%
A	Brachinites, pallasites	Olivine	Red slope: moderate increase Band suppression: 20% decrease?
Q	H, L, LL chondrites	Olivine, pyroxene, metal	Albedo: 20–30% decrease Band suppression: 20–30% decrease
Lunar	Lunar meteorites	Basalt, feldspar	Albedo: 50–75% decrease Red slope: moderate to strong increase Band suppression: 50–75% decrease

Table 2.01: This table is taken from CLARK *et al.*, (2002) and list the estimated mineralogy for different asteroid classes.

A large variety of studies in astronomical and cosmochemical fields show that Mg-rich silicates are major components of extraterrestrial rocks. Olivine and pyroxene are suggested to be part of the main minerals in forming asteroids (Tab. 2.01) or comets (e.g. 81P/Wild 2) (CLARK *et al.*, 2002; NOGUCHI *et al.*, 2014; ZOLENSKY *et al.*, 2006). Also they are known as constituents in chondrites (GOODING & KEIL, 1981; CLARK *et al.*, 2002; RUBIN, 2005; NORTON & CHITWOOD, 2008; HOPPE, 2009; OKRUSCH & MATTHES, 2014;). Primarily olivine but also pyroxene are confirmed to form IDPs and ISD or at least extraterrestrial dust shows signatures of silicates containing Mg, Ca and Fe (CHRISTOFFERSEN & BUSECK, 1986; DRAINE, 2003; KIMURA *et al.*, 2003; SRAMA *et al.*, 2008;

HILLIER *et al.*, 2009; WESTPHAL *et al.*, 2014; ALTOBELLI *et al.*, 2016). Therefore, the focus was set in obtaining large, homogenous, if possible gem stone quality crystals of olivine and pyroxene for impact experiments.

The following samples were selected as targets for micrometeorite impact experiments, SEM, LSM and EMP investigations:

- **Olivine: Forsterite $(\text{Mg,Fe})_2[\text{SiO}_4]$**

Forsterite is the Mg end member of orthorhombic olivine and known as a major constituent extraterrestrial rocks. The forsterite crystals in this study are all from the same sampling site in Turkey, bought by a retailer (Fig. 2.01).

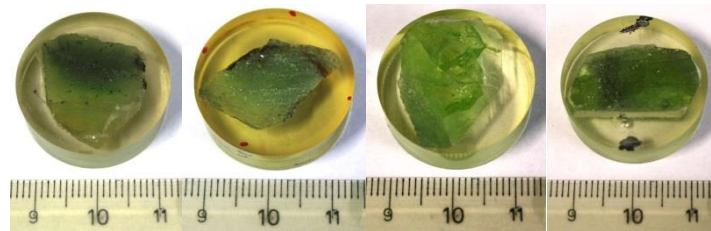


Figure 2.01: From left to right: Olivine_6 (bombarded), Olivine_5 (bombarded), Olivine_7 (non-bombarded), Olivine_4 (microprobe specimen). All samples were cut in half before, polished and embedded into epoxy resin.

- **Orthopyroxene: Enstatite $\text{Mg}_2\text{Si}_2\text{O}_6$**

Enstatite is the orthorhombic pyroxene Mg-end member and also a major constituent of extraterrestrial rocks. Pyroxenes can occur in almost every type of terrestrial igneous rocks and are the most important group of rock-forming ferromagnesian silicates (DEER, *et al.*, 1992). The enstatite crystals in this study are all from the Merelani mine in Tanzania, bought by a retailer (Fig. 2.02).

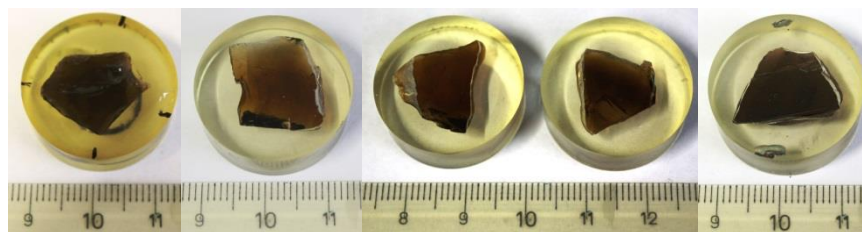


Figure 2.02: From left to right: Enstatite_5 (bombarded), Enstatite_6 (bombarded), Enstatite_7 (non-bombarded), Enstatite_8 (non-bombarded), Enstatite_3 (microprobe specimen). All samples were cut in half before, polished and embedded into epoxy resin.

- **Clinopyroxene: Diopside ($\text{CaMg}_2[\text{Si}_2\text{O}_6]$)**

Diopside is a monoclinic CaMg-rich variation of pyroxene. All diopside targets are produced out of one whole-rock sample. The original sample is obtained from the institutes archive, but the origin is unknown (Fig. 2.03).

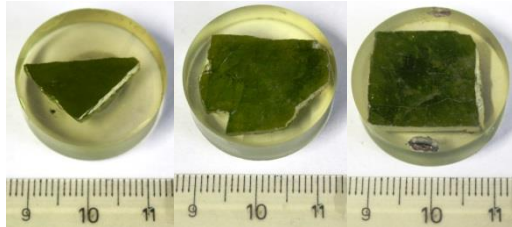


Figure 2.03: From left to right: Diopside_6 (bombarded), Diopside_4 (non-bombarded), Diopside_7 (microprobe specimen). All samples were cut from a whole-rock sample, polished and embedded into epoxy resin.

- **Serpentine subgroup mineral: antigorite $\text{Mg}_6[(\text{OH})_8\text{Si}_4\text{O}_{10}]$**

Antigorite is a hydrous alteration product of serpentine group minerals which are in turn alteration products of olivine and pyroxene. Terrestrial antigorite can form, in regions of progressive metamorphism, when temperatures are above 500°C , accompanied by talc $\text{Mg}_3\text{Si}_4(\text{OH})_2$ and water. Forsterite, talc and water can react to antigorite (Okrusch & Matthes, 2014). Antigorite can be considered as a representative hydrated Mg-bearing silicate and alteration product of forsterite. Micrometeorite impacts on hydrous minerals have not been studied before. All antigorite targets were produced from one whole-rock sample. The original sample is obtained from the institutes archive, but the origin is unknown (Fig. 2.04).

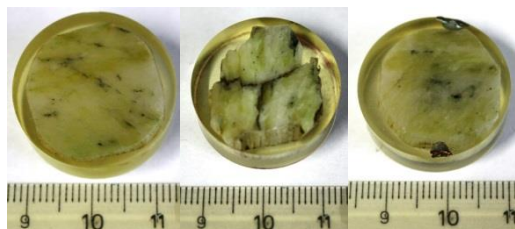


Figure 2.04: From left to right: Antigorite_6 (bombarded), Antigorite_8 (non-bombarded), Antigorite_7 (microprobe specimen). All samples were cut from a whole-rock sample, polished and embedded into epoxy resin.

- **Carbonaceous chondrite: Allende CV3**

Allende is a carbonaceous chondrite of type Vigarano, Italy. In general it can be referred to as a breccia of chondrules in a fine grained matrix with hydrous phases and carbon content of about 0.5–5 %. Allende consists of 0.5–2 mm large chondrules, mainly olivine (~ 43 % vol.); a matrix (~ 38.4 % vol.) primarily made of olivine and pyroxene; Ca-Al-rich inclusions (CAI; ~ 9.4 % vol.); opaque minerals (~ 3.1 % vol.) like troilite and kamacite; lithic and mineral fragments (~ 2.9 % vol.). Allende experienced hydrothermal and high-temperature metamorphism (McSWEEN, 1977; WEISBERG *et al.*, 2006; FLORES-GUTIÉRREZ *et al.*, 2010; OKRUSCH & MATTHES, 2014) (Fig. 2.05).

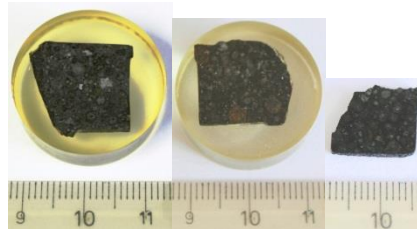


Figure 2.05: From left to right: Allende_R (bombarded), Allende_4 (non-bombarded), Allende_6 (non-bombarded). All targets are cut from an initial piece and got polished. All Allende targets are embedded in epoxy, except for Allende_6.

- **Eucritic achondrite: NWA 6966**

NWA 6966 is an eucritic achondrite (i.e., without chondrules) of basaltic composition and a member of the HED-group (Howardites, Eucrites, Diogenites). As howardites are considered to be impact breccias made of eucrites and diogenites, it is likely that eucrites are derived from the upper asteroidal crust and diogenites from the lower crust or mantle. Studies assume that HED chondrites represent fragments of asteroid 4 Vesta. In the early stages of the solar system, 4 Vesta apparently underwent basaltic volcanism and later got overprinted by shock metamorphism caused by meteorite bombardments (4.1–3.5 Ga ago). Eucrites show similarities to terrestrial basalts, consisting of low Ca-clinopyroxene, hypersthene, plagioclase, olivine, but also troilite and chromite (MISAWA *et al.*, 2005; BOGARD, 2011; OKRUSCH & MATTHES, 2014). All NWA 6966 targets were made out of one piece, bought by a retailer (Fig. 2.06).



Figure 2.06: From left to right: NWA_6966_R (bombarded), NWA_6966_8 (non-bombarded), and remaining non-bombarded NWA 6966 pieces (4, 5, 6, 7) for applications of LSM, SEM and EMP. All targets are cut from one initial piece and got polished. Only the NWA_6966_R & NWA_6966_8 were embedded in epoxy.

Except for diopside and antigorite, all samples were bought from retailers. Diopside, antigorite, Allende and NWA 6966 targets are produced out of one initial piece. Forsterite and enstatite targets were made out of different crystals divided in the middle, but these have been collected all at the same sample location.

Except for olivine (once - VEDDER, 1971), natural minerals or chondrites were never used as target material for micrometeorite impacts before.

The raw target candidates were sliced into 2–5 mm thick sections, with a surface measure between 0.8 x 0.8 up to 2 to 2 mm and got highly polished by our mechanical workshop. As producing thin sections of antigorite, Allende and NWA 6966 were

problematic due to crumbling the weak structure of thin sections, the production of thick sections was preferred. 18 targets are simple thick sections, 8 samples were additionally embedded in epoxy resin. This embedding is necessary to conduct electron microprobe or ion probe analyses subsequently. In total these 26 mineral targets have been bombarded. After sorting out test targets for calibration of the dust beam, adjusting sample mounting and dust source compositions, 17 targets (nine thick sections; eight embedded in epoxy) remained for in-depth investigations or for further experiments (e.g. radiation, heating). The surface roughness of these samples is $\sim 10\text{--}20$ nm measured with the Keyence VK-X200 laser microscope (using preparations described in section 2.4.3 *Measuring procedure with a Keyence confocal laser microscope*). This thesis contains the data of the epoxy embedded targets, while the non-embedded thick sections are part of a different study (FIEGE *et al.*, 2017, in prep.)

2.2 Methods of impact experiments

The primary task of an impact experiment is the investigation of crater morphology produced by a specific projectile. Typical crater morphologies are shown in Figure 2.07. The major parameters to determine the crater morphology are the crater's diameter and the depth relative to the surface. The crater is confined by a smooth elevation called "rim" which occasionally has a so called "lip" (Fig. 2.07). In this study the method of measuring crater diameter and crater depth is based on the study of NAGEL & FECHTIG (1980). KEARSLEY *et al.* (2007) used crater lip-to-lip measurements to determine diameters. The method used in this study is measuring the crater diameter as mean value of four different directions or sections. In this case, a lip-to-lip measurement is not applicable, as lips do not necessarily occur completely around craters. Lip-to-lip measurements are only suitable for uniform impact morphologies, when all projectiles are almost homogenous in composition and perfectly spherically shaped.

In the experiment of this thesis not every impact resulted in the creation of a crater. There are also particles attached or sticking in/on to the surface, e.g. largely intact projectiles rather than a simple projectile residue. Similar observations were reported by NEUKUM *et al.* (1970). For micro-impact features on target material the following nomenclature will be used in this thesis: the diameter is designated as "**D**". Both the depth of a crater, i.e., the vertical distance from the lowest point to the surface, and the height of projectile residues or contaminating particles, i.e., the vertical distance from the highest point to the surface, is designated as "**d**". For the projectiles the diameter is designated as "**D_P**", which is a property of a particle before the impact (Fig 2.07).

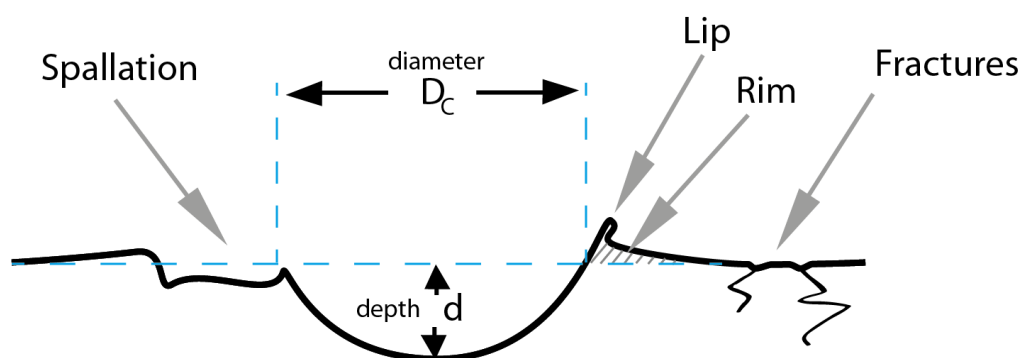


Figure 2.07: A simplified schematic of a crater profile, illustrating different morphological features and their corresponding terms.

Figure 2.07 shows a more complex crater with fractures and spallation effects outside the rim. The typical appearance of a crater shows a crater pit and a rim surrounding the pit with the highest elevated and overlapping zone known as the crater lip. Lips often look like unfolded petals. It is considered that on the olivine target shallow elevated zones around craters are rims without pronounced lips (Fig. 2.08).

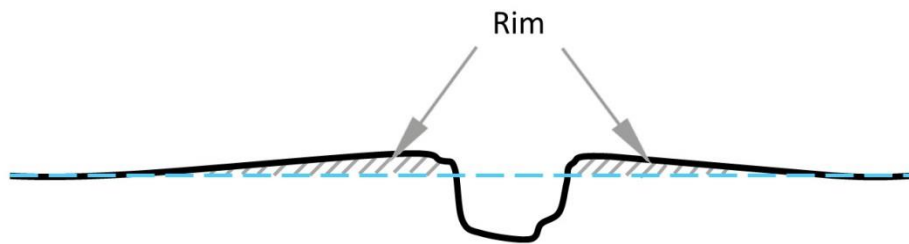


Figure 2.08: Illustration of shallow elevated zones around craters considered as rims.

As stated above an impacting particle does not necessarily cause a rim or a lip. In this work the preliminary investigation indeed showed a rare occurrence of lips. This could be an effect of the rigid nature and polished surface of the targets.

The only published results on olivine targets are from VEDDER (1971). He used spherical aluminum projectiles and polished transparent crystal olivine targets from San Carlos, Arizona. He suggested that due to low material strength olivine would tend to extensive fracturing and uplifting at craters compared to glass or oligoclase. VEDDER also noticed that at higher velocities the inner crater is smoother and shows the flow of material. In addition, spallation effects left a rough surface around the inner crater structure (Fig. 2.09).

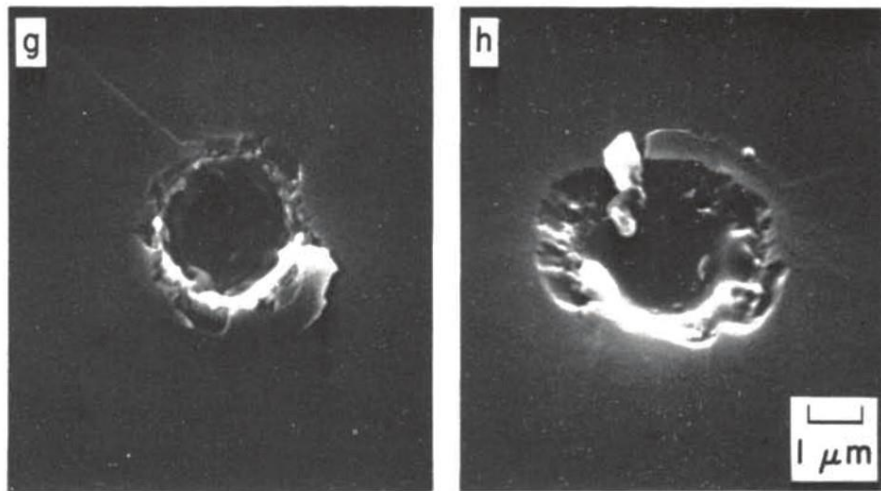


Figure 2.09: Olivine targets formed by orthogonal impacting aluminum projectiles. (g) 5.8 km/s, 4.6 pg, surface tilting of 7°. (h) 13.1 km/s, 3.2 pg, surface tilting of 45°. The scale applies to all images (VEDDER, 1971). These images illustrate craters in olivine with spallation effects and no crater lips.

In addition, according to VEDDER & MANDEVILLE (1974), high impact energies are necessary to cause spallation effects to rim zones and more distal areas. MERZHIIEVSKY, (1997) and BRASLAU (1970) claim that a target's strength would play a major role in crater formation. Such, crater size and morphology differ in plastic materials (metals), brittle materials (glass, rock), and composite materials (glass plastics and carbon epoxy plastics). Summarising these statements, crater shape should be a result of two major parameters: impact energy and the target's mechanical properties.

For impact studies in general, the most common used projectile acceleration facility is either a light gas gun (LGG) or a Van de Graaff accelerator. The first facility is designed for studies with projectiles of any composition in millimeter or centimeter sizes at velocities above a few km/s. A two-stage LGG can even accelerate particles of several kilograms, and small projectiles may even reach velocities of about 8 km/s (BURCHELL *et al.*, 1999; LEXOW *et al.*, 2013). However, a Van de Graaff accelerator is the only facility that meets the requirements of hyper-velocities, in the tens of km/s regime, and projectiles less than one micron in diameter. Such accelerators are restricted to conductive projectiles, as these are accelerated electrostatically.

For further readings and introduction to LGG experiments see ASAY & SHAHINPOOR, (1993).

2.3 Dust accelerator

To study hypervelocity impacts of micron sized particles a Van de Graaff accelerator is a perfect tool (FRICHTENICHT, 1962). In collaboration between the Cosmo Chemistry Group at the Institute for Earth Science of Heidelberg University and the Cosmic Dust Group from the Institute of Space Systems at the University of Stuttgart (IRS), a 2 MV dust accelerator located at the Max Plank Institute for Nuclear Physics (MPIK) in Heidelberg was operated for this experiment.

The dust accelerator of the Cosmic Dust Group is a modified 2MV Van de Graaff electrostatic accelerator running since the late sixties and was steadily enhanced. It is capable to accelerate nano to micron sized dust particles to velocities between 1 and 60 km/s (SRAMA, 2009; MOCKER *et al.*, 2011). Simulations of velocities for interplanetary and interstellar dust particles show that the dust accelerator can lay down the requirements for cosmic dust very well (FIEGE *et al.*, 2017, in prep.).

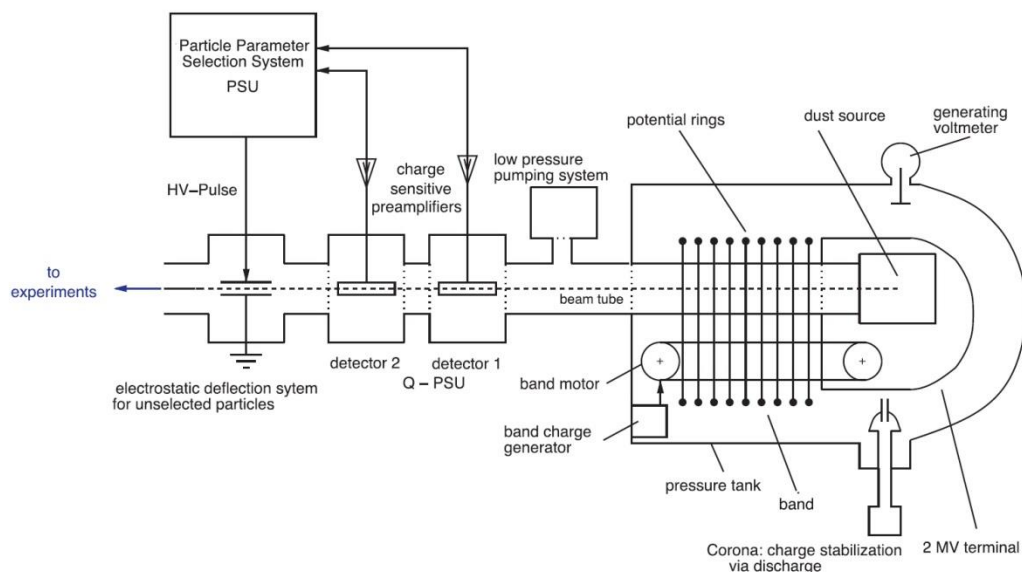


Fig. 2.10: Schematic of the dust accelerator and the primary compartments (from MOCKER, 2015).

A band charge generator sprays charge onto a latex belt, which transports the charge inside the accelerators pressure tank (Fig. 2.10). At a high voltage terminal the charges are wiped from the band and collected. The desired potential (max. 2 MV) is stabilised by Corona discharges. Furthermore the tank is filled with gas (SF_6 and CO_2) that shield the device from sparking and discharging. The latex belt passes through 60

potential rings inside the tank, which ensure a homogenous electric field from 2 MV (in front of the dust source) down to 0 MV (in the direction of the experiment). When dust particles are released into the beam line they are accelerated by the electrostatic field of potential rings. Hence, only conductive projectiles or particles with conductive coating can be used for this process. The electrostatic fields also work as focus lenses, similar to those in an optical pathway (Fig. 2.11). It is possible to relocate the focal point of the particle beam (MOCKER *et al.*, 2011) by altering the electrostatic fields of the focusing cathode and the first two potential rings as well.

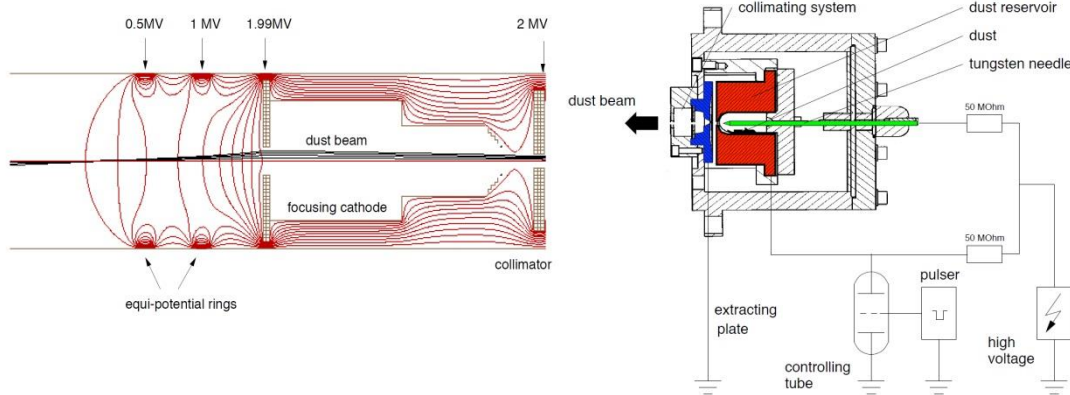


Figure 2.11, left: A schematic visualisation of electrostatic field (red lines) of the focusing cathode and the equi-potential rings.
 Figure 2.12, right: A schematic of the dust source used in this experiment (images are taken from MOCKER *et al.*, 2011).

An ultra-high vacuum (10^{-7} mbar) inside the beam line is provided by a pumping system. The dust source basically consists of three major components (Fig. 2.12): the reservoir, which can carry some milligrams of dust, a tungsten needle with an etched tip of $1 \mu\text{m}$ and the extraction plate. The reservoir cylinder is 25 mm long and 10 mm in diameter, which is pierced by the needle in the center. By applying pulsed charge onto the dust reservoir and combined with the vacuum inside the system, dust particles are levitated to the axis of the beam line. From the tungsten needle in the center, particles receive their final charge. A different potential at the extracting plate causes the particles to engage into the dust beam.

The particle selection unit (PSU) is able to detect the charge and velocity of particles with the help of three different single detectors in real time. In general every particle is deflected by a 4 kV gate on default. The PSU allows individual dust grains with se-

lected mass and velocity to pass through, by opening deflection for a couple of microseconds. All other particles outside of the defined mass or velocity window are sorted out of the beam line (SRAMA, 2009; MOCKER *et al.*, 2011).

For this study the dust accelerator was operated in continuous mode at 1.8 MV. To find appropriate particle fluxes for various Cu dust sources, different ranges of velocities and masses were applied. However, a sharp definition of velocity and mass increases the number of particles rejected by the PSU, and decreases the projectile flux and the impact density number on the target, making it potentially more difficult to find and identify impact features. Hence, the most experiments were conducted without speed and mass restrictions to ensure a high projectile flux, e.g., in the case of the Olivine_6 target. The size of Cu projectiles used in this experiment range from several hundreds nanometer to tens of micrometer. These particles were accelerated to velocities of $\sim 0.5 - 10$ km/s (and faster) and shot perpendicular ($\theta = 90^\circ$) onto the target.

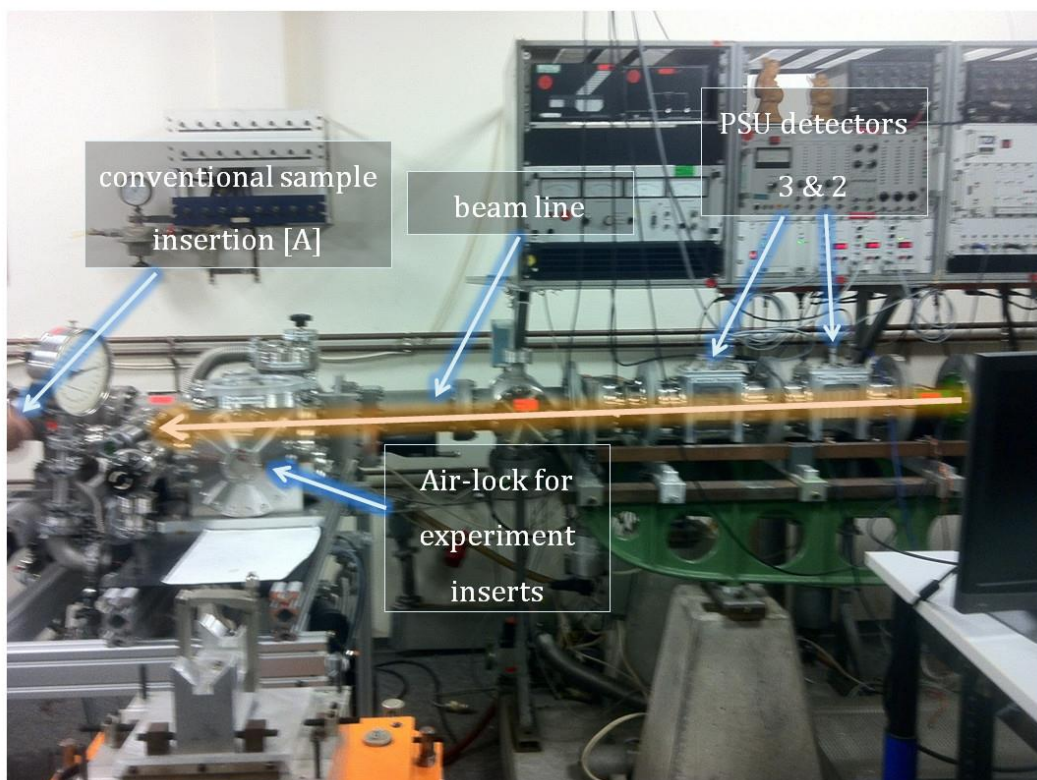


Figure 2.13: Side view of dust accelerator, without pressure tank.

The initially applied procedure to place the target into the dust beam (Fig. 2.13: conventional sample insertion [A]) was time consuming concerning the exchange of targets. It was necessary to unscrew parts of the beam lines rear section and required prolonged pumping for re-establishing the vacuum. With completion of the new air-lock insertion (Fig. 2.14: new sample insertion [B]), no deconstruction was necessary and pumping time was reduced. In addition, with a rotating table, which allows holding up to four targets, the speed of target exchange further increased.

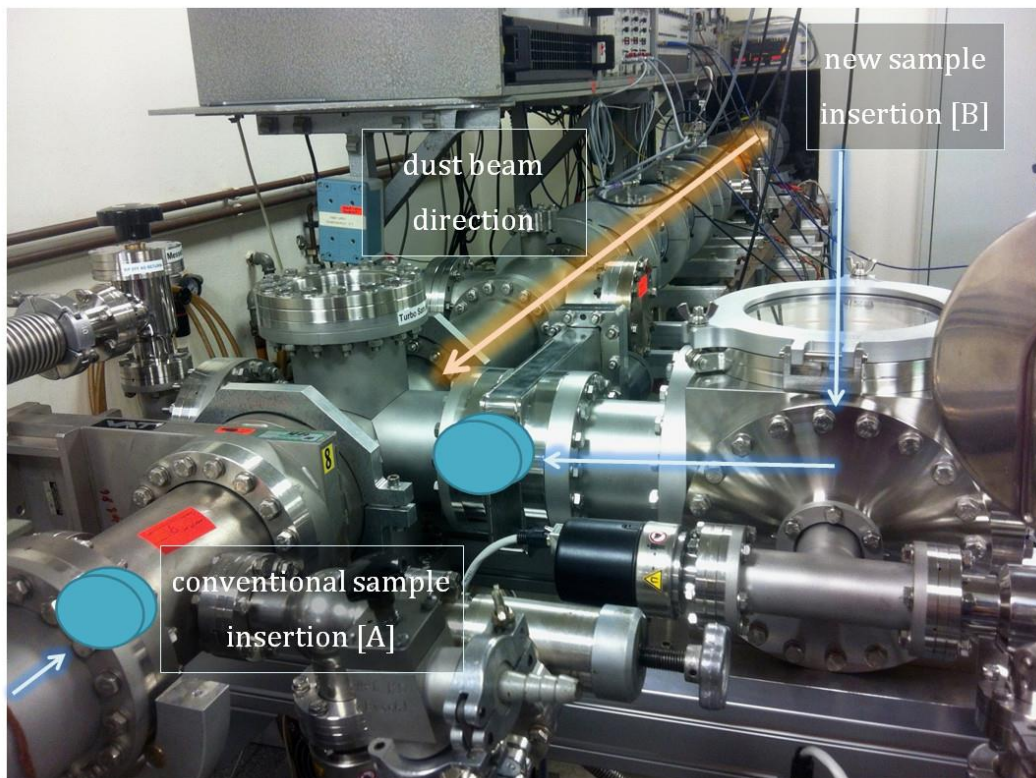


Figure 2.14: Front view of the dust accelerator, with pressure tank behind the wall. The prior conventional sample insertion [A] took a lot of time. The new target insertion by entering over the air-lock was quicker and took only a few work steps.

2.4 Laser microscopy for studying surface features of polished mineral surfaces

Conventional morphological analyses of micro impact craters are conducted with SEM on a gold coated surface, and use a secondary electron detector, resulting in detailed images (SE) with high lateral resolution. However, gold coating contaminates the surface and impedes further chemical analyses. Applying carbon instead of gold coating allows chemical analyses, but worsens depth resolution in SEM-SE images, so that morphological features are barely visible. Moreover, once applied, coating cannot be removed from the target without destruction of impact features. In addition the SEM can be considered as partly destructive due to the electron beam, which ablates the uppermost layers of a sample (Fig. 2.15), and may cause heating due to the electron beam. Obtaining crater depths in general is not easy when using SEM (WALSH *et al.*, 1993). Craters of less than 1 μm diameter cannot be measured accurately with the SEM. Precise SEM measurements of absolute crater depth is only applicable on large craters ($>30 \mu\text{m}$). Even though there are advanced software products commercially available to make stereoscopically investigations much easier, still accurate SEM imaging depends on the limitation of spatial resolution of SEM optics (KEARSLEY *et al.*, 2007).

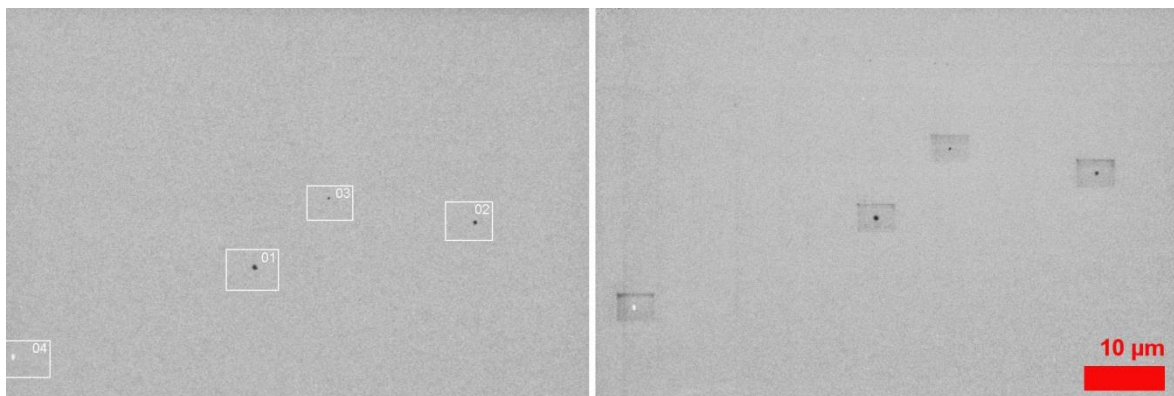


Figure 2.15: Two SEM-BSE images of preliminary SEM investigations at the same location on a diopside target. (Left) On this very homogeneous target four detailed sections (white frames with numbers) were chosen for closer investigation. Frame 1-3 were cavities of unknown origin and 4 was most likely a copper particle. (Right) It is noticeable that every detailed scan caused a rectangular depression by the ablation of the targets upper layers. For the detailed frame the beam voltage was 20kV at a magnification of 80,000 times.

Laser scanning microscopy combines optical and laser light (408 nm) to generate images that are not only very sharp and detailed but can also be used to construct a 3D image of the surface. This makes it superior to SEM analyses, particular with respect to non-destructive morphology investigations and measurements.

In general the Keyence VK-X200K LSM is an instrument developed for material science and quality control of products with high requirements (Metal and automobile industries, electrical machinery and electronics industries, chemical and raw materials industries). However, in this study it evaluated also as a valuable instrument for impact investigations (see section below).

2.4.1 Laboratory situation and sample handling

After the samples were cut, embedded in epoxy resin and polished, they were put into separately capped sample boxes (Fig 2.16). Only during bombardment the sample surface was orientated in a vertical position. Afterwards the surface of each target was kept horizontal during storage, LSM or SEM analyses. It should be noted that Cu oxidises under normal conditions. The sample boxes are stored in a cabinet to shield them from sun light. Special sample boxes, which could be filled with argon air would be appreciated and might be desirable for future works.

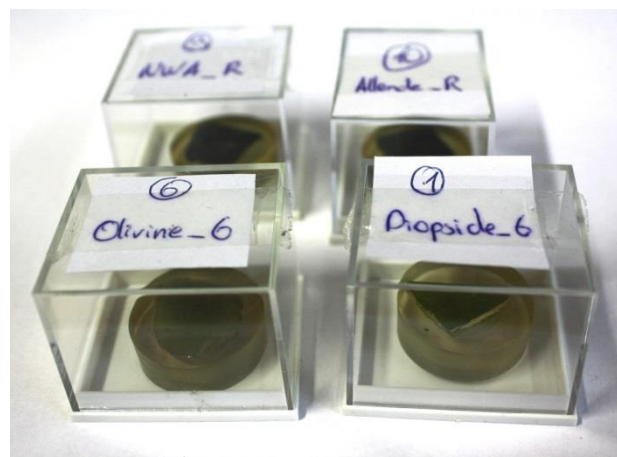


Figure 2.16: Example of mineral target storage after bombardment.

The dust accelerator, LSM and SEM laboratory both do not have any clean lab status, so these conditions can be also considered as normal.

2.4.2 Principles of confocal laser microscopy

In this study a Keyence VK-X200K confocal laser microscope with an electric stage controller (X-Y directions) was used (Fig. 2.17). The exact technical and precision parameters are shown in Table 2.02.

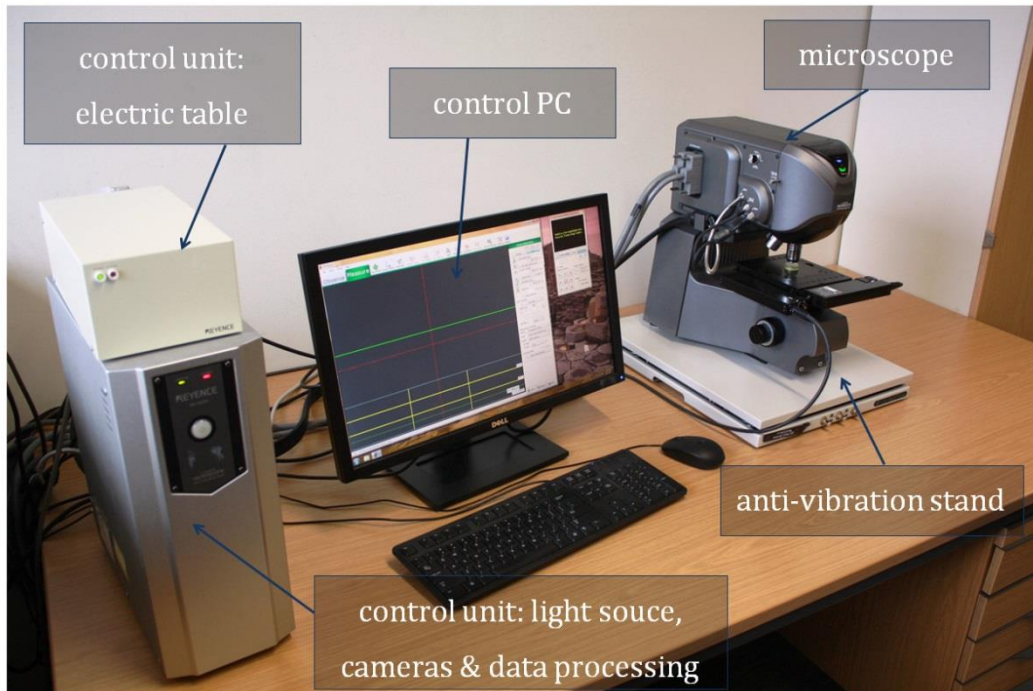


Figure 2.17: Component overview of the Keyence VK-X200K confocal laser microscope.

Table 2.02: This information's are derived from the VK-X200K user's manual. (Keyence, 2011). * The maximum pixel resolution is only accessible with a 150x objective lens.

Laser light wavelength	408 nm
Maximum output	0.95 mW
Monitor magnification	3000 x
Objective lens magnification	150 x
Operation distance	0.2 mm
Numerical aperture (N.A.)	0.95
Depth of field	0.45 μm
Height repeatability (3σ)	36 nm
Height display resolution	$\sim 0,5$ nm
Width repeatability (3σ)	20 nm
Width display resolution	~ 1 nm
Measurement quality	2048 x 1536 pixels
Maximum pixel resolution (1 px)*	~ 21.5 x 21.5 nm
Maximum angle	87.1°

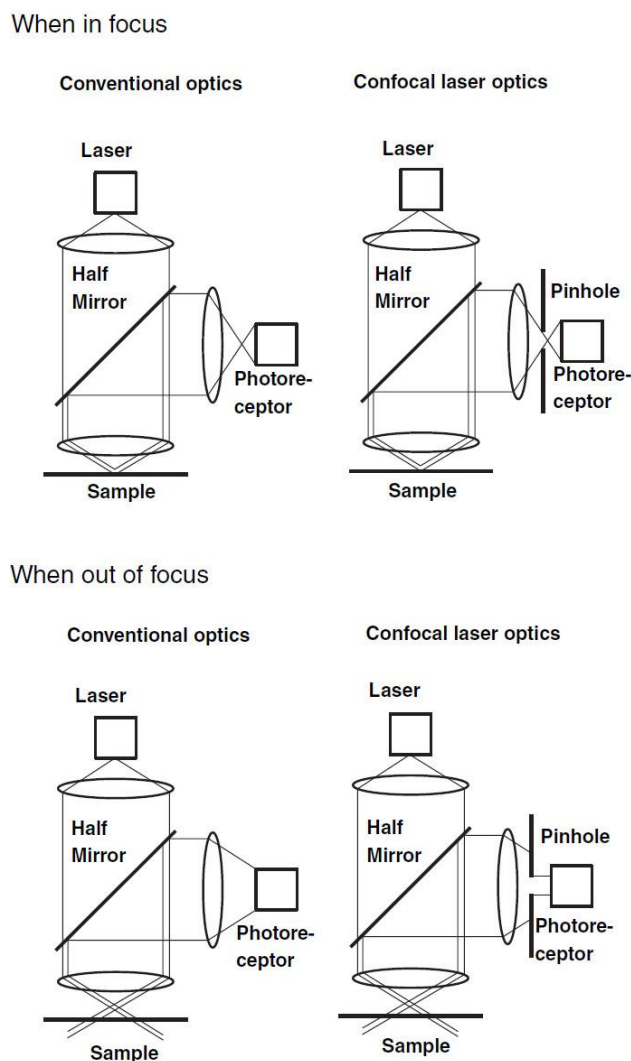


Figure 2.18: Principles of light path in conventional optics and confocal laser optics. Figure taken from KEYENCE (2011).

When the light is reflected from the specimen it enters the photoreceptor in the conventional optics and confocal laser optics pathway. The principles are the same except for the confocal laser optics, which has a pinhole before the photoreceptor that allows only a fraction of light to enter (Fig. 2.18). Hence, when laser light is out of focus it does not reach the photoreceptor (KEYENCE, 2011). A confocal laser microscope only illuminates one single point at a time, which avoids unwanted scattering of light (RAI & DEY, 2011). The smaller the pinhole diameter (it cannot be infinitely small), the better the resolution of the system (WILHELM *et al.*, 2003).

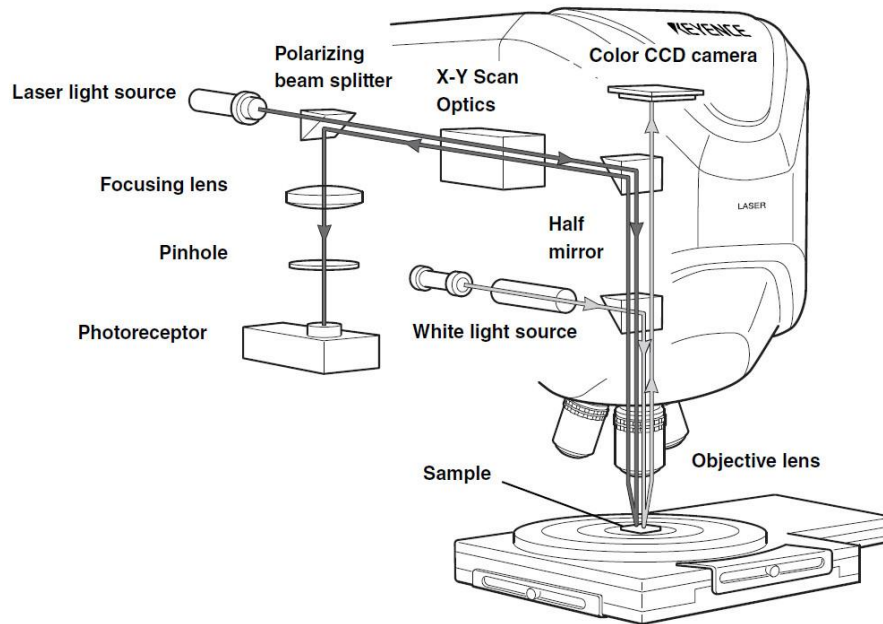


Figure 2.19: Simplified schematic of a Keyence LSM (KEYENCE, 2011).

There are two light paths in the LSM (Fig. 2.19). One starts at a white light source, pass through mirrors onto the sample stage, where it gets reflected from the specimen and is received by the Color CCD camera in the end. This can be considered as the conventional optical light path. The second light path starts at the laser light source (408 nm), and is lead to the specimen by mirrors and optics to adjust X-Y point orientation on the specimen. The reflected laser intensity, travels back and gets filtered by unwanted light bands in the polarizing beam splitter, and then focused to the pinhole. The pinhole is a crucial component in confocal laser microscopy, which allows only light from the focal point to reach the photoreceptor.

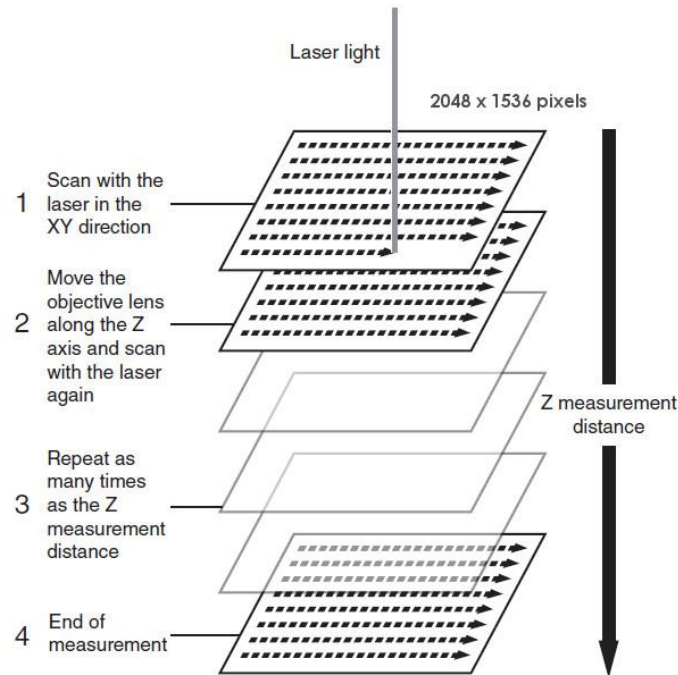


Fig 2.20: Illustration of confocal LSM scanning process (Keyence, 2011).

The scan process of a specimen (by the LSM used in this study) is facilitating single beam scanning (Fig. 2.20). The semi-conductor laser first scans a pixel in horizontal (resonant scanner) and then in vertical (galvano scanner) direction.

After the scanning of an optical slice is completed, the objective moves one step (z-pitch) along the z-axis and repeats the scan procedure. This can be compared roughly with tomography. By scanning every slice in progressing z-positions, a pixel's information will be replaced with those of higher intensity. This ensures that each pixel obtains only the information with the highest laser intensity or RGB data. Capturing the information of a single optical slice alone contains no height information and is carried out within seconds (KEYENCE, 2011).

After the scanning process is completed, the data (RGB values of CCD camera and laser intensity values) of each pixel are combined and fused into one large image.

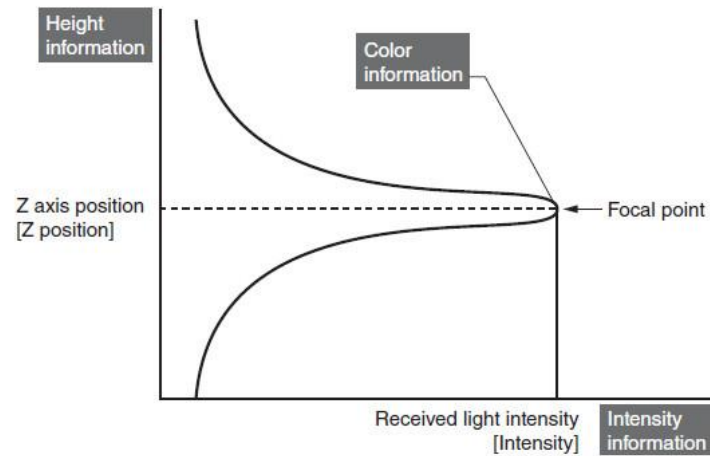


Figure 2.21: Illustration of the acquisition of pixel information. The focal point represent the point of maximal light intensity along a given z-axis (Keyence, 2011).

By repeating scans along the z-axis, the reflected laser intensities of any z-position are obtained for each pixel. The position with the maximum intensity detected represents the focal point. A focal point holds the information of height, color and laser intensity (Fig. 2.21). The construction of a deep field color image, the laser intensity image and a height image is based on this information.

The optical slice thickness (aka. depth discrimination, WILHELM *et al.*, 2003) or z-pitch (for Keyence user) is exclusively dominated by the pinhole diameter, for any given objective lens. However, it should be taken into account that z-resolution in confocal laser microscopy can never be as good as its lateral resolution, which is inherent for nature of such optical devices (WILHELM *et al.*, 2003).

2.4.3 Measuring procedure with a Keyence confocal laser microscope

In this chapter the methods for acquiring the measurement data of mineral targets are explained in detail. All necessary steps to ensure reproducibility are described in two following guiding sections – the Keyence *VK-Viewer* and the Keyence *VK-Analyzer Modul*. Although this guideline is aligned to Keyence instrument and software packages, the following section should be applicable to similar LMS's instruments and associated software.

For the purpose of this demonstration, a mineral defect on the non-bombarded, non-bombarded Olivine_7 target will be investigated and measured as an example.

VK-Viewer

The *VK-Viewer* is the graphical user interface (GUI) application to remotely operate the VK-X210 LSM. It is possible to fully control the specimen table (X-Y directions) and the working distance of the optics (z-direction), at least within a range of 7 mm for the fine adjustments. All images in the following section are taken from *VK-Viewer* application (Fig 2.22).

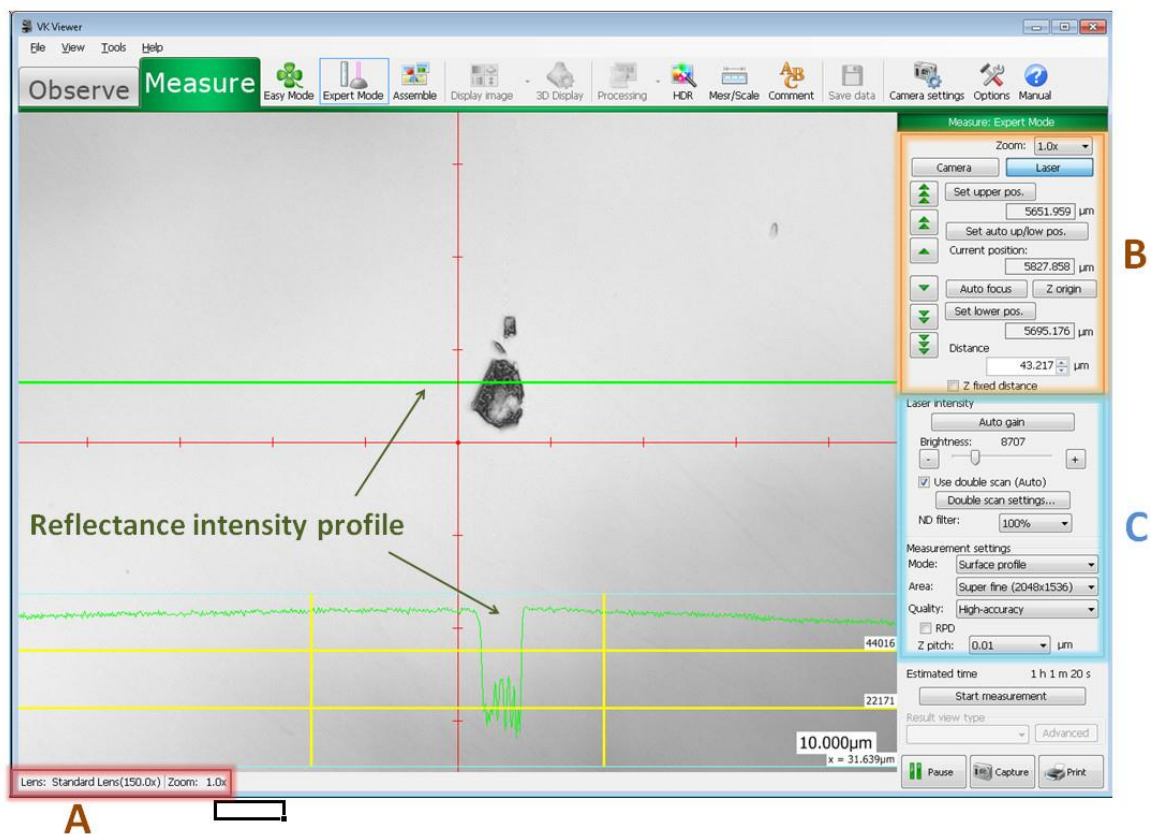


Figure 2.22: The GUI for the Keyence VK-X210K LSM. Section [A] shows the selected lens and zoom factor; section [B] shows all necessary options for the laser scanning process regarding the z-axis; section [C] shows all options for laser intensity, the image resolution and the steps along for the working distance (z-axis). The reflectance intensity profile (green line) and its corresponding graph in the lower section illustrate the less bright (dark colors) mineral defect compared to the surrounding surface (bright colors). When intensity in the graph reaches zero, this can be considered as signal intensity of zero. No information can be gathered at such pixels or regions. On the other hand, when the signal is too strong it causes an intensity oversampling, resulting in bad information.

Explaining method of the VK-Viewer GUI by acquiring a scan of a minerals surface:

- Section A
 - For the highest *magnification* a *150x lens* was used. This is indispensable for micro-feature investigations. Furthermore, with a smaller lens it is not possible to have access to very fine scanning of optical slices (z-pitch = 0.01 μm).
In addition, when using the maximal magnification at the lowest z-pitch value, any vibration of the microscope will disturb the result of the scanning process. Placing an anti-vibration stand or comparable below the LSM will compensate the majority of vibrations.
- Section B
 - *Zoom (digital)*
Using any magnification of digital zooming does not give any advantages in scanning the samples. However, comparable functions to digital zooming are always available after the scanning process, in the *VK-Analyzer*.
 - *z-distances*
Due to the nature of crystalline properties (transmission effects) of the targets, it was always necessary to apply the correct *z-distance* of measurement manually. This defines the starting and end position along the z-axis for the scanning process. Depending on depth of craters or a mineral defect, or on the height of an overlying object, this value varies, and needs to be adjusted for any new selected frame on the surface.
 - *Laser intensity*
The *laser intensity* is derived by the brightness that gets reflected from the specimen. For this example, the actual reflectance intensity is illustrated by the green profile drawn over the mineral defect (Fig. 2.22). Finding the sufficient amount of intensity is crucial for an accurate investigation of surface features subsequently. Experience showed that the use of *double scan* option increases the accuracy of scans during this study. Although time consuming it should be considered.

The use of maximum resolution is highly recommended. High resolutions will later decrease the chance of noise or graphical artefacts, after *filter process* and *noise reduction* are applied. The maximum resolution available for VK-X200K was 2048 x 1536 pixels.

Z-pitch is synonymous with the distances between each step (optical slice thickness) along the z-axis used for a scanning process. For this study the minimal possible step size of 0.01 μm was selected. The reduction of the *z-pitch* massively increases the scanning time.

Dividing the *z-Distance*, from section [A] by the *z-pitch*, gives the amount of optical slices that will be recorded by the scanning process.

77 random samples were used to test if z-pitch (0.01 μm) and/or the laser wavelength (408 nm) result in recurring diffraction patterns and if they affect the interpretation of surface morphology. Although the investigations of this study entered the sub-micron scales, such an effect could not be verified.

VK-Analyzer

As stated above, the Keyence VK-200K is actually a product established for material sciences especially for surface roughness investigations. Such, the *VK-Analyzer* is strongly focussed on roughness applications (Fig. 2.23).

Every scan that is completed by the *VK-Viewer*, will automatically open the *VK-Analyzer*. The reference manual for the *VK-Analyzer* does not include certain aspects of the method explained in the following section of this chapter; neither was it designed for impact studies. For that reason the relevant tools and key-functions of this software, that are important to this work, are explained in detail and placed in chronological order. All images in the following section are taken from *VK-Analyzer* application. Crucial parts of the GUI are highlighted with orange boxes and referring numbers.

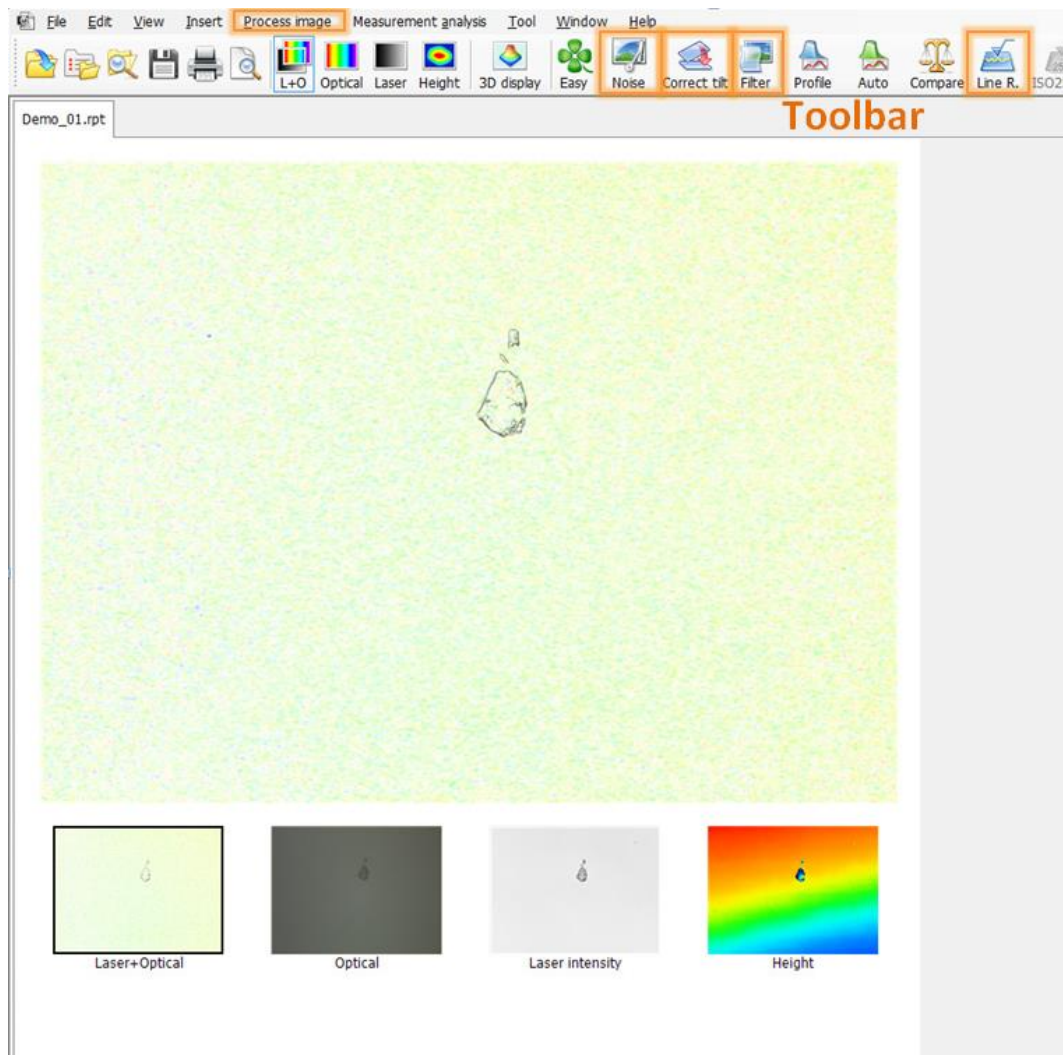


Figure 2.23: This image shows the default view that automatically appears after a scanning process is completed, or when an existing file is loaded into the *VK-Analyzer* (Image captured from Keyence *VK-Analyzer* application).

The important *VK-Analyzer* functions of this work are (Fig. 2.23):

- Correct tilt
- Noise reduction
- C-Laser DIC image creation
- Filter
- Line roughness tool for measurements

Correct tilt:

In general tilt correcting is the first crucial step for preparing the data for any kinds of measurements or other tools. If not applied, measurements may become incorrect. “Correct tilt” can be started via the toolbar (Fig. 2.23).

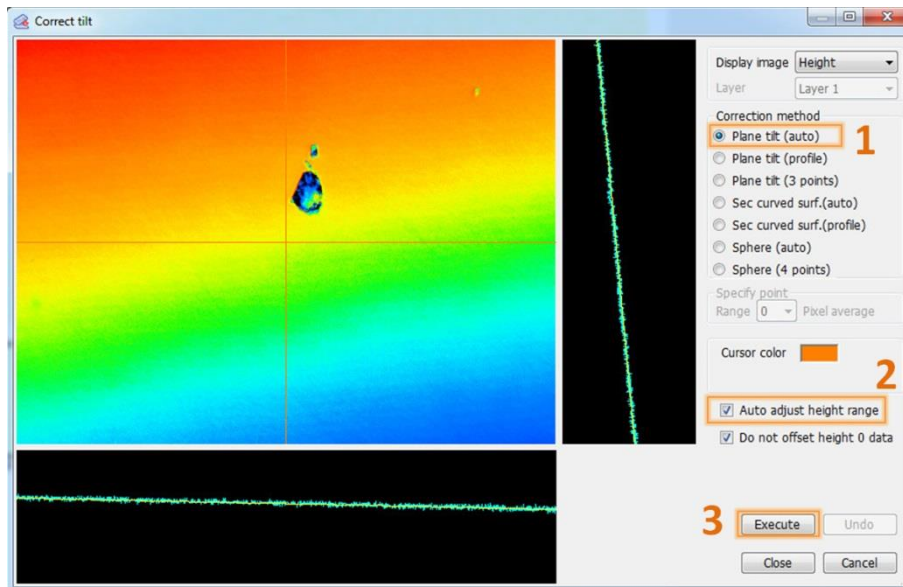


Figure 2.24: This image shows the tilt correction menu before applying the necessary options.

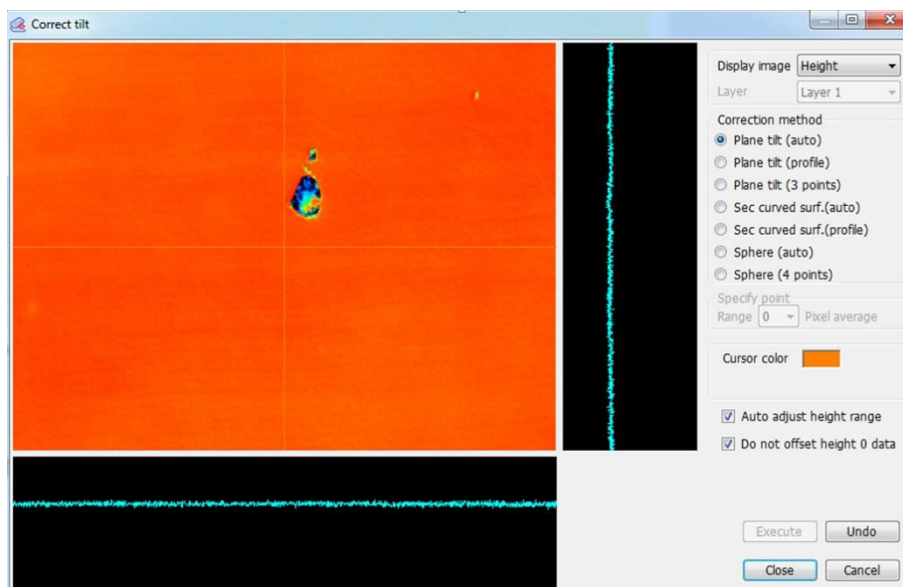


Figure 2.25: This image shows the tilt corrected image with new applied height colors.

The large box on the left shows the actual surface and its degree of tilting by height colors (Fig 2.24). In the black box at the bottom the inclination in x-axis is shown. The black box on the right shows the inclination of the y-axis. The orange reticule in the large box marks the inclination profile for the x-y-axis. [1] For the most cases the “*plane tilt (auto)*” option is sufficient. [2] Checking the “*auto adjust height range*” option re-applies the height colors appropriately to the new surface. Applying a specimen or a target onto the microscope table with a less inclined surface is recommended. This does not only save scanning time, it also reduces the degree of tilt correction, and hence it reduces the chance of adding noise to the data. [3] Settings are confirmed by clicking “*execute*” (Fig. 2.25).

Noise elimination:

It is recommended to reduce noise for submicron to micron scaled investigations. “*Noise elimination*” can be started over the toolbar (Fig. 2.23).

This menu shows a basic auto noise elimination function. [1] Using “*normal*” noise detection and [2] confirming it with “*OK*” satisfies all the requirements (Fig. 2.26).

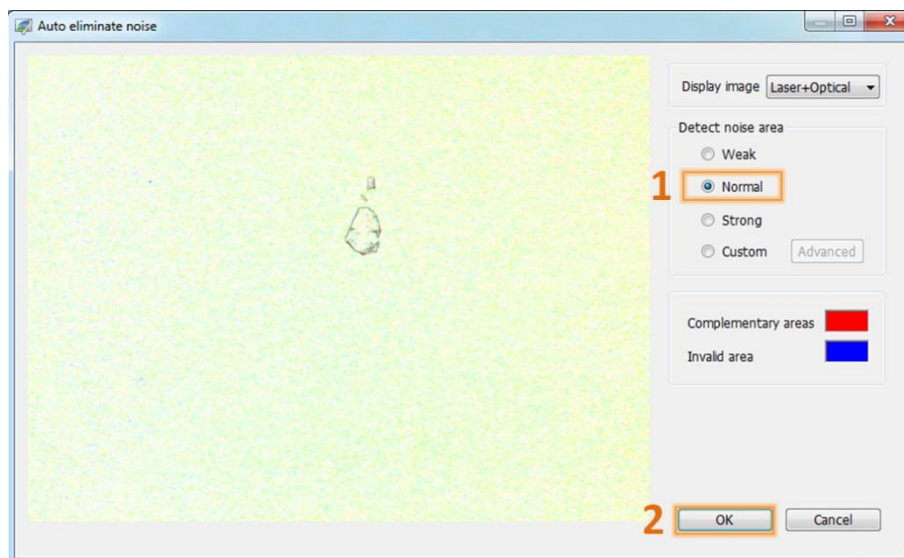


Figure 2.26: This image shows a basic noise reduction menu.

C-Laser DIC

The replacement of the „*Laser+Optical*“ image by the creation of a „*C-Laser DIC*“ image is a great opportunity to see even more details than the regular images will exhibit. The menu for „*Laser+Optical/C-Laser DIC*“ is started from the „*Process image*“ dropdown menu (Fig. 2.27).

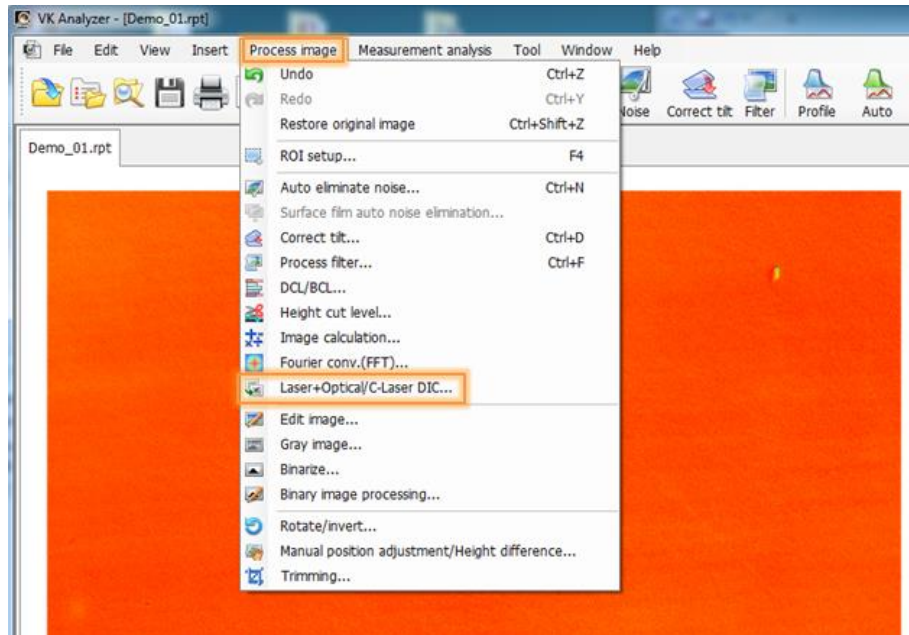


Figure 2.27: By default C-Laser DIC creation is not listed on the toolbar.

The C-Laser DIC technique, which is used in the software is a computational method and should not be confused with the technical procedure where a Wollaston or a Nomarski prism is used to enhance the contrast of an image (BRANDMAIER *et al.*, 2016).

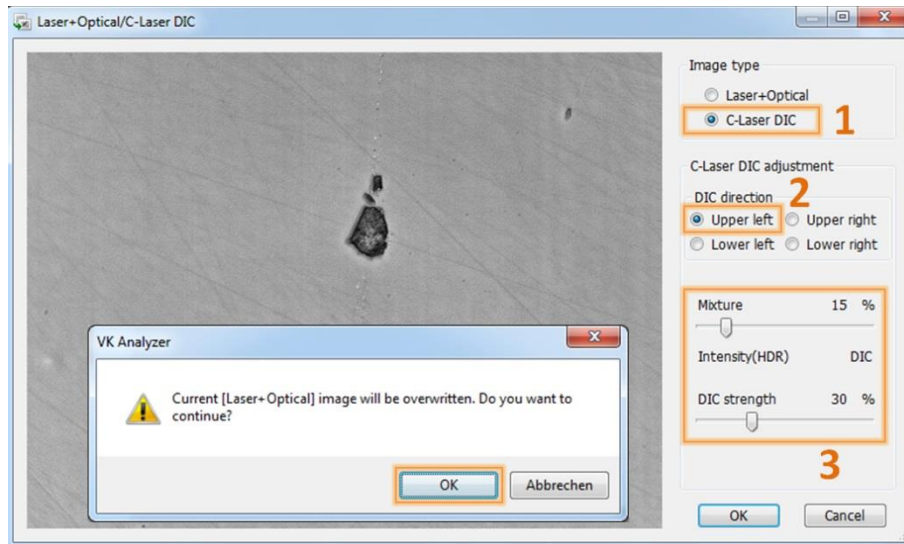


Figure 2.28: Settings in the “*Laser+Optical/C-Laser DIC*”, which yield the best results for purpose of this work.

By combining the laser intensity image and the height image with an artificial light cast the software performs differential calculation to depict minute irregularities on the specimen’s surface.

First it is necessary to check [1] “*C-Laser DIC*” as “*Image Type*” to enable all other DIC options (Fig. 2.28). [2] The “*DIC Direction*” allows choosing the position from which direction the artificial light should be cast. The default value “*Upper left*” was kept for all investigations. Finally the appropriate setting for the *C-Laser DIC* image can be made. The effects of changing the position of any slider [3] will be shown in the large preview window on the right in real time. The “*Mixture*” slider represents how the proportion of the laser intensity image (left end) and the height image (right end) is weighted. 15 % turned out to be the most efficient for this study. The “*DIC strength*” slider regulates how strong the effect of the artificial light cast is taken into account. 30 % turned out to be the sufficient for this study. By confirming the settings on “*OK*” button the user is asked to verify the overwriting of the “*Laser+Optical*” image, with the creation of the “*C-Laser DIC*” image. As it was not necessary to work with “*Laser+Optical*” images there are no objections in overwriting it.

Process filter:

This menu allows adding further and the final noise reducing filters. It can also help to improve issues of pixels with signal intensities of zero. “*Process filter*” can be started by using the toolbar (Fig. 2.23).

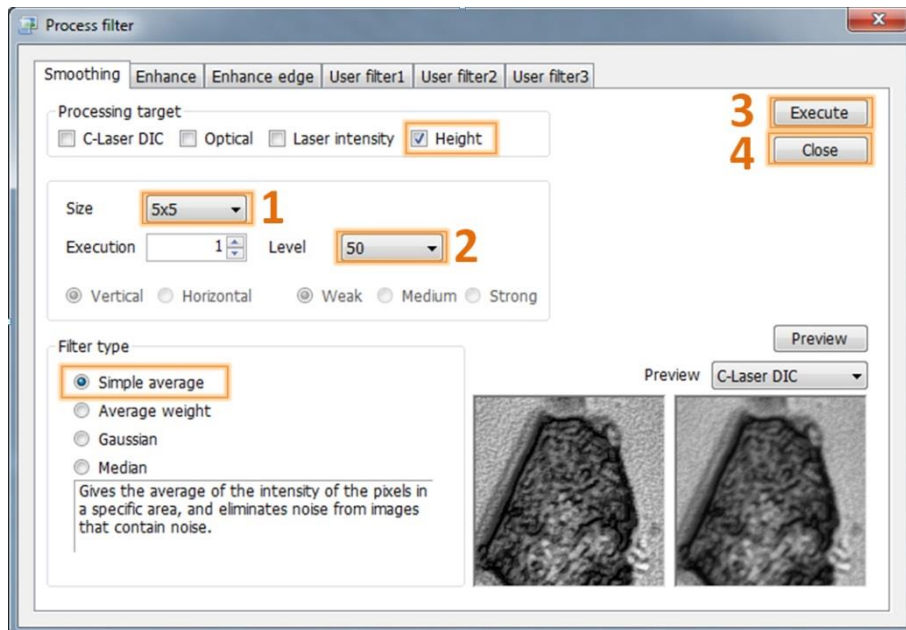


Figure 2.29: The “Process filter” tool is a good method to further reduce noise and the majorities for pixels with signal intensity of zero.

Keep the “*processing target*” checked to “*height*” is crucial for subsequent measurements (Fig. 2.29). If only the enhancement of image quality is desirable, the corresponding image needs to be targeted. Experience showed that keeping the “*Filter type*” with the setting “*Simple average*” is appropriate for the targets aimed in this study. “*Average weight*” was also decent. “*Gaussian*” and “*Median*” filtering was not as useful. It is recommended to [1] use a “*Size*” of “*5x5*” with [2] a “*Level*” of “*50*”. This will help to de-noise the major disturbances on the target surface, but will still keep enough details to other topologies. The “*5x5*” option can also slightly help do reduce pixels with signal intensity of zero. The best influences of the filter effect can be observed, when “*C-Laser DIC*” is selected in the “*Preview*” box. This preview box is displaying in real time. [3] Settings are confirmed by clicking on “*Execute*”.

Users should *test the process filter* settings themselves in order to achieve:

- Further noise reduction of the surface by keeping as many details as possible on interesting morphologies
- Reduce the effects of pixels with signal intensity of zero, if there are such

When all preparations of tilt correction, noise reduction and the creation of C-Laser DIC image are done, the surface investigation can be started.

Line roughness

To investigate a scanned target surface I recommend the “*Line roughness*” tool over the “*Profile*” tool, as it can store multiple profiles. It should be noted that files could get very large, when saving hundreds of profiles. The “*Line roughness*” tool can be started by the toolbar (Fig. 2.23). Measuring the roughness of surfaces is one of the flagship features of the Keyence LSM, thus the respective tool covers an overload of functions and information, which are not important for impact studies.

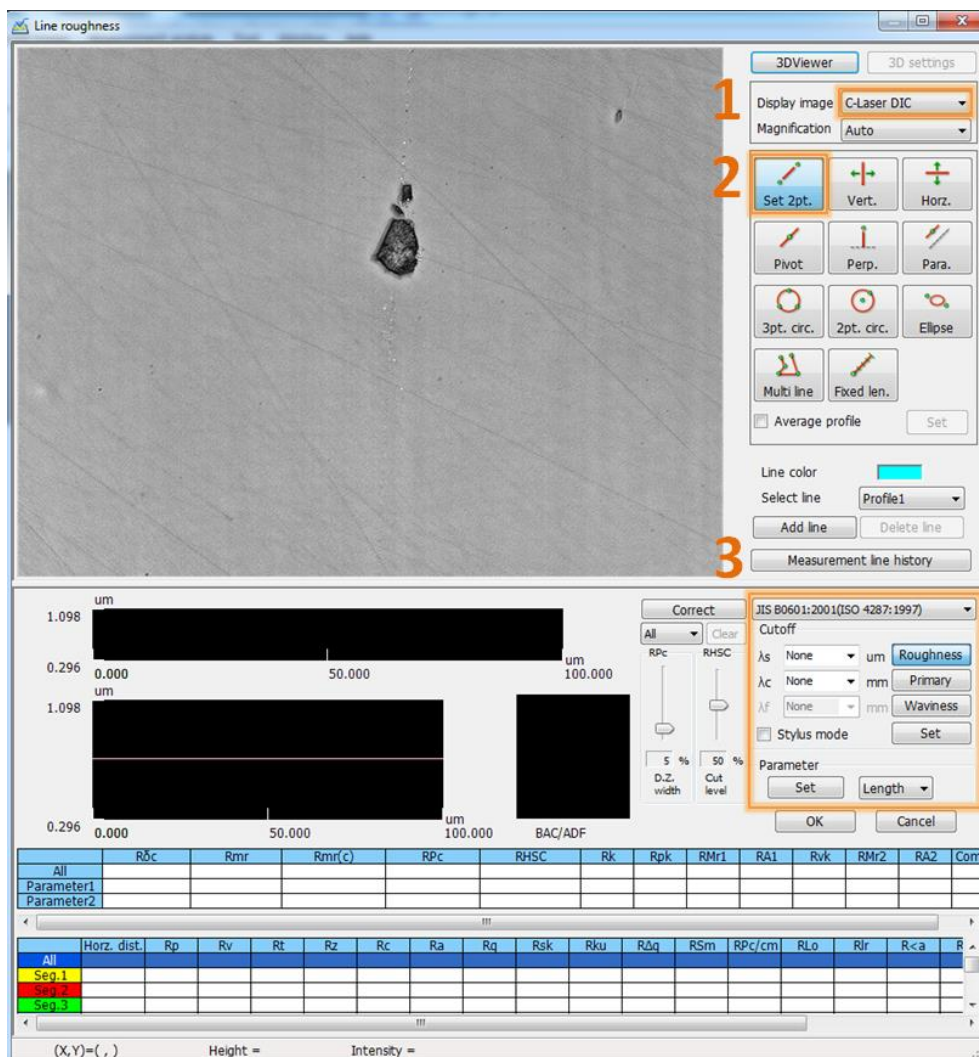


Figure 2.30: The default view of the “*Line roughness*” tool and the basic pre-settings for multiple profile acquisition.

To prepare acquisition of multiple profiles (Fig. 2.30) it is recommended to choose [1] either “*Height*” or “*C-Laser DIC*” as “*Display image*”, which helps to identify surface irregularities much easier. If not already highlighted [2] “*Set 2pt.*” tool should be se-

lected, which allows the drawing of point to point measurements in the main overview window (top left). The section at the right shows the standards and parameters for roughness control [3]. They can be left on default as they have no effect on diameter and absolute height or depth acquisition.

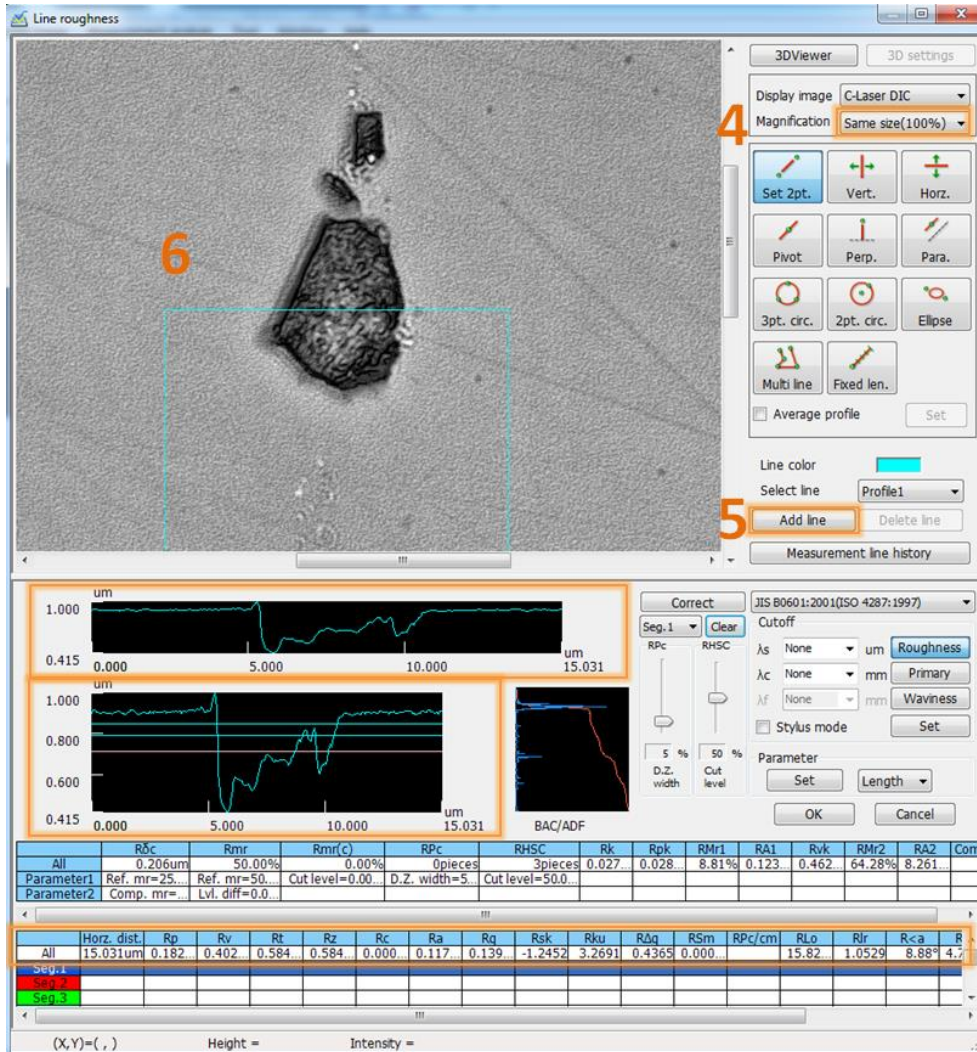


Figure 2.31: Drawing a profile with the “Line roughness” tool.

Depending on the size of the surface feature of interest the [4] the maximal “Magnification” is selected (Fig. 2.31). Besides the feature itself, a sufficiently large surface area should be included in the main overview window and in the profile. For this particular example “Same size(100%)” is the most appropriate magnification. The next step is [5] “Add line”, which allows to [6] draw a point to point measurement into the main overview window. The first click marks the starting point of the profile. By hovering of regions of the target, the profile window in the bottom section will show the

(Seg.1; yellow) represent the diameter of the mineral defect, that is now colored in yellow. This segment can also be [8] followed in the main overview window, with a yellow line. Now in the spreadsheet the diameter value can be picked [9] from the “Horizontal distance” of the first Segment 1. The “Rz” value in this demonstration represents the depth. It can be observed that the “Rz” value for “All” and “Seg.1” are identical. “Rz” is always computed as overall maximum difference in z-axis within a segment. As the left starting point of “Seg.1” is on a very steep edge, the program picked the “Rz” value from the closest position, of the highest point where a change in gradient occurs. In this demonstration the closest position, with the highest point with a change in gradient is also the maximal elevation of this profile. It is even beyond the surfaces level. Picking this particular “Rz” value as depth would be wrong, so a second segment is needed, which is mostly the case for negative features, like surface defects or craters.

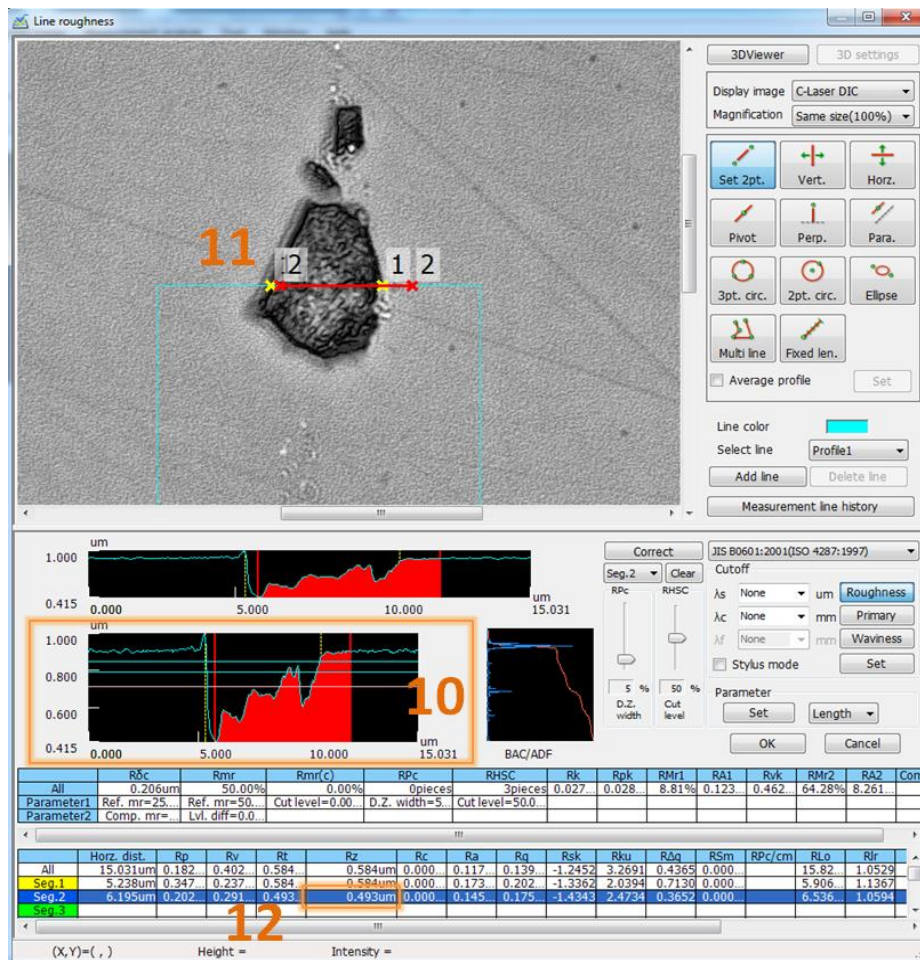


Figure 2.33: To derive the depth of a feature in most cases a second segment is necessary.

For positive elevation features (sticking or attached particles) it is not always necessary to apply a second segment (red). But using two segments ensures that “Rz” value, which represents height or depth, can verify the value of Segment 1 (yellow). This demonstration shows a negative feature (i.e. mineral defect), so a second segment needs to be applied.

To apply a second segment one needs to proceed in the same way as for the first segment (Fig. 2.32). For the correct depth value a [10] new segment is drawn in the lower profile box, ranging from the lowest point at the bottom of the profile to the surface (Fig. 2.33). Again the [11] new segment (Seg.2, red) can be followed in the main overview window. For “Rz” the software computes the maximal differences in z-direction within a segment. The correct depth [12] can be found in the row “Seg.2” (red) as “Rz” in the spreadsheet below.

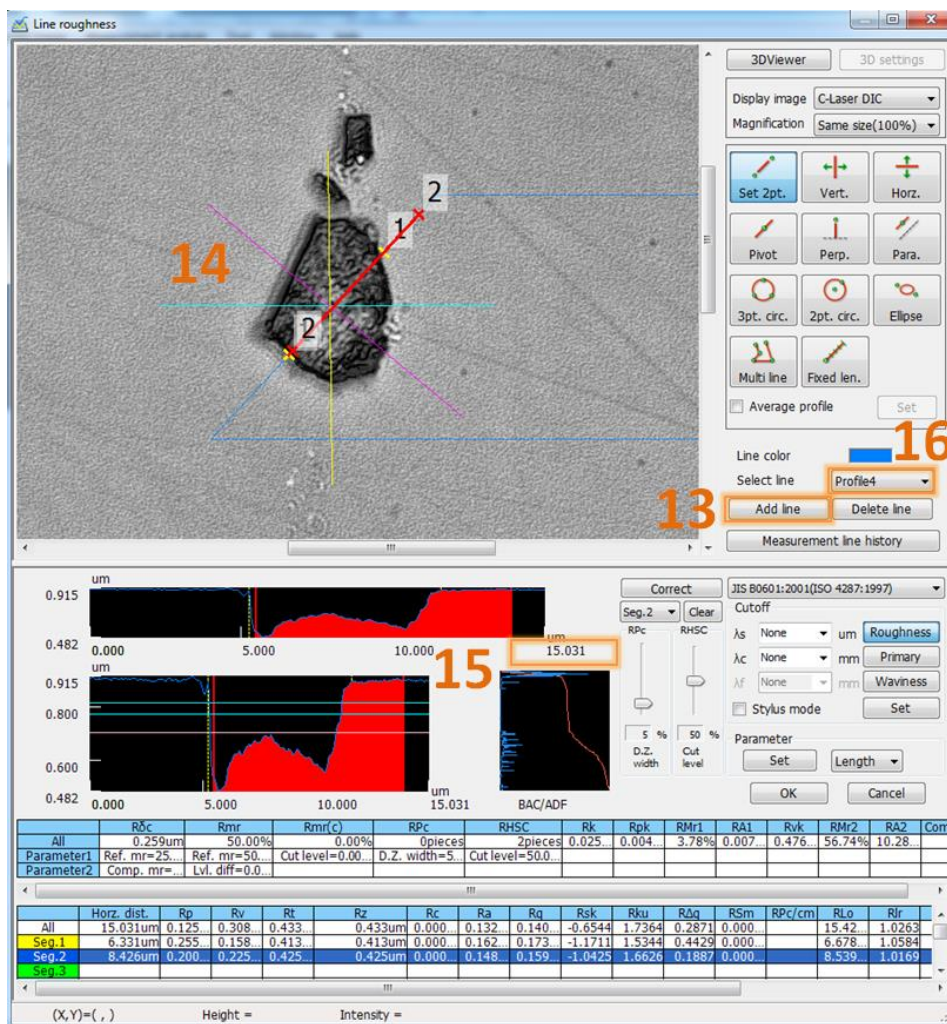


Figure 2.34: Taking four profiles ensure representative values for diameter and depth or height.

To complete the measurements of this demonstration, additional three profiles need to be drawn (Fig. 2.34). First step is again [13] “Add line”, which allows to [14] draw a new profile into the main overview window. Here the procedure repeats from step [7] to [14] until four separate measurements/profiles are acquired. It is recommended to use the same [15] distance of a profile for a single feature. This guarantees the comparability between every profile of this feature. The current number of a profile and all its information are stored and can be followed in the [16] “Select line” drop-down menu.



Figure 2.35: Verification of the intensity of laser reflectance. A 0 value intensity can be observed highlight in the orange circle.

To ensure the quality of a profile it is possible to review the reflectance of laser intensity (Fig. 2.35). By [17] clicking “Correct” and [18] selecting “DCL/BCL” (Dark Cut Level/Bright cut Level) from the drop-down menu a new windows appears. In the top

box the green profile represents the intensity of laser reflected from the objective's surface. The box below shows the interpreted profile, taken into account the height values of every pixel. The "DCL/DCL" menu can be used to set new thresholds and cut out specific values of dark or bright light, which results in smoothing of the profile curves. It can be also used to see if there are any low intensities of laser reflectance. In this demonstration the [19] curve is reaching signal intensity of zero (orange circle in Fig. 2.35). This means in turn that at this special pixel the information is interpolated from the surrounding pixels. In this particular example, one pixel is not an issue, but if more pixels are affected, this can result in inaccurate profiles.

Especially on the Olivine_6 target it could be observed that crater profile was often asymmetric, which happened to be the case for the majority of craters on the mineral targets (Fig. 2.36). To take into account this effect it was decided to take four profiles for each investigated feature. This should ensure the given mean values will represent the diameter and depth or height more accurately. Moreover, this method helps to provide a more secure acquisition of the depth parameter, which might be an issue, as light waves cannot travel infinitely through a pit/hole and are reflected back.

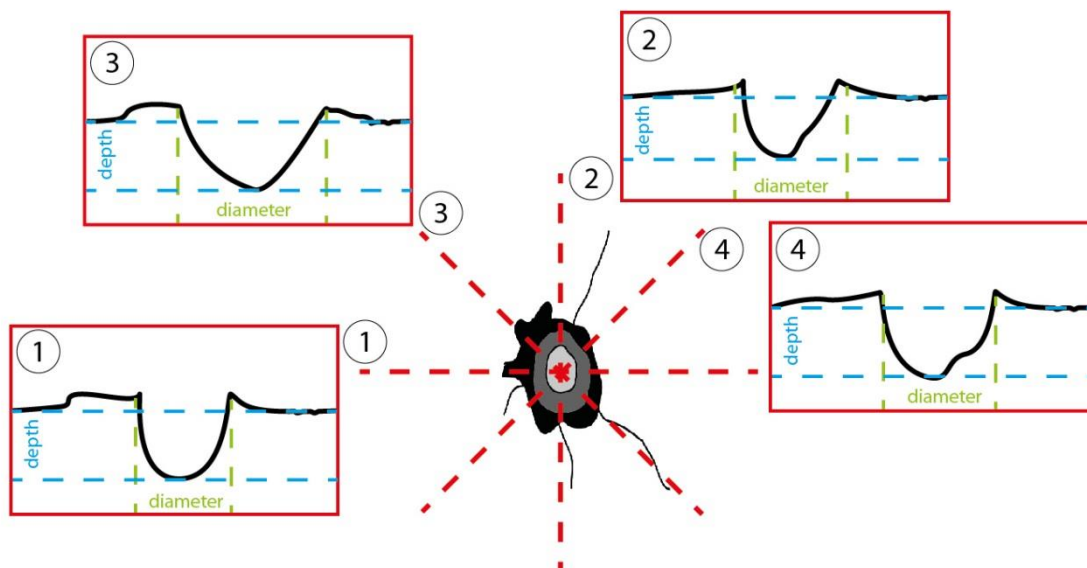


Figure 2.36: Simplified schematic of profile acquisition. It illustrates an asymmetric appearance of an olivine crater. Each of the four profiles slightly varies when compared to the others. Such, the acquisition of four values for depth or height and diameter is useful to get an appropriate mean. This asymmetric appearance is most likely due to the nature of minerals, which have their own cleavage preferences; e.g., olivine fractures occur rather conchoidal.

Another advantage of crater analysis with LSM compared to SEM is the aspect of time. There is no need for coating, evacuating and pumping of a sample chamber, stereo scanning and computing of crater dimensions or similar objects of interest. After a basic investigation method is laid down, impact feature evaluation is less time consuming with the LSM

For the investigations on impact features, a section of the bombarded target was selected which held the most impact features. This could be determined by taking individual pictures with low resolution and generate a stitched overview. In the designated olivine section, sampling frames were taken and analysed with analysing software "*VK-Analyzer*" provided by Keyence. The control data are acquired on a second non-bombarded olivine target.

3 Projectile properties

3.1 Shape and morphology of Copper projectiles

For the particle's accelerating process it is necessary to use conductive materials. Copper dust has been chosen instead of commonly used iron or aluminum dust, as the latter can be lattice elements of olivine, enstatite, diopside or antigorite. By choosing Cu, projectile identification on targets and a clear distinction of target and projectile residues is easily achieved. In addition, Cu has a higher atomic number compared to Fe and Al, and can be easily identified on SEM-BSE images.

Different Cu dust samples with variable sizes and shapes were used in test bombardments. For the olivine target two particular dust samples were used in this study: an inhouse produced mixture ("*Cu-Charge A*"; Fig. 3.04 and 3.05), and a commercial sample bought from "*Goodfellow*" company (Fig. 3.01 and 3.02). During the bombardment of the Olivine_6 target with "*Cu-Charge A*" dust particles, particle fluxes were low. LSM and SEM investigations showed that these particles were irregularly shaped, fused clusters or agglutinating. If a Cu dust contains too large individual particles, these can damage the pulsing needle or jam the exit of the dust source in the dust accelerator. None of the "*Cu-Charge A*" manufactured dust samples performed as good as the commercial product from the special material vendor "*Goodfellow*" bought later on. These are ~ 96 % spherical, less agglutinating and have size fractions below 400 nm, as seen by LSM and SEM investigation.

BROWNLEE *et al.* (1973) stated that micrometeorites are roughly equidimensional and have densities of about 2.5 g/cm³. Therefore, using spherical particles is desirable.

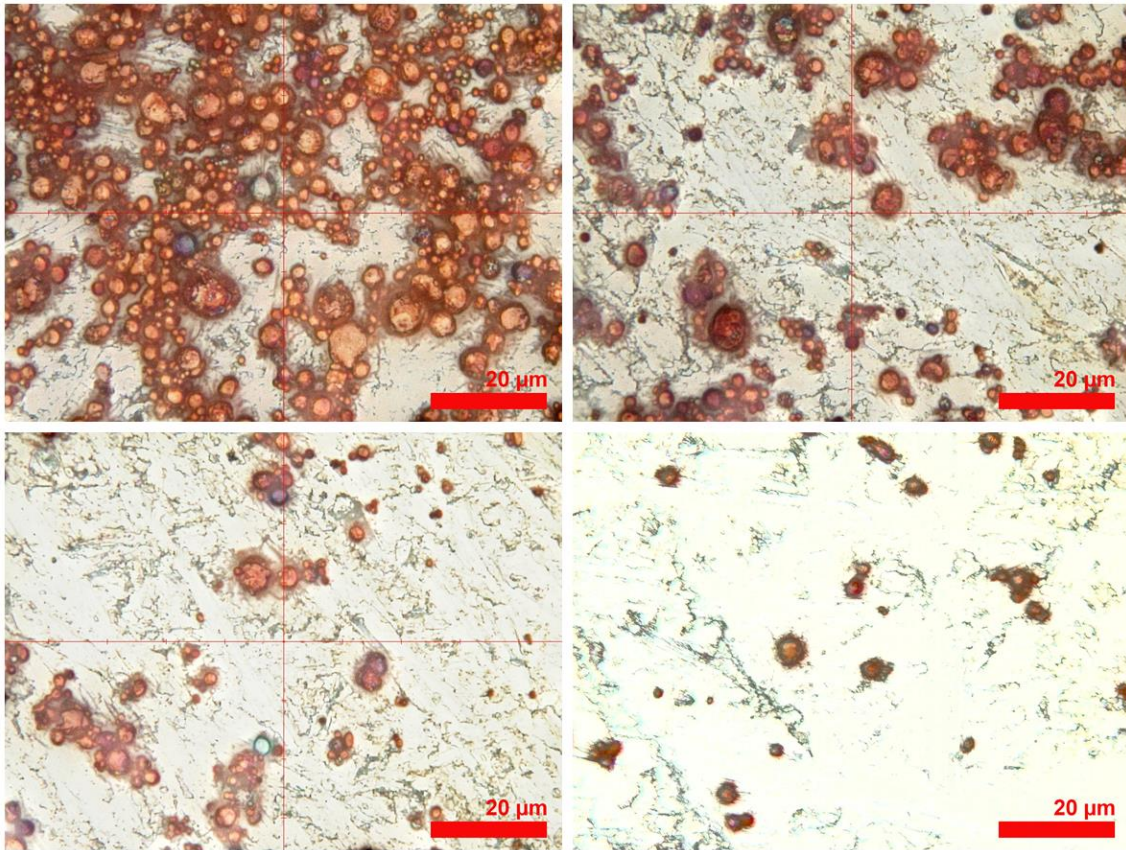


Figure 3.01: LSM depth of field images of "Goodfellow" Cu particles.

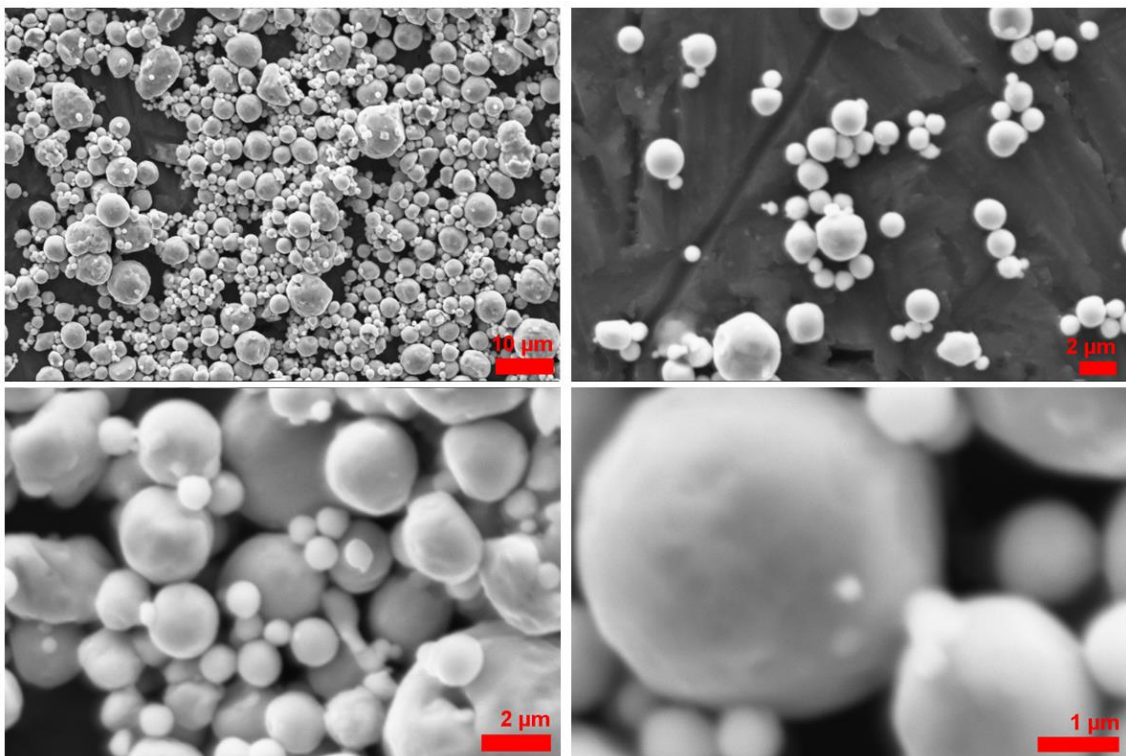


Figure 3.02: SEM-SE images of the "Goodfellow" Cu particles.

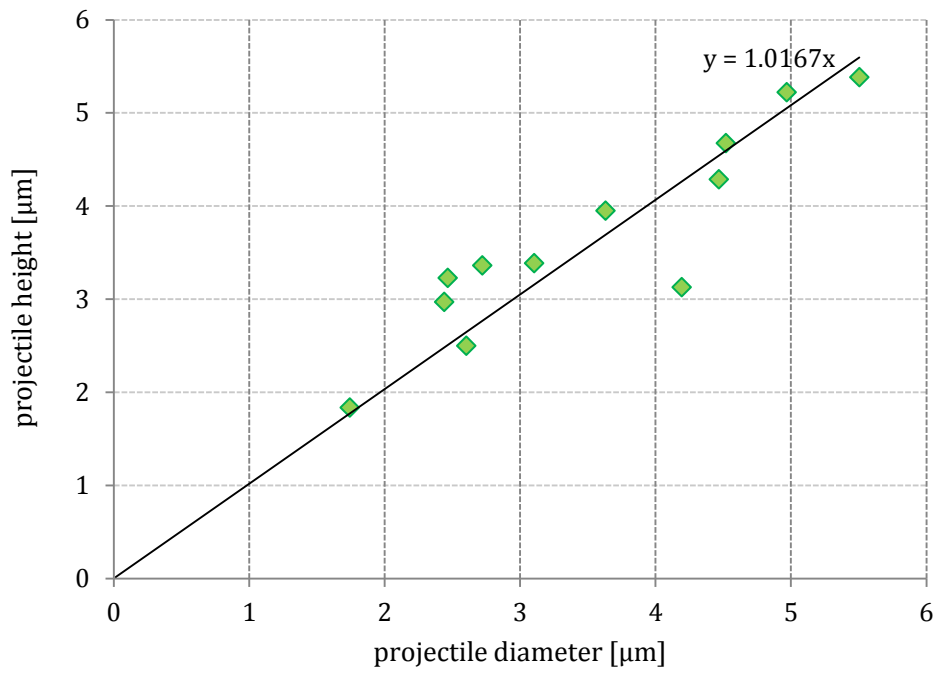


Figure 3.03: This plot shows the scattering of "Goodfellow" Cu particles by the measurements of their height and diameter. Particles are nearly spherical.

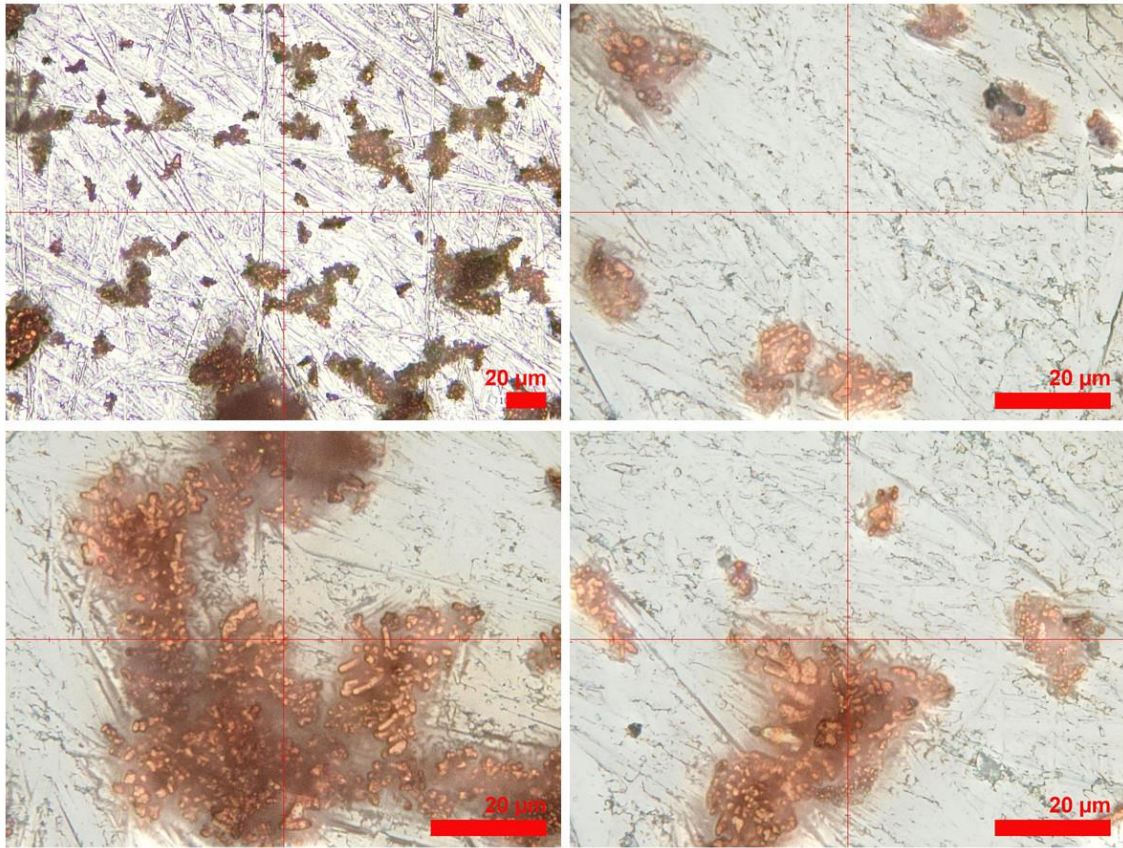


Figure 3.04: LSM depth of field images of “Cu-Charge A” Cu particles.

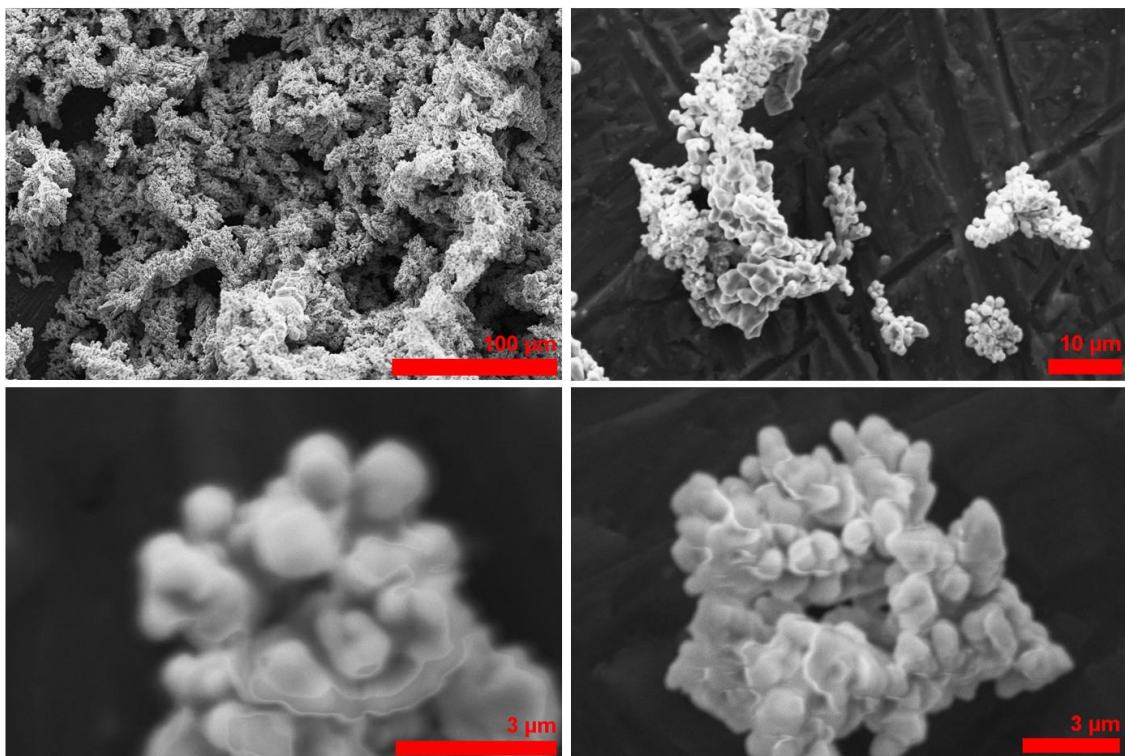


Figure 3.05: SEM-SE images of the “Cu-Charge A” Cu particles

LSM optical and SEM-SE images (Fig. 3.01 & 3.02) of “*Goodfellow*” dust show nearly ideal spherical appearance of Cu particles, confirmed by plotting height to diameter ratio d/D_p of 0.96 (Fig. 3.03). Images of “*Cu-Charge A*” (Fig. 3.04 & 3.05) show clustering and large sizes of Cu particles, which is undesirable for the purpose of this study.

3.2 Bombardment flux rates and impact counts

Every target was mounted onto a sample holder and placed in the center of the beam line through an airlock specially designed for such kind of experiments. The sample holder can be manually adjusted into the center of the beam line with the help of a laser focusing system. Among various targets used in this experiment, Olivine_6 achieved the highest impact counts (Tab. 3.01). Unfortunately, during bombardment of this particular target, the fixation slightly loosened and the target was shifted relative to the dust beam. This issue was found later by the LSM investigations. The actual maximum of impact features was located close to the edge of the Olivine_6 target and not in the center, where it was supposed to be. Identifying impact features was challenging during initiation of this study. As the mineral targets had to be exceptionally large (measured against natural samples), monomineralic rocks had to be chosen. As monomineralic rocks are frequently result of hydrothermal activity, these can have defects or small fluid inclusions, which appear as cavities after polishing and have to be distinguished from micro impact craters.

Besides introducing the LSM for the first time to microimpact crater studies on mineral targets, several other non-standard techniques were applied, i.e., using a Van de Graaff accelerator facility to achieve hyper-velocity impacts, and using large targets of natural minerals. Hence, several time consuming complications had to be mastered:

- 1) Adjustment of a sufficiently high particle flux and target orientation within the Van de Graaff accelerator facility
- 2) Setup and measurement strategy of the LSM
- 3) Comparison and control of results with SEM
- 4) Interpretation of LSM results

Particular the last point turned out to be extremely challenging: as the LSM offered the analytical capabilities down to detection of nanometer-sized features, numerous tiny non-impact features were detected that remained undiscovered in previous studies of this kind, and that had to be distinguished from impact craters.

The maximum diameter of the dust beam was < 10 mm as stated by the technicians of the facility, in agreement with KOBUSCH *et al.* (2009) reporting 9 mm in their experiment, using the same facility at MPIK Heidelberg.

Preliminary investigations yielded a surprisingly low number of impact features on targets Enstatite_4 and Diopside_1, which were among the first bombarded targets. As the particle counts of the Olivine_6 target were by far higher (Tab. 3.01), the efforts were focused on this particular target in order to find as much as possible impact features. In addition, from a chemical and a crystallographic point of view, olivine is considered as the simplest target material, compared to all other samples in this experiment. Due to the above mentioned challenges, it turned out that a detailed analysis of this individual target including all previously unrecognized small non-impact features required the total time available for this thesis. However, this primary dataset enables to evaluate targets with lower impact counts in future studies.

Mineral-Target	target shape	total projectiles leaving the source	velocity limitation [km/s]	from PSU selected projectiles	total bombardment duration[s]	mean flux [per sec]	largest projectile diameter [µm]	mean projectile diameter [µm]	Cu dust charge	impacts on target
Allende_2	thick section	87,762	0.4 - 200	87,135	4,476	19.5	11.2	1.59	Cu Charge A	32,447
Antigorite_1	thick section	17,400	1 - 52	10,162	7,269	1.4	4.3	0.57	Cu Charge1;2;3;4	599
Antigorite_2	thick section	242,716	0.4 - 200	241,765	15,741	15.4	10.0	0.98	Cu Charge4	11,740
Diopside_1	thick section	10,204	1 - 47	4,047	444	9.1	4.1	0.58	Cu Charge1	149
Diopside_3	thick section	53,926	1 - 37	10,288	2,219	4.6	3.6	0.58	Cu Charge4	349
Enstatite_4	thick section	300,889	0.4 - 127	300,680	12,968	23.2	6.5	1.04	Cu Charge4	4,876
NWA_2	thick section	99,375	0.4 - 200	98,524	5,260	18.7	11.3	1.57	Cu Charge A	34,725
Olivine_2	thick section	501,820	0.4 - 200	500,829	20,388	24.6	10.4	0.99	Cu Charge4	30,626
Olivine_3	thick section	534,725	0.4 - 200	534,336	22,548	23.7	6.6	1.05	Cu Charge4	8,862
Allende_R	epoxy embeded	103,976	0.4 - 200	99,263	3,328	29.8	10.6	1.10	Cu Goodfellow	39,937
Antigorite_6	epoxy embeded	123,494	0.4 - 200	122,523	5,672	21.6	11.1	1.57	Cu Charge A	11,740
Diopside_6	epoxy embeded	122,126	0.4 - 117	121,363	7,649	15.9	11.1	1.45	Cu Charge A	33,212
Enstatite_5	epoxy embeded	541,629	0.4 - 200	540,285	16,121	33.5	10.5	1.04	Cu Charge4	3,580
Enstatite_6	epoxy embeded	86,849	0.4 - 200	86,130	4,250	20.3	10.1	1.60	Cu Charge A	31,403
NWA_R	epoxy embeded	100,109	0.4 - 200	94,555	2,786	33.9	10.8	1.11	Cu Goodfellow	42,777
Olivine_5	epoxy embeded	384,198	0.4 - 172	360,474	16,523	21.8	8.0	1.04	Cu Charge4	12,242
Olivine_6	epoxy embeded	993,850	0.4 - 200	929,807	31,307	29.7	11.4	1.23	Cu Charge A, Cu Goodfellow	239,587

Table 3.01: In this overview all targets are listed which experienced suitable bombardment for impact studies. The green row marks the target, which was detailed analysed within this study. *Velocity limitation window*: “mixed” means that the velocity windows were changed during bombardment. *impacts on target*: The bold black numbers are determined by a signal detector ~ 2 cm before the actual target. After removing the detector for the sake of space and to use a rotating target swapping mount, the corresponding values were estimated and are less reliable (red numbers). The coloured bar in individual cells represent relative quantities within their corresponding column.

3.3 Projectile statistics of the olivine target in the dust accelerator

3.3.1 Velocities of projectiles

Velocities of individual projectiles were recorded by the PSU (Fig. 3.06).

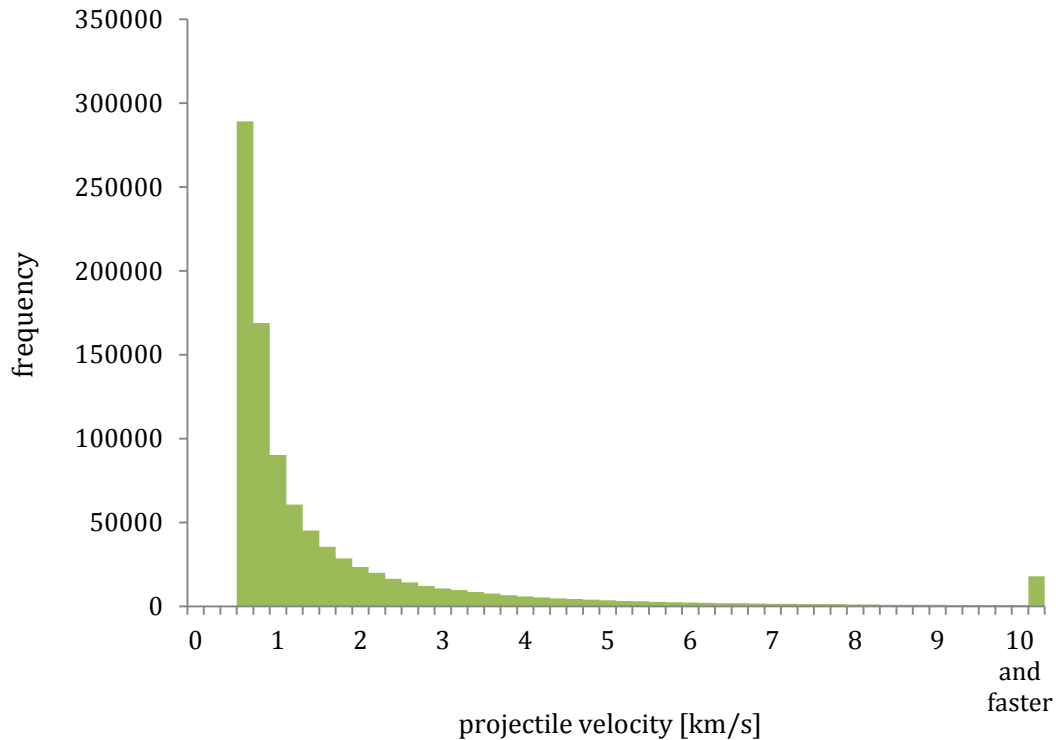


Fig. 3.06: Distribution for particle velocities of the bombarded olivine target.

In figure 3.06 the maximum of 289,142 particles is around 0.6 km/s. 99.7 % of all particles had velocities below 13.01 km/s. Binning the projectile velocities (Tab. 3.02) shows that 33.8 % of all projectiles were between 0.5 – 0.75 km/s, and ~ 72 % below 1.5 km/s.

Table 3.02: Velocity distribution of particles on olivine_6 target.

v [km/s]	count	percentage
< 0.5	112766	12.1%
0.5 - 0.75	314251	33.8%
0.75 - 1	121152	13.0%
1 - 1.5	124790	13.4%
1.5 - 2	68349	7.4%
2 - 3	73318	7.9%
3 - 4	38357	4.1%
4 - 6	35368	3.8%
> 6	41456	4.5%

The data collected by the PSU are considered as very accurate. The errors for the acceleration potential is $\sim 1\%$, for charge measurement $\sim 3\%$ and for velocity measurements $\sim 5\%$ (MOCKER, 2015).

3.3.2 Diameters of projectiles

The diameter $[\mu m]$ is computed from the measured mass (Fig. 3.08), assuming that every particle is spherical. The first equation [1] yields the volume and the second equation [2] yields the radius assuming sphericity. The density of copper (ρ_{Cu}) was operated with 8.9 kg/m^3 .

$$[1] \quad m = \rho_{Cu} V_{sphere}$$

$$[2] \quad V_{sphere} = \frac{4}{3} \pi r^3$$

Using equations [1] and [2] the diameter can be calculated as shown in equation [4].

$$[3] \quad \frac{m}{\rho_{Cu}} = \frac{4}{3} \pi r^3$$

$$[4] \quad d = \left(\frac{6m}{\rho_{Cu}\pi} \right)^{\frac{1}{3}}$$

As already stated above, two different kinds of Cu projectiles were used on Olivine_6. PSU observations indicate that 929,807 Cu particles passed through the PSU and an estimation of 239,587 hit the target. 64,889 (6.98 %) of the total projectiles are made of the dust “*Cu Charge A*”, which are non-spherical projectiles and can be described as more irregular shaped or fused clusters. However, the majority of all Cu projectiles (93.02%) are spherical. The calculated diameters and energies are considered to be valid. It is considered that the small sized fractions of the projectiles are most likely spherical because they would not fuse into larger grains.

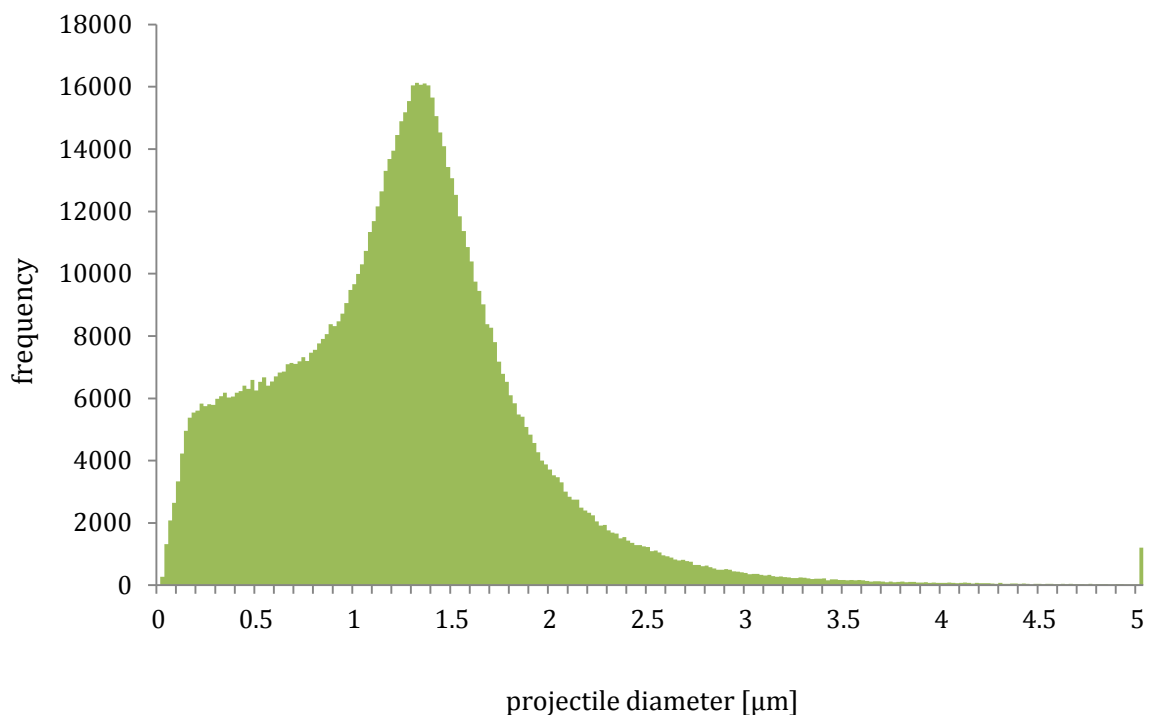


Figure 3.07: Distribution for particle diameter fired onto the olivine target detected by the PSU with maximum at 1.32 μm.

The maximum frequency (Fig. 3.07) with 16,125 events was at a projectile diameter of 1.32 μm. The mean diameter for Cu projectiles is $1.238 \pm 0.651 (1\sigma)$ μm, which means that 99,7 % of all particles had diameters below 3.18 μm.

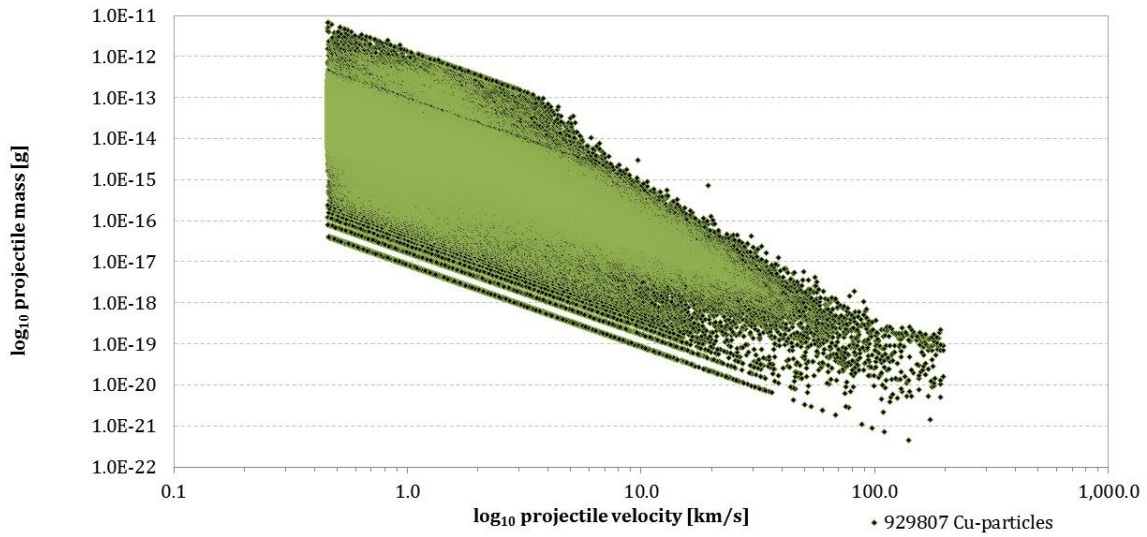


Figure 3.08: Projectile mass to velocity plot detected by the PSU.

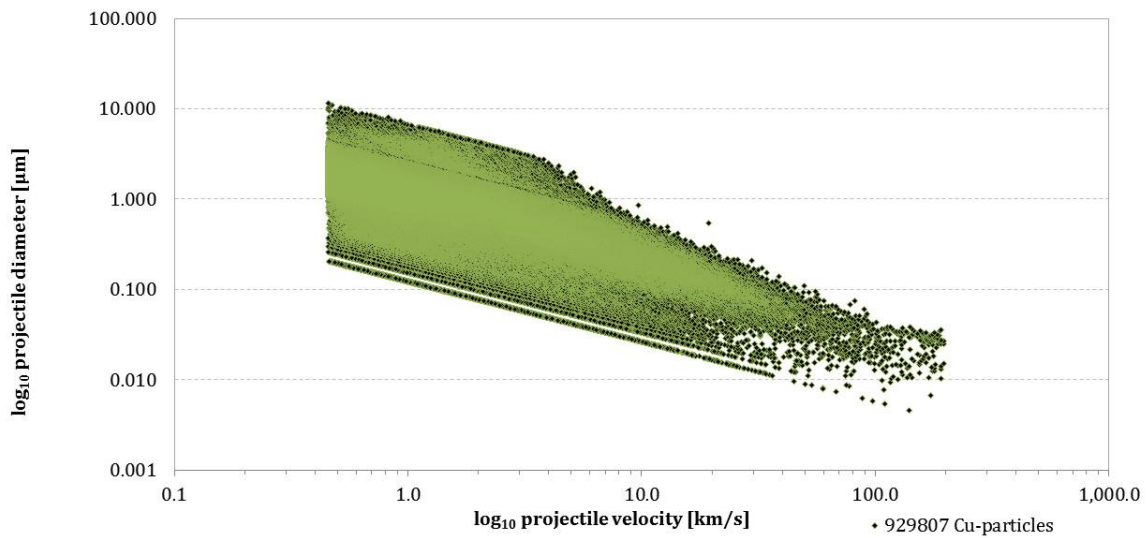


Figure 3.09: Projectile diameter to velocity plot detected by the PSU.

Figure 3.09 illustrates the distribution for projectile diameters range between 0.3 up to 3 μm with velocities between 0.5 and 7 km/s. With projectiles shot on the target without any speed and size limitations the maximum recorded Cu projectile diameter (assumed it is spherical) was 11.4 μm .

Table 3.03: Distribution of diameter fractions detected by the PSU.

D [μm]	count	percentage
< 0.1	9646	1.0%
0.1 - 0.25	40234	4.3%
0.25 - 0.5	76937	8.3%
0.5 - 1	190391	20.5%
1 - 2	529409	56.9%
2 - 4	79586	8.6%
4 - 5	2400	0.3%
larger 5	1204	0.1%

Dividing the projectiles diameter into different fractions (Tab. 3.03), it is shown that ~ 34 % of all projectiles can be considered as submicron sized particles, and 57 % are between 1 –2 μm .

3.3.3 Kinetic energies of projectiles

The kinetic energy (Fig. 3.10) is determined by equation [5].

$$[5] \quad E_{Kin} = \frac{1}{2}mv^2 \text{ [J]}$$

It is considered that m is the mass of spherical body.

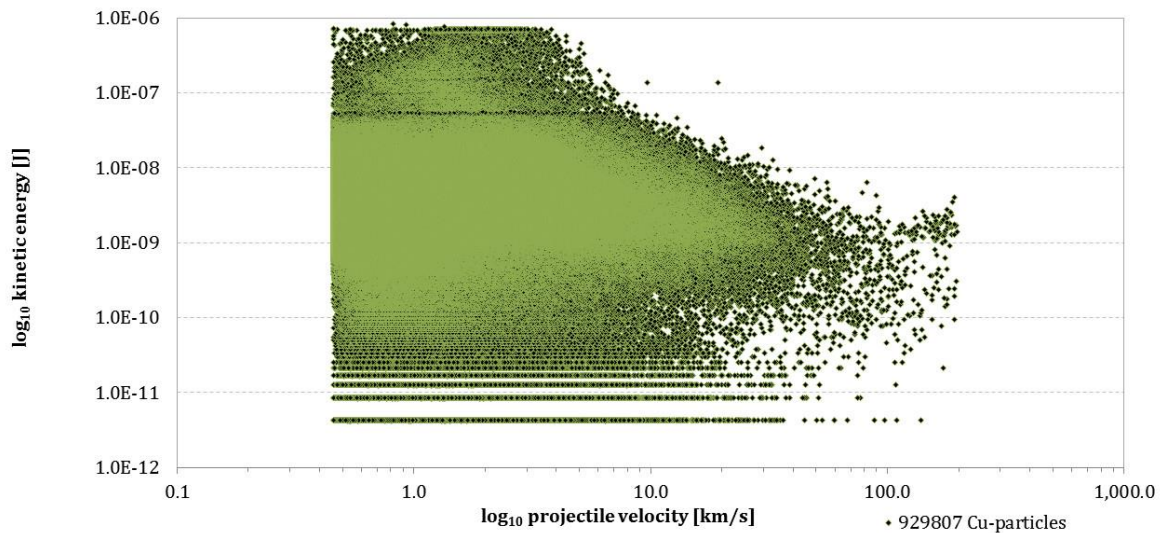


Figure 3.10: The kinetic energy to velocity plot detected by the PSU.

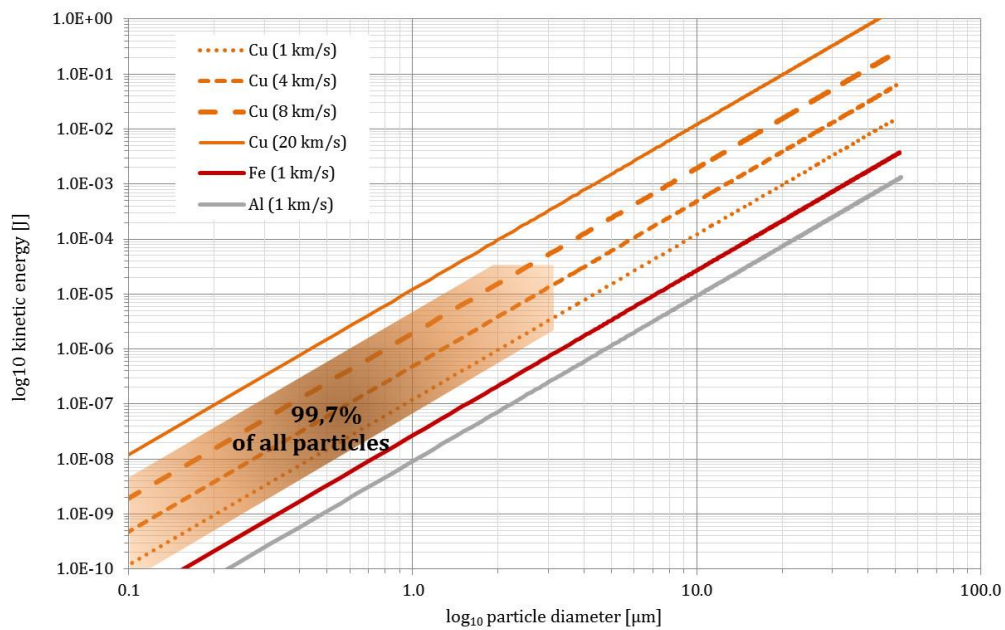


Figure 3.11: The orange array presents all the data within 3σ in respect to their velocity and diameter. This plot is only applicable, when particles are spherical.

Depending on different material densities of Al (2.71 kg/m³), Fe (7.9 kg/m³) and Cu (8.92 kg/m³), for a spherical projectile equation [6] can be applied

$$[6] \quad m_{Cu} = 3.3 \quad m_{Al} = 1.1 \quad m_{Fe}$$

With projectiles of same diameter but different materials (Al, Fe, Cu) the velocity of a Cu projectile in dependency of the densities ρ can be expressed as

$$[7] \quad v_{Cu} = \sqrt{\frac{\rho_{Al} v_{Al}^2}{\rho_{Cu}}} = \sqrt{\frac{\rho_{Fe} v_{Fe}^2}{\rho_{Cu}}}$$

For same kinetic energy in dependency of a same projectile mass it can be guessed

$$[8] \quad v_{cu} (E_{kin}, m) = 1.81 * v_{Al} \quad \text{and} \quad v_{cu} (E_{kin}, m) = 1.06 * v_{Fe}$$

Henceforth Cu needs less velocity to reach the same kinetic energy as Al or Fe projectiles (Fig. 3.11). This fact should be considered as most previous impact studies speak of velocity dependency. For better comparison it should be rather regarded to the kinetic energy, when different types of projectile materials are used.

3.3.4 Energy densities of projectiles

The areal related energy density $D_{E(A)}$ (Fig. 3.12) is determined using the following equation [9] (MOCKER, 2015).

$$[9] \quad D_{E(A)} = \frac{E_{Kin}}{\pi r^2} \text{ [J/m}^2\text{]}$$

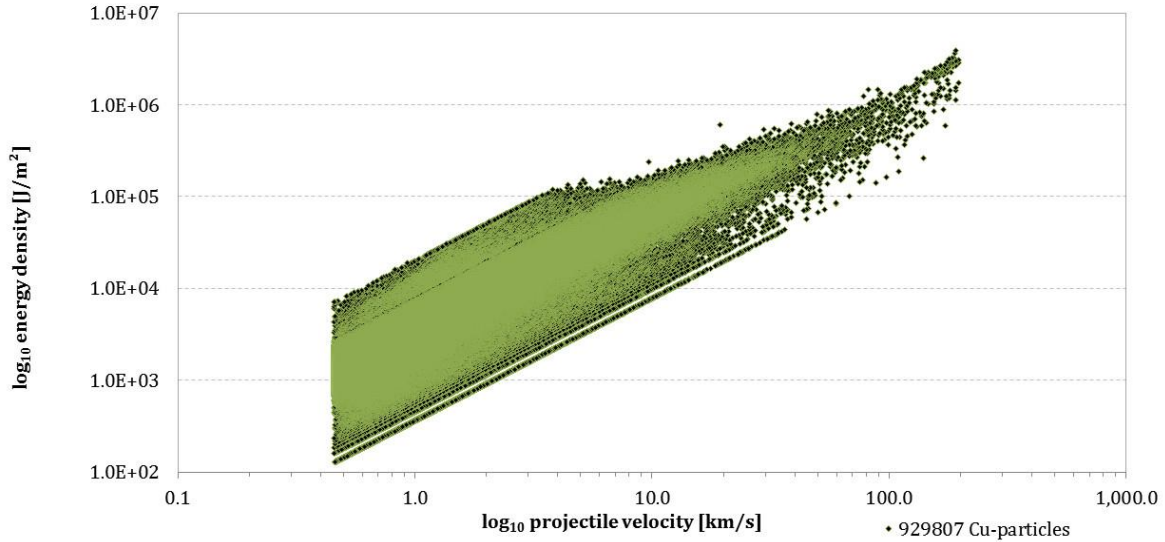


Figure 3.12: The areal energy density to velocity plot detected by the PSU.

The energy density combines a projectile's velocity, its density and area of impact, assuming it is a spherical projectile.

To include the aspect of volume related energy density $D_{E(V)}$ and the effect of its porosity, the following equation [10] can be used.

$$[10] \quad D_{E(V)} = \frac{E_{Kin}}{V_{Cu} - V_{poros}} \text{ [J/m}^3\text{]}$$

The Cu projectiles can safely be considered as solid objects and hence in this experiment the porosity is negligible, which is expressed in equation [11].

$$[11] \quad D_{E(V)} = \frac{3 E_{Kin}}{4\pi r^3} \text{ [J/m}^3\text{]}$$

Characteristics of PSU data

The data obtained from the PSU are of limited accuracy for several reasons. First, particle mass and size are derived from the charge of individual particles. However, the influence of particle shape is not taken into account. Particularly for low particle size and mass, the charge is at the detection limit of 0.1 fC, and due to the transformation of analogue voltage to digital values by an AC-DC converter, the data appear as discrete lines limiting the data area to low sizes (Fig. 3.08, 3.09, 3.10 and 3.12). The upper region of the diagrams is limited by the field emission limit and is depending on the projectile material. It is the threshold of the maximum constant field strength a Cu particle can hold without suffering fragmentation. This conditions are described in SRAMA *et al.* (2004) and MOCKER (2009).

4 Analysis of olivine targets

4.1 The chemical composition of olivine samples

During the course of the study, olivine, enstatite and diopside were analysed via SEM to determine the qualitative elemental composition, followed by quantitative analysis via electron microprobe (EMP). No EMP analysis was conducted for antigorite, Allende and NWA 6966 to this point, since the Olivine_6 sample turned out to become the primary subject of this thesis. The classification of olivine was applied according to DEER *et al.* (1992).

Olivine_6 can be classified as forsterite with Fo_{90.7} containing accessory magnetite, a spinel group mineral, and pyroxenes. The forsterite's chemical composition can be expressed as $(\text{Ni}_{0.01}\text{Fe}^{2+}_{0.18}\text{Mg}_{1.83})_{\Sigma=2.02}\text{Si}_{\Sigma=2.00}\text{O}_4$. Magnetite inclusions show a low magnesian signature in composition with $(\text{Ni}_{0.02}\text{Fe}^{2+}_{0.48-0.95}\text{Mg}_{0.04-0.50})_{\Sigma=1.00}(\text{Fe}^{3+}_{1.99-2.00}\text{Cr}_{0-0.1})_{\Sigma=2.00}\text{O}_4$. The high Mg-values are likely to stem from the surrounding Mg-rich forsterite.

Tables showing the quantitative analysis of olivine, enstatite and diopside are listed in *Appendix A: EMP measurements* (Tab. A.01–A.07). Ideal structural formulae are taken from DEER *et al.* (1992).

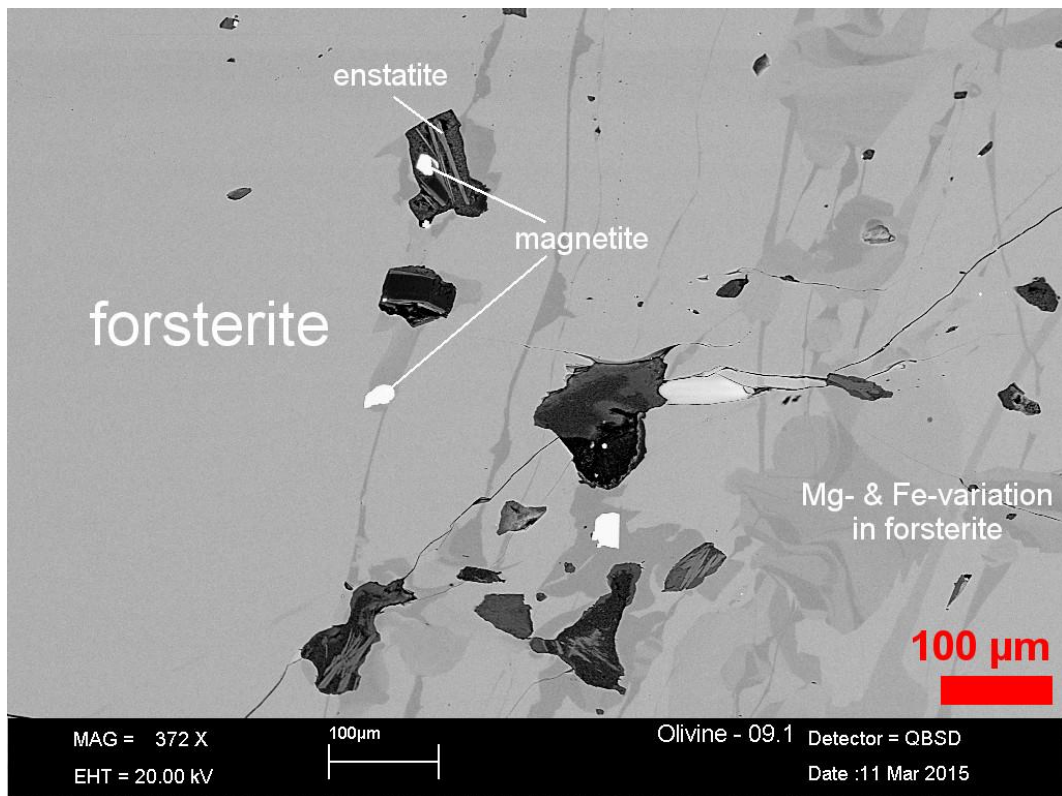


Figure 4.01: Close up view of an altered section of Olivine_6. Different grey shades display variations of Mg/Fe ratios of olivine close to inclusion trails. In such part of the sections, magnetite inclusions (white) can be found as well as, though more rarely, enstatite inclusions, recognizable as fine grey bars. Black zones illustrate surface cavities due to sectioned fluid inclusions, where electron scattering or emission is ineffective.

4.2 Investigation of a non-bombarded target

To understand the effects of an impact of a particle onto a mineral surface, it is necessary to evaluate a non-bombarded sample of the same mineral. Such a comparative target is mandatory to distinguish impact features (e.g., craters and spallation) from naturally occurring phenomena on the sample surface (e.g., cavities, cracks or opened fluid inclusions).

The non-bombarded target, referred to as Olivine_7, measures $\sim 1.3 \times 1.9$ cm (Fig. 4.02). Every olivine used in this experiment has been sampled from the same location, meaning that its chemical composition and texture is generally the same for all olivine targets used in this study; differences can be seen in the position of cracks and melt inclusions appearing at the surface. Cracks can also be produced during the sample preparation process (i.e., polishing or cutting) and are therefore not necessarily of natural origin.

Fig. 4.02 shows an overview of Olivine_7. While the major part appears homogeneous, some areas contain impurities. Particularly in the lower part a large inclusion trail is crosscutting the section. Within the red square different frames for scanning were chosen to analyse a representative diversity of surface features and their morphologies. However, frames with clearly recognisable, large cavities of tens of micrometer size were not analysed, but rather frames with smaller surface features in the size range of the expected crater sizes of a few micrometer or smaller.

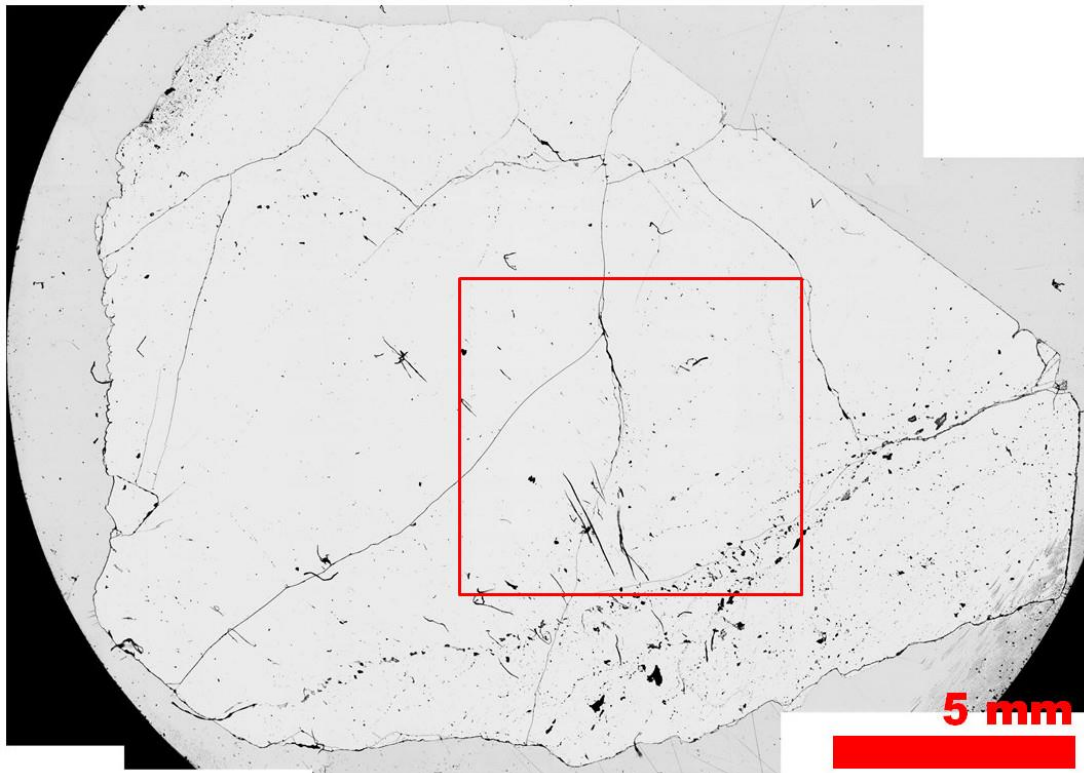


Figure 4.02: Stitched LSM laser image of non-bombarded Olivin_7 target. The red box shows the section where random sampling was performed.

4.3 Results of the non-bombarded target

22 frames, each measuring 95 x 71 μm , were selected from areas showing variable degrees of alteration. Investigations resulted in 221 recorded features (Fig. 4.03).

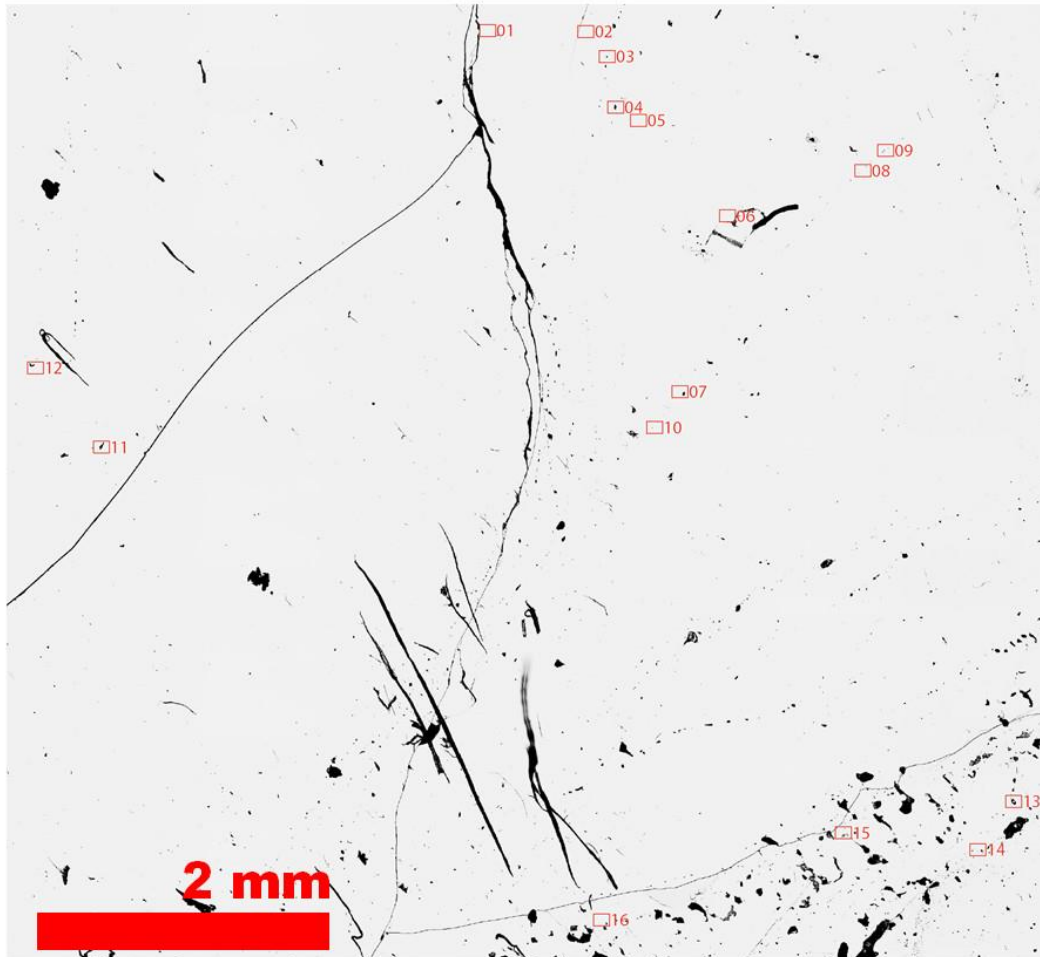


Figure 4.03: Overview of the analysed sections on Olivine_7. Small red boxes with numbers illustrate the frames where laser scanning was performed.

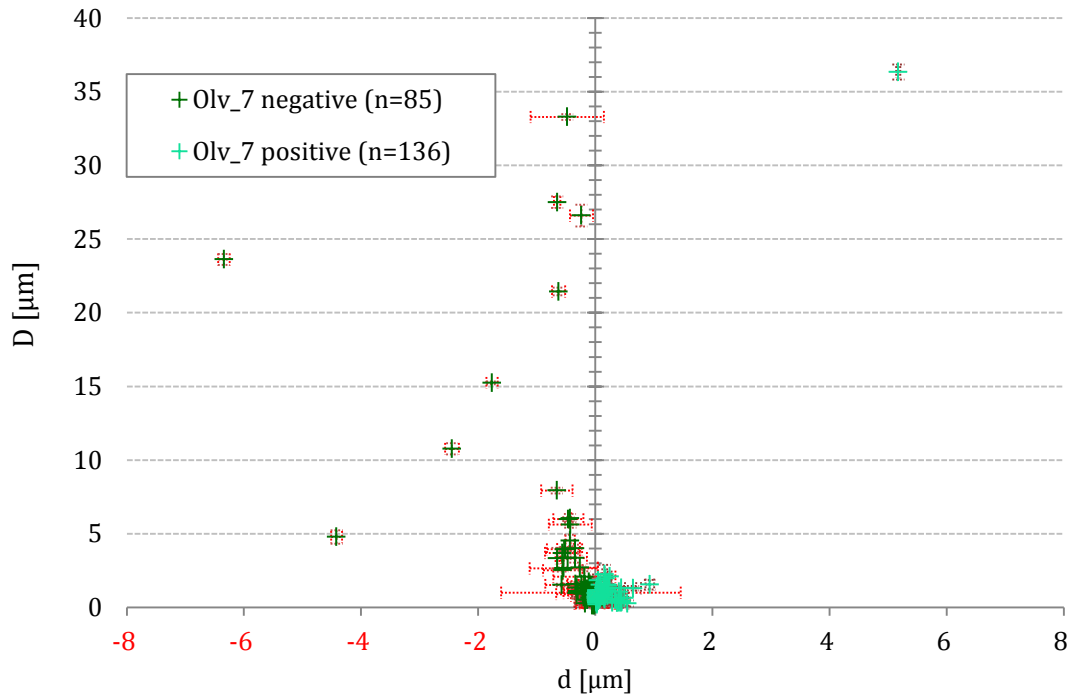


Figure: 4.04: All features measured on Olivine_7 with error bars (red). Negative x-values (dark green plus-symbols) correspond to depths of mineral defects; Positive x-values (light green plus-symbols) correspond to elevations of particles laying on the surface, likely contaminations consisting of very tiny (submicron-sized) environmental/laboratory dust.

Within this thesis, all surface cavities, imprints or holes are referred to as “negative features”. All overlaying or stuck particles, no matter if they are projectiles or just contaminating laboratory dust are referred to as “positive features”. In diagrams comparing negative and positive features, the depth of negative features is shown as negative number.

Most features shown in Figure 4.04, have diameters below 5 μm, a depth between -1 and 0 μm or a height up to 1 μm. More extreme diameter and depth values belong to structures which can be in detail inspected by LSM. Their boundaries appear as crystallographic planes and have strong irregular shapes, as scans in different directions across these cavities yield varying diameter values. Hence, these are likely remnants of former mineral inclusions that broke apart during polishing. Furthermore remarkable is an extremely large surface contaminant in the upper right of Fig. 4.04. This large particle and probably also smaller ones are likely a result of the non-clean lab conditions in the course of this study. The colours and symbols used in the dia-

grams (Diameter to height or depth, diameter/height to diameter and diameter/depth to diameter) are carried forth through this thesis.

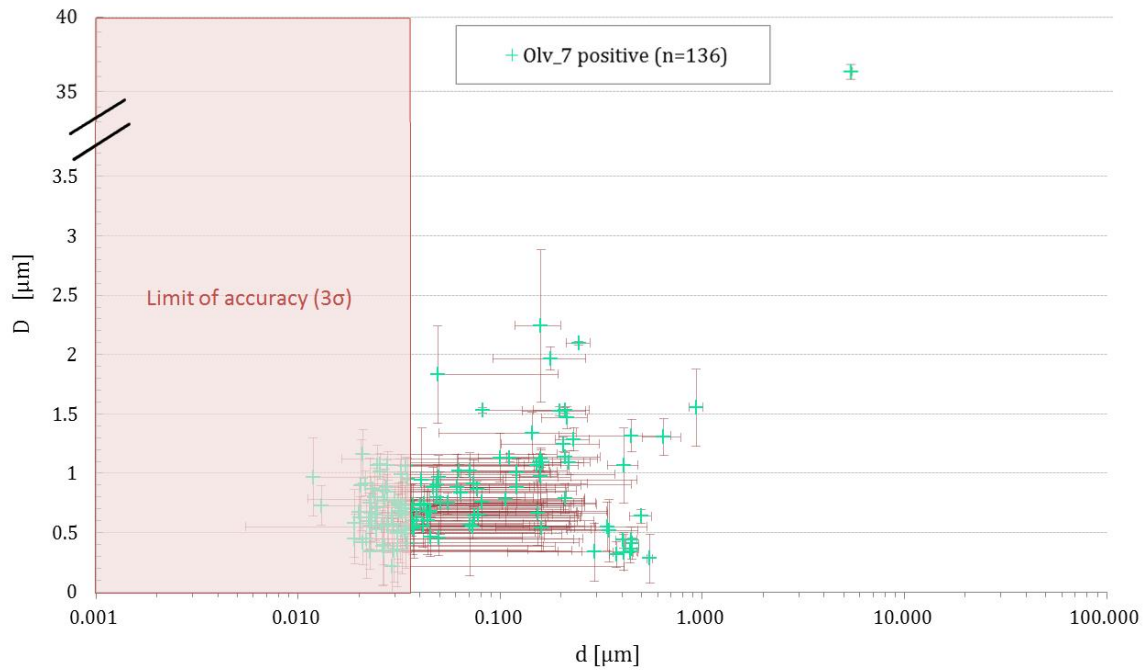


Figure 4.05: All positive features on Olivine_7 with error bars (red) and a y-axis break between 3.5 and 35 μm. The red box indicates the limit of accuracy (in vertical direction) of the instrument (within 3σ).

Looking in detail at all analysed positive features, it can be shown that almost all features are below 1 μm in height and lesser than 2.5 μm in diameter (Fig. 4.05).

In a diameter/height to diameter diagram (D/d - D) frequent values around ~ 0.8 μm diameter can be observed (Fig. 4.06). This demonstrates that contamination particles have similar sizes indicating a quite homogeneous population in size, but with varying elevations.

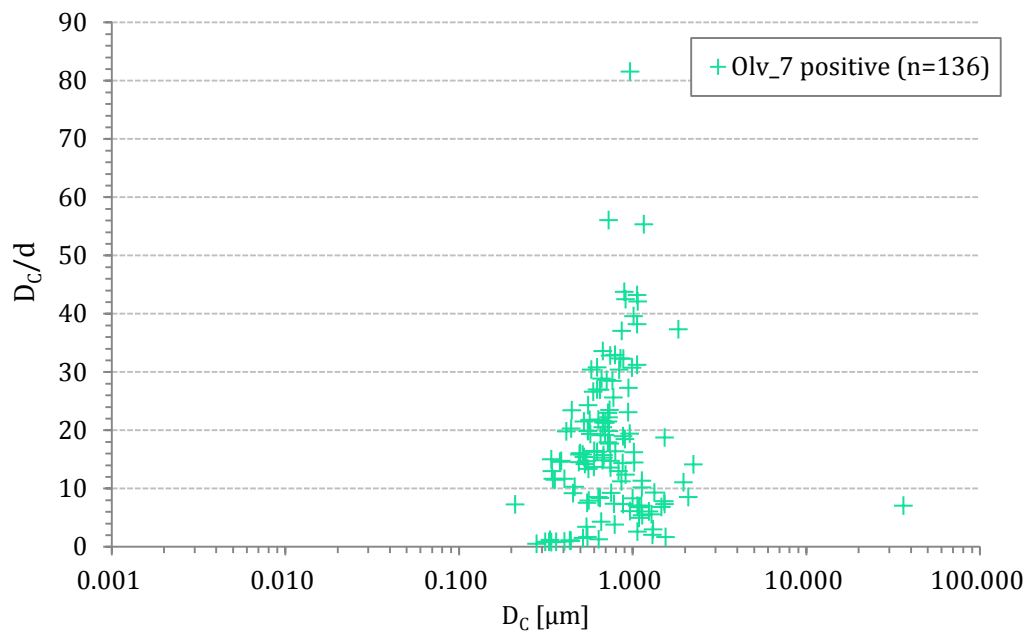


Figure 4.06: All positive features on Olivine_7 in a D/d-D plot.

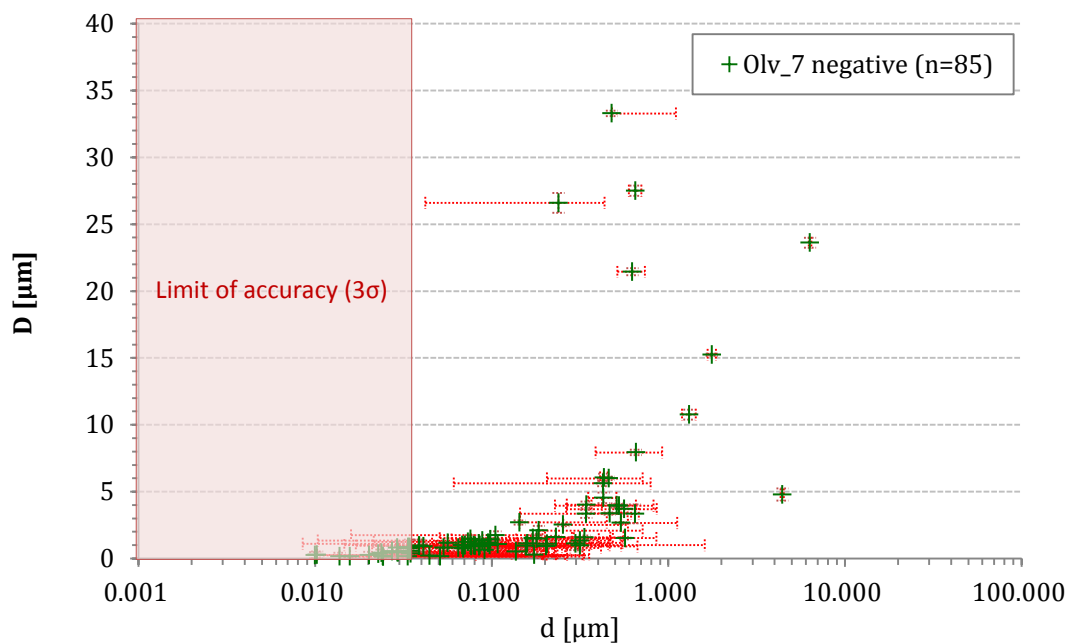


Figure 4.07: All negative features on Olivine_7 in a D/d-D plot. The red box indicates the limit of accuracy (in vertical direction) of the instrument (within 3σ).

The analysis of all negative features in D/d diagrams (Fig. 4.07) shows a wide scatter of the data, which is expected due to the large variation in diameter and shape of the mineral defects. However, the majority of all measurements show a diameter below

2 μm and depth between 0.04 and 0.5 μm . The negative features shown in the D/d-D diagram below (Fig. 4.08), underline the variation of defects observed in the D-d diagram. Most defects are variable in size, but commonly flat.

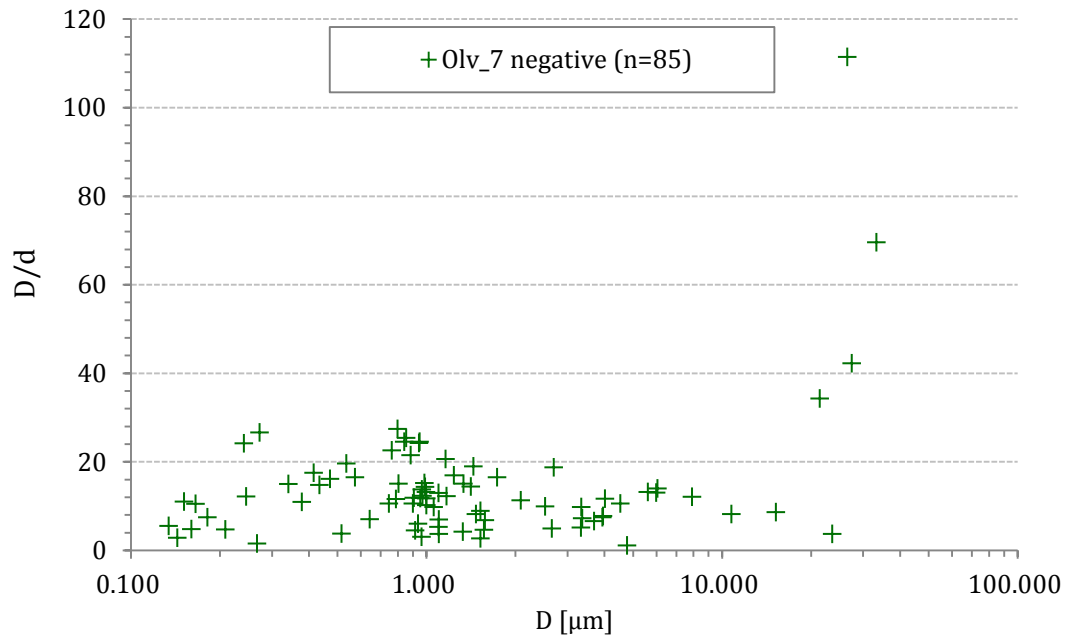


Figure 4.08: All negative features on Olivine_7 in a D/d-D plot.

The data indicate that the majority of positive and negative features scatter around a diameter of $\sim 1\mu\text{m}$ (Fig. 4.06 & 4.08).

This can be better shown by histograms (Fig. 4.09 & 4.10), which are generated with a cell width $h=0.2$ after FREEDMAN & DIACONIS (1981). Fig. 4.10 shows the same distributions, but normalised, in order to ensure comparability with the bombarded target. Features with diameters greater than 5 μm represent a fraction of larger mineral defects, as already stated.

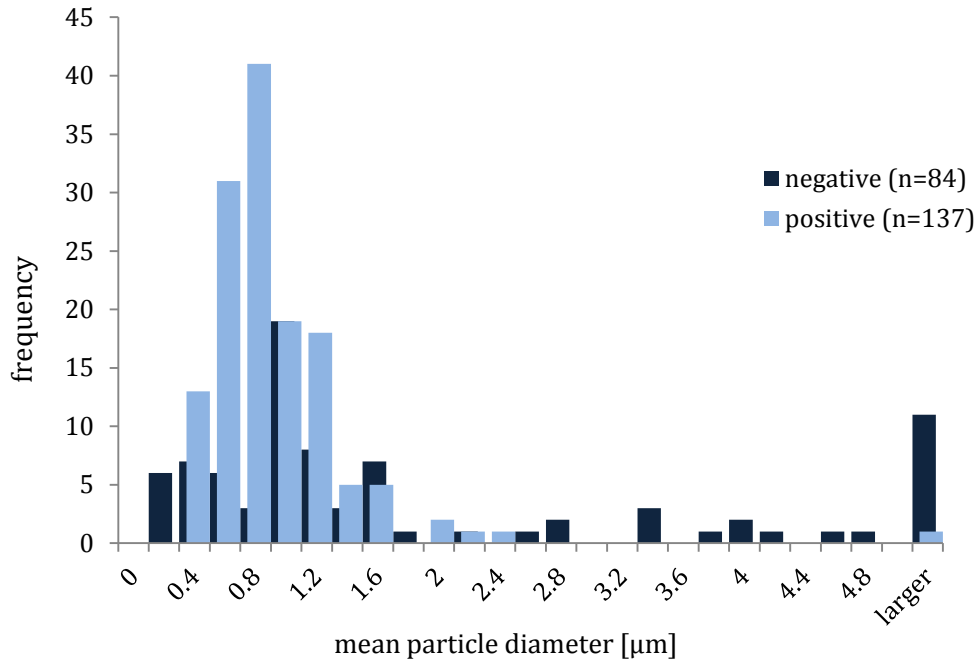


Figure 4.09: Absolute distribution for measured mean diameters of all features on Olivine_7 with their frequency of occurrence on the y-axis.

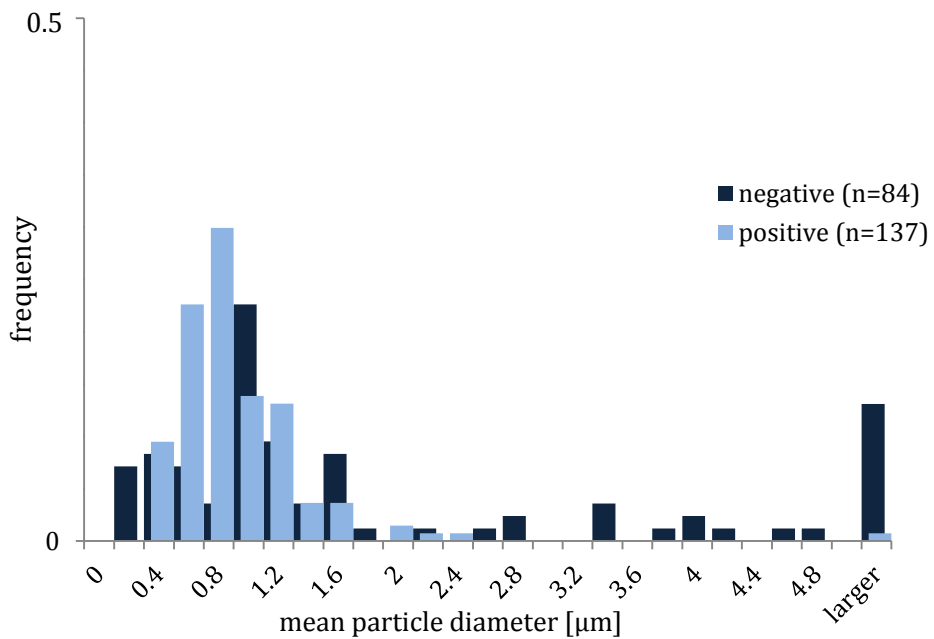


Figure 4.10: Relative distribution for measured mean diameters of all features on Olivine_7, with their frequency of occurrence on the y-axis normalized to 1.

Figure 4.11 and 4.12 also show histograms, but for height and depth data. Here a cell width $h=0.1$ (Fig. 4.11) was used. In figure 4.12 height and depth frequencies are normalized to 1 to make them comparable with the bombarded target (see later sections).

Positive features peak at heights of $\sim 0.1 \mu\text{m}$, heights larger than $0.5 \mu\text{m}$ are rare. The distribution for negative features shows that the majority of surface defects have depths around $0.1 \mu\text{m}$. Cavities below $0.6 \mu\text{m}$ are rare.

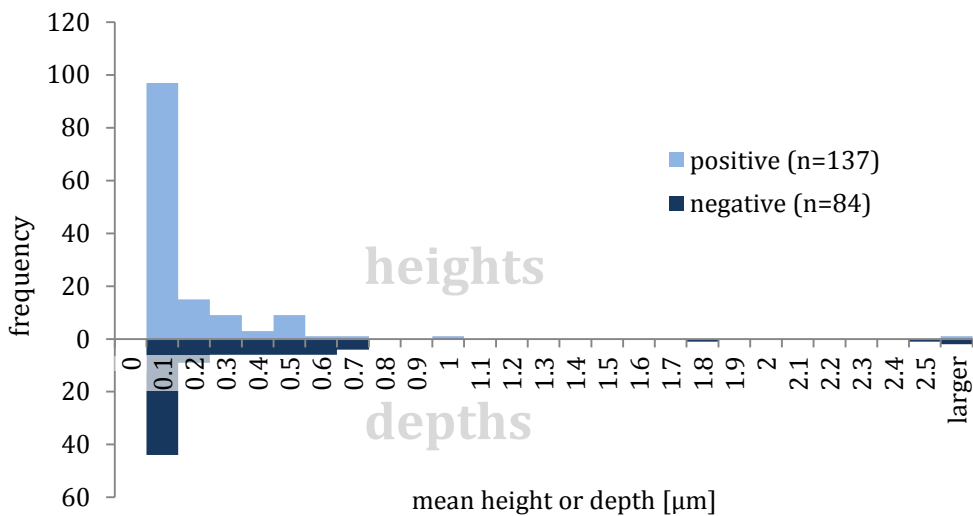


Figure 4.11: For better overview the histograms for height (top) and depth (bottom) are presented in a single diagram. The x-axis shows the value of height in case of positive features or depth in case of negative features. The y-axis displays the frequency of occurrence.

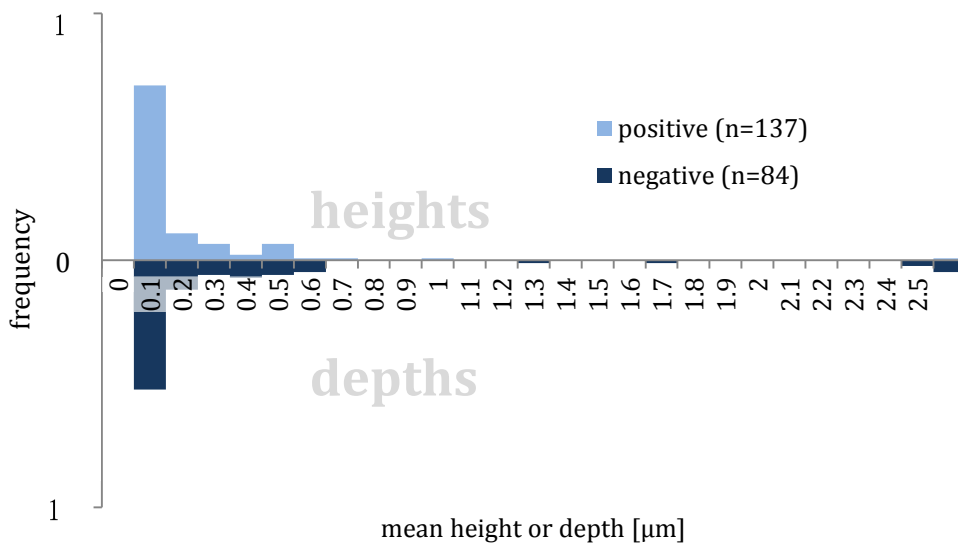


Figure 4.12: Normalised histogram with same data as in Fig. 4.11.

4.4 Investigation of the bombarded olivine target

The bombarded Olivine₆ - target can be divided into two major parts: The upper part is more heterogeneous with a number of melt inclusion trails, and the lower part which shows lesser to none inclusion trails and mineral cracks and is homogenous.

By aiming the dust beam (accelerator operating principle see section 2.3 *Dust accelerator*) onto the Olivine₆ target via the laser targeting system, the dust beam was supposed to hit the sub-center part of the olivine target (Fig. 4.13). Due to unintended loosening of the sample fixation, the beam was hitting part of the epoxy resin and the lower part of the olivine section. Fortunately, this part of the olivine section was still quite pure and unaffected by alterations, contrary to the upper parts of the olivine section (Fig. 4.13). The beam diameter in this experiment is < 10 mm.

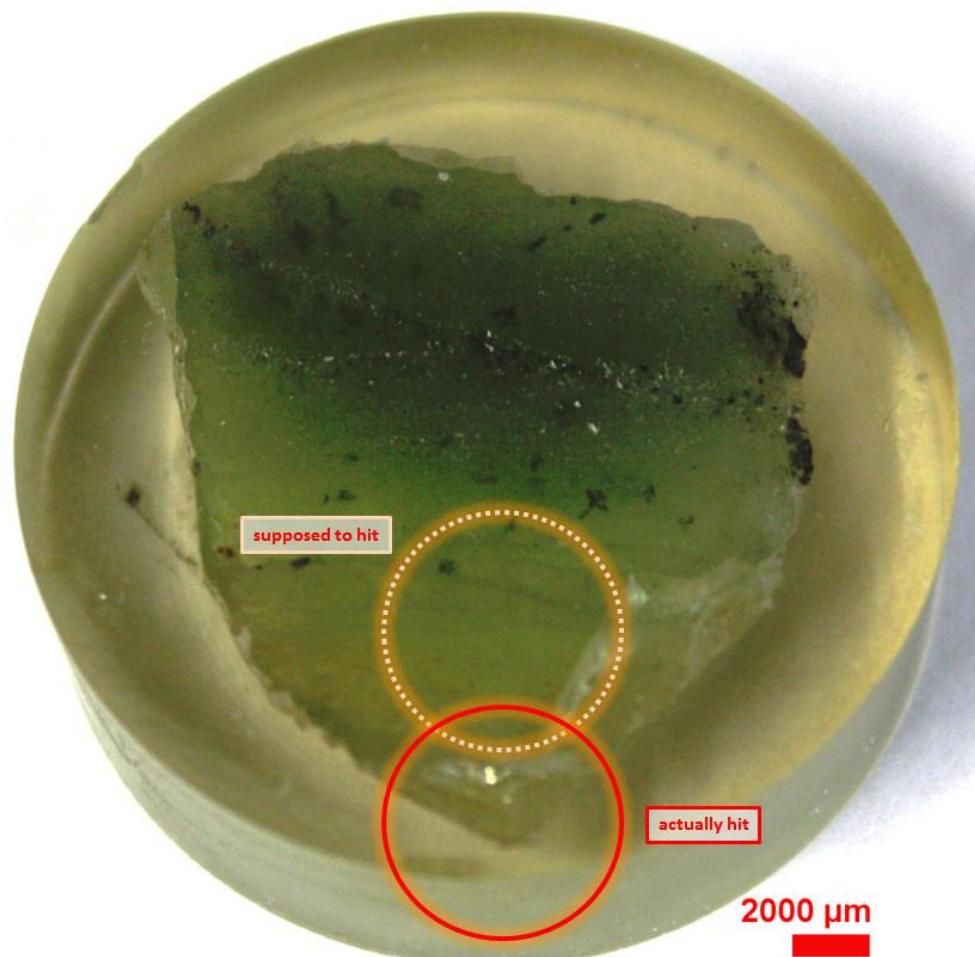


Figure 4.13: Image of the Olivine₆ target, embedded in epoxy resin. The target was placed into the beam line upside down to this presentation. The dashed orange circle illustrates the supposed impact region. The red circle marks the zone where the actual bombardment occurred, as an effect of loosening fixation.

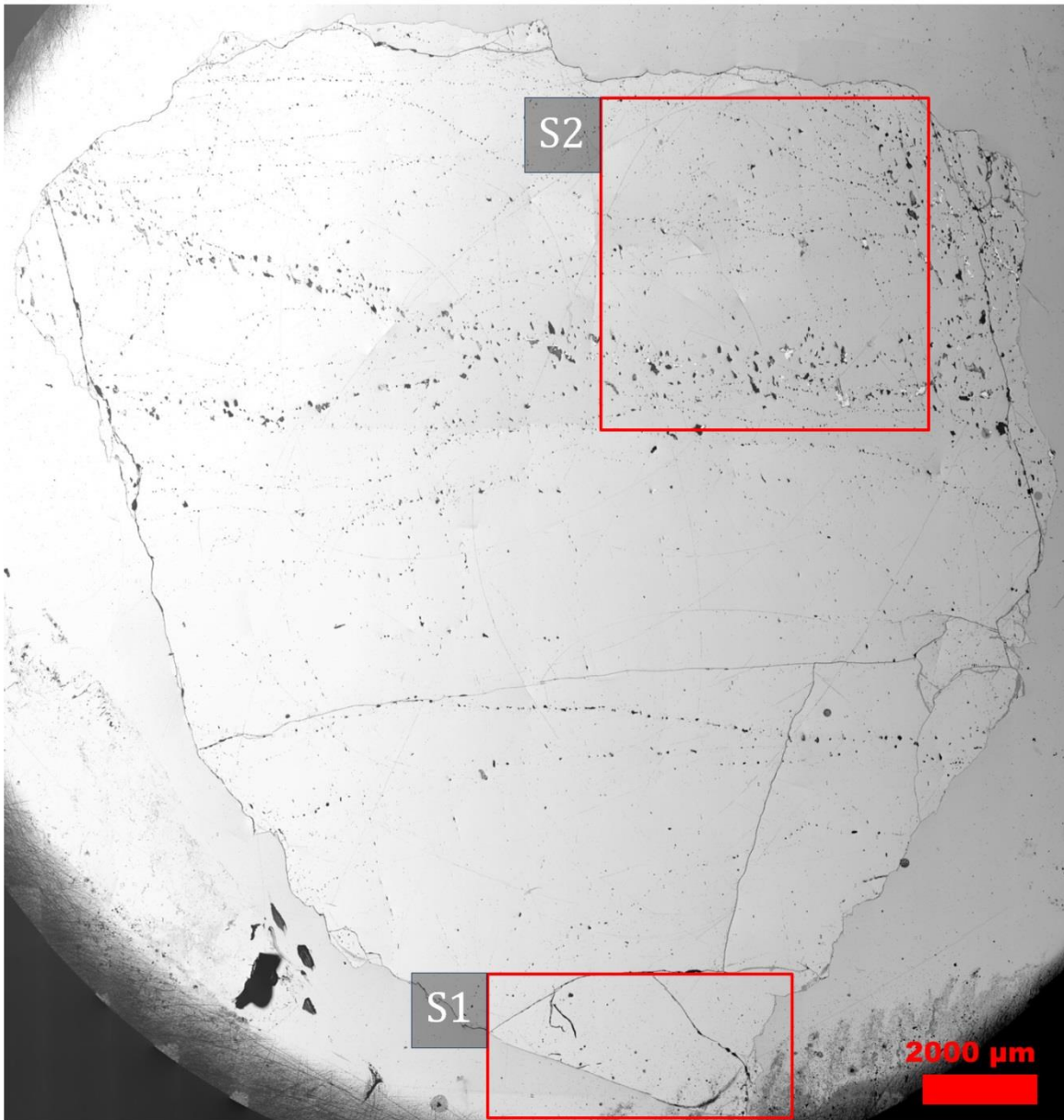


Figure 4.14: Stitched LSM laser intensity image. Section S1 represents the homogeneous part of Olivine_6 with most of the impact features found. Section S2 is an area of massive melt inclusion trails, which was used for comparison purposes on the target surface.

The shift of the target and the beam center induced a time-consuming crater search: The supposed impact zone showed almost no impact features, while the accelerator's Particle Selection Unit (PSU) counted over 900,000 projectiles onto Olivine_6. Finally, a stitched image (Fig. 4.14) of hundreds of single laser intensity images (magnification: 1000x) helped to find the actual region of bombardment.

The investigation of the actual bombardment area S1 with a magnification of $\sim 120\times$ shows a surface with a somewhat “speckled” appearance (Fig. 4.15). However, only with a magnification of $\sim 1000\times$ it is possible to identify larger craters and stuck particles.

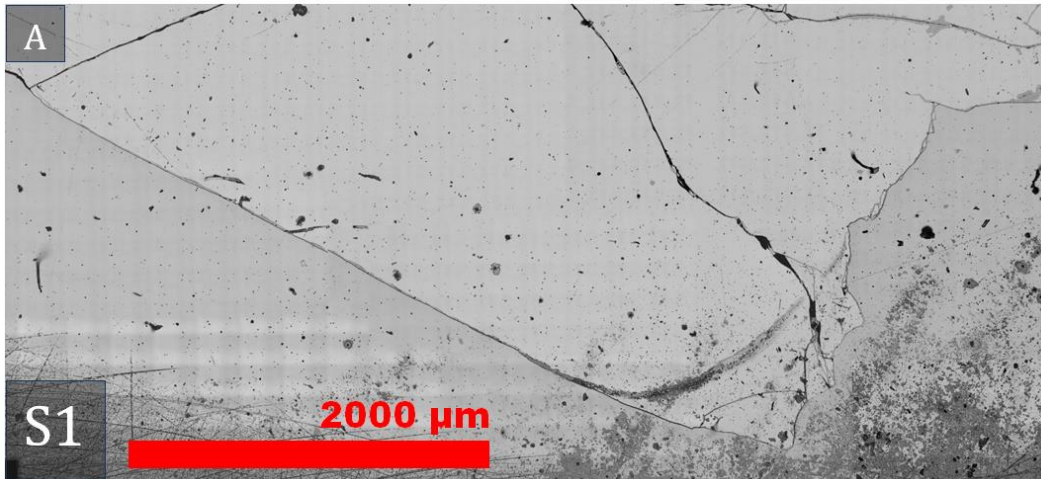


Figure 4.15: Laser intensity image of region S1-A showing the area of primary interest. The “speckled” appearance allows to surmise impact features, which, however, can only be safely detected using much higher magnification.

Section S2 was investigated at a later stage of this study in order to compare to S1 with respect to mineral defects, also serving as additional cross check to the non-bombarded Olivine_7 sample. Samples in S2 were taken to investigate if any impact related features can be found between the dominating inclusion trails and to determine, whether or not these phenomena are distinguishable from mineral defects (Fig. 4.16).

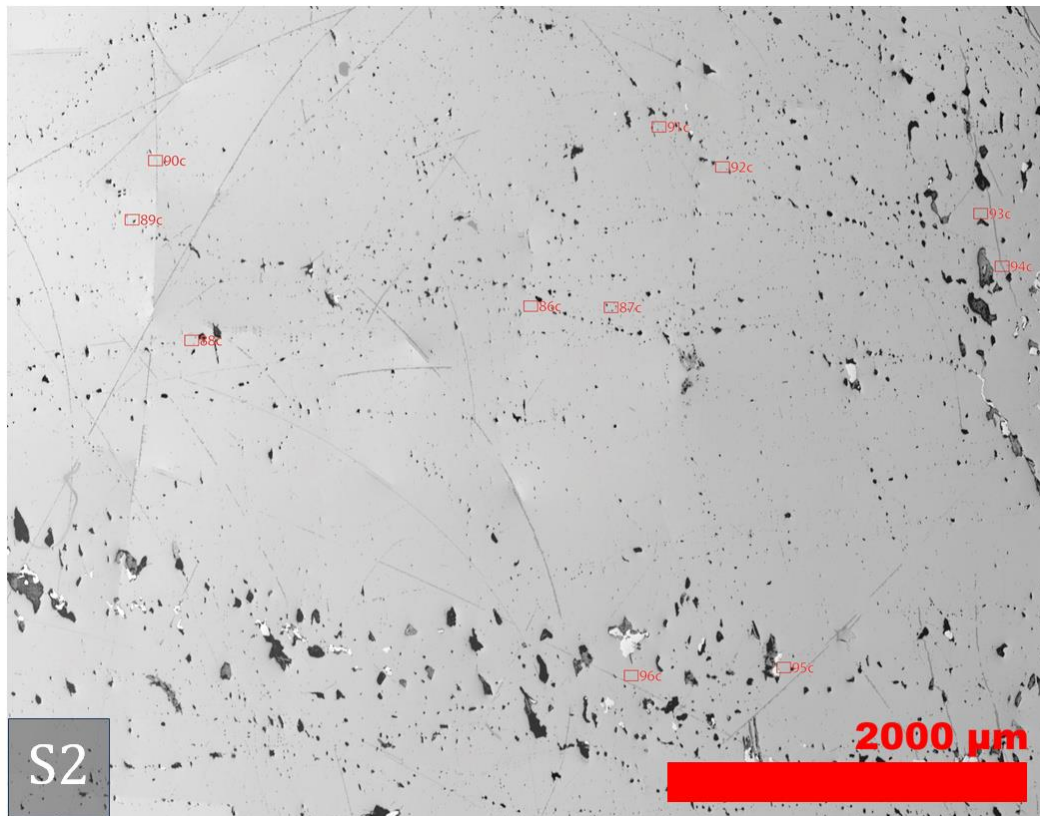


Figure 4.16: The laser intensity image of area S2 shows that the area contains a multitude of inclusions. Red, numbered boxes indicate scanned frames. In the end, no impact features were found in area S2.

4.5 Comparison of LSM- and SEM-imaging

With the benefits of LSM imaging explained in the preceding chapters, this chapter aims at comparing LSM C-Laser DIC images with SEM-BSE images, regarding methodical differences, quality and resolution and general limitations. These SEM investigations could only be performed after LSM measurements were completed, as it was unclear, in how far carbon coating would influence or distort LSM imaging, in addition to the SEMs destructive considered electron beam.

Fig. 4.17a and 4.17b show a comparison of SEM and LSM images displaying details within section S1. Fig. 4.17a [A] shows four craters in SEM, and a large irregular defect. LSM shows the same structures in much more detail, with distinct cracks and blocky fragments, and numerous additional structures, which can be identified (see chapters below) as sticking projectiles or extremely flat crater precursors. However, also non-impact features can be discerned. This multitude of features required a new approach in categorisation of features, as described in chapter 4.6.2. Moreover, highly resolved details of positive features, e.g., sticking Cu projectiles (Fig. 4.17a [D], 4.17b [F], [H]) are visible. Shock related effects surrounding a large sticking Cu projectile can be seen on 4.17b [F].

SEM images with SE detection provide in general significantly better details, due to the higher depth of field. This method, however, requires coating of the sample with Au (atomic number 79), which in turn interferes with the detection and identification of Cu (atomic number 29). Hence, for BSE imaging the olivine target was coated with a ~ 30 nm thick layer of carbon (atomic number 6), having only a minimal effect on the resulting X-ray spectrum (REED, 2005). The focal point of the probe is then set to the targets surface, which results in a blurry and out-of-focus display of crater pits or particles stuck on the surface. The beam voltage was set to 15 kV, since lower values had negative effects on the general contrast of an image. Voltage higher than 15 kV will on the other hand result in significant damage to the mineral surface.

With this setup, however, Cu remnants or particles are relatively easy to find, as they appear much brighter in BSE images than the olivine surface itself. Therefore, the features, presumably craters, found via LSM, were then reasonably verified in SEM, since they showed signals of Cu - either as small residues or recognisable remnants. Addi-

tionally, a number of large Cu particles, stuck in the surface, were observed, and a Cu-track (see *chapter 4.6.5 Cu-track*).

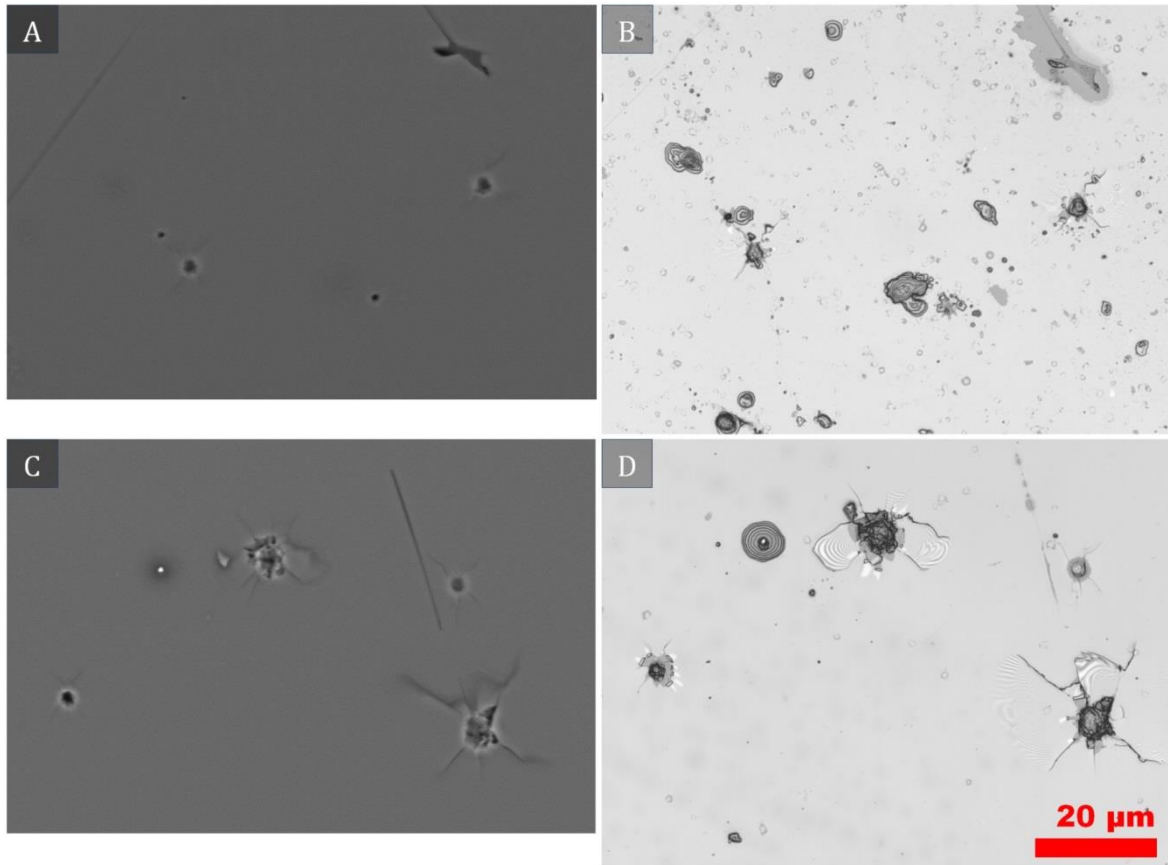


Figure 4.17a: This image shows SEM-BSE images (left) and corresponding LSM C-Laser DIC-images (right). [A] shows four craters (black circles), a defect (black irregular shape, upper right corner) and a polishing mark (diagonal line from upper middle to the right middle). The corresponding LSM image [B] shows the same features, however, much more additional details in speckled appearance.

[C] and [D] show four craters recognisable by surrounding fractures and spallation cracks which are much better visible in LSM imaging [D]. A Cu particle appearing bright in [C] shows a surrounding rings in LSM imaging. Chemical analysis on the two larger craters showed signals of Cu, which indicate residues of the projectile. Scale bar in the bottom right corner applies to all images.

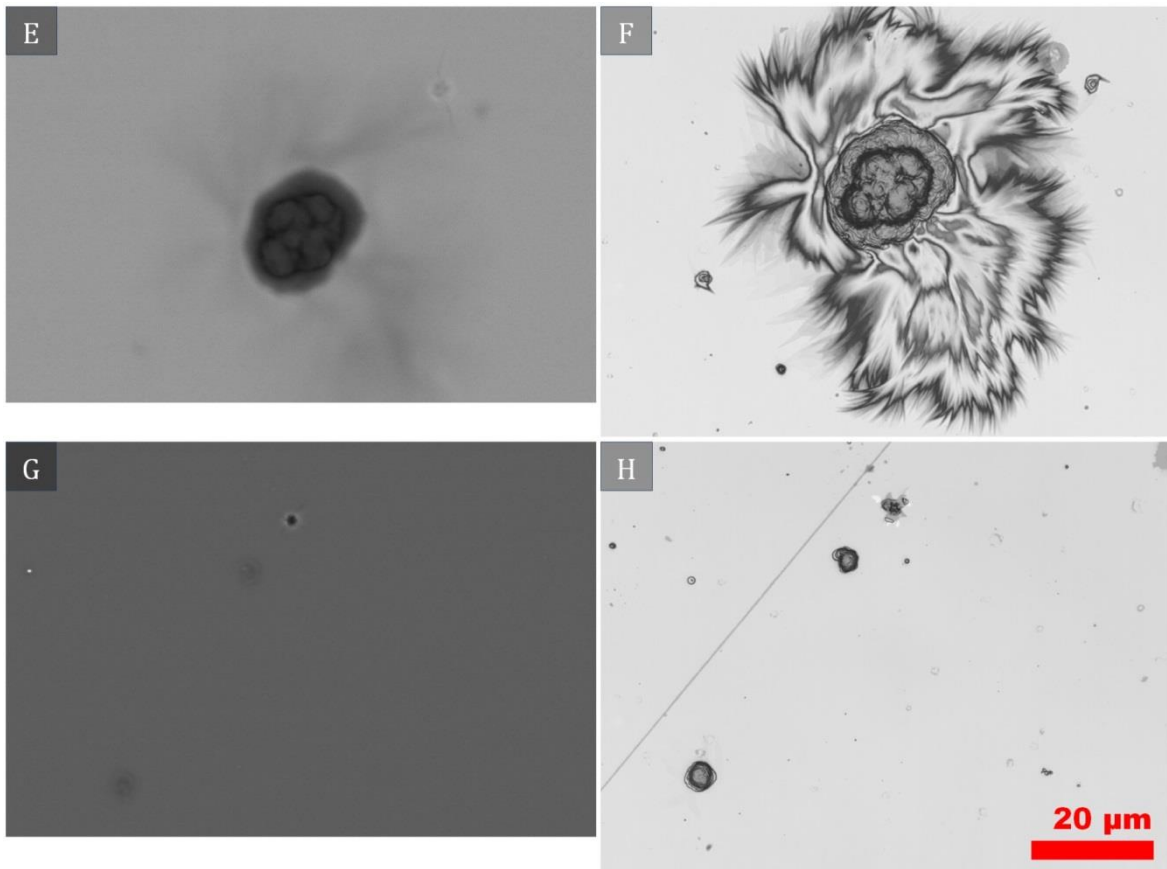


Figure 4.17b: This image shows SEM-BSE images (left) and corresponding LSM C-Laser DIC-images (right). [E] and [F] show a large stuck Cu particle. Although it should be brighter in BSE imaging it appears almost black in the SEM. The shape of the particle is most likely due to melting, which might also cause darkening of the particle in SEM where oxidation might play a role. The shocked zone around the impacted particle is barely noticeable in SEM. The diffraction of optical and laser light enables shocked zones to become visible in LSM images.

The LSM image [H] shows a crater, two larger stuck Cu particles and a smaller one (upper left section). In the corresponding SEM image [G], only the crater and the smaller Cu particle are clearly visible. Both larger particles are indicated by only slightly darker zones in the SEM image. Scale bar in the bottom right corner applies to all images.

SEM-BSE imaging can help to verify, whether an impact experiment, with copper or other projectiles with an atomic number notably higher than the bombarded target, was successful. An SEM-BSE overview image using false contrast was created, that allows recognition of Cu residues and associated impact features on the Olivine_6 surface (Fig. 4.18a).

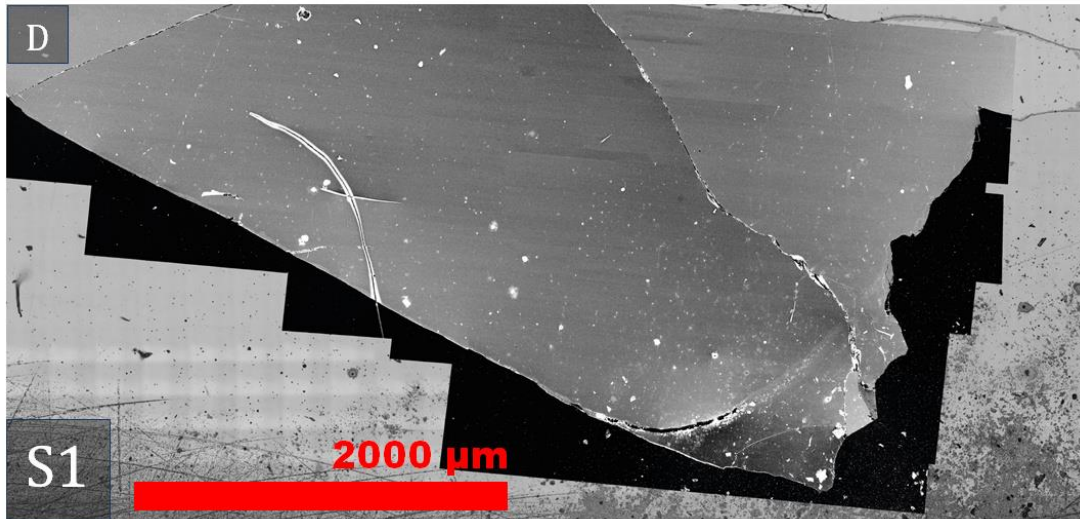


Figure 4.18a: S1-D is high resolution overview image created out of single SEM-BSE-images. To get a better impression of the section's location this overview is embedded into the LSM laser contrast picture. The SEM image is a manipulated BSE image with false colours. The black area is the epoxy used for embedding the target, which itself appears grey scaled. All white dots represent Cu residues and impact features. This confirms area S1 as the actual section of bombardment.

4.6 Results of the investigation of bombarded olivine

Since the preliminary investigations of other mineral targets turned out to be rather difficult because of their low impact feature density, we focussed on the Olivine_6 target due to the high projectile flux and long bombardment time (Table 3.01). However, the impact density in the supposedly impacted region of the target were disproportionately low compared to the high flux-rates (Tab. 3.01), so a time consumptive search for the actually bombarded area was inevitable. During this search using high resolution LSM, many new – both small and numerous – features hitherto unrecognised by SEM (Fig. 4.17a/b) were encountered and methods had to be developed to classify and identify them as impact or non-impact related. As high resolution LSM analyses are time consumptive, only a small portion of the target could be searched and analysed with high resolution.

After section S1 turned out to be the focus of the beam of accelerated Cu projectiles, a total of 85 frames were scanned (Fig. 4.18b). Ten out of these 85 frames contain features related to a Cu-track (see chapter 4.6.5 *Cu-track*) where 74 individual features were analysed taking topographical profiles. Within the remaining 75 frames, 43 frames selected and 884 additional features were analysed. From those 43 frames, initially eleven frames were investigated in greater detail, meaning every single feature found on the olivine surface was analysed by line profiles. The investigations of the smallest features found in those eleven frames were sufficient for categorisation, so they could be omitted in subsequent evaluation of 32 frames, where only middle-to large-sized features were analysed.

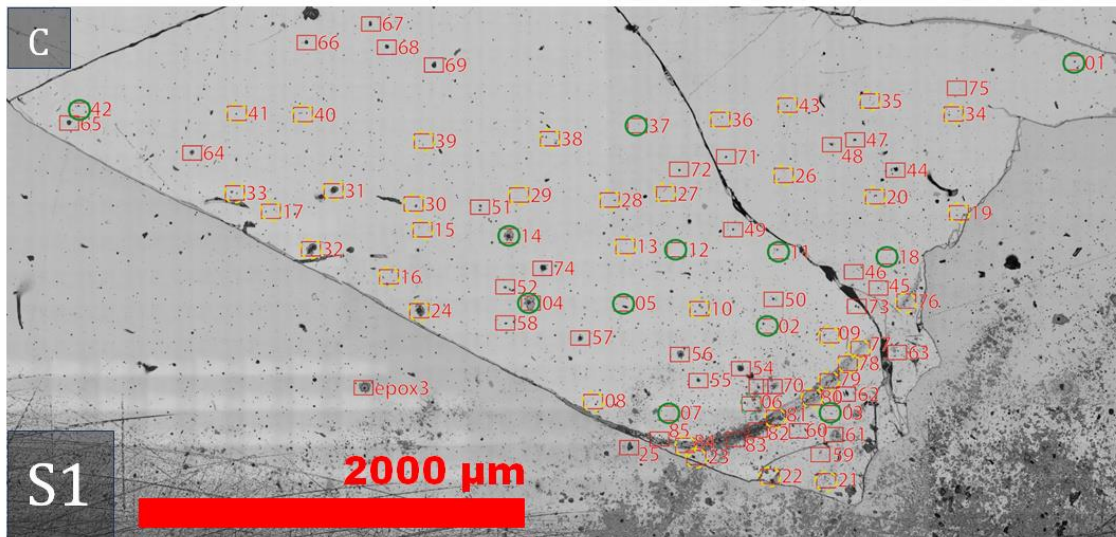


Figure 4.18b: The red boxes represent recorded frames in section S1, of the most intensely bombarded area. The green circles represent frames, which were in-depth evaluated (11 frames in total) by taking line profiles of features, and the yellow, dashed circles represent evaluated frames omitting very small features, since specific parameters (diameter & depth) could not be reliably acquired (only Types: A, B, C, D, N₁, P₁, see below). Red boxes without green or yellow marks are not evaluated yet.

4.6.1 The determination of the impact center of the accelerator particle beam

Unpublished studies, undertaken by the Cosmic Dust research group at the dust accelerator laboratory of the University of Stuttgart (Fig. 4.19) shows that the impact feature distribution on a bombarded target can be described as a confined Gaussian shaped distribution (Fig. 4.20).

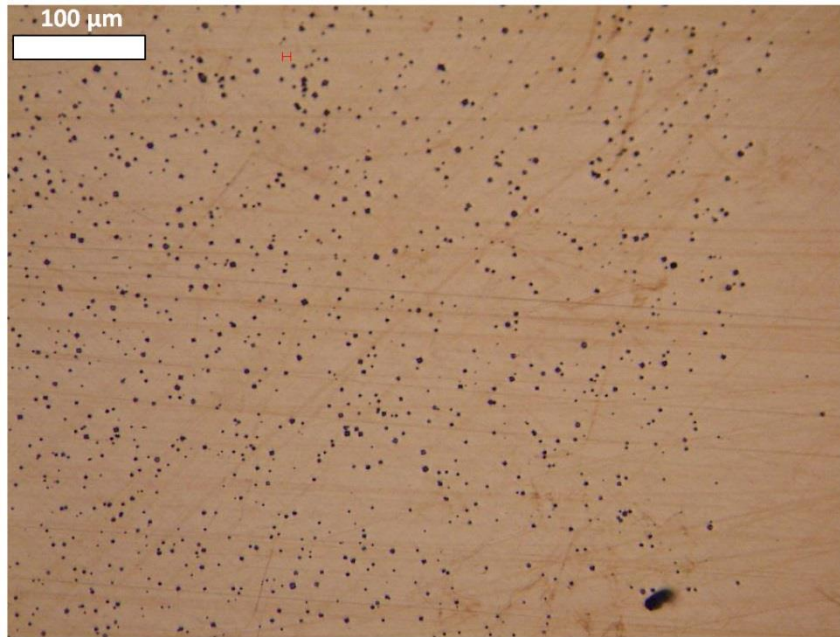


Figure 4.19: Image showing impact features on the surface of a Cu target, resulting from high-velocity bombardment with iron particles, resulting in approx. 1000 impacts (black dots) The sharp edge between the bombarded and the non-bombarded area is clearly visible.

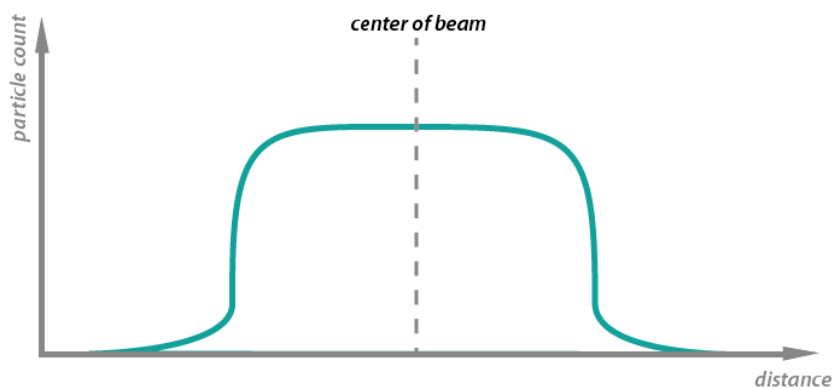


Figure 4.20: The particle density appearing as a confined Gaussian-like distribution reflects a well-defined dust beam under ideal experimental conditions.

As shown above, the area of bombardment was found in the lowermost part of the olivine target (see chapter 4.4 *Investigation of the bombarded olivine target*). To identify the beam center more precisely, five triangulation points were placed along a tangent through the lowest edge of Olivine_6 (Fig. 4.21). The space between each triangulation point is 513 pixels, corresponding to $\sim 1180 \mu\text{m}$. For each measurement frame, the density of impact related features (see definition and categorisation below) was determined and then plotted against the distance to individual triangulation points (Figs. 4.22 and 4.23).

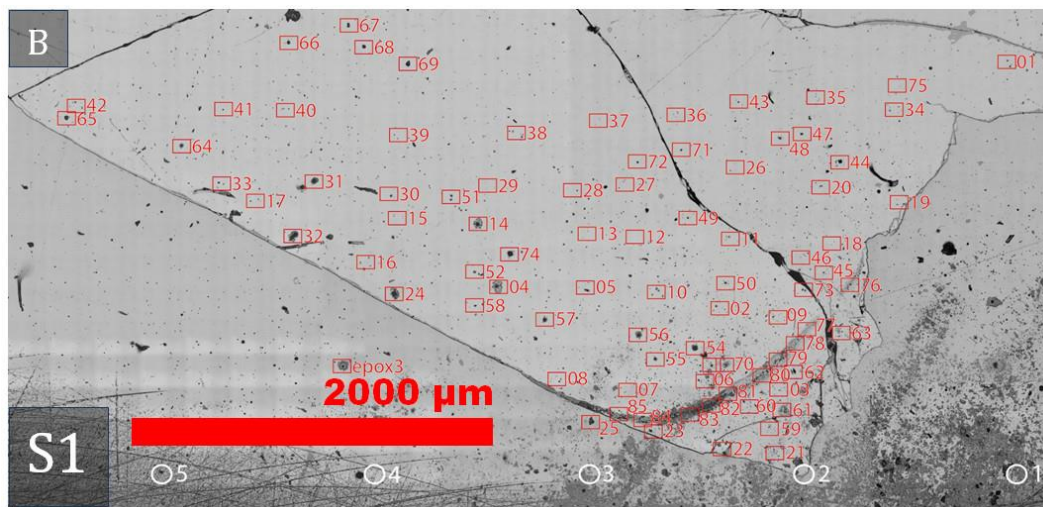


Figure 4.21: To triangulate the center of bombardment, we used the S1-B LSM laser intensity image. Red numbered boxes represent recorded frames; white circles at the bottom represent the triangulation points along the tangent line with their corresponding number.

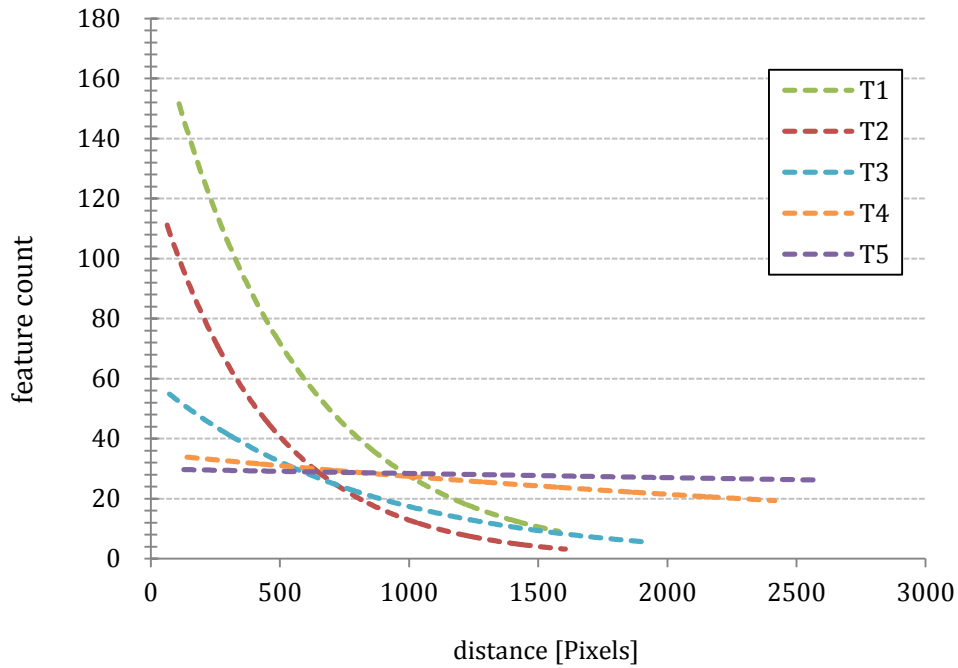


Figure 4.22: Exponential trend lines for triangulation points T1-T5 (only data for in-depth evaluated frames). Closer to the location of T1 & T2 the feature count shows the highest increase.

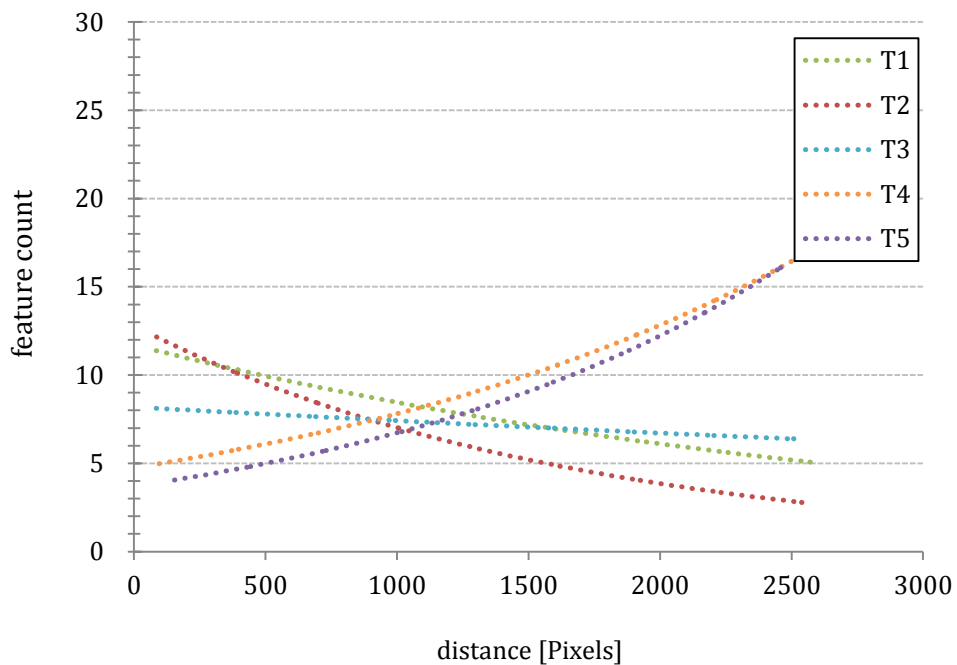


Figure 4.23: Exponential trend lines for triangulation points T1-T5 (only data for frames evaluating middle and large features only). Here also, closer to the location of T1 & T2, the feature count shows the highest increase.

It can be verified (Fig. 4.22 and 4.23) that there appears to be a trend of increasing feature density approaching the triangulation points T1 and T2. For completely evaluated frames (Fig. 4.22) and for frames without very small features (Fig. 4.23), the result is almost the same. Hence, we conclude that the center of the dust beam is located towards the triangulation points T1 or T2, hitting the target very close to the lowermost edge. By assuming a compact or blocky-shaped distribution with a beam diameter of less than 10 mm, the bombarded region is far away from the sample's inclusion regions in the area S2 (Fig. 4.14).

4.6.2 Categorisation of features on olivine targets

To be able to distinguish and differentiate the multitude of hitherto unclassified smaller and larger micro-features detected by the LSM, a categorisation needed to be established. One major classifying aspect of a feature is, whether it is positive or negative. In the henceforth applied categorisation scheme a feature is positive when it is located on the surface in any form or shape with the exception of crater rims or lips. Should a feature's main morphology be located below, or in, the surface in the form of a cavity, hole or imprint, it is regarded as a negative feature. During the course of this study it was possible to distinguish between two major types: i) impact related types and ii) miscellaneous types. Miscellaneous types are non-impact related and therefore natural features or features with an unknown origin (e.g., secondary or laboratory contamination). Each major type is further divided into sub-types which are described in this section below. Illustrative examples for every type are shown in table 4.01 on page 99ff.

i) Impact types:

The impact types are further divided into four subtypes.

A type: Impact projectiles

The A type comprises all positive impact features, i.e. all particles that remained partially or totally attached to the surface. These features can be unaltered or heated and deformed projectiles, or excavated target fragments. Some of these projectiles can retain their initially circular shape to a certain degree, even when they are compressed to the surface, but others are strongly deformed.

- **A₁:** This subtype consists of projectile particles that are stuck on the surface and appear to have several concentric rings (Fig. 4.25, left) on LSM images. This causes their profile to appear as wavy pattern (Fig. 4.24). Such effects might result from laser reflections issues or directly from interferences due to the specific surface properties of copper projectiles. It is also possible that

these effects could be influenced by airy diffraction patterns. However, it turned out that carbon coating can reduce this issue, which is discussed in chapter 4.9 *The effect of carbon coating and laser microscopy measurements.*



Figure 4.24: Sketch of A_1 type positive impact feature profile.

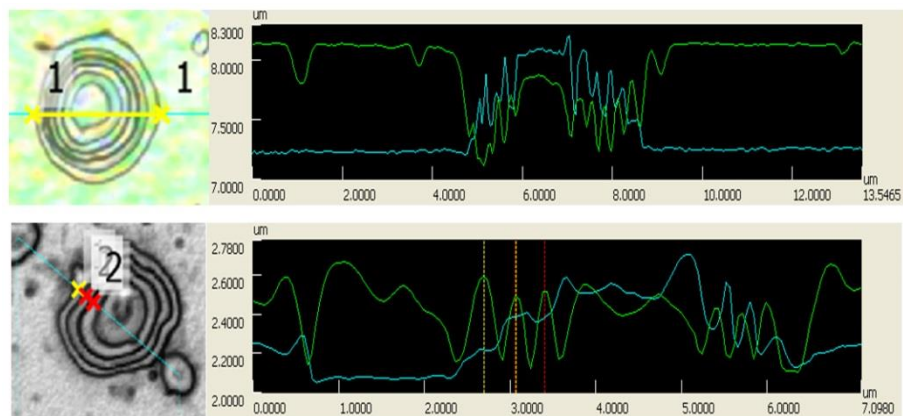


Figure 4.25: Two examples of concentric rings appearance of an A_1 type feature. Visible on the left is the LSM image and on right the corresponding profile (blue line), in addition with the intensity of the laser light (green). Decreasing intensity is likely a result of very steep edges or surface reflectance issues. Red and yellow crosses seen on the profile of the A feature in the lower panel are marks.

- A_2 : This type comprises all particles that are attached or stuck to the surface, but show no concentric rings (A_1 type). In some cases, it was observed that these particles caused a slight deformation or fracturing of the surface. Some larger particles even show flattened edges, an effect likely caused by compression and/or heating of the projectile (Fig. 4.26).

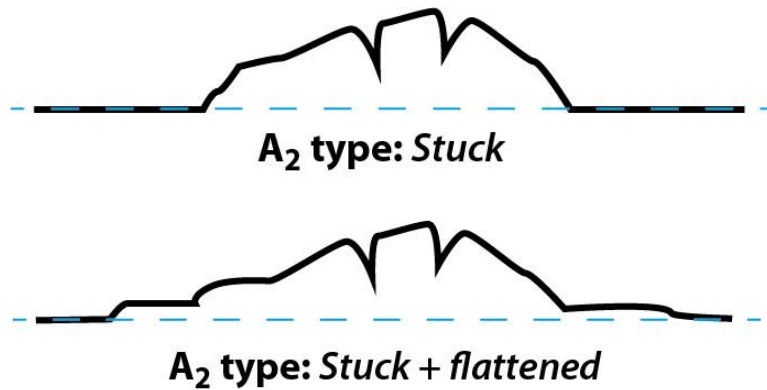


Figure 4.26: Sketches of A_1 impact types with a stuck particle (top) and stuck particle with flattened edges (bottom).

- **A₃**: This type can look like A_1 or A_2 , but display an additional effect of a surrounding halo. It appears mostly with a star shaped colourful pattern covering the surroundings of a stuck particle close to an impact feature in the LSM optical images. The star shaped halo has a very low surface elevation of only tens of nanometers. It is possible that this effect is linked to heating- or shock-effects in the upper layers of the mineral surface. It seems that this effect causes some kind of light diffraction, and hence appears in different colours in LSM optical images (see Table 4.01: A_3).

B type: Splash- or flat cone features

These types are also positive features, but are different to any A type in being more extended and flat. B types obviously include Cu projectiles which likely have undergone a sufficient degree of heating and/or melting to cause splash and flattening effects, covering a wide-range of the surface. Both B_1 and B_2 are quite flat, which is clearly shown by larger D/d ratios than A types (see chapter 4.6.4 *Statistics on the bombarded target*).

- **B₁**: This type represents the splash features, which are very flat and appear dispersed. The splash features consist of a bulky central zone and are surrounded by many nearby small-scale features sprinkled around the center (Fig. 4.27). Splash or spray effects were reported by VEDDER (1971) using LSM

investigation. On soda lime glass struck by Al projectiles, a splattering of the projectiles and indentations were observed at low velocities, also using a Van de Graaff accelerator (MANDEVILLE & VEDDER, 1974). Due to the colourful appearance of B₁-features in LSM optical images, it is assumed that oil residues could be involved, which might work as an adhesive.



Figure 4.27: Sketch of the B₁ impact type, which is more extended and flatter than any A type and shows the effect of sprinkling.

- **B₂:** This type was only found in the Cu-track, which will be discussed in detail in a later section (see chapter 4.4.5 *Cu-track*). The features show a minor elevated part in the center and an outward dispersion, which sometimes appears as ring-shaped steps on C-LASER DIC images. This subtype can be described as a flat cone (Fig. 4.28). In some images it seemed that B₂ is a Cu projectile pressed into a crater pit or a precursor crater, which is indicated by low degrees of fracturing.



Figure 4.28: Sketch of the B₂ impact type, which is as well more extended and flatter when compared to any A type, and appears like a flat cone.

Profiles of B₁ and B₂ can often look very similar and hence, they cannot be classified by their profile shape only. It is always necessary to inspect the close surroundings for sprinkled small-scale features characteristic for B₁ types. However, as B₂-features were only found in the Cu-track and only examined after carbon coating, it could well be that details of the original shape of these features were smoothed.

C type: Crater

The crater type is a negative feature and can be easily identified in LSM images without the aid of profile scans. The morphological criteria for crater characteristics on millimetre- or micron-scales were described in section 2.2 *Methods of impact experiments*, see also MANDEVILLE & VEDDER (1971), HÖRZ, *et al.* (1975) and NAGEL & FECHTIG (1980). The observed craters on Olivine_6 usually consist of a crater pit, which is intact or barely destroyed and is surrounded by fractures that extend radially from the crater. A few craters also show spallation effects, which are easily visible as optical refraction in LSM images, due to the nature of damaged olivine surface. Additionally, positive morphological effects can be found around craters. These show angular shapes and are smaller than the crater itself. These features are displaced fragments and are assigned to their own type (E type). Almost flat craters without fractures can only be verified via LSM profile measurements. Commonly, all detected craters tend to be spherical or slightly elliptical, if not destroyed by material spall-off, show rims and rarely lips, except when they experienced severe spallation effects that cause irregular shapes. These characteristics help to distinguish between a surface defect and a flat crater.

D type: Dents, precursor crater stages and impact rings

Impact experiments were conducted with the horizontal dust beam perpendicularly hitting the target surface. Should an impacting projectile have insufficient kinetic energy for the production of a crater or sticking to the surface, it would then rebound and leave an imprint on the target surface. Those imprints or indentations show as small rings, or, depending on the impact energy, as a precursor crater stage. These features appear negative due to their slightly lowered central part. A simplified illustration of D features is shown in the sketches below (Fig 4.29). Dents rarely show very fine radial fractures, which are only visible in close-ups of C-Laser DIC images. In general dents can be easily identified on C-Laser DIC images, as their shaded ring shape is clearly recognisable on the surface. VEDDER & MANDEVILLE (1971; 1974) observed similar features as dents before, describing them as rebounding particles leaving behind a shallow crater with a slightly raised and smooth rim. Although they used

soda lime glass as target material, which is a rigid material, they argue that this feature is an effect of plastic deformation



Figure 4.29: Sketch of D impact types, which appear as indentation on the surface.

Even in the 11 frames that were studied in great detail, it was impossible to measure every feature suspected to be D type with LSM, because of their low depths, sometimes close to the level of surface roughness of $\sim 10\text{--}20$ nm. Noteworthy is that dents are underrepresented in the later measurements and statistics, as they are difficult or not measurable at all.

E type: Displaced fragments

These features are situated exclusively in the surroundings of craters, hence, they must be related to the cratering process. Although they cannot be described as typical ballistically ejected material, it is likely that they are excavated debris or fragments due to the impact process. Many E types fragments show an inclination of their top surface directed away from the crater center (see table 4.01). They surround the crater in a radial pattern. VEDDER (1971) reported small spheres surrounding a crater in close vicinity as a result of the spraying of molten droplets. Due to the fact that E type features are angular or show a blocky shape, they cannot be explained with the mechanism advocated by VEDDER (1971). It is assumed that these fragments were somehow displaced from the initial crater, or may have been excavated in radial directions. Also E types are underrepresented in the measurements and statistics, as during evaluation of the impact features they were found to be morphological assets of craters (C type) and not an individual impact feature by their own and therefore not further recorded in detail.

ii) Miscellaneous types:

N type: Miscellaneous negative Features

This type includes all negative features that are found on Olivine_7 and morphologically indistinguishable features on Olivine_6 that are not obviously impact related.

- **N₁**: This subtype consists only of mineral defects, which are characterised by irregularly shaped cavities with larger diameters and depths when compared to subtype N₂.
- **N₂**: This subtype comprises all other negative features, which are too small to be clearly classified and show a shallow or slight irregular pit profile (Fig. 4.30). Those features were already described for non-bombarded Olivine_7 (see section 4.2 *Investigation of a non-bombarded target*) and showed diameters between 0.134 to 1.735 μm and depths between -0.01 to -0.317 μm . There are some features that show a zig-zag-like pattern in their profile (Fig. 4.31).



Figure 4.30: Sketch of the N₂ non-impact related types, which are very small and found on non-bombarded and bombarded targets.

Zig-zag patterns can be induced, when the laser light strikes on a very steep edge of a particle/pit, hereby causing reflection intensity problems. For such very small features it matters, how accurate and on which part of the feature the profile was applied (Fig. 4.32). Exact measurements of these types of small features are limited by the image resolution of the LSM. The features have depths ranging from -0.02 to -0.52 μm and a diameter between ~ 0.8 and ~ 1.17 μm . The lateral resolution accuracy for the LSM is 0.21 μm (3σ), so these features can be assumed as real and not as artefacts.



Figure 4.31: Sketch of other non-impact related N_2 features, which are very small and found on non-bombarded and bombarded targets. Their profile shows a zig-zag pattern with major negative contribution.

Due to resolution limit and minimal displacement on C-LASER DIC images, which have always a minimal shift compared to height images (see chapter 2.4.3 *Measuring process with a Keyence confocal laser microscope*), zig-zag patterns can arise. Since these small features are generally not visible on laser intensity- or height-images, using C-LASER DIC images is the only way to discover them. As it is not always possible to place a proper profile over the center of these features, it is very difficult to measure them accurately. The same applies to the positive counterpart of this particular subgroup: P_2 . Zig-zag patterns generally extend over ~ 3 pixels, which are ~ 140 nm in diameter. Several attempts are generally needed to achieve the most appropriate profile and optimum of morphological information. This then also determines, whether the zig-zag pattern is positive or negative (Fig. 4.32). It is considered as a pit, if the larger profile contribution of the zig-zag pattern is negative.

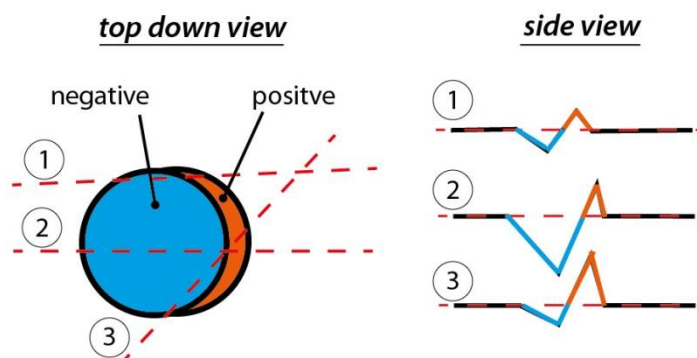


Figure 4.32: This schematic drawing is an example of a small N_2 type zig-zag feature covering a region of ~ 140 nm in diameter. Depending on how accurate height data are transformed into image information and depending on the orientation of the profile, the profile pattern can vary. Case (1) and (2) are considered as negative zig-zag features, because negative proportions dominate in the side view. Case (3) is considered positive, because of its major positive contribution in the side view.

Another effect that leads to the appearance of zig-zag patterns in profiles are issues that cause bad reflectivity and signal intensity of zero (Fig. 4.33).

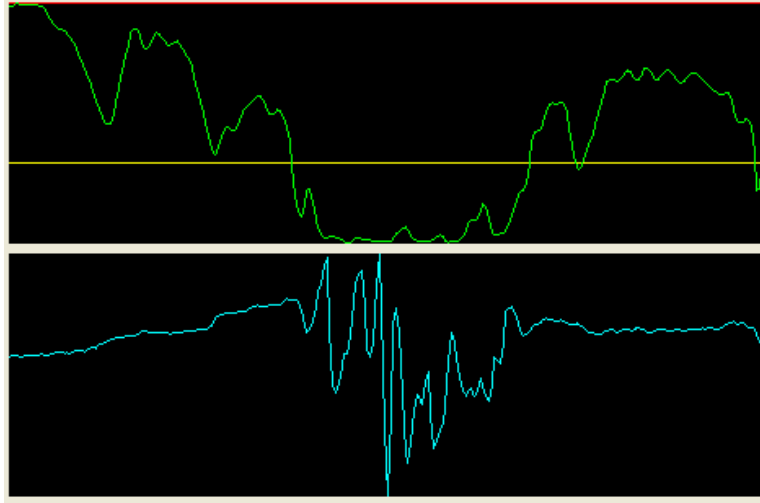


Figure 4.33: These two images show an example for an extremely poor intensity reflectance of a feature. The top profile shows intensity (green), the bottom profile shows the topographical interpretation (blue). When intensity of reflectivity reaches the bottom (signal intensity of zero), this pixel is interpreted as flat. Such, if pixel information is over or under sampled they can lead to zig-zag patterns.

P type: Miscellaneous positive features

This feature type includes all positive features found on Olivine_7 and similar non-impact related features on Olivine_6.

- **P₁:** This subtype covers all features identified as dust (no Cu) or contamination particles and is not impact related. In general, these types have larger diameters and heights as compared to the following subtype P₂.
- **P₂:** This subtype covers all other small, positive features which are not impact related and also not classified as P₁ type. When the profile shows one single ridge, it is considered a “peak”. With the occurrence of several sub-peaks, it is classified as “rougher peak”. In addition, if the larger peak of the zig-zag pattern is positive it is considered a positive peak (Fig. 4.32). A simplified illustration of each P₂ feature is shown in Figure 4.34.

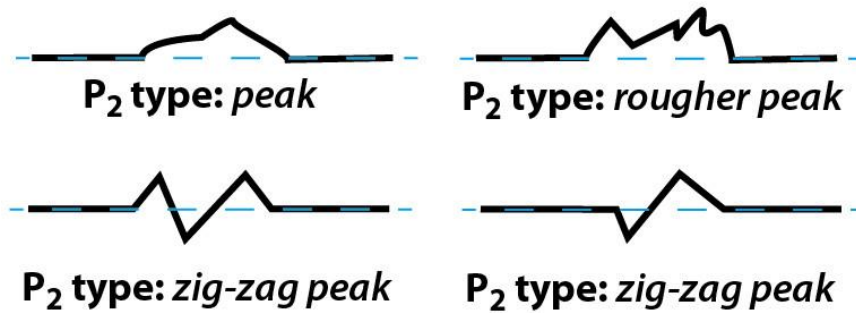
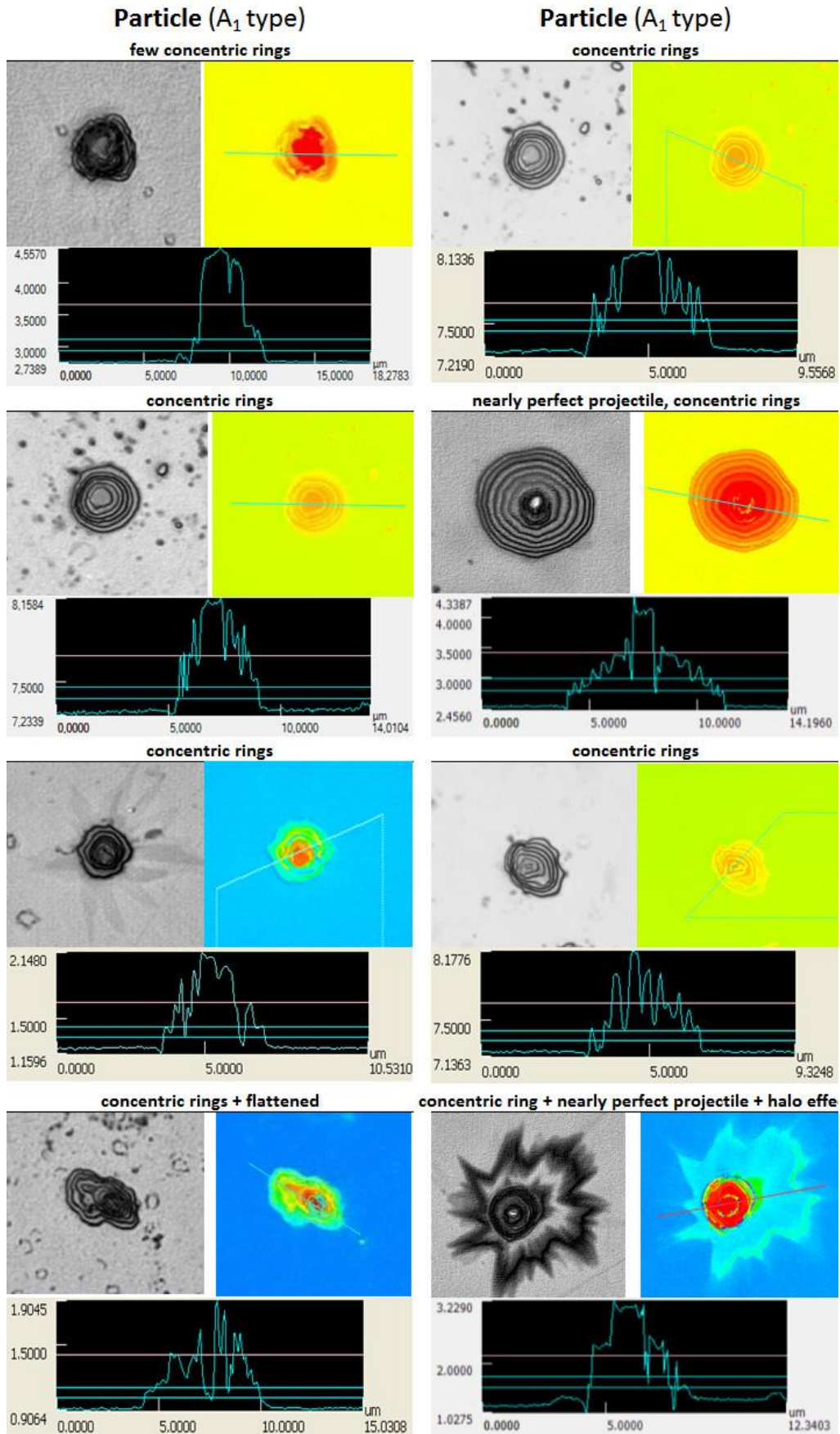


Figure 4.34: Sketch of the P_2 non-impact related types, which are generally very small and can be found on non-bombarded and bombarded targets. When a profile shows a zig-zag pattern and the major contribution is positive, the feature is considered as P_2 .

The following register shows a comparison in C-Laser DIC-images and height-images with their associated profile. One exemption is made for the A_3 subtype, where also laser and optical images were added to show the colourful refraction effect of this feature. It needs to be noted that the height-scale of the displayed line profiles is usually stretched when compared to the x-scale in order to show topographical details. Hence, there visual impression of the flatness of the structures may be misleading.

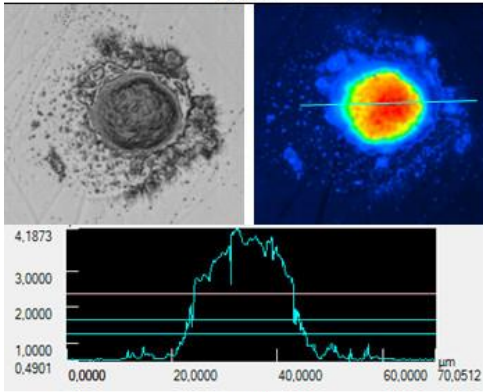
It is also important to note that the 2D-height images are cut-outs of larger pictures, so the colour coding may not cover the full range in each picture. The straight lines in colored 2D-height images correspond to the horizontal dimensions of the panel displaying the profiles. The three different horizontal lines in the profile panels are related to the surface roughness application of the *VK-Analyzer* (see section 2.4.3 *Measuring procedure with a Keyence confocal laser microscope*) and are of no importance for the purpose of illustration. Crosses along a profile line in 2D-height images are marks corresponding to vertical lines in profile panels. Furthermore, the different colours of the profile lines are of no special meaning.

Table 4.01: A compilation of features found on non-bombarded and bombarded olivine targets.



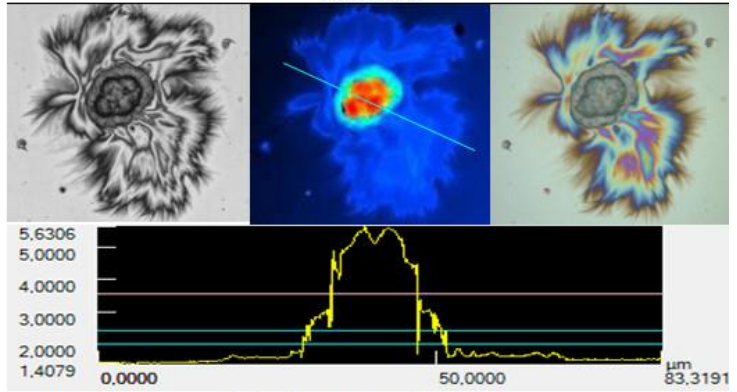
Particle (A₂ type)

stuck

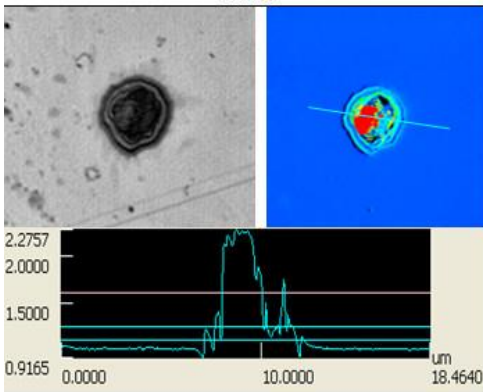


Particle (A₃ type)

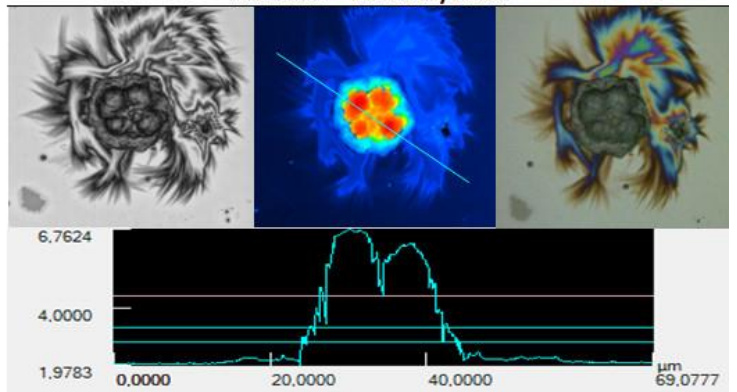
halo effect



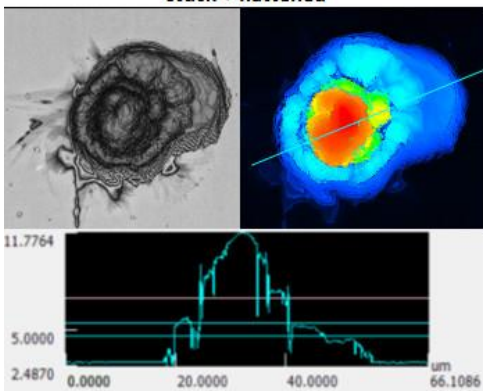
stuck



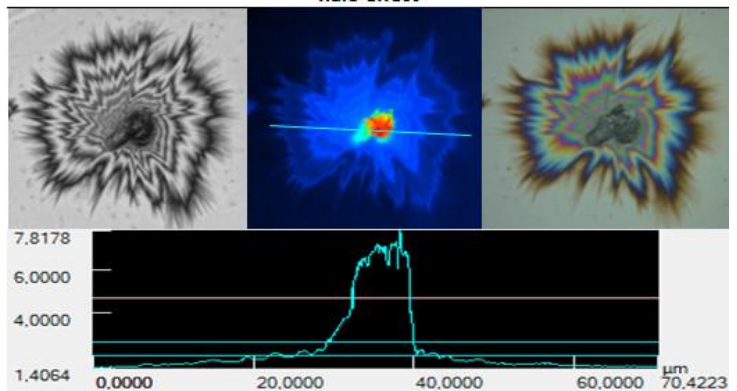
halo effect + secondary crater



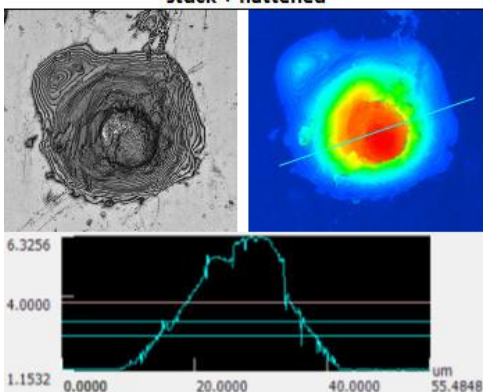
stuck + flattened



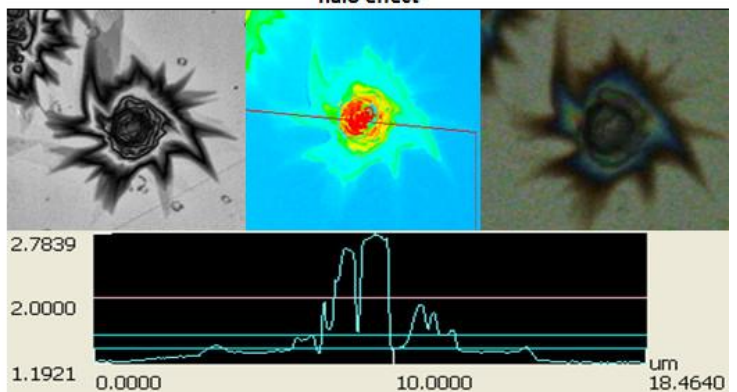
halo effect

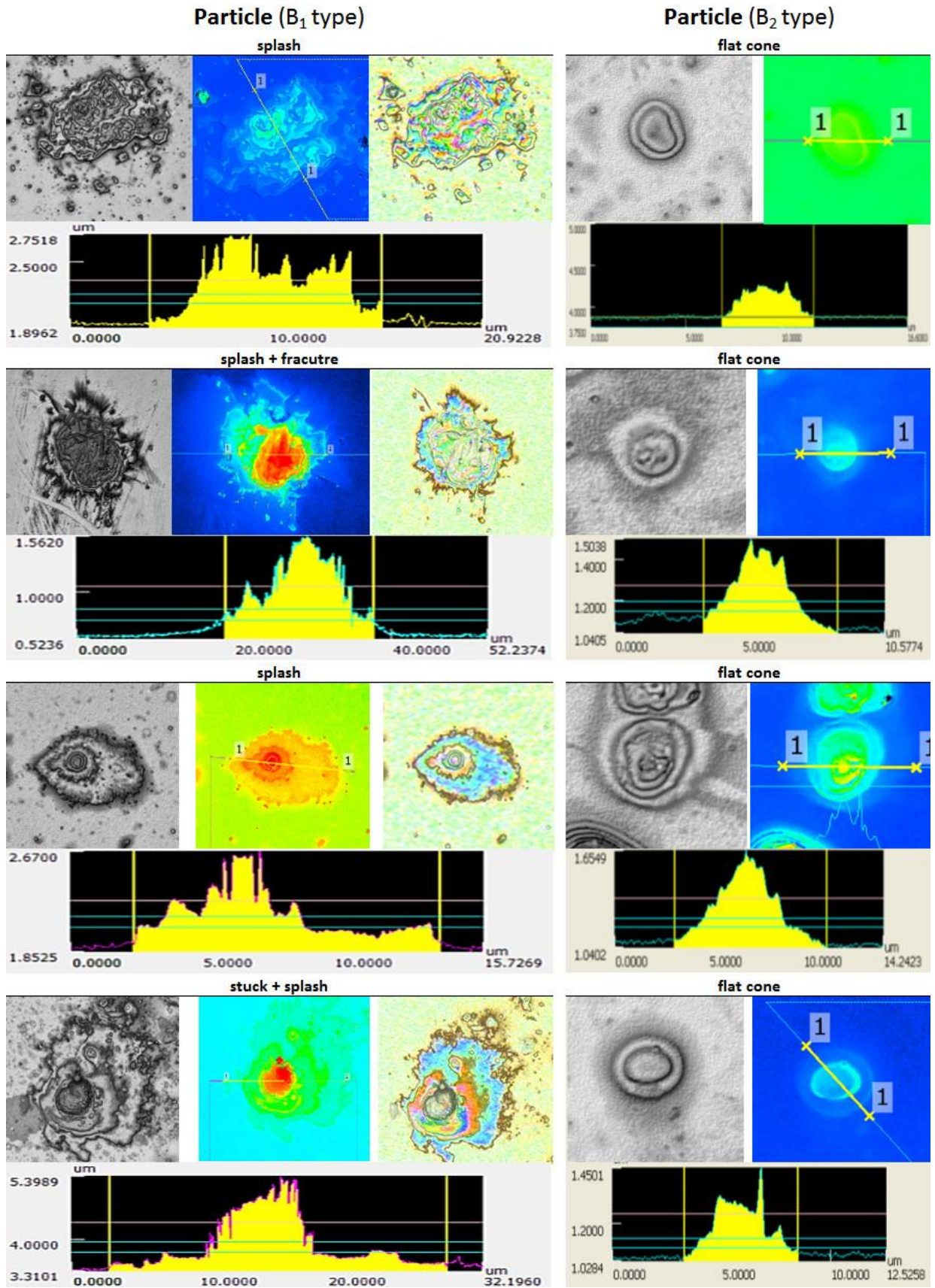


stuck + flattened



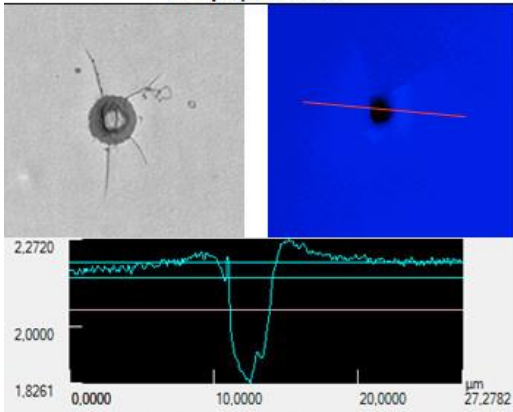
halo effect





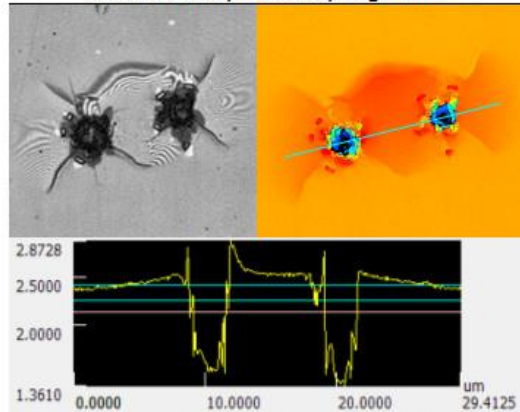
Crater (C type)

simple, fractures

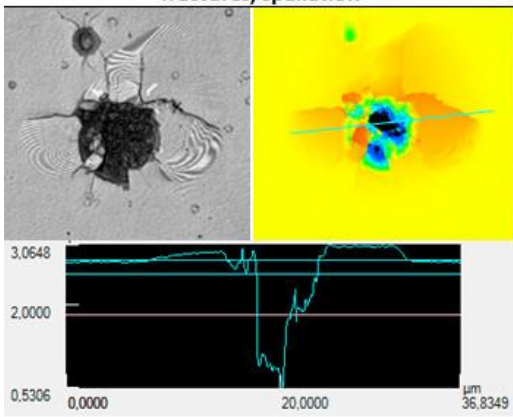


Crater (C type)

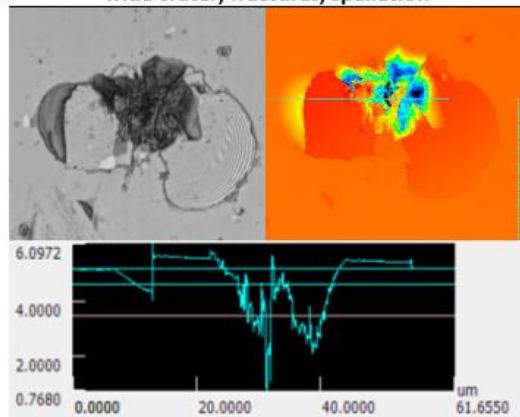
double crater, fractures, fragments



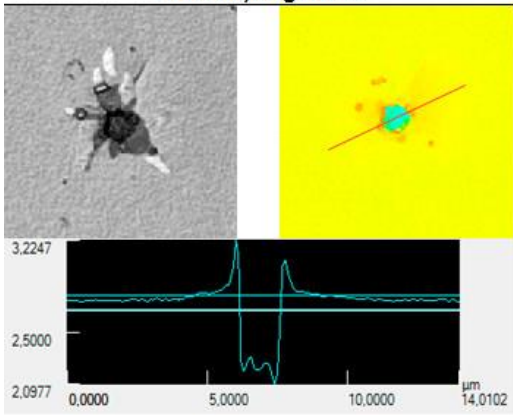
fractures, spallation



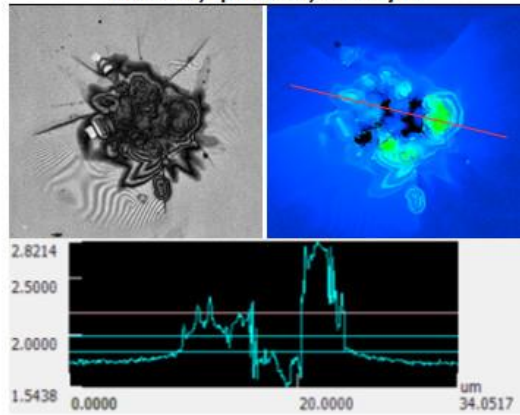
wide crater, fractures, spallation



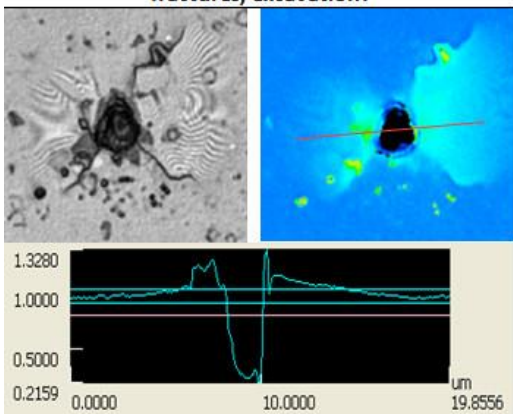
fracture, fragments



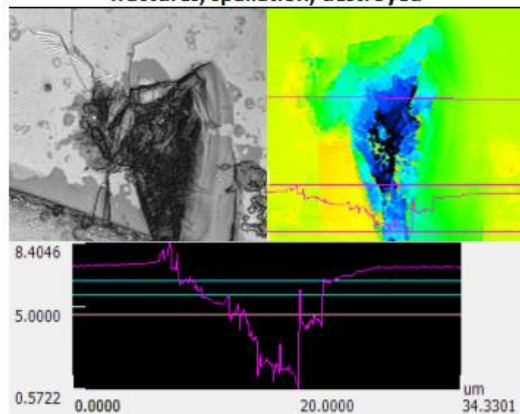
fractures, spallation, destroyed

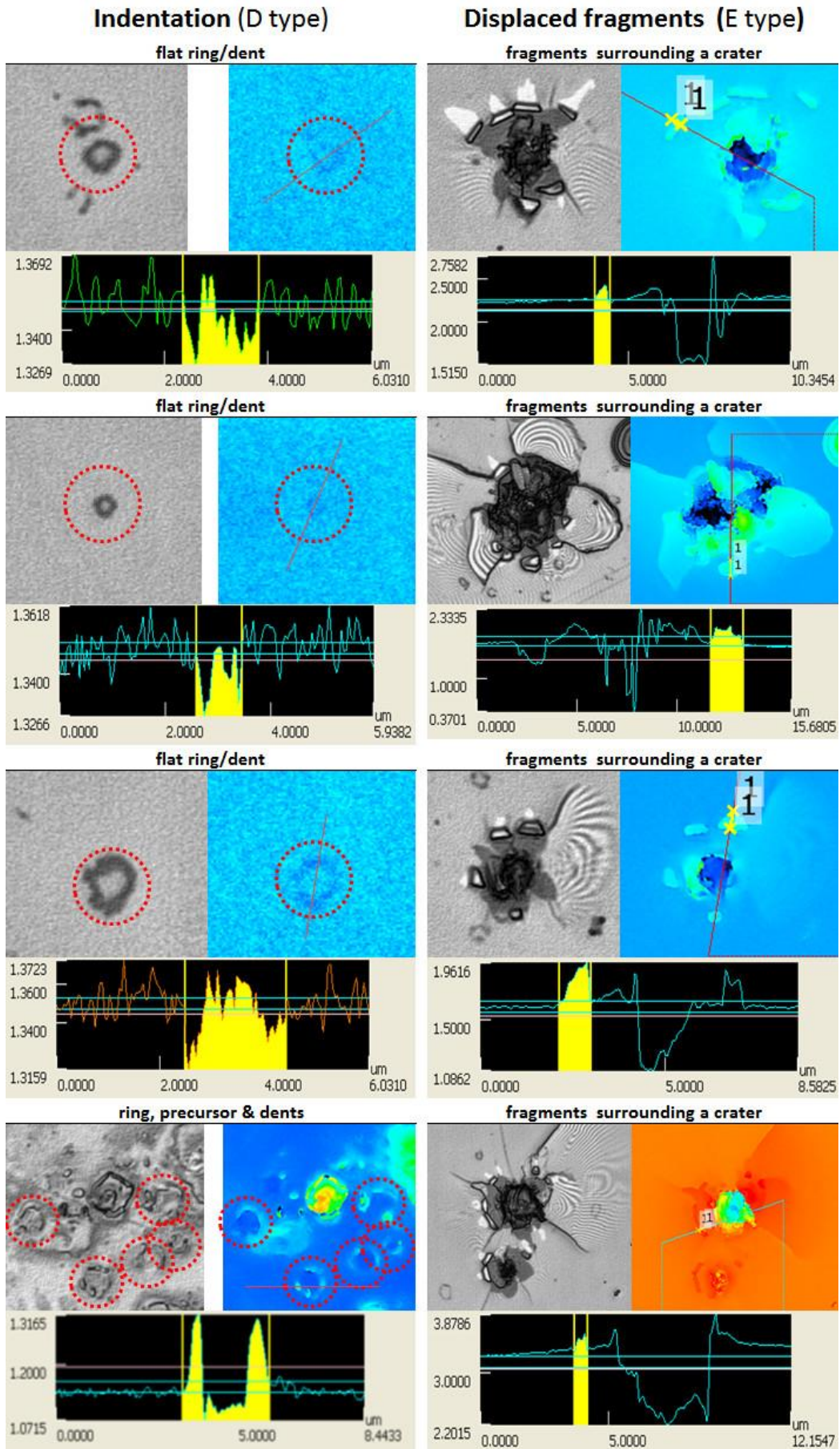


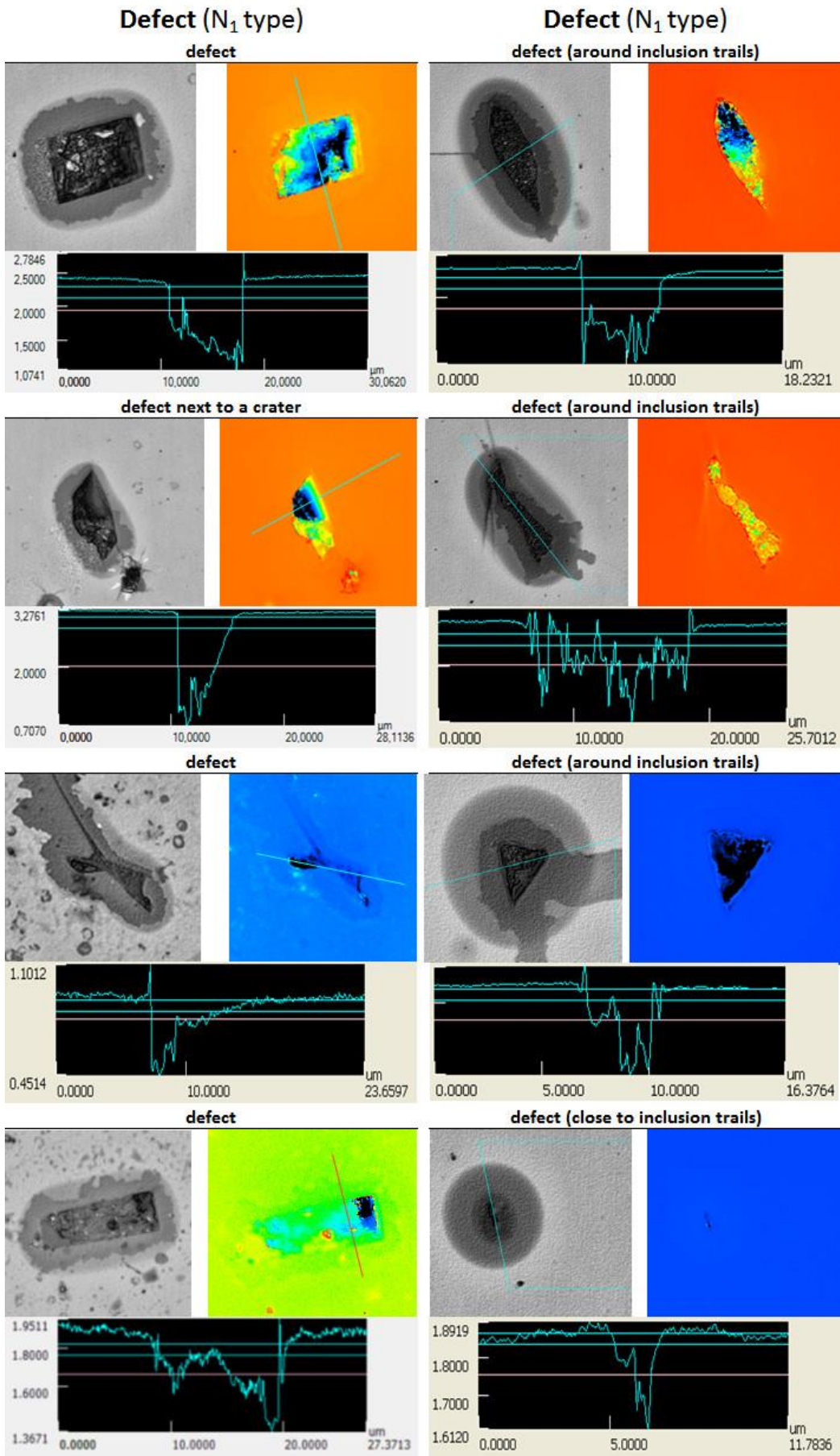
fractures, excavation?



fractures, spallation, destroyed

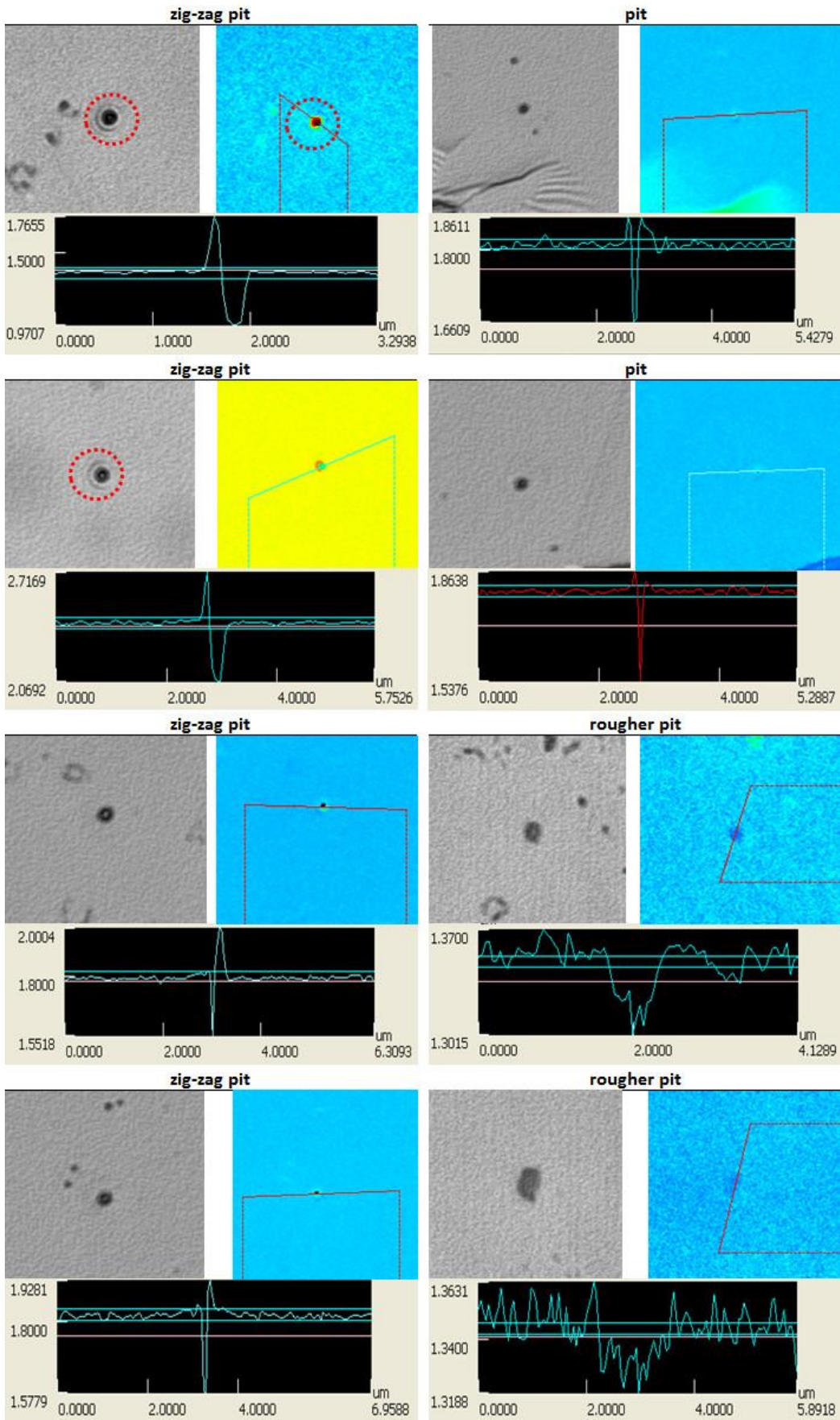




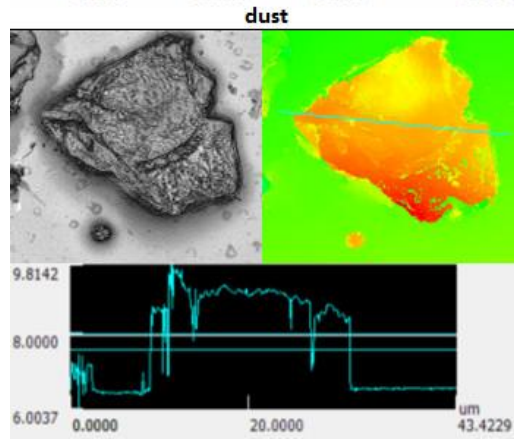
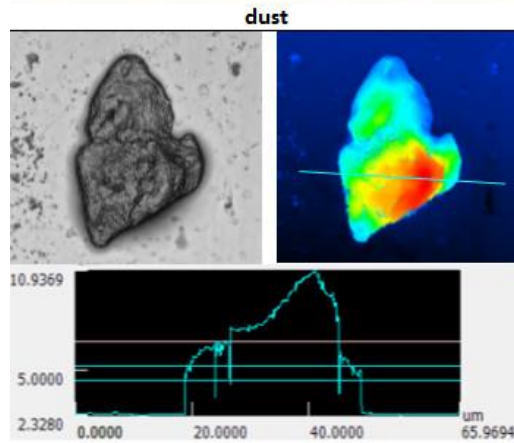
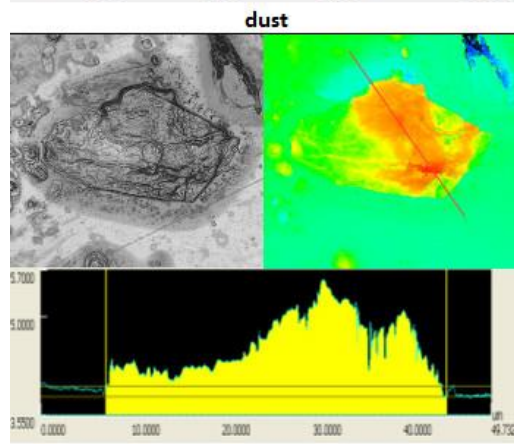
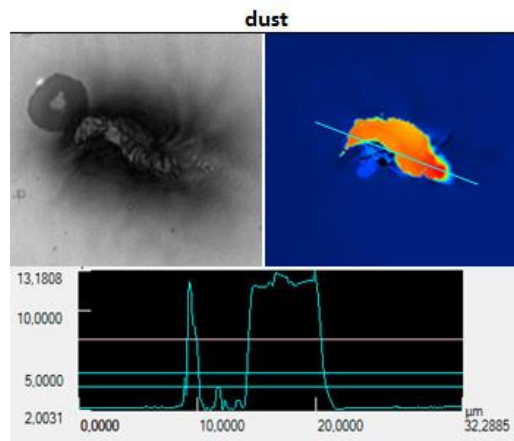


Misc. negative feature (N₂ type)

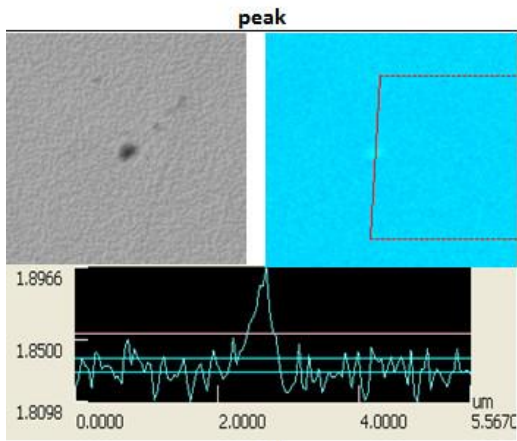
Misc. negative feature (N₂ type)



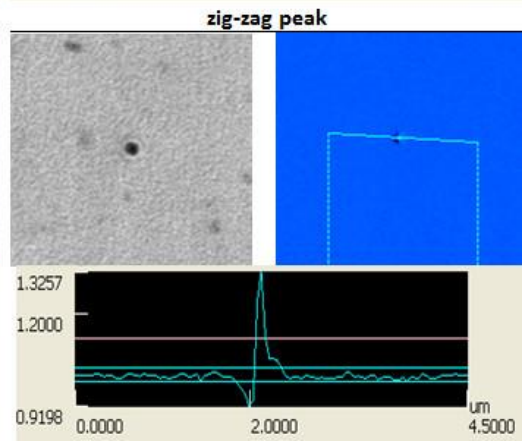
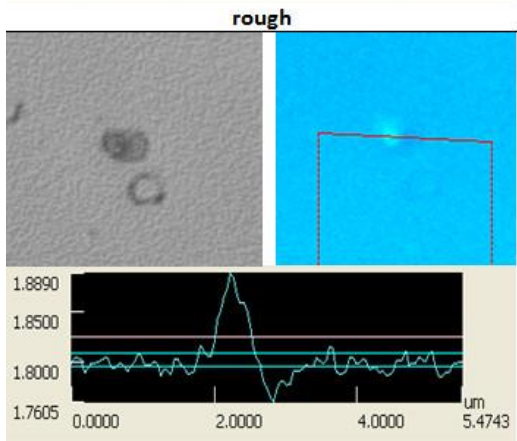
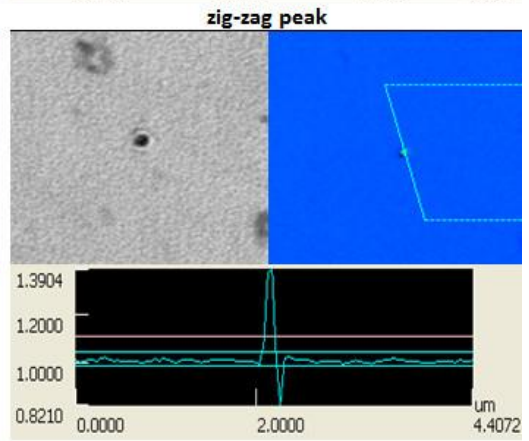
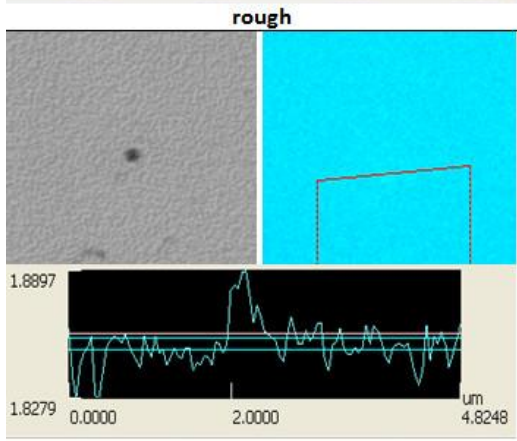
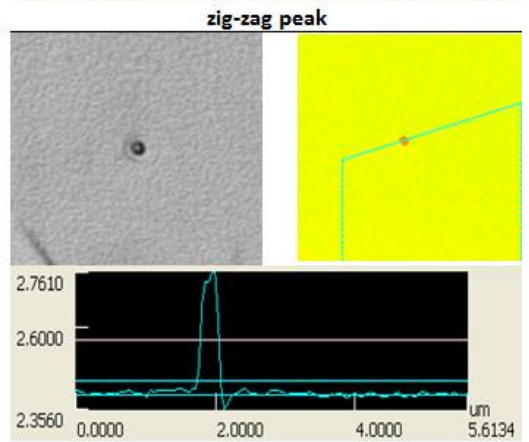
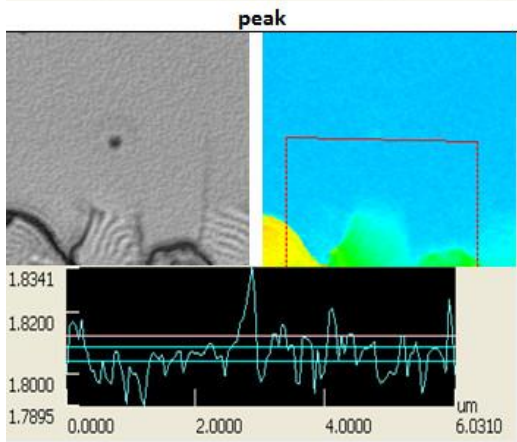
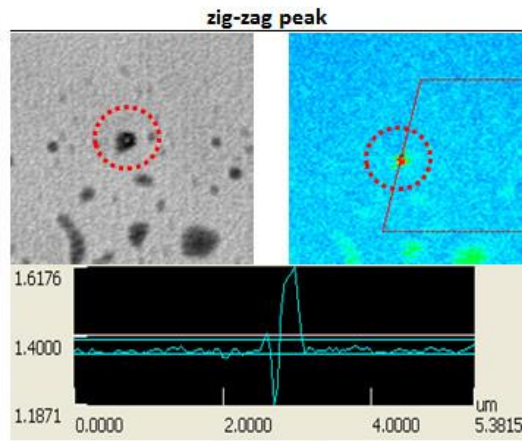
Contamination (P₁ type)



Misc. positive feature (P₂ type)



Misc. positive feature (P₂ type)



4.6.3 Concentration of impact features

To get a better impression of the bombarded area of the impacted olivine, a heat map of Section S1 was generated (Fig. 4.35). The data for the heat map are based on the number of impact related types A, B and C within a recorded frame. D types are not taken into account, because not every D type was measurable. Also E types are neglected, since they are considered to be side products of C types. The map was prepared by hand similar to geological maps and then digitized on the computer. It is noticeable that the region of largest impact feature density is related to the Cu-track (see chapter 4.6.5 *Cu-track*).

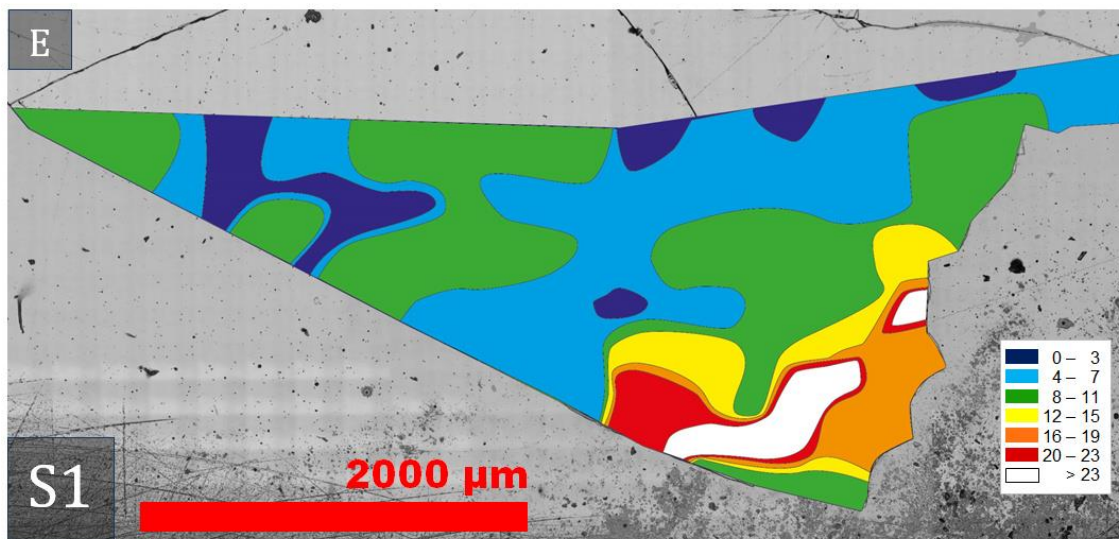


Figure 4.35: The colours represent densities of impact related features (Type: A, B & C): 0-3 dark blue, 4-7 light blue, 8-11 green; 12-15 yellow, 16-19 orange, 20-23 red, 23+ white, all numbers per frame.

4.6.4 Size distributions on the bombarded target

The following section shows histograms of diameter and depth or height of analysed features (all 43 frames) to get a first overview of distribution differences between non-bombarded Olivine_7 and bombarded Olivine_6, regardless of feature types defined above.

To facilitate a comparison, the histograms cell width for mean diameters ($h = 0.2$), depth and height ($h = 0.1$) on bombarded Olivine_6 and non-bombarded Olivine_7 were chosen to be the same. Histograms for non-bombarded Olivine_7 were already shown in section 4.3. *Results of the non-bombarded target.*

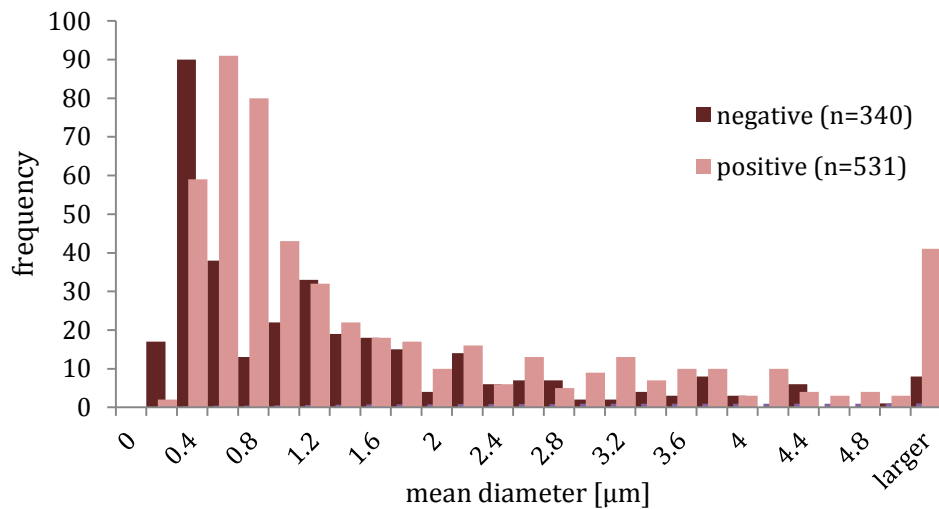


Figure 4.36: Frequency distribution of diameters of all features on Olivine_6.

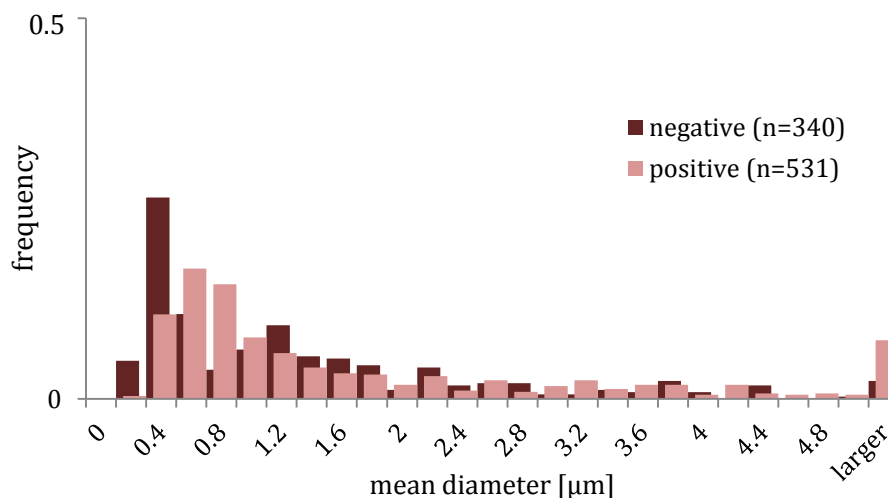


Figure 4.37: Normalised frequency distribution of diameters of all features on Olivine_6.

The distributions of the diameter (Fig 4.36 and 4.37) show that negative and positive features on Olivine_6 cover a broad range up to 5 μm , and larger. Negative features have a maximum of 0.4 and 1.2 μm , while positive features have their maximum at 0.6 μm . It needs to be noted, that in general very small features found on the 11 de-tailed frames have diameters below 0.4 μm .

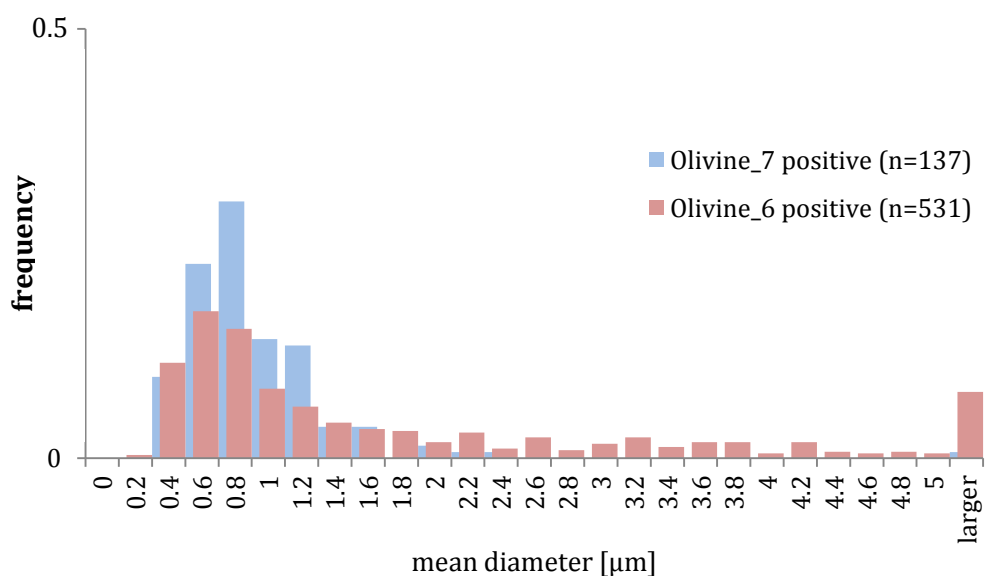


Figure 4.38: Comparison of normalised frequency distribution for positive features on Olivine_6 and Olivine_7.

Comparing the distribution of positive features on the surfaces of the non-bombarded Olivine_7 and the bombarded Olivine_6 (Fig. 4.38), the location of maxima (mainly extremely flat P₂ type non-impact features) are similar at about 0.6 and 0.8 μm , respectively. However, Olivine_6 shows a significantly more pronounced tail to larger feature diameters. This is mainly due to sticking Cu projectiles of mainly type A and also B and E, which will be shown below in diagrams displaying categorised features

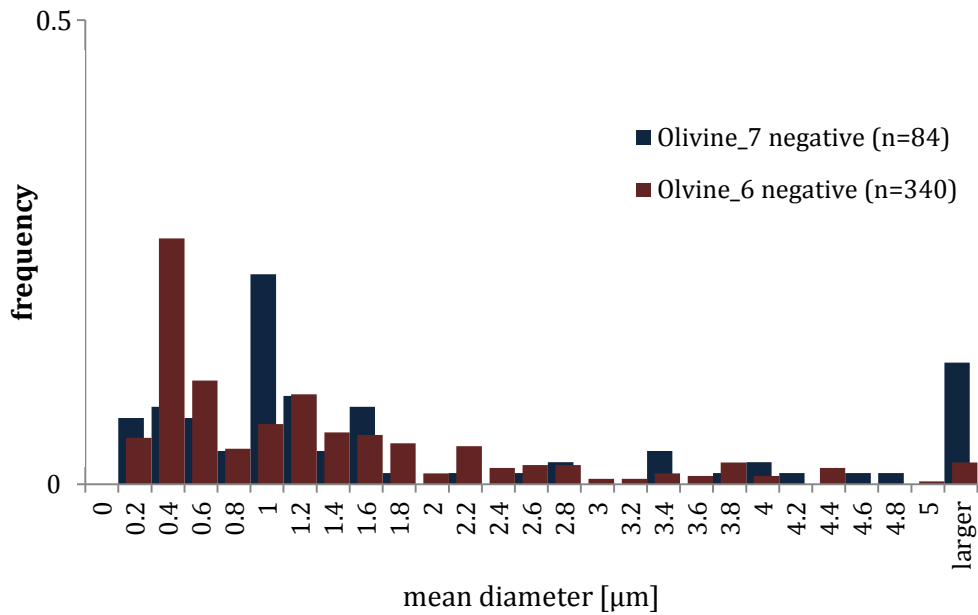


Figure 4.39: Relative distribution for negative Olivine_6 and Olivine_7, with their occurrence frequency on the y-axis normalized to 1.

By examining the diameters of negative features, the differences become clearer (Fig. 4.39). Before the bombardment there were two peaks, one at 1.0 – 1.2 μm and the second above 5 μm , which is strongly related to large surface defects (N_1 type). However, on the bombarded surface, measured was a zone with lesser surface defects, shows a decline of features greater than 5 μm and a shift from a maximum of 1.0 μm downwards to 0.4 μm , which is related to dents. The strong contrast is obviously an effect of impact craters and dents (C and D type).

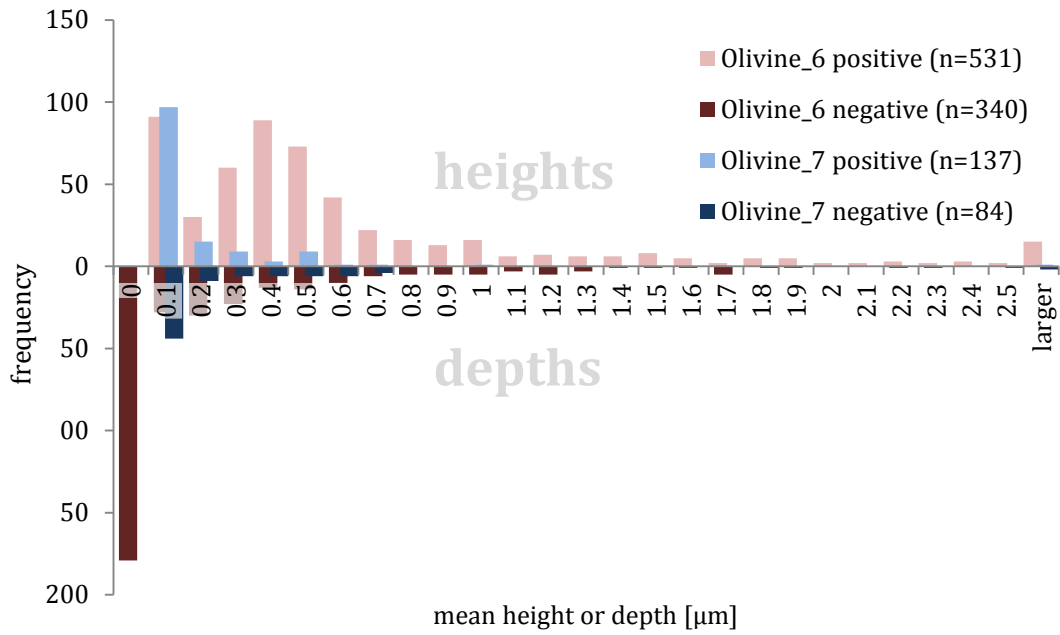


Figure 4.40: For better overview the histograms for height (top) and depth (bottom) were put in to one single diagram but represent two separate data. The x-axis represents either the value of height for positive features or value of depth for negative features. The y-axis displays the frequency of occurrence in both directions as absolute distribution.

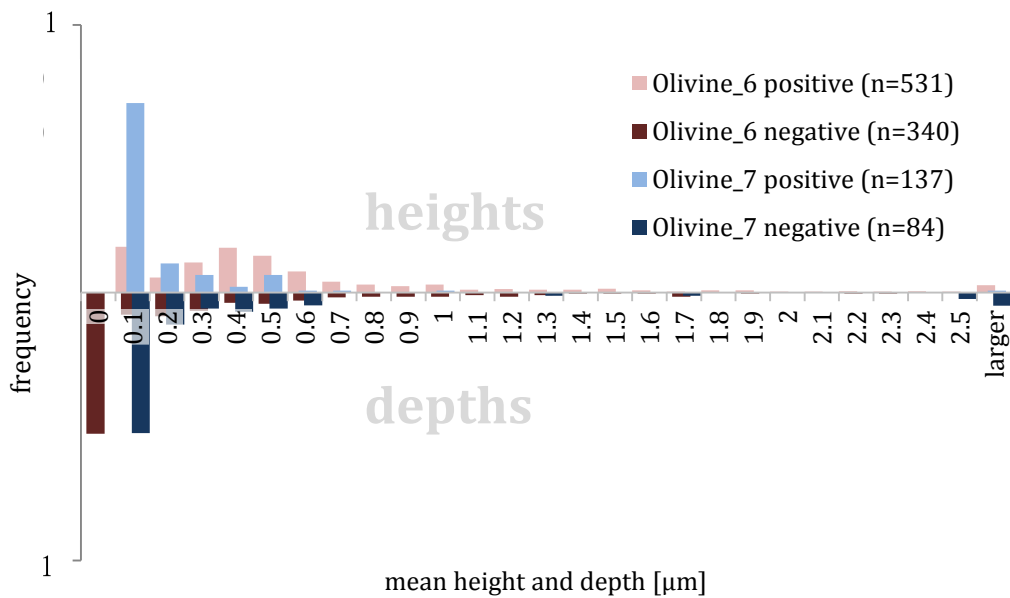


Figure 4.41: For better overview the histograms for height (top) and depth (bottom) were put in to one single diagram but represent two separate data. The x-axis represents either the value of height for positive features or the value of depth for negative features. The y-axis displays the frequency of occurrence in both directions as a relative distribution.

Whilst on Olivine_7 positive features having a maximum at heights of $\sim 0.1 \mu\text{m}$, this dispensed on Olivine_6 to all sizes showing two minor peaks, again around $0.1 \mu\text{m}$ and around $0.4 - 0.5 \mu\text{m}$ (Fig. 4.40). This is an effect due to sticking particles (A and B type), which remain on the surface of Olivine_6.

The major depths on Olivine_7 were also around $\sim 0.1 \mu\text{m}$. This dramatically shifted to lower depths on Olivine_6, most likely due to dents (D type). In addition, the distribution for depth has dispensed to deeper values up to $-1.3 \mu\text{m}$ (Fig. 4.41). This can be related to cratering effects (C type) with certainty.

4.6.5 Cu-track

The Cu-track is a phenomenon that became apparent during SEM investigation. A corresponding LSM image is shown in Fig. 4.42. Alongside the track, several frames with sequential numbers were scanned (green). These frames are LSM optical images and are displayed in detail in the following Fig. 4.43 – 4.45. Frame #76 shows the lowest impact feature density. The density of impact features - predominantly Cu particles laying or sticking on top - increases to a maximum at frame #83 and decreases to frame #85. The track is divided by the dashed blue lines into different sections which are characterised concerning visibility of Cu particles or B type features, and impact features like craters (C type) and dents (D type). Fig. 4.43 – 4.45 show that positive features are abundant, while negative features are rare, indicating predominantly low impact speeds of Cu projectiles or that crater where covered by subsequent impacting projectiles. The higher the impact feature density of low speed Cu projectiles covering the surface, the less specific negative impact features are recognisable. In the first sections Cu particles, craters and dents are distinguishable, but become more and more indistinguishable when approaching the maximum feature density of the Cu-track. This is an effect of massive impact feature overlapping.

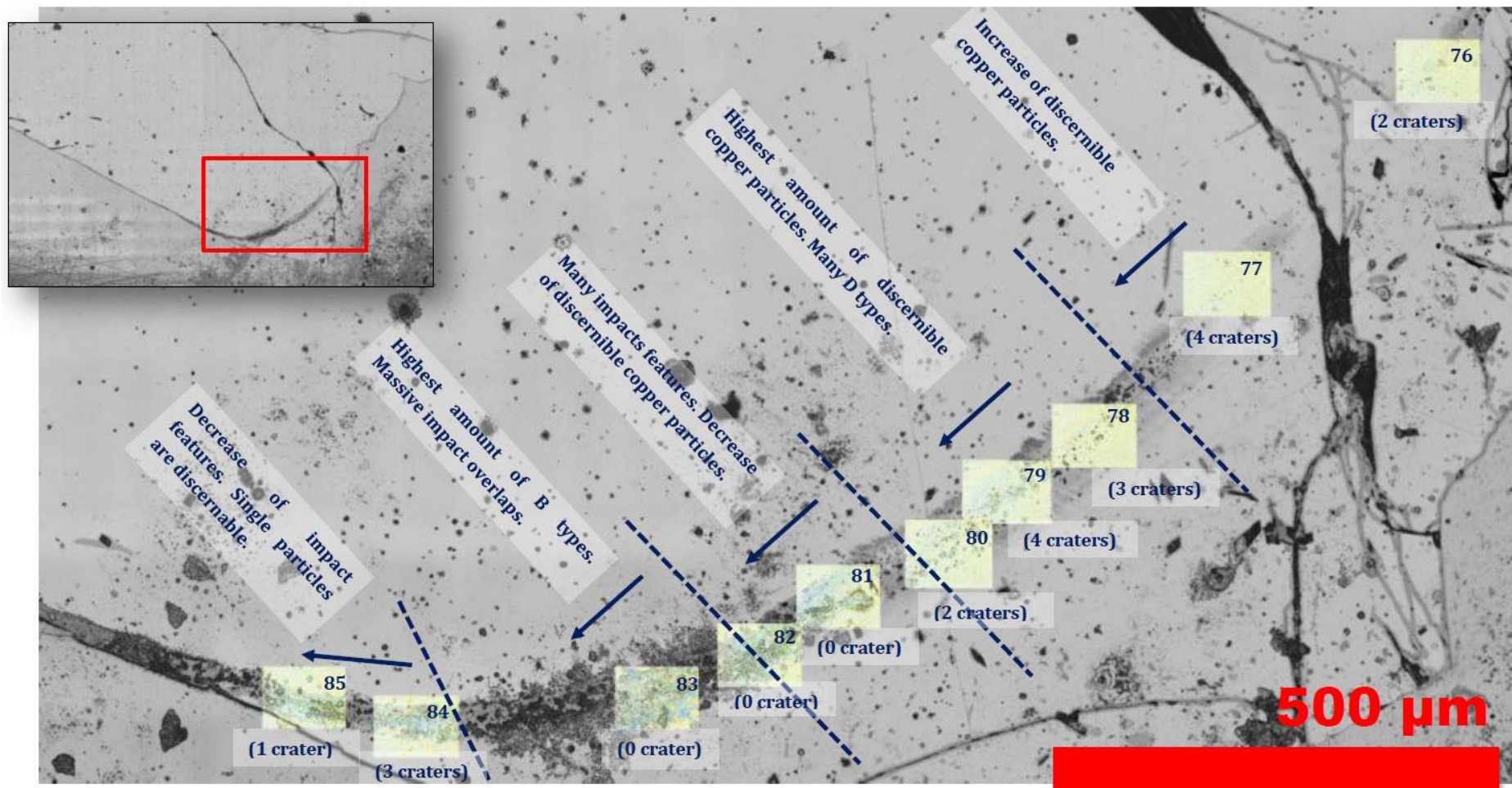


Figure 4.42: This LSM laser intensity image shows an overview of the Cu track. The top left image shows the section where the Cu track is located. The crater indication below each image shows only discernible features. Most likely there are craters in frames where the indication is zero.

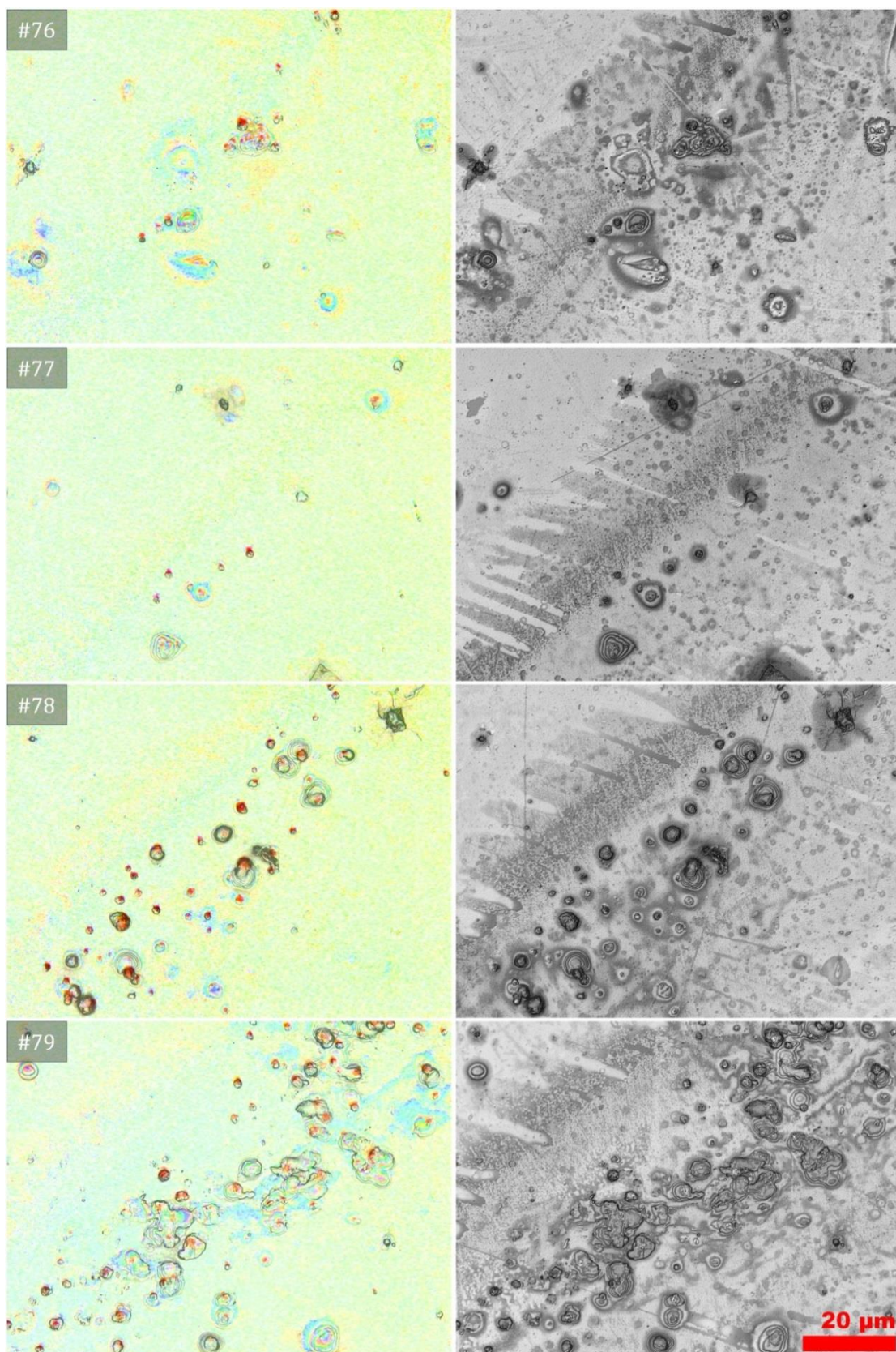


Figure 4.43: (Left: Combination of LSM Laser and optical image; Right: C-Laser DIC) These images represent the first sections of this Cu-track. The optical images show reddish colours, which are Cu particles.

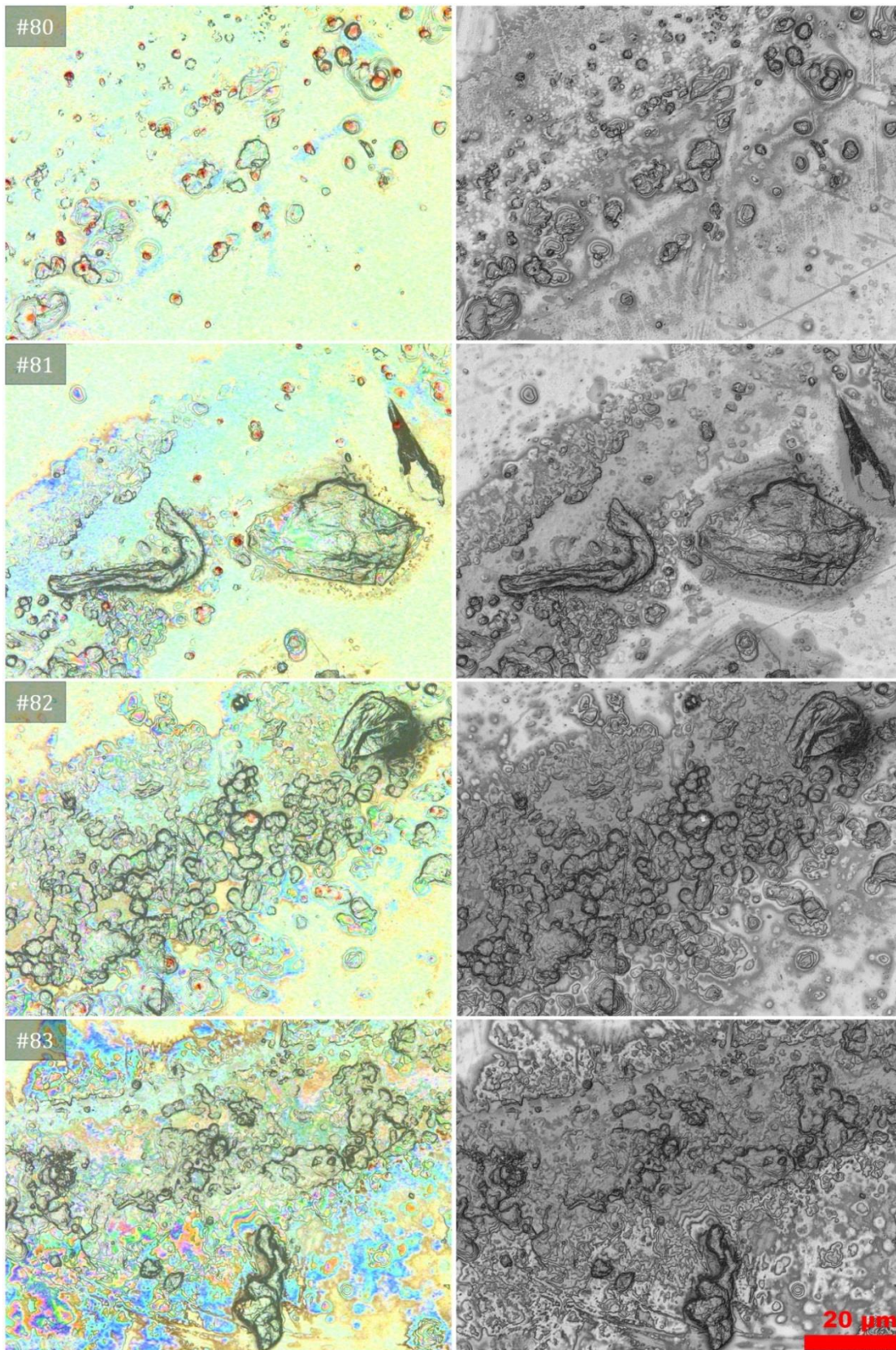


Figure 4.44: (Left: Combination of LSM Laser and optical image; Right: C-Laser DIC) These images illustrate the transition from recognisable (#80, #81) towards the maximum of overlapping features (#82, #83). The colourful parts in #83 are due to a combination of heating, Cu sputtering, and oil residues from the beam line with overlapping impacts.

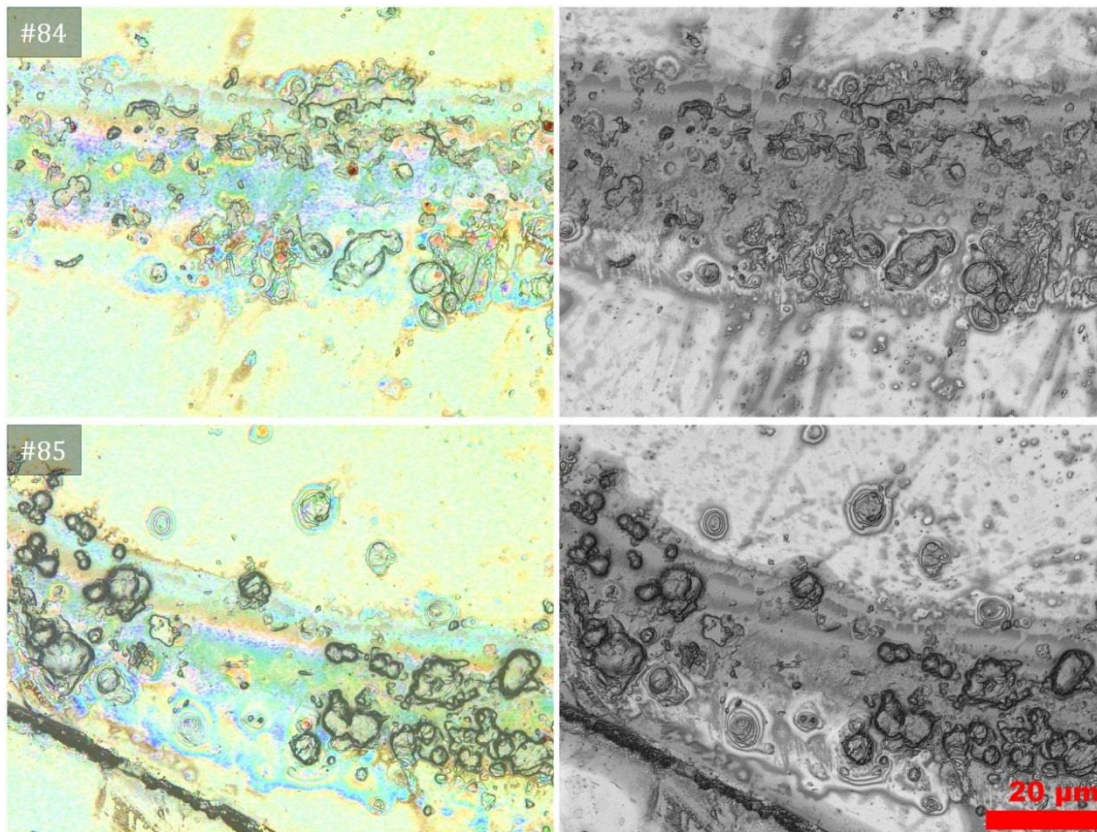


Figure 4.45: (Left: Combination of LSM Laser and optical image; Right: C-Laser DIC) These images illustrate the decrease of impact features after the maximum. Here, it is also possible to recognise individual features.

3D images of the Cu-track show additional important details of the morphology and feature density on the surface. The predominantly positive impact features due to Cu particles that impacted at relatively low speed, increase significantly from frame #80 (Fig. 4.47) to frame #82 (Fig. 4.48). Concerning negative features, few recognisable craters caused by high velocity Cu projectiles, and dents, are visible on #80 (Fig. 4.47), but none on #82 (Fig. 4.48). Due to the large amounts of low velocity impacting projectiles, visible e.g. in frame #82, the olivine surface apparently got continuously covered with copper particles, making it impossible to recognise negative crater features no matter if these formed before, during or after Cu particle covering.

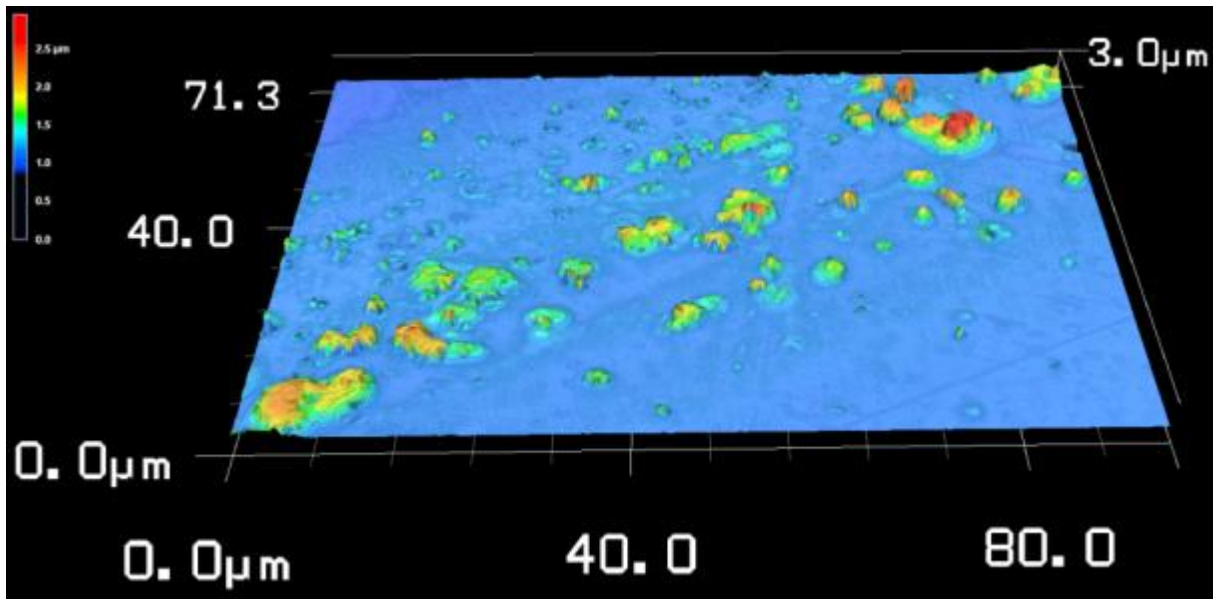


Figure 4.47: Frame #80 has roughly over 50 countable features within an area of $95 \times 71 \mu\text{m}$, predominantly positive, few negative.

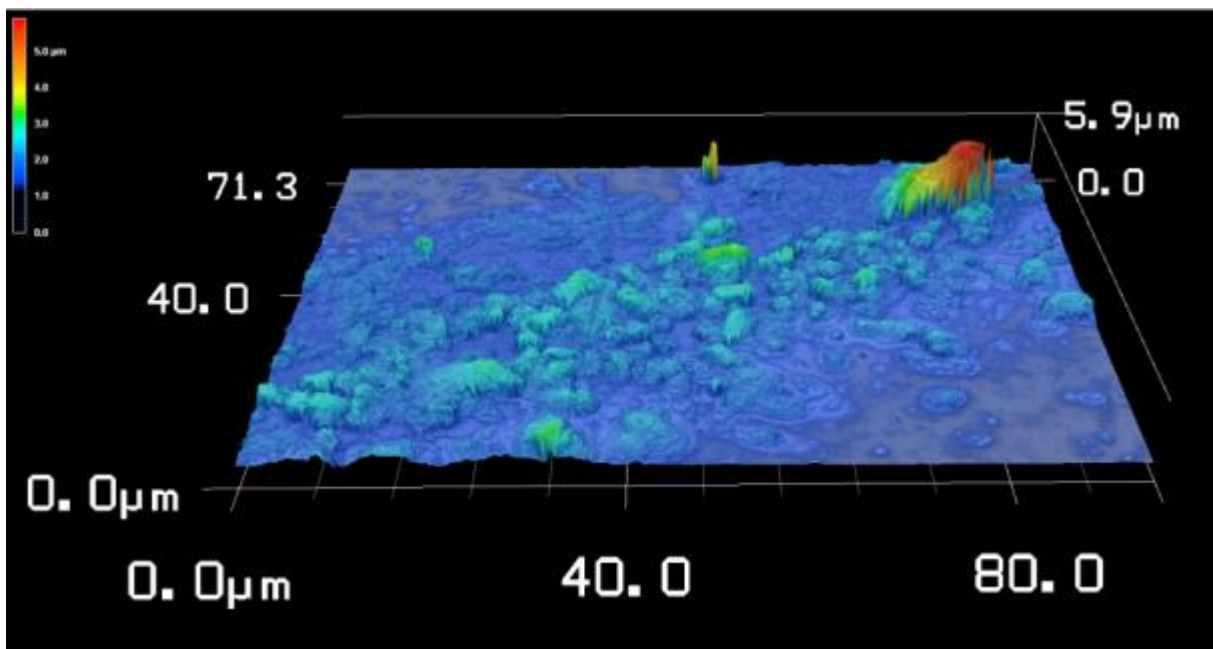


Figure 4.48: Frame #82 has more than 100 countable features within an area of $95 \times 71 \mu\text{m}$, exclusively positive. Most structures can barely be resolved or identified due to massive overlapping.

It is unlikely that a movement of the accelerator beam caused the Cu track. As it was anyway demonstrated that the beam hit the olivine target at an unexpected section (see section 4.4 *Investigation of the bombarded olivine target*) due to target dislocation, it is likely that the target itself moved not only before, but also during bombardment. The sample holder was a rotating plate, able to carry four samples fixed with Kapton tape.

This tape probably loosened during the vacuum conditions and the bombardment. It is assumed that loosening of the Kapton tape and target slipping during the intense dust bombardment caused the Cu-track feature.

4.6.6 Qualitative analysis using the SEM

SEM investigations were conducted for the purpose of checking if in general bombardment was visible (Fig. 4.50–4.52). Of great importance was to verify, if features previously determined to be stuck particles, are in fact Cu particles, and not contamination or similar. For the SEM-BSE investigation, the target was coated with a carbon layer of approximately 30 nm, which aids electrical grounding. Testing different electron beam settings, it was found the acceleration voltage of 15 keV was nicely suitable for visual and analytical results, while at the same time the least possible alteration of the surface was possible. Detail SEM scanning was only performed on frames, which were already scanned via LSM. Figure 4.49 shows section S1 in LSM laser image with frames scanned by SEM.

It turned out that every feature previously tagged as a crater showed small signals of Cu. By observing simple contrast images of BSE, it is possible to see the bright phases inside larger craters, and subsequent chemical analyses proved these phases to be Cu. In general, when no visual material contrast in craters could be observed, a Cu signal was apparent. In addition, almost every bright feature on Olivine_6 is a Cu particle and related to types A or B. Shining halo effects (A_3 type) are barely visible on SEM-BSE images and in most cases not at all.

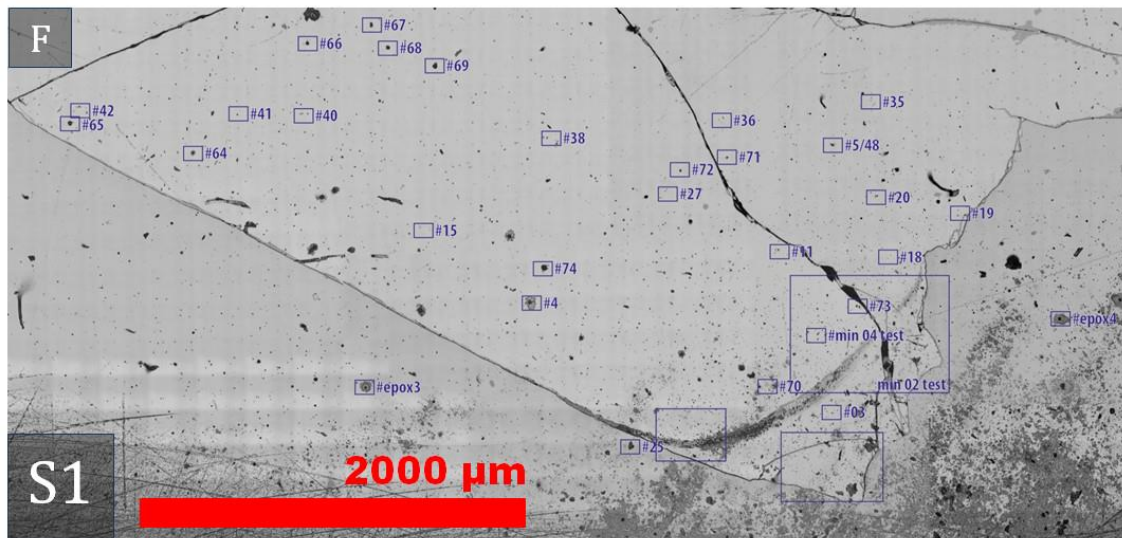


Figure 4.49: Section S1 in LSM laser image with blue boxes highlighting the frames, scanned via SEM in BSE mode.

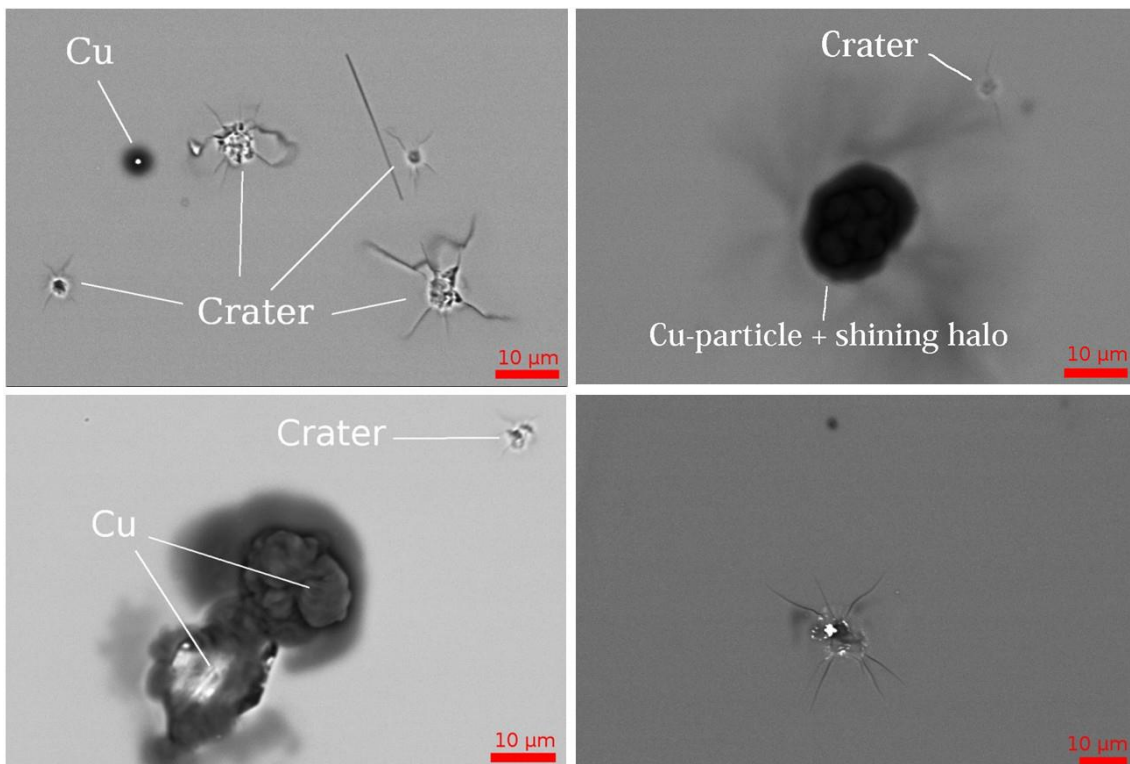


Figure 4.50: Illustrations of SEM-BSE images. The selection of images shows craters (C type) with fractures and projectile residues, and further very large examples of stuck particles (subtypes of A₂, A₃). Chemical analysis shows signals of Cu, and larger Cu particles can be determined via image contrast (Cu appears white). Features that were determined to be stuck Cu particle could be verified with chemical analysis.

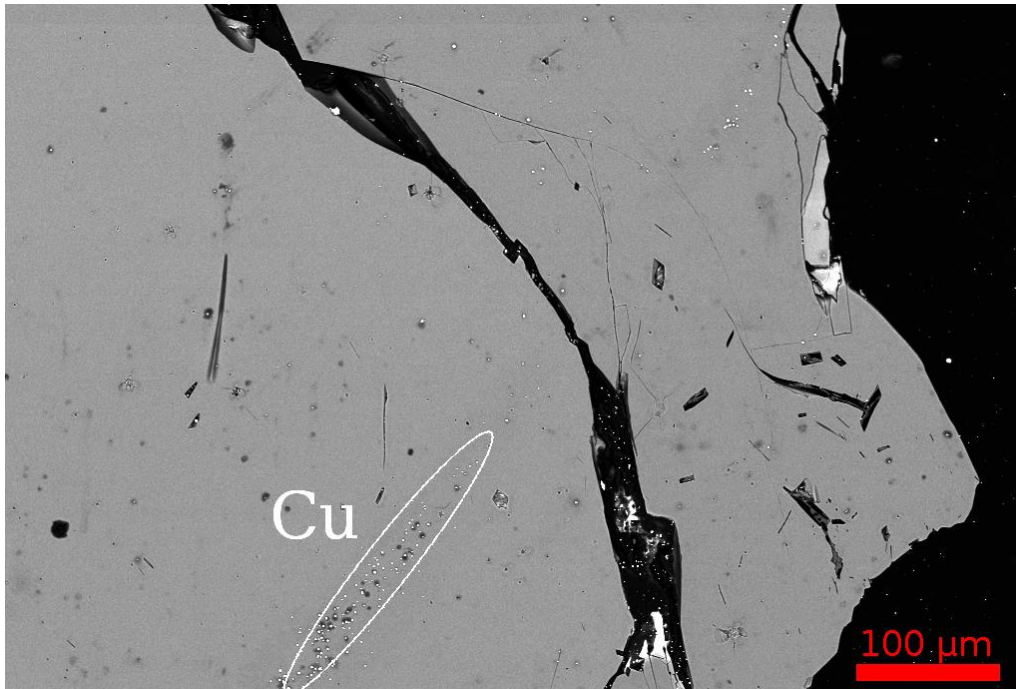


Figure 4.51: The white oval frame shows the first section of the Cu-track with many stuck Cu particles (white dots).

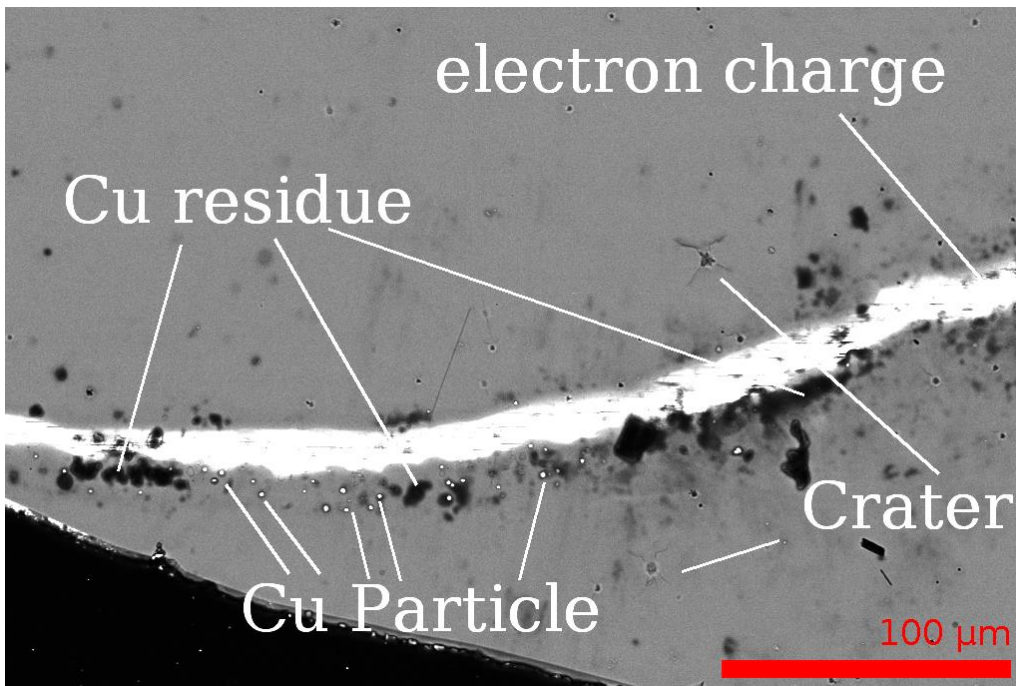


Figure 4.52: The white band ranging from left to right is caused by oversampling due to a high number of electrons, which were not properly discharged. This is an effect caused by abundant Cu projectiles sticking on the surface. To the left side impact density in the Cu track decreases and Cu particles are again recognisable. Black areas, marked as “Cu residues” are an effect of overlapping bombardment, here impact features and particles are mixed up with oil residues (most likely) and carbon coating.

4.7 Comparing categorised features on the non-bombarded and the bombarded olivine targets

After categorisation of surface features in scanned frames of Olivine_6 and Olivine_7 (see *chapter 4.6.2 Categorisation of features on olivine targets*), this chapter will investigate if morphologically distinct features are also distinguishable by their dimensions (diameter, height, depth) and not only by visual classification. For better comparison, features of Olivine_7 are displayed in the foreground, as there are less data than for Olivine_6.

For all plots applies: In overview plots without type specific symbols (e.g., 4.53 and 4.54), data of the non-bombarded target are designated with a “+”-symbol and data of the bombarded target with an “x”-symbol. In detailed plots specifying the feature types (e.g. 4.57 ff.), impact related features have circular symbols, miscellaneous types on the non-bombarded target have angular symbols, and miscellaneous types on the bombarded target have filled angular symbols.

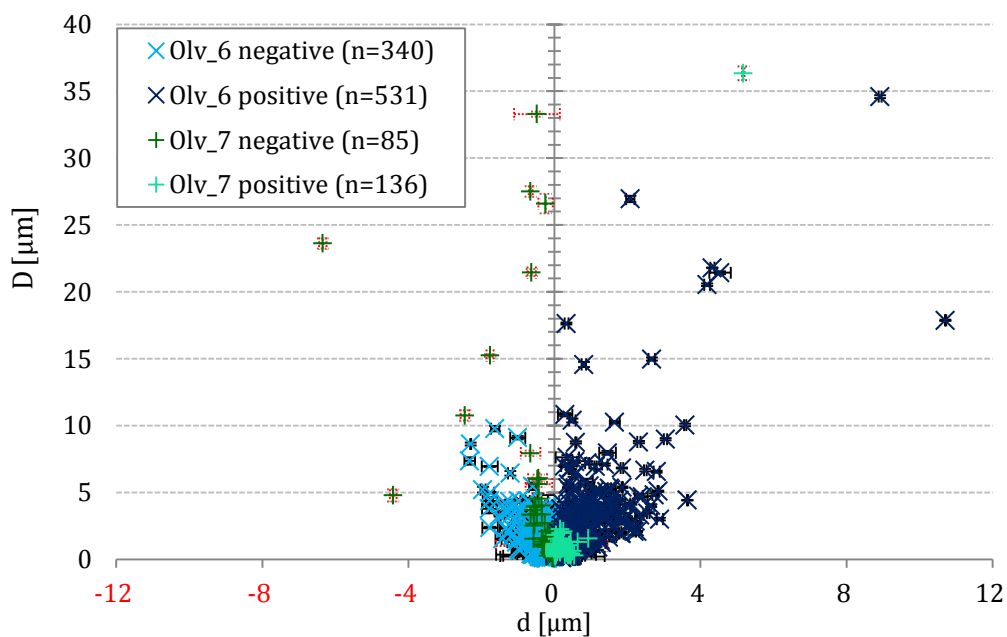


Figure 4.53: D-d diagram of Olivine_7 and Olivine_6 features. Error bars are shown as red lines.

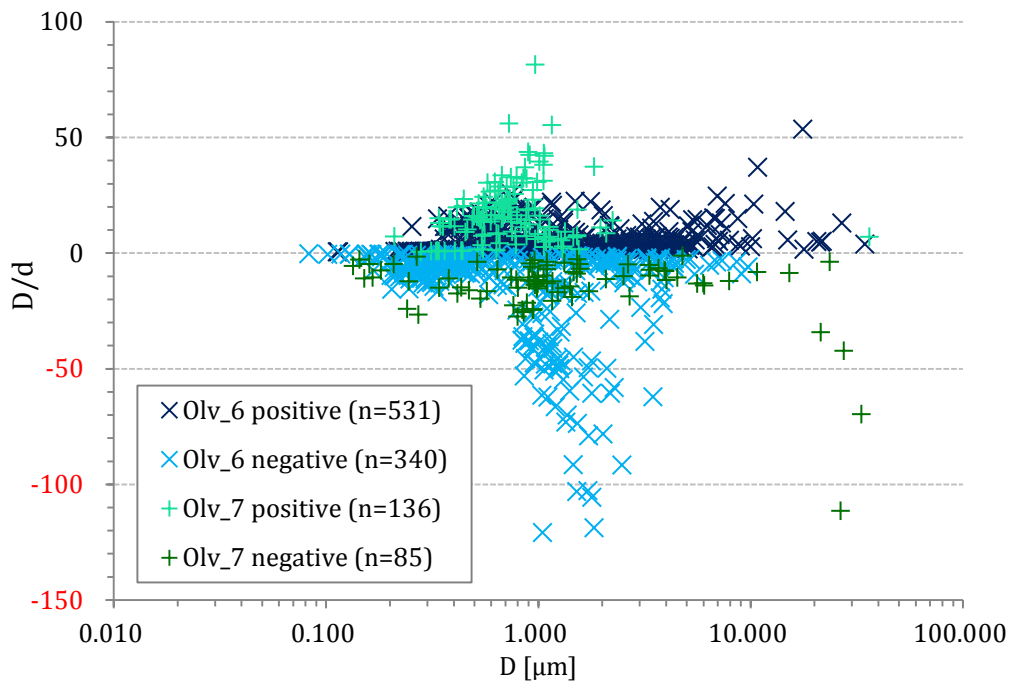


Figure 4.54: D/d-D diagram of Olivine_7 and Olivine_6 features.

In both diagrams (Fig. 4.53 and 4.54) it is clearly visible that the bombarded target shows some data similar to the non-bombarded target, plus additional data populations, e.g., extending to larger diameters and depths/elevations. The in-depth analysis of these data is performed in the following sections of this chapter.

4.7.1 Diameter to height diagrams: Positive features

Figure 4.56 shows additional positive features on the bombarded Olivine_6 target, which are mainly impact related features of type A and B (Fig. 4.57). They cover distinct areas in the diameter to height (D-d) diagram (Fig. 4.57). As E type features represent displaced fragments, they are smaller than the majority of the other positive primary impact types.

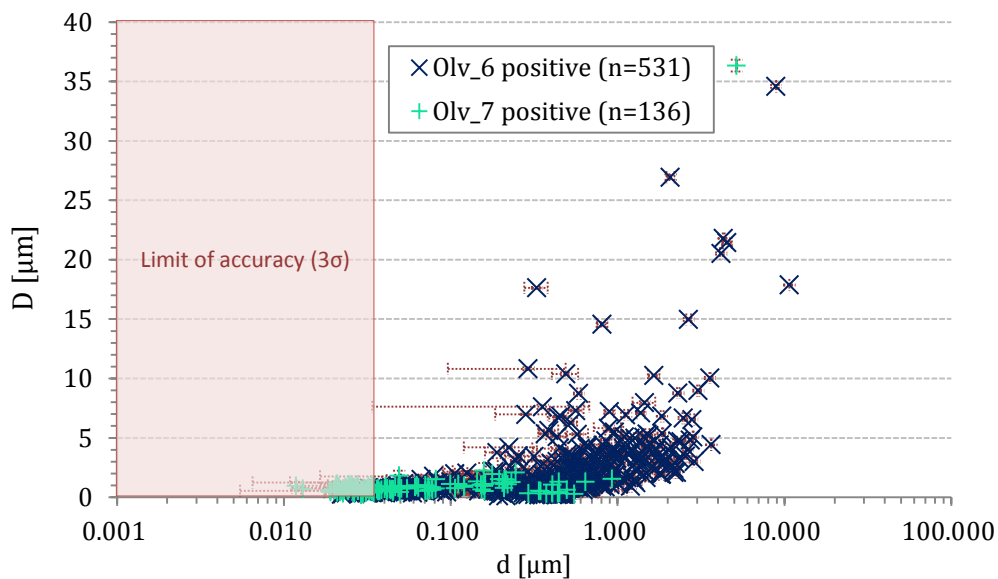


Figure 4.56: The D-d diagram for positive features shows additional features with diameters larger than 2.5 μm , and a mean height between $\sim 0.8 - 3 \mu\text{m}$. The red box indicates the limit of accuracy (in vertical direction) of the instrument (within 3σ).

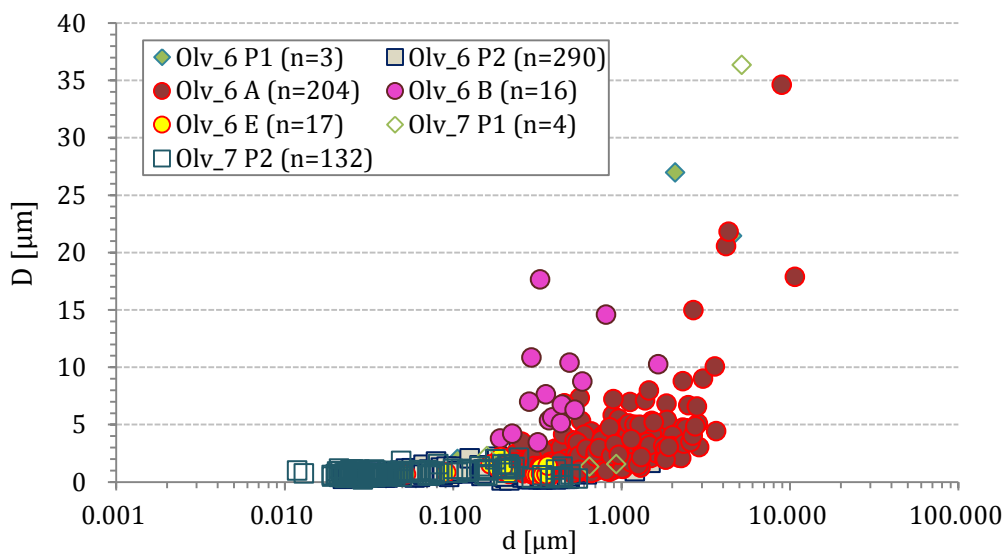


Figure 4.57: The D-d diagram shows how B and A type features are distinguishable from the miscellaneous non-impact features occurring on both targets.

Figure 4.58 displays a cut-out for smaller features. Here it is noteworthy that some of Olivine_6 P₂ types are mixing up with smaller A types. It seems likely that some of the P₂ features, classified as miscellaneous and unidentifiable, are in fact A types (Fig. 4.58). This supposition is supported by comparing impact-related types with Olivine_7 P₂ types only (Fig. 4.59). Olivine_7 P₂ does barely mix up with A types.

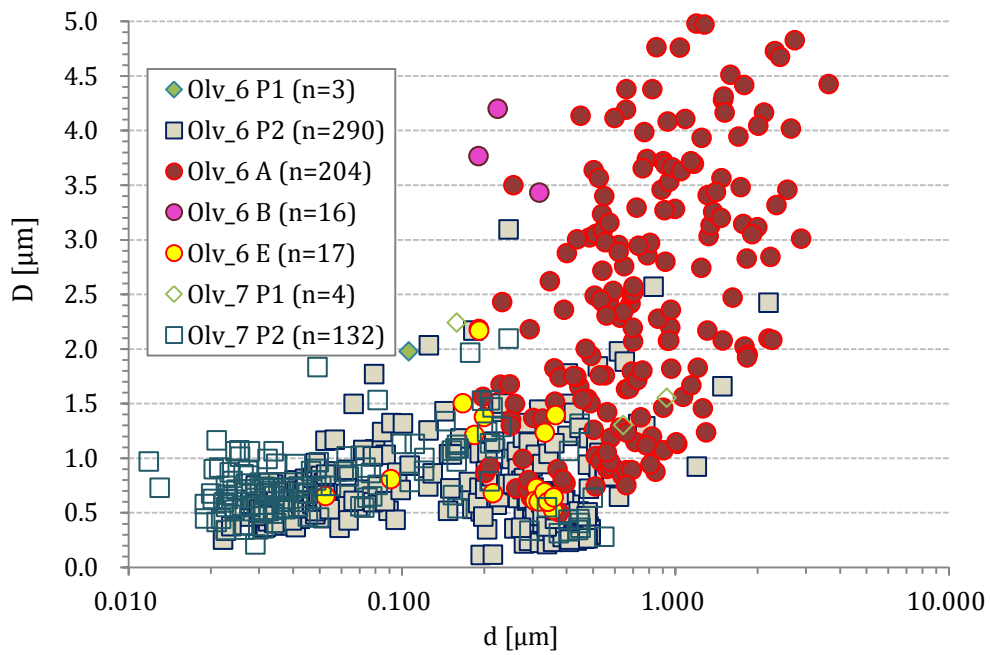


Figure 4.58: Detailed view of D-d diagram showing large P₂ features mixing up with smaller A types. It is likely that these P₂ features are misclassified A types.

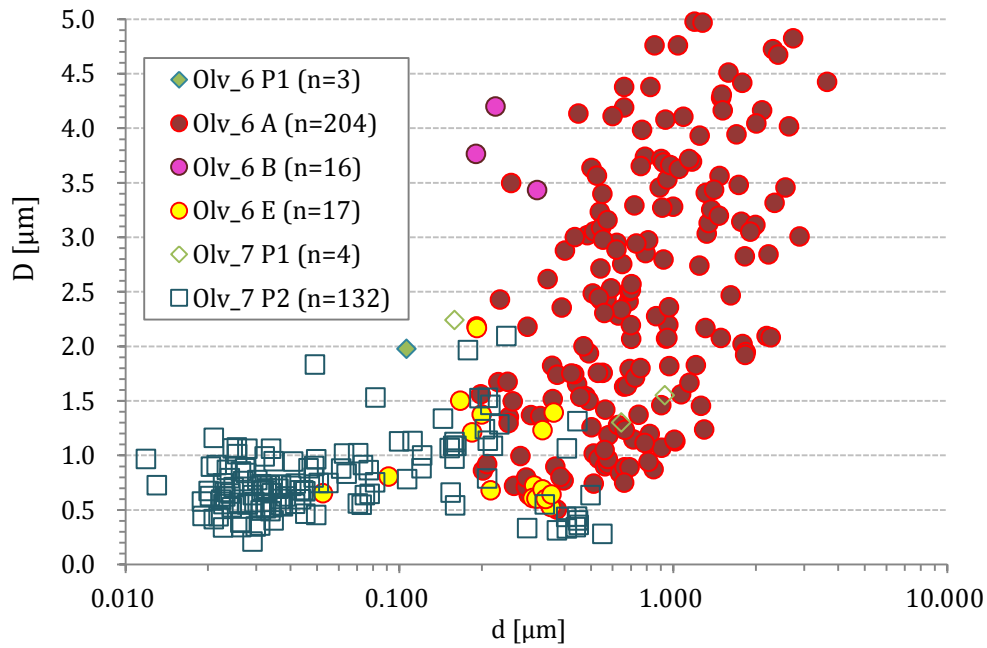


Figure 4.59: Detailed view of D-d diagram showing that Olivine_7 P₂ features barely mix up with Olivine_6 A type.

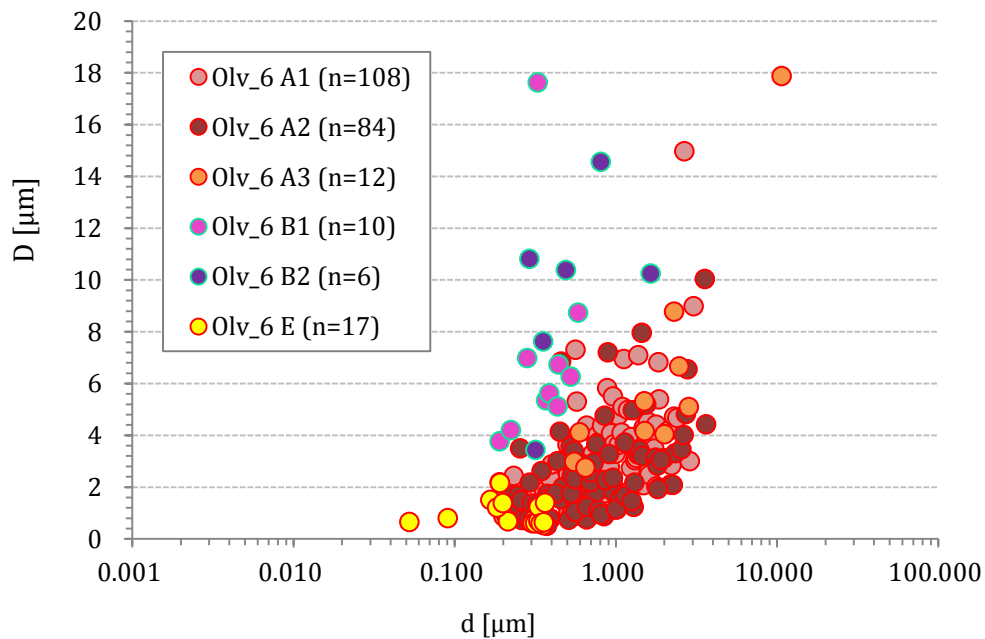


Figure 4.60: Detailed view of a D-d diagram showing that B subtypes are not clearly distinguishable from each other. On the other hand, subtype A₃ only appears at diameters of $\sim 3\mu\text{m}$ and larger, with a height of at least $0.5\mu\text{m}$. A₁ and A₂ share almost the same area.

Fig. 4.60 shows also subtypes of A and B features. B₁ and B₂ subtypes cannot be distinguished from each other in terms of depth and diameter. The same is true for A₁ and A₂.

Only A_3 appears to cover a somewhat distinct field beyond $\sim 3 \mu\text{m}$ of diameters and heights larger than $0.5 \mu\text{m}$ (Fig. 4.60).

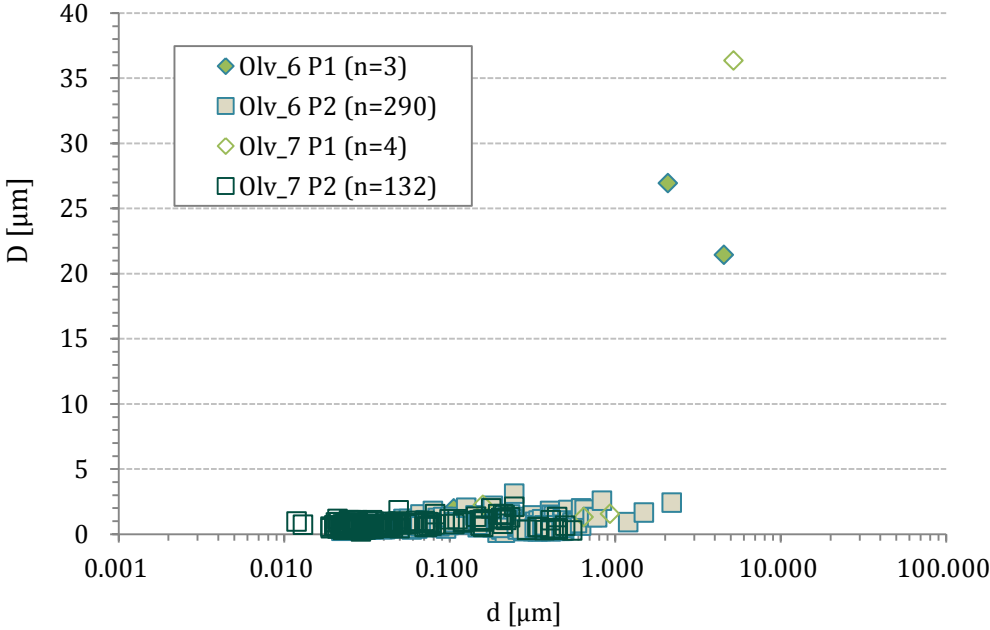


Figure 4.61: D-d diagram showing congruent appearance of non-impact related types for Olivine_6 and Olivine_7.

Considering only non-impact related types (Fig. 4.61), these clearly cover a specific range and coincide for both Olivine_6 and Olivine_7. For both samples, extreme values represent P_1 features with large variations in their dimensions

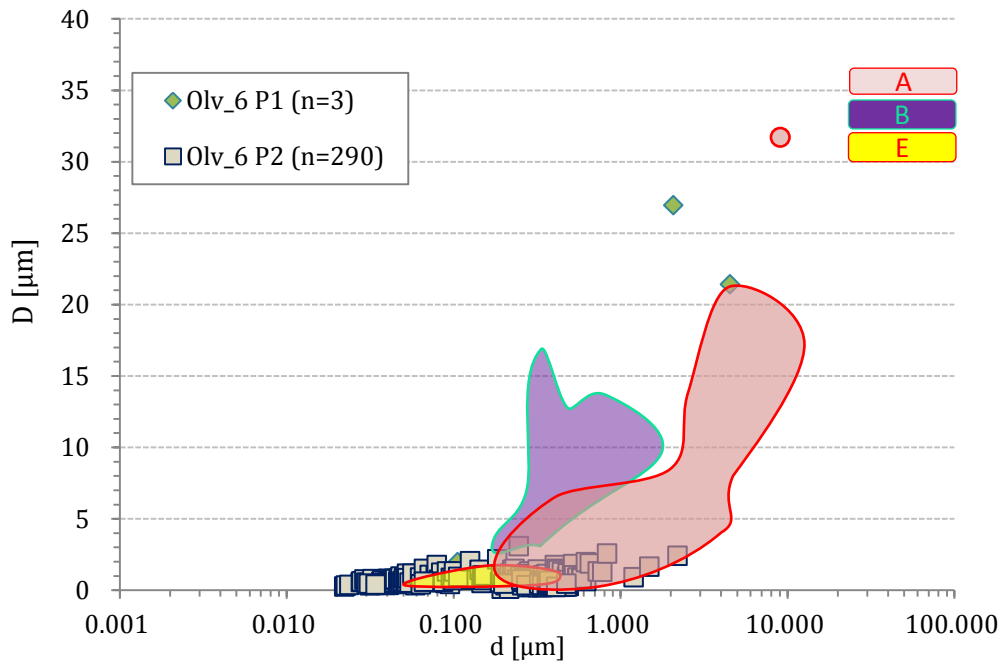


Figure 4.62: D-d diagram showing non-impact related types of Olivine_6 and impact types presented as fields for easier comparison. In the top right section of the diagram, the colour coding for each corresponding feature type is given.

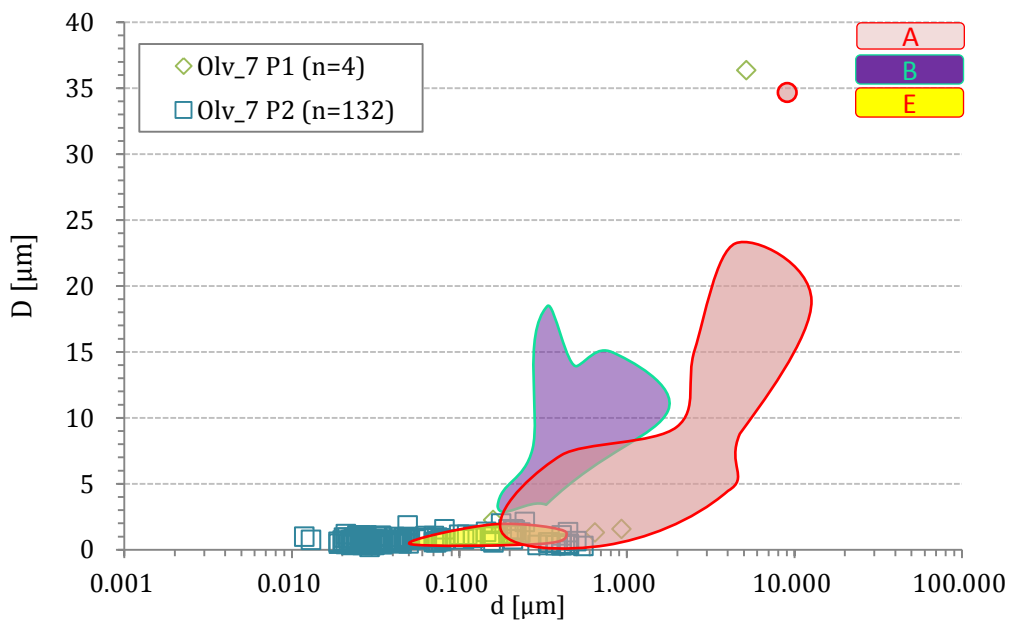


Figure 4.63: D-d diagram showing non-impact related types of Olivine_7 and impact types of Olivine_6 presented as fields for easier comparison.

All in all, A and B types can be distinguished from each other and non-impact features by their diameters and elevations and not only by LSM inspection, except for smaller E type

features. The characteristics of B type features to appear very flat in LSM inspection can be clearly observed in the diagrams. They are clearly separated from all other features and especially from P types, which also means that the B type is consistent in its definition. The region of A types marginally overlaps with features of B, E, P₁ and P₂, but only for smaller sizes (Fig. 4.62 and Fig. 4.63).

In general, features with diameters larger than 2.3 μm are usually impact-related with the very rare exception of P₁ types, which is considered as contamination. P₂ features on Olivine_7 reach a maximum height of 1 μm. This means that the P₂ features in Olivine_6 with heights above 1 μm are probably impact related.

E type impact features are most safely identified by LSM visual inspection.

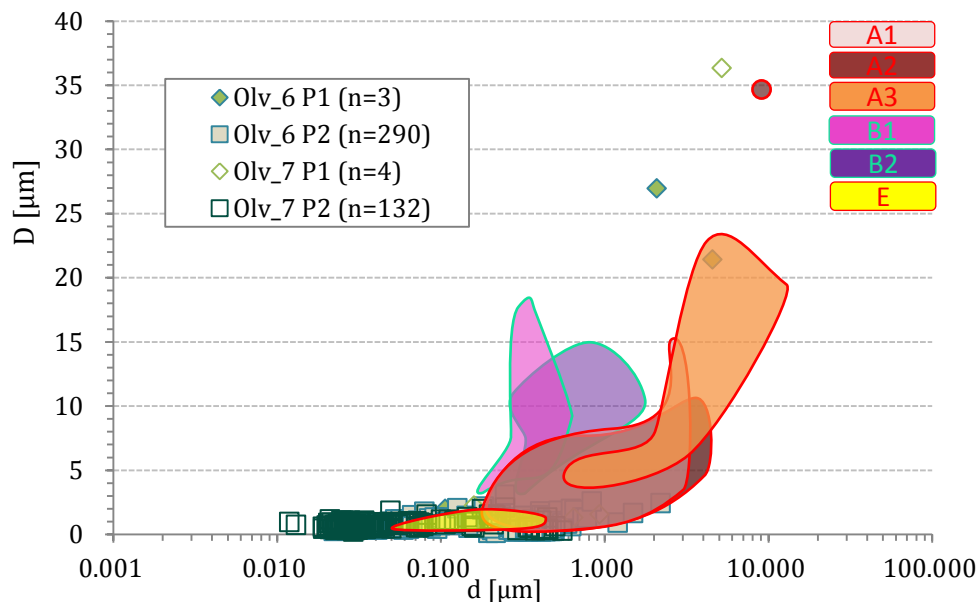


Figure 4.64: D-d diagram showing non-impact related types of Olivine_7 and Olivine_6 compared to fields of impacted related subtypes.

The subtypes A₁ and A₂ cover almost the same range of diameter and height, except for one extreme feature with a diameter around 35 μm. This supports the notion that these types are similar types of impacts, and only distinguished by the visual classification, which could involve issues related to reflection intensity or influences of airy patterns. In addition, it seems that only larger impactors can generate shining halo effects, which is the criterion for A₃ (Fig. 4.64).

For the B types there is a fluent transition between B₁ - categorised as splash effects - and B₂, categorised as flat cones. B₁ apparently never exceeds heights of 0.8 μm.

Extreme features with larger diameter are primarily P₁ and can be neglected with respect to impact features, as they represent contamination. Only one particle of type A₂ is standing out from all others. The particular appearance of this particle is almost symmetrical, except for the outer edges (Fig. 4.65 and 4.66). It looks like it was squeezed and welled out to one side. It is possible that in this case the impactor might have been spherical once.

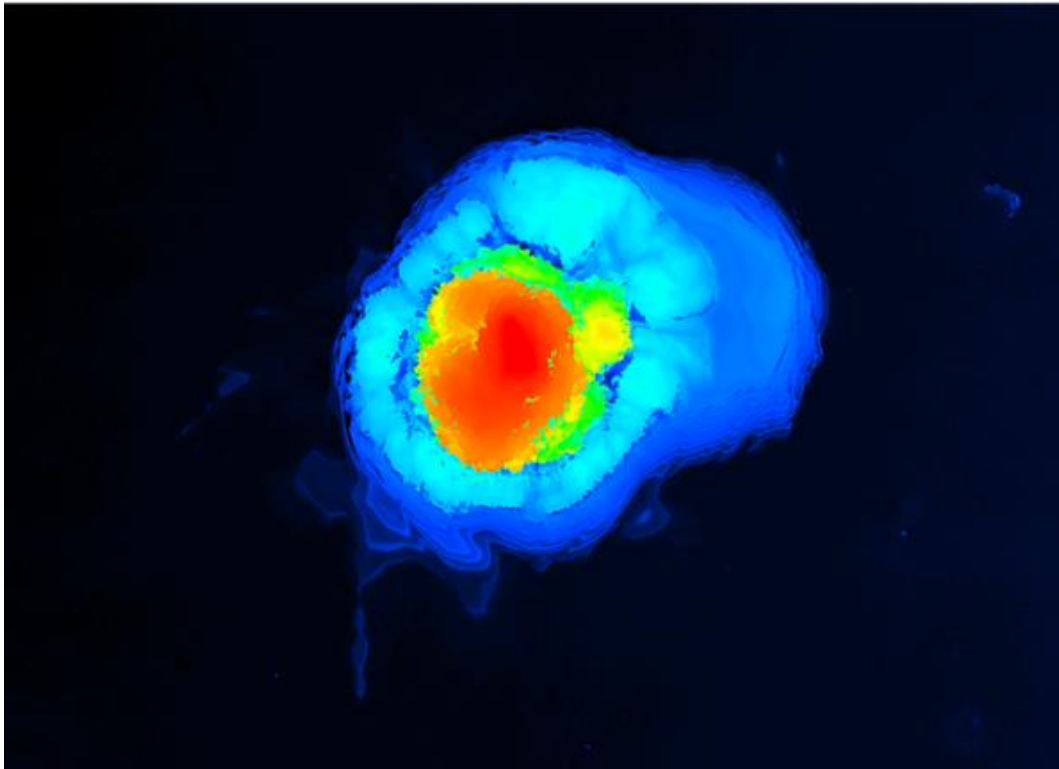


Figure 4.65: Height image of a very large projectile (A₂ type).

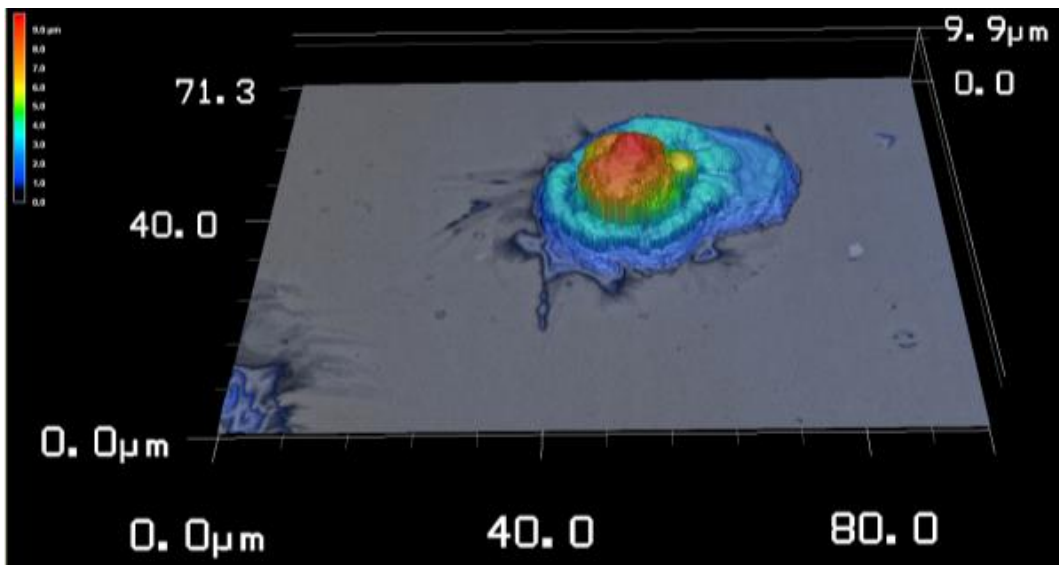


Figure 4.66: 3-dimension view of a very large projectile (A₂ type).

4.7.2 Diameter/height to diameter diagrams: Positive features

Analysing the diameter/height to diameter (D/d - D) interpretation of the data from impact experiments on the bombarded target, the differences in the data in comparison with the non-bombarded target are apparent. While the majority of data from Olivine_7 ranges from widths between 0.2 up to 1.2 μm and D/d - D ratios from 5 to 40, the data from Olivine_6 show smaller D/d ratios and diameters beyond 10 μm . This underlines the conclusion that a large number of positive impact related features, which are not craters, reside on the surface of Olivine_6 (Fig. 4.67).

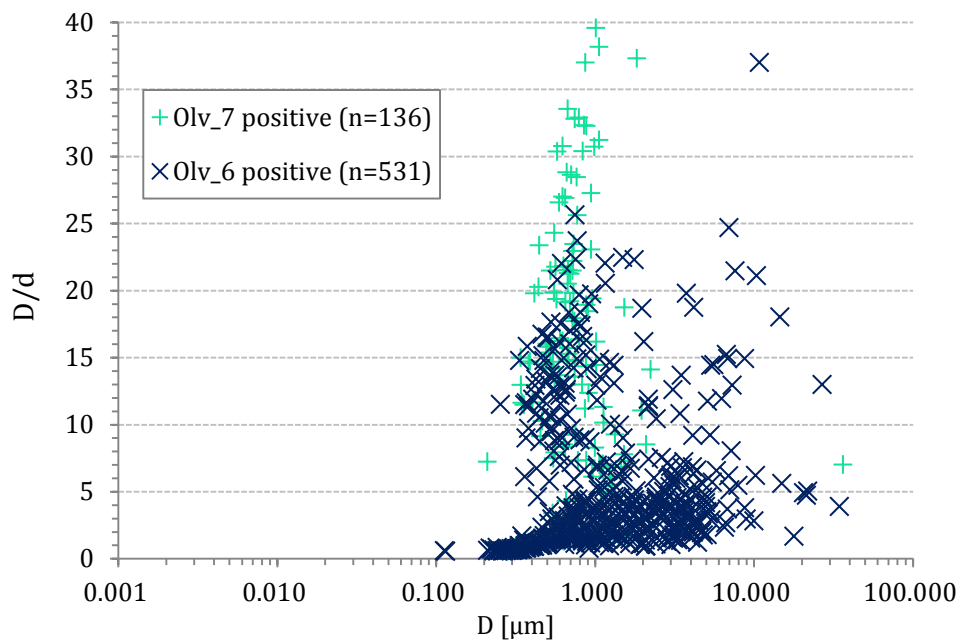


Figure 4.67: The D/d - D diagram shows all positive features of Olivine_6 and Olivine_7 data.

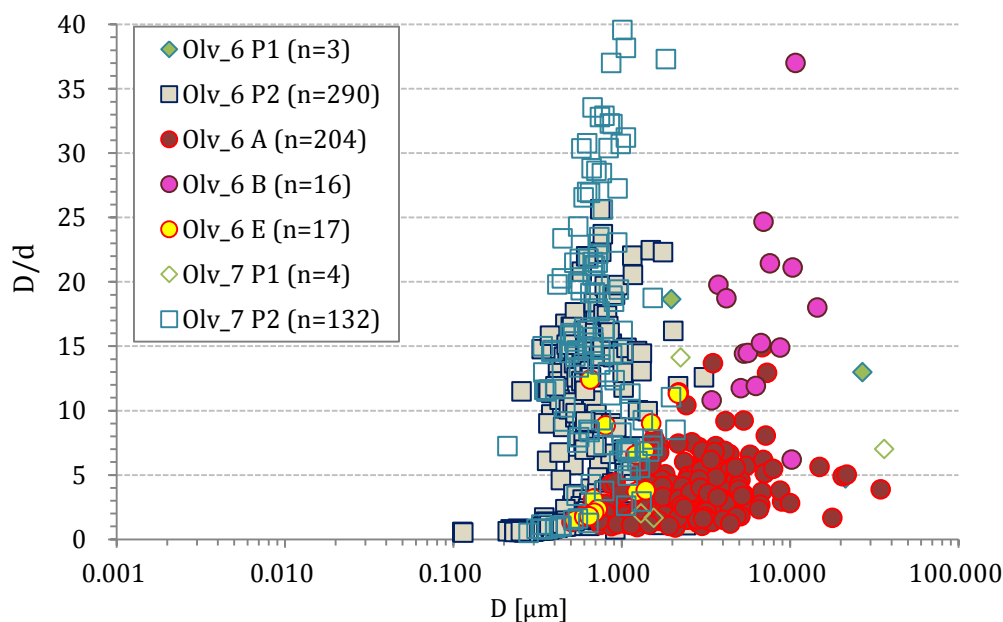


Figure 4.68: The D/d-D diagram shows all positive features of Olivine_6 and Olivine_7 according to their types. The difference between bombarded and non-bombarded target is obvious.

Again, A and B types clearly differ from P₁ types. The majority of A and B types cover an individual zone within the D/d-D diagram (Fig. 4.68).

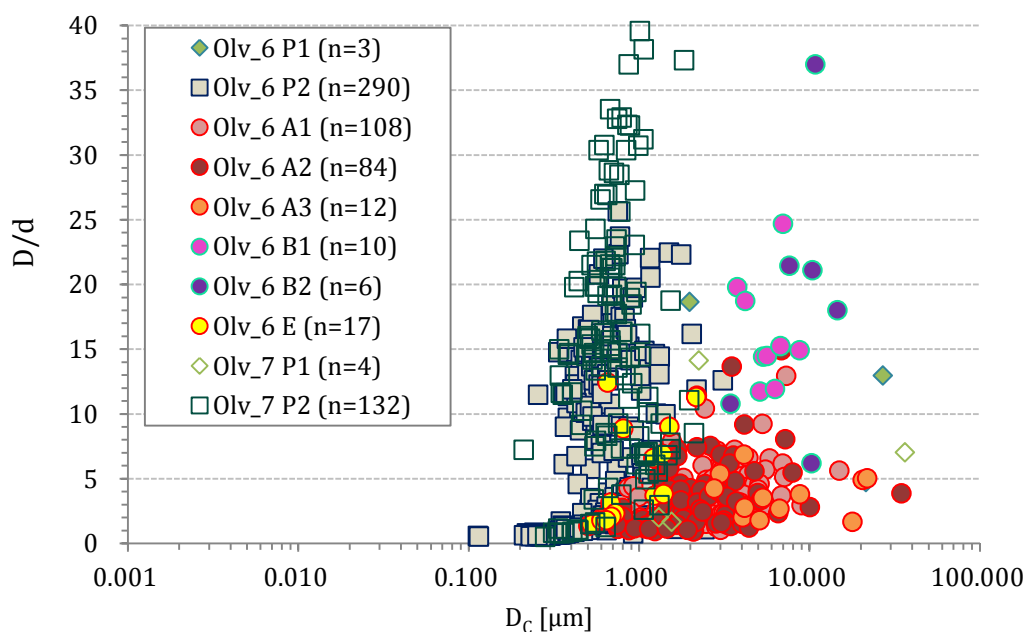


Figure 4.69: The D/d-D diagram shows all features of Olivine_6 and Olivine_7 according to their subtypes. Only A₃ stands out against other A types. B types are not distinguishable from each other.

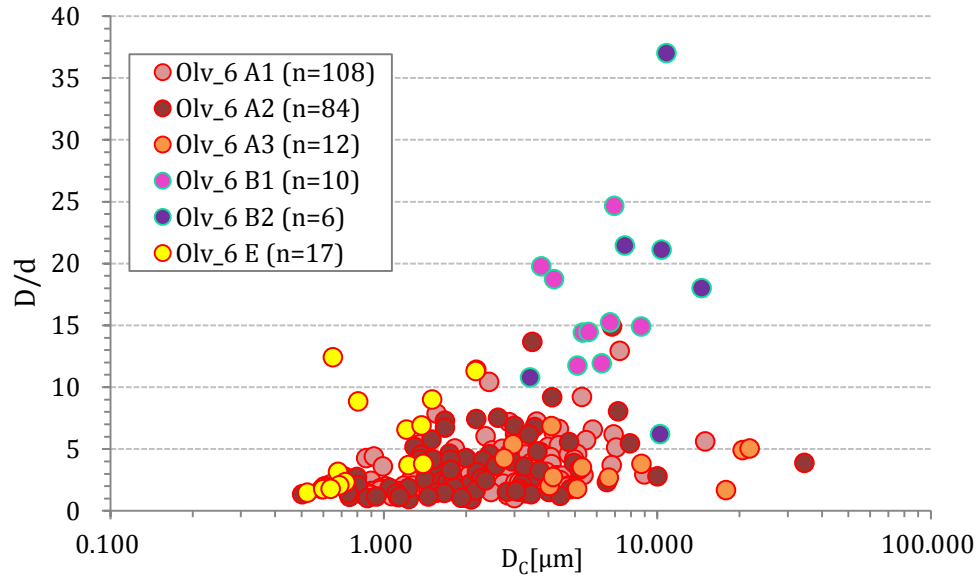


Figure 4.70: The D/d - D diagram for only impact related types underlines that A_2 and A_3 can be considered as very similar subtype.

There is a tendency of B_1 and B_2 features having higher D/d - D ratios, often above 10. This is consistent since they were classified as either very flat or squeezed and spread out over a wide area. Compared to sticking A types, the debris E type tends to extend to higher D/d ratios, but can also be also located at the lower end of A_1 or A_2 types (Fig. 4.70).

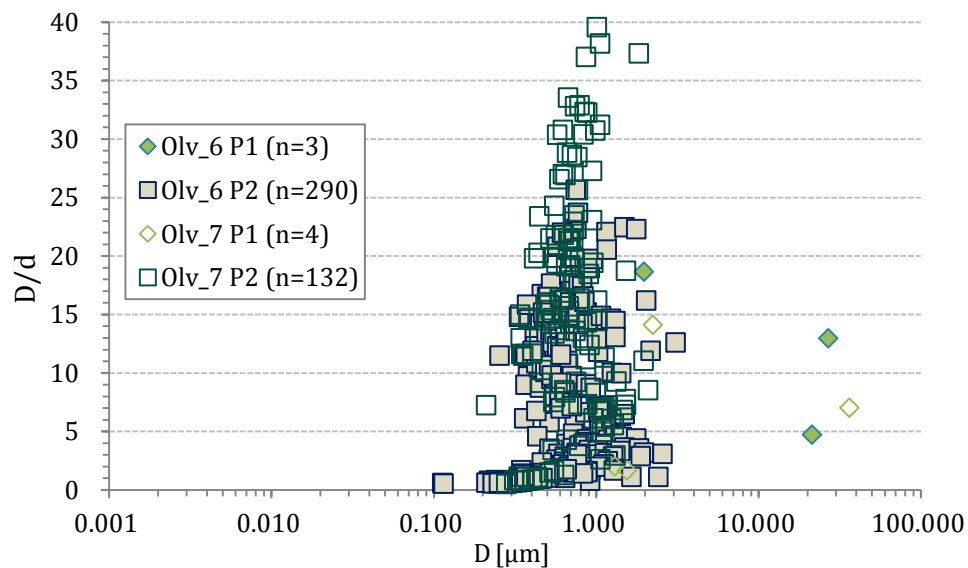


Figure 4.71: In the D/d - D diagram non-impact types cover nearly indistinguishable areas.

4.7.3 Diameter to depth diagrams: Negative features

The negative features of Olivine_6 show an additional data population from 0.5 to 1.1 μm depth, when compared to Olivine_7 (Fig. 4.72). The deepest measured feature was an N_1 type with 6.34 μm . The deepest feature as compared to a small diameter was a N_2 type (indeterminable pit) with a diameter to depth ratio D/d ratio of $0.40 \pm 24 \%$. The deepest crater has a D/d ratio of $0.64 \pm 32 \%$ with a maximum depth of 0.64 μm .

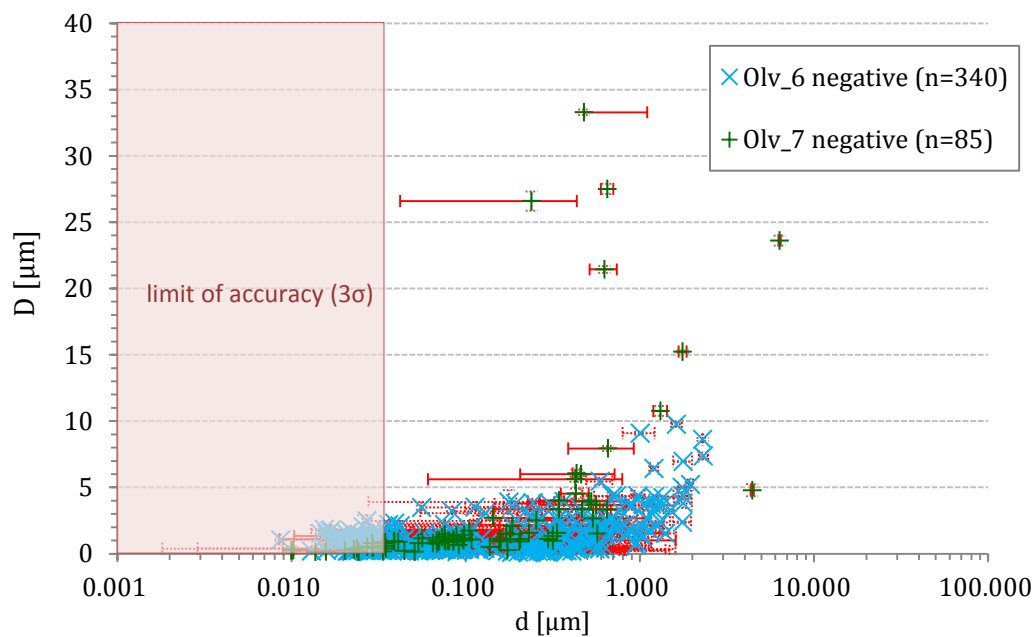


Figure 4.72: The D-d diagram show all negative feature data of Olivine_6 and Olivine_7. Error bars are shown in red lines. The red box indicates the limit of accuracy (in vertical direction) of the instrument (within 3σ).

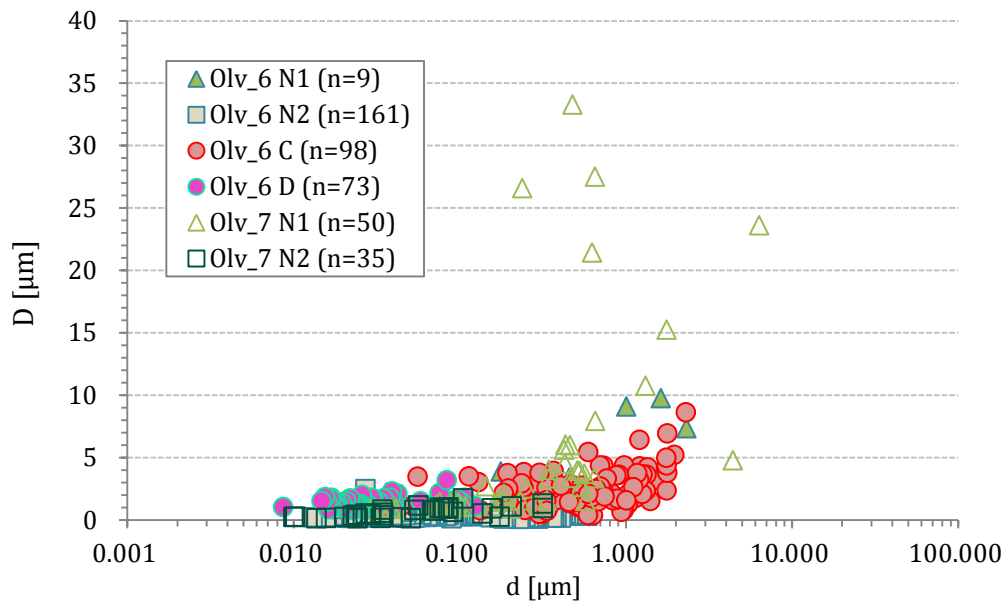


Figure 4.73: The D-d diagram shows all negative features of Olivine_6 and Olivine_7.

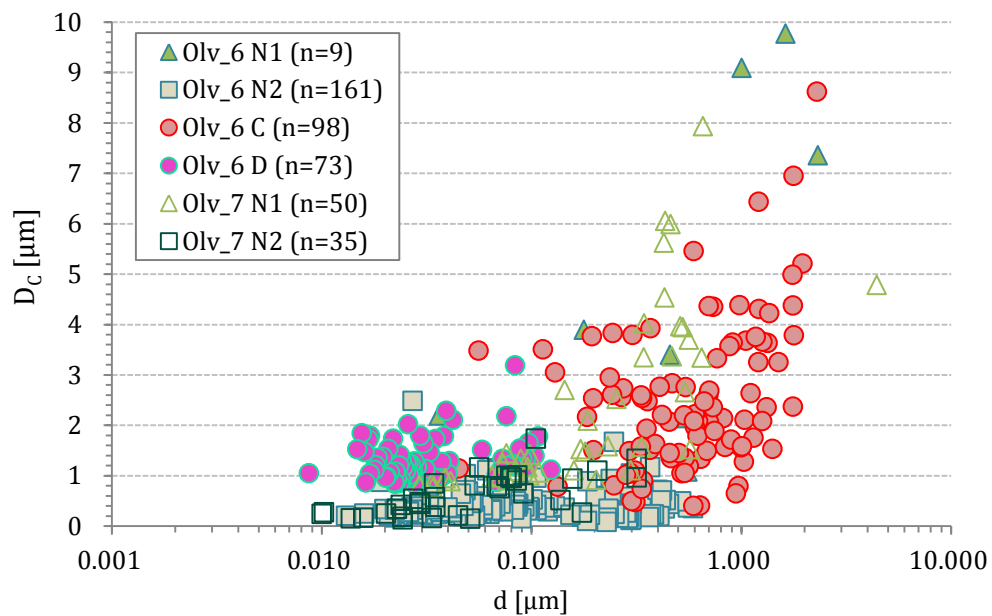


Figure 4.74: This D-d diagram shows a detailed view of all negative features of Olivine_6 and Olivine_7. C and D types stand out against all N type features.

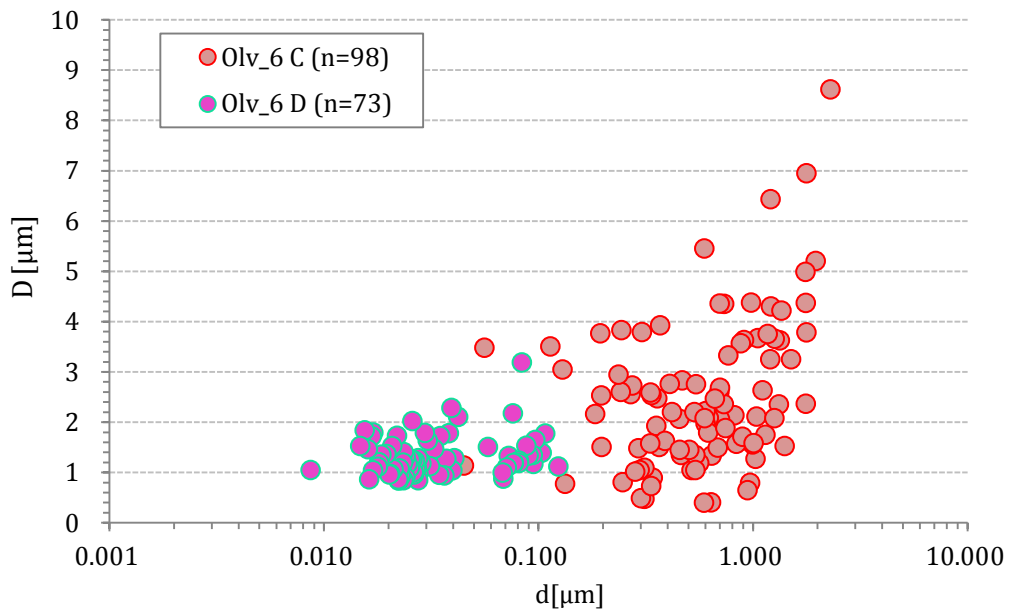


Figure 4.75: The D-d diagram shows only negative impact features related to the C and D types of Olivine_6. Both blend into another at depths at $\sim 0.1 \mu\text{m}$ and diameters of ~ 1 to $\sim 2.5 \mu\text{m}$.

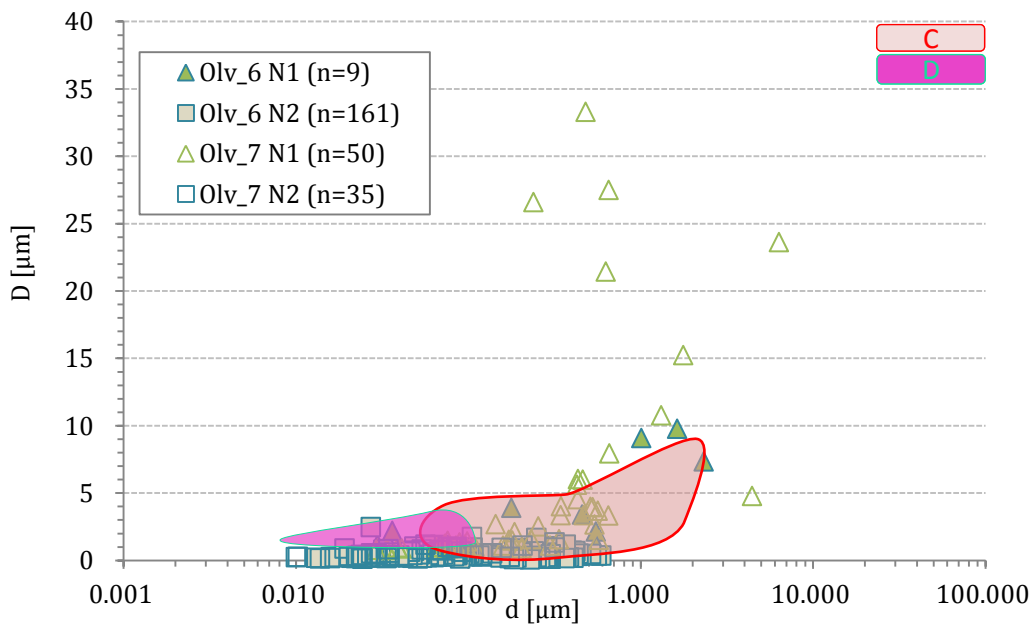


Figure 4.76: The D-d diagram shows all negative non-impact related features of Olivine_6 and Olivine_7 as compared to the fields of impacted related features (C and D type).

Figure 4.73–4.76 illustrate that the 0.5 to 1.1 depth range is dominated by craters of C type. D types are classified as dents representing a precursor crater stage. D types reach only maximum depths of $\sim 0.1 \mu\text{m}$ and blend over into C types (Fig. 4.75). D types have generally diameters of ~ 0.8 to $\sim 2.5 \mu\text{m}$, while the identified C types range from ~ 0.6 to $\sim 8.6 \mu\text{m}$. Still, it is likely that there are crater types below a diameter of $0.6 \mu\text{m}$, since there are larger numbers N_2 data points between 0.2 and $0.4 \mu\text{m}$ diameters right below the zone of C types.

It is very well imaginable that very tiny particles with sufficient impact energy could cause such small craters, but is not possible to distinguish them from non-impact features via the optical capabilities of LSM (see section 4.8 *The approach to deducting sub-micron scaled craters*).

In general, it is possible to classify the majority of negative impact related types just by visual parameters.

The extremely sized features in negative types can be easily explained by large irregular shaped surface defects (N_1 type). These defects can be the result of voids inside the olivine crystal system probably due to defects in crystal lattices, fluid or gas inclusions or accessory mineral inclusions lost during polishing. Fluid inclusions should rather form more spherical or ellipsoidal shaped cavities, as compared to the large irregular shaped cavities found on Olivine_7.

For the investigation of further differences within the crater types (Fig. 4.76), the latter were subdivided into i) very small craters, ii) simple craters, which appear as ideal craters, iii) flat craters without any rim zone, iv) craters with fractures/spallation, v) craters surrounded by fragments, vi) craters with fractures/spallation and fragments, vii) craters with the projectile sticking in the impact zone, and viii) craters which collapsed most likely as a result of very strong spallation or a subsequent impact .

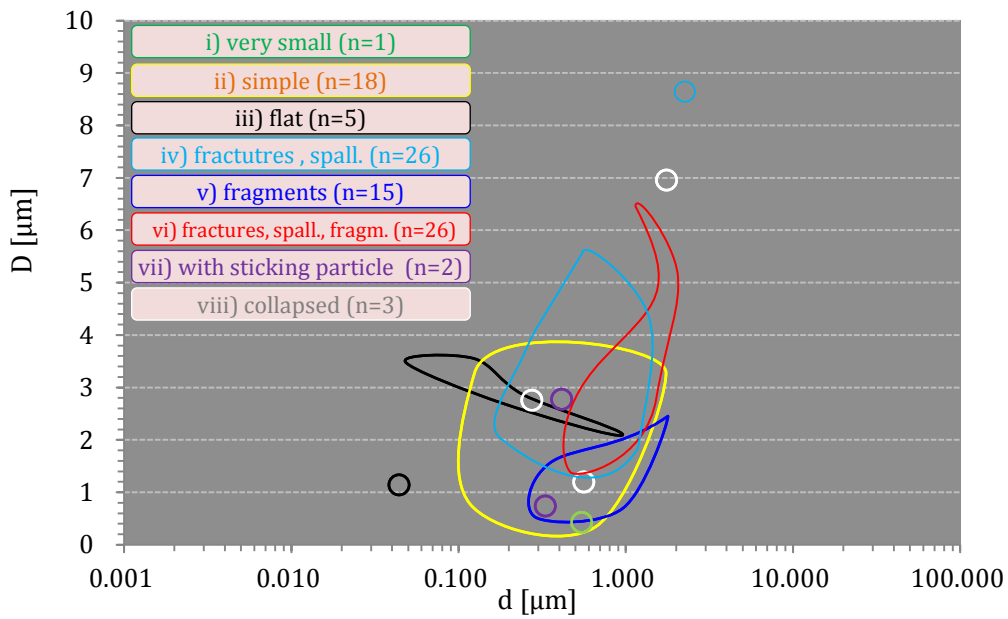


Figure 4.76: D-d diagram only for subtypes of craters (C type). Debris and fractures seem to occur only at depths larger than 0.2 μm .

Fig. 4.76 allows proposing additional conclusions. Fractures and spallation effects only occur at diameters above 1.2 μm and depths above 0.18 μm . If the depth increases up to 0.3 – 0.5 μm , debris (E type features) can be recognised around the craters. Simple or classical shaped craters are found almost in the same size dimensions as fractured/spalled craters or craters accompanied by blocks. This means that fracturing/spallation and debris are not strictly related to depth and width of a crater, but rather to impact energies. Finally it is to be noted that pure E type features decrease with increasing crater dimensions, but larger craters have E type features that in addition display spallation effects.

For soda lime glass and fused quartz targets, higher velocities cause larger spallation zones and dislodge lips by ejection of an inner spallation ring. When projectiles are large, they usually cause large or complete spall-offs. Also, smaller craters can eject their spallation, due to melt bonding (VEDDER & MANDEVILLE, 1974).

4.7.4 Diameter/depth to diameter diagrams: Negative features

The most outstanding impact related types in the D/d - D diagrams are D features, which are dominant at D/d ratios around -50. C types overlaps with N_1 and sometimes with N_2 . It is very likely that random mineral defects could have the ratios of a crater. In addition, some of the large N_2 types overlap with small craters (Fig. 4.77 & 4.78).

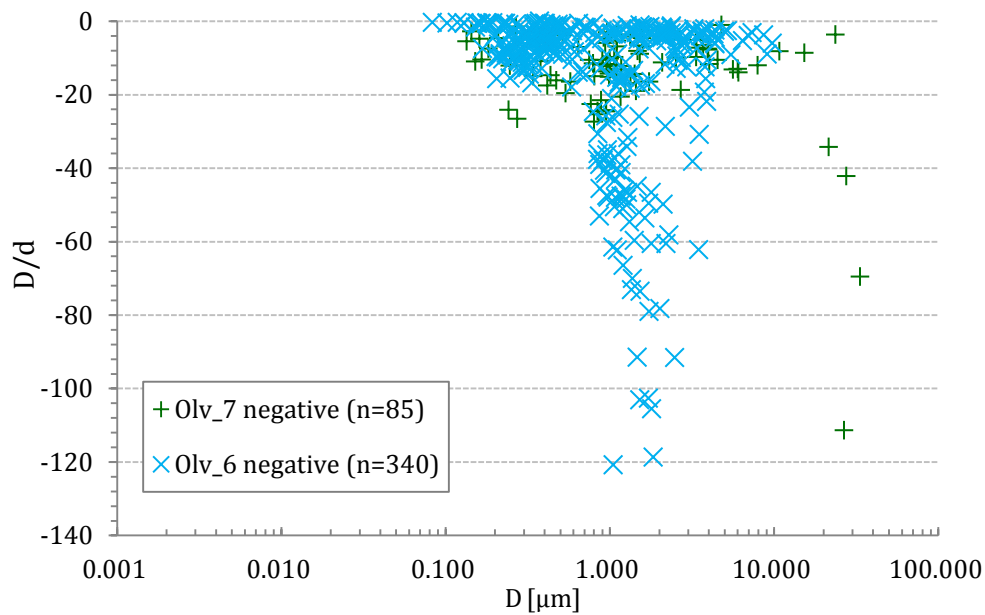


Figure 4.77: The D/d - D diagram shows all negative features of Olivine_6 and Olivine_7. Differences between both targets are evident.

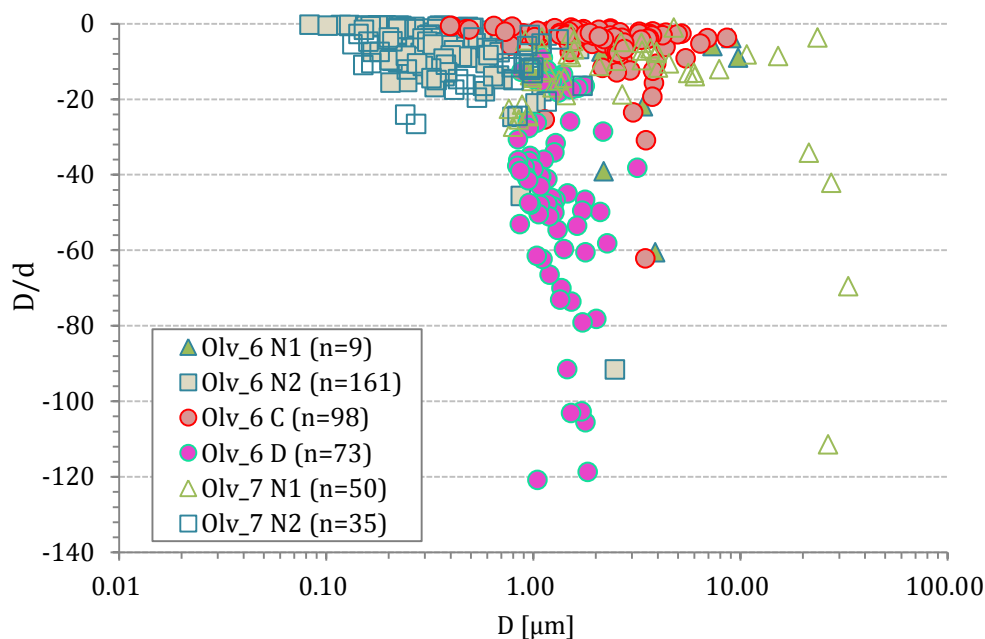


Figure 4.78: The D/d - D diagram shows all negative features of Olivine_6 and Olivine_7, according to their types. D types stand out against all other types.

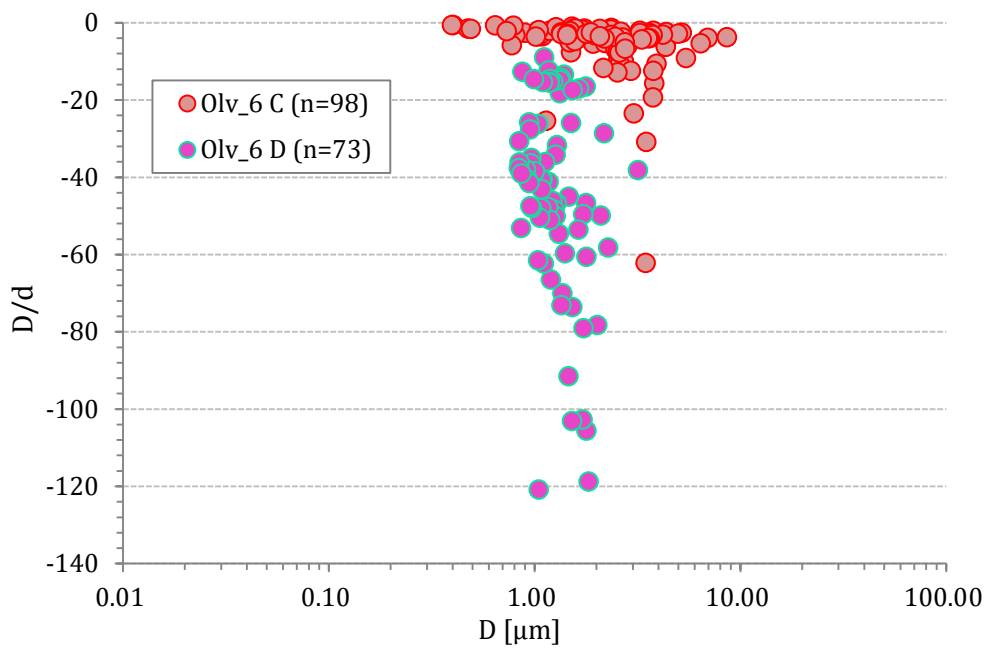


Figure 4.79: The D/d-D diagram for only impact related C and D types show that they are likely related to each other.

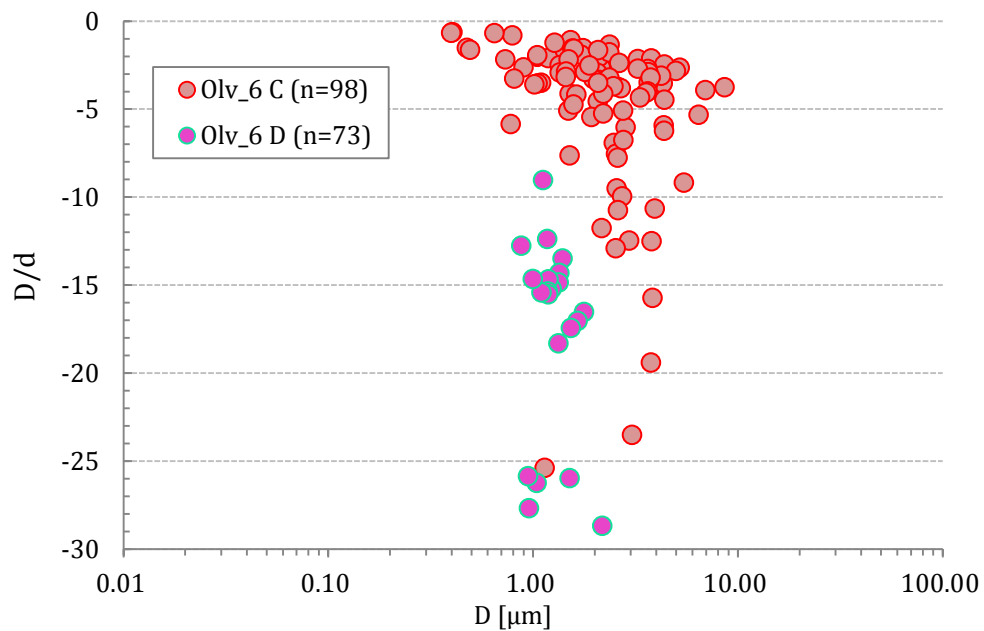


Figure 4.80: The detailed D/d-D diagram for only impact related C and D types shows their interconnectedness. A transition zone of these two types seems to be a D/d around -10–25.

In D/d diagrams dents and crater show overlapping areas. This is also observed in $D/d-D$ ratios (Fig. 4.79 and 4.80).

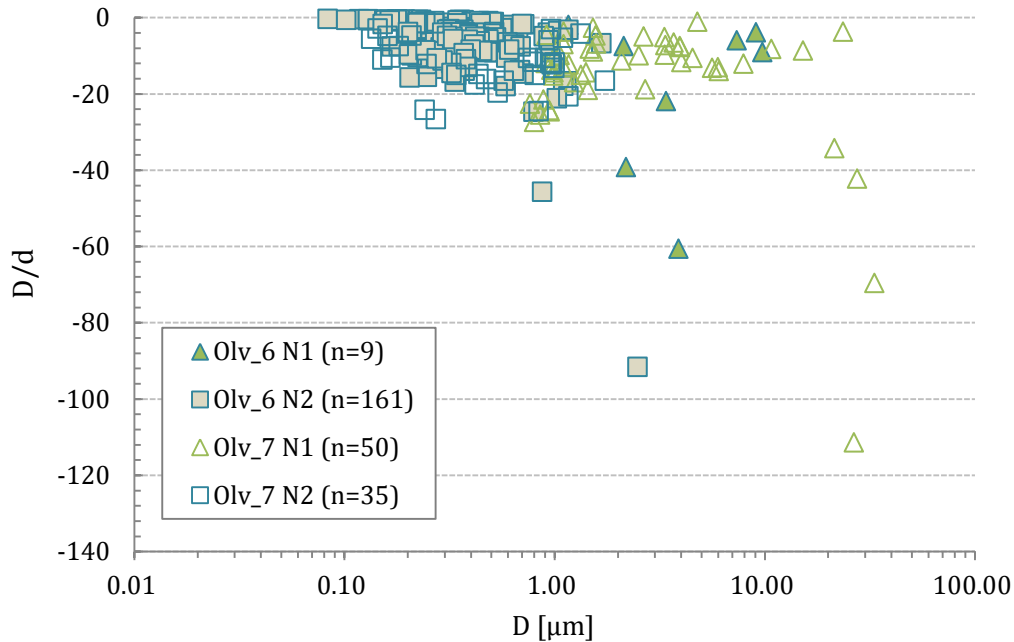


Figure 4.81: The $D/d-D$ diagram shows all negative non-impact related features in Olivine_6 and Olivine_7.

In the $D/d-D$ diagram, D type features stand out even clearer. For rebounding projectiles the penetration depth compared to the projectile diameter is rather low, and the D/d ratio reach high negative values. N_2 types of Olivine_6 and Olivine_7 are nearly identical except for certain irregularities, which come with the nature of N_1 type. D/d ratios for the majority of D type range from about -20 to -80, with diameters from ~ 0.8 – $2.5 \mu\text{m}$, the majority occurring around $1 \mu\text{m}$ (Fig. 4.81). The majority of craters show D/d ratios of ~ -3 to -5 , with diameters of ~ 1 – $6 \mu\text{m}$.

4.8 Identification of submicron-scaled craters

As described above, Fig. 4.74 shows that the bombarded Olivine_6 target has a higher abundance of N₂ type features at diameters <0.6 and depths around -0.3 micrometer. When compared to the N₂ population of the non-bombarded target, this population has lower D/d ratios. Hence, a possible way to identify additional craters among undeterminable N₂ types is searching for features with low crater-type D/d ratios. First, D/d ratios of all negative Olivine_7 and Olivine_6 features are compared (Table 4.02). The most extreme D/d value of the N₂ feature from the non-bombarded olivine target would set the threshold for non-impact related N₂ features on Olivine_6. In Table 4.02 45 negative features (N₁, N₂, very small C) are listed ordered by their D/d ratios, up to the first occurrence of N₂ on Olivine_7 (bottom of the table).

The next step then is to calculate the minimum possible D/d with the maximum possible errors for all features of Olivine_6. For the one value of Olivine_7's N₂ feature the maximum possible D/d with the maximum possible errors is calculated. The new values are now used to reorder the table by D/d ratios and the new N₂ value of Olivine_7 marks the new threshold at which cratering could occur on Olivine_6. The last step removes all N₂ zig-zag pits from the table to ensure that only features without reflectance issues are listed. The new Table 4.03 now shows five additional possible craters, beyond the N₂ Olivine_7 threshold, with reasonable D/d ratios when compared to other identified craters in the list. It is also noticeable that some already verified small craters are below the calculated threshold.

This workaround is simply an approach to overcome the issue of none discernible N₂ features, which very likely contain submicron scaled craters. The five additionally determined crater candidates nicely fit to the dimensions of craters determined via LSM imaging. Furthermore, the majority of these candidates show a more roundish shape which supports the possibility of them being actual craters.

Still, SEM-SE investigations on such candidates need to be conducted to verify this method as a legitimate approach for determining small craters.

Table 4.02: Table of negative Olivine_7 and Olivine_6 features up to the first occurrence of N₂ on Olivine_7 (red), sorted by D/d ratios. The small craters found on Olivine_6 are highlighted in blue, defects on Olivine_7 in light-red, defects on Olivine_6 in yellow.

ID	Type	description	D/d	D/d error	mean D	diameter error	mean depth	depth error	diameter shape
485	N ₂ (zig-zag)	pit	- 0.37	68%	0.083	23.51%	-0.23	60.96%	roundish
465	N ₂	pit	- 0.40	24%	0.118	6.69%	-0.30	18.66%	roundish
500	N ₂ (zig-zag)	pit	- 0.43	44%	0.129	7.35%	-0.30	39.70%	roundish
470	N ₂ (zig-zag)	pit	- 0.48	27%	0.194	25.46%	-0.41	8.58%	roundish
471	N ₂ (zig-zag)	pit	- 0.50	42%	0.179	22.04%	-0.36	29.39%	roundish
396	N ₂ (zig-zag)	pit	- 0.54	31%	0.155	30.82%	-0.29	9.66%	irregular
488	N ₂ (zig-zag)	pit	- 0.56	65%	0.102	7.57%	-0.18	62.77%	irregular
468	N ₂ (zig-zag)	pit	- 0.59	19%	0.225	10.66%	-0.38	9.98%	roundish
719	N ₂	pit	- 0.60	29%	0.355	16.18%	-0.59	17.16%	roundish
156	N ₂ (zig-zag)	pit	- 0.61	37%	0.178	12.27%	-0.29	29.25%	irregular
153	N ₂ (zig-zag)	pit	- 0.63	37%	0.232	11.43%	-0.37	29.66%	irregular
159	N ₂ (zig-zag)	pit	- 0.63	63%	0.163	18.62%	-0.26	55.67%	irregular
714	C	crater	- 0.64	32%	0.404	14.29%	-0.64	21.99%	roundish
467	N ₂	pit	- 0.64	65%	0.129	24.90%	-0.20	56.31%	roundish
620	N ₂	pit	- 0.67	26%	0.369	3.20%	-0.56	23.15%	roundish
709	C	crater, micro	- 0.67	52%	0.398	85.28%	-0.59	11.50%	irregular
117	N ₂ (zig-zag)	pit	- 0.67	50%	0.157	7.58%	-0.23	46.12%	irregular
492	N ₂	pit	- 0.68	60%	0.186	47.31%	-0.27	41.19%	elliptical
563	C	crater, block	- 0.69	33%	0.646	14.59%	-0.94	22.89%	roundish
416	N ₂ (zig-zag)	pit	- 0.72	57%	0.165	23.17%	-0.23	46.66%	irregular
85	N ₂	pit	- 0.77	33%	0.229	16.35%	-0.30	22.53%	roundish
342	N ₂	pit	- 0.80	27%	0.346	21.75%	-0.43	10.95%	irregular
705	C	crater, block	- 0.82	30%	0.792	22.30%	-0.97	14.92%	elliptical
202	N ₂ (zig-zag)	pit	- 0.94	46%	0.485	19.99%	-0.52	34.61%	irregular
414	N ₂ (zig-zag)	pit	- 0.95	89%	0.268	7.53%	-0.28	112.25%	roundish
727	N ₂ (zig-zag)	pit	- 0.97	24%	0.438	10.76%	-0.45	16.01%	roundish
113	N ₂ (zig-zag)	pit	- 0.98	35%	0.243	9.16%	-0.25	28.88%	irregular
91	N ₂	pit	- 1.05	62%	0.182	26.54%	-0.17	51.33%	roundish
47	N ₁	defect	- 1.08	38%	4.782	45.88%	-4.42	9.23%	irregular
176	C	crater, block	- 1.09	28%	1.527	9.87%	-1.41	20.86%	irregular
17	N ₂ (zig-zag)	pit	- 1.18	63%	0.224	33.05%	-0.19	50.42%	irregular
579	N ₂ (zig-zag)	pit	- 1.18	29%	0.515	4.23%	-0.44	26.38%	roundish
604	N ₂	pit	- 1.19	3%	0.405	1.65%	-0.34	1.01%	roundish
397	N ₂ (zig-zag)	pit	- 1.22	42%	0.504	33.19%	-0.41	23.36%	irregular
744	C	crater, block	- 1.24	29%	1.275	4.53%	-1.03	26.02%	roundish
89	N ₂	pit	- 1.32	73%	0.283	68.18%	-0.21	54.87%	roundish
389	C	crater, block	- 1.34	25%	2.367	5.45%	-1.76	21.02%	roundish
403	N ₂	pit	- 1.37	43%	0.457	42.43%	-0.33	18.67%	roundish
881	N ₁	defect	- 1.43	29%	1.479	35.10%	-1.03	4.12%	irregular
18	N ₂ (zig-zag)	pit	- 1.46	74%	0.223	82.22%	-0.15	52.49%	irregular
328	N ₂ (zig-zag)	pit	- 1.48	70%	0.345	22.73%	-0.23	136.72%	irregular
238	N ₂ (zig-zag)	pit	- 1.48	37%	0.446	27.27%	-0.30	20.40%	roundish
10	C	crater	- 1.52	15%	0.476	2.22%	-0.31	12.66%	roundish
410	C	crater, block	- 1.54	28%	1.752	12.67%	-1.14	19.28%	roundish
19	N ₂	pit	- 1.54	22%	0.268	16.73%	-0.17	9.27%	roundish

Table 4.03: Table of negative Olivine_7 and Olivine_6 features sorted by maximum D/d ratios, including their errors. All N₂ that were labelled as zig-zag patterned pits, are removed to ensure a list with features without possible LSM reflectance issues. Craters are highlighted in blue, defects in Olivine_7 in light-red, defects in Olivine_6 in yellow and the first occurrence of N₂ on Olivine_7 in red. ID 19, the N₂ feature on Olivine_7, sets the threshold for cratering to occur statistically.

ID	Type	description	max D/d incl.Errors	D/d	D/d error	mean D	diamter error	mean depth	depth error	diameter shape
465	N2	pit	-0.52	0.40	24%	0.118	6.69%	-0.30	18.66%	roundish
719	N2	pit	-0.84	0.60	29%	0.355	16.18%	-0.59	17.16%	roundish
620	N2	pit	-0.89	0.67	26%	0.369	3.20%	-0.56	23.15%	roundish
714	C	crater	-0.93	0.64	32%	0.404	14.29%	-0.64	21.99%	roundish
563	C	crater, block	-1.02	0.69	33%	0.646	14.59%	-0.94	22.89%	roundish
342	N2	pit	-1.09	0.80	27%	0.346	21.75%	-0.43	10.95%	irregular
85	N2	pit	-1.16	0.77	33%	0.229	16.35%	-0.30	22.53%	roundish
19	N2	pit	-1.17	1.54	22%	0.268	16.73%	-0.17	9.27%	roundish
705	C	crater, block	-1.17	0.82	30%	0.792	22.30%	-0.97	14.92%	elliptical
604	N2	pit	-1.22	1.19	3%	0.405	1.65%	-0.34	1.01%	roundish
709	C	crater, micro	-1.41	0.67	52%	0.398	85.28%	-0.59	11.50%	irregular
176	C	crater, block	-1.51	1.09	28%	1.527	9.87%	-1.41	20.86%	irregular
492	N2	pit	-1.69	0.68	60%	0.186	47.31%	-0.27	41.19%	elliptical
47	N1	defect	-1.74	1.08	38%	4.782	45.88%	-4.42	9.23%	irregular
744	C	crater, block	-1.75	1.24	29%	1.275	4.53%	-1.03	26.02%	roundish
10	C	crater	-1.78	1.52	15%	0.476	2.22%	-0.31	12.66%	roundish
389	C	crater, block	-1.79	1.34	25%	2.367	5.45%	-1.76	21.02%	roundish
467	N2	pit	-1.84	0.64	65%	0.129	24.90%	-0.20	56.31%	roundish
881	N1	defect	-2.02	1.43	29%	1.479	35.10%	-1.03	4.12%	irregular
410	C	crater, block	-2.14	1.54	28%	1.752	12.67%	-1.14	19.28%	roundish
403	N2	pit	-2.40	1.37	43%	0.457	42.43%	-0.33	18.67%	roundish
91	N2	pit	-2.72	1.05	62%	0.182	26.54%	-0.17	51.33%	roundish
89	N2	pit	-4.93	1.32	73%	0.283	68.18%	-0.21	54.87%	roundish

4.9 The effect of carbon coating in laser microscopy measurements

In chapter 4.5 *Comparison of LSM- and SEM-imaging* it was demonstrated that LSM imaging was superior to SEM-SE imaging, e.g., a higher sensitivity in detecting small, particularly shallow features, measuring subtle changes of surface properties and quantifying topographic profiles. However, the SEM had one invaluable ability, i.e. identifying impact features via measuring the elemental composition of Cu residues, either as projectiles or residues in craters. As a combined application of both LSM and SEM techniques seems desirable for future investigation, it is both necessary and interesting to clarify, whether carbon coating alters the results of LSM analytics. Except for the measurements at the Cu-track, all other zones were examined before and after carbon coating for SEM imaging. A carbon layer of $\sim 15\text{--}30$ nm was applied with a TEX MED 020 sputtering and vaporization device (Fig. 4.82).



Figure 4.82: TEX MED 020 sputtering and vaporization device at the Institute of Earth Sciences at the University of Heidelberg.

In general, measurements before and after carbon coating showed no significant differences. With the help of the *Keyence VK-Analyzer* it is possible to compare two profiles (*Compare*) of the same transect with each other and visualise any differences. Random sampling showed that for few instances there are minor differences between profiles before and after carbon coating. This could be explained by either the precision of the instrument, or the fact that it is almost impossible for an operator to place the specimen

on the microscope table in the same position and orientation twice. There are always variations in specimen orientation, which affect angle of surface tilt, and subsequently, user specific image corrections and noise reduction filters, which affect the final result of the profile. In addition to LSM operation, it might be an issue that samples are stored in a sample container that is not evacuated, so that Cu residues on the targets may acquire an oxidation film.

From selected frames, comparative measurements were taken before carbon coating (No-C) and on three different days after the coating process (C1, C2, C3). For several corresponding frames, diameter and depth or height were re-measured along transects using triangulation of prominent surface markers. Two examples are illustrated in this chapter (Fig. 4.83 and 4.84).

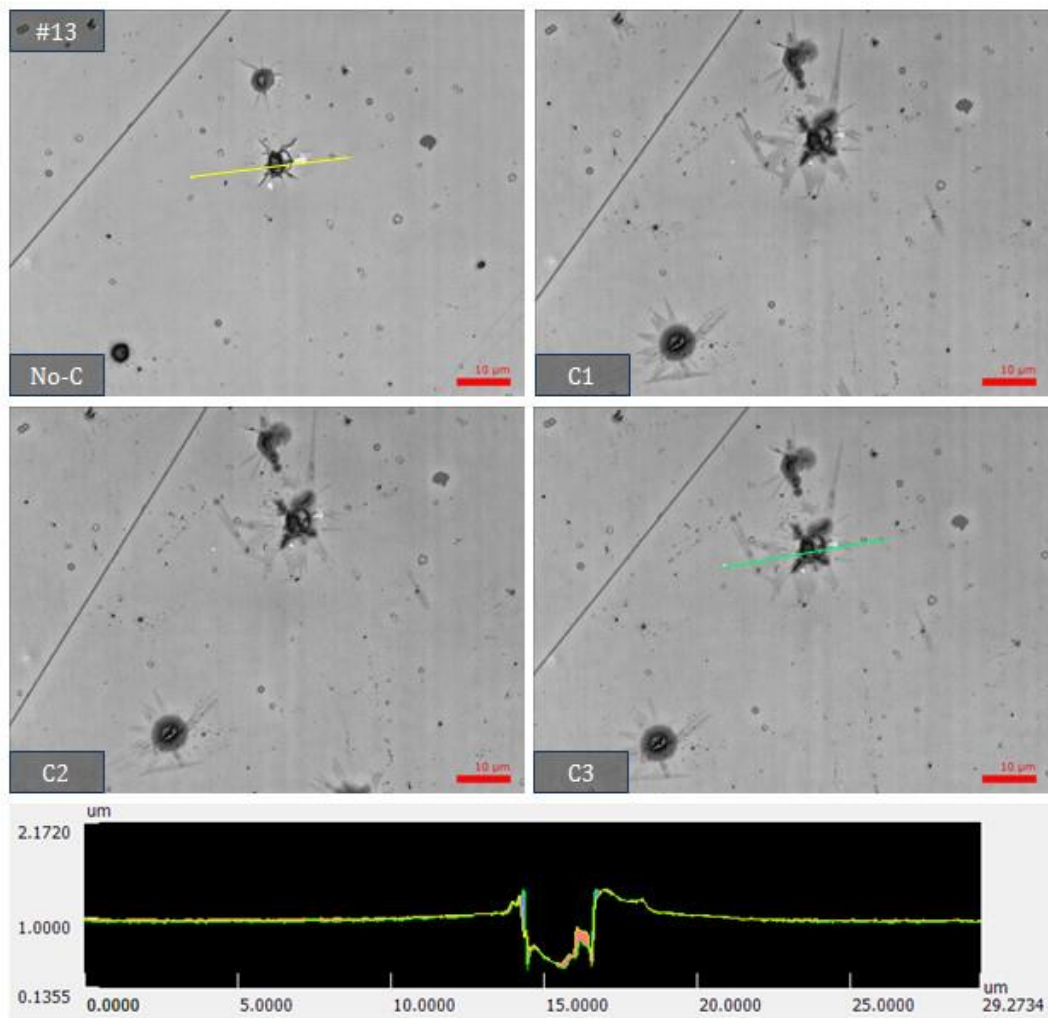


Figure 4.83: This comparison shows frame #13 with its corresponding C-Laser DIC images (No-C = without carbon coating; C1, C2, C3 after carbon coating). The profile at the bottom shows the direct comparison without carbon coating (No-C; yellow line) and the third measurement of the same zone after carbon coating (C3; green line). The red and blue areas show only very minor variations of the crater profile (C type). The diagonal line from the top mid to left side of the image is a polishing mark. Carbon coating caused less noticeable details, due to the shadowing effect of carbon at the craters, but uncovers halo like effect surrounding the impacts, which were not visible before.

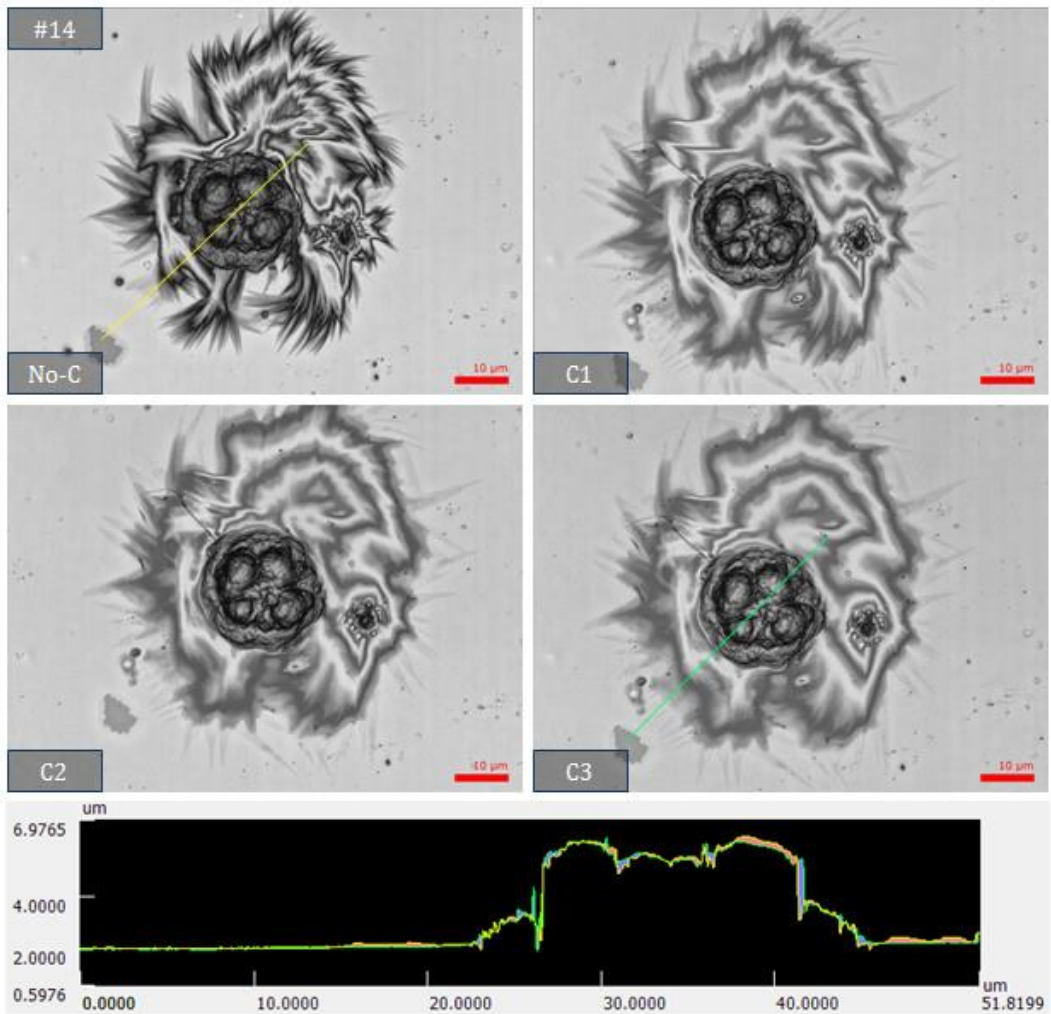


Figure 4.84: This comparison shows frame #14 with its corresponding C-Laser DIC images (No-C = without carbon coating; C1, C2, C3 after carbon coating). The profile at the bottom shows the direct comparison without carbon coating (No-C; yellow line) and the third measurement of the same zone after carbon coating (C3; green line). The red and blue areas show the variations of the sticking projectile measurements (A_3 type). Carbon coating caused less noticeable feature details at the neighbouring crater, due to the shadowing effect of carbon and especially smoothed out the shining halo effect (A_3 type), but also adds additional spikes to the halo.

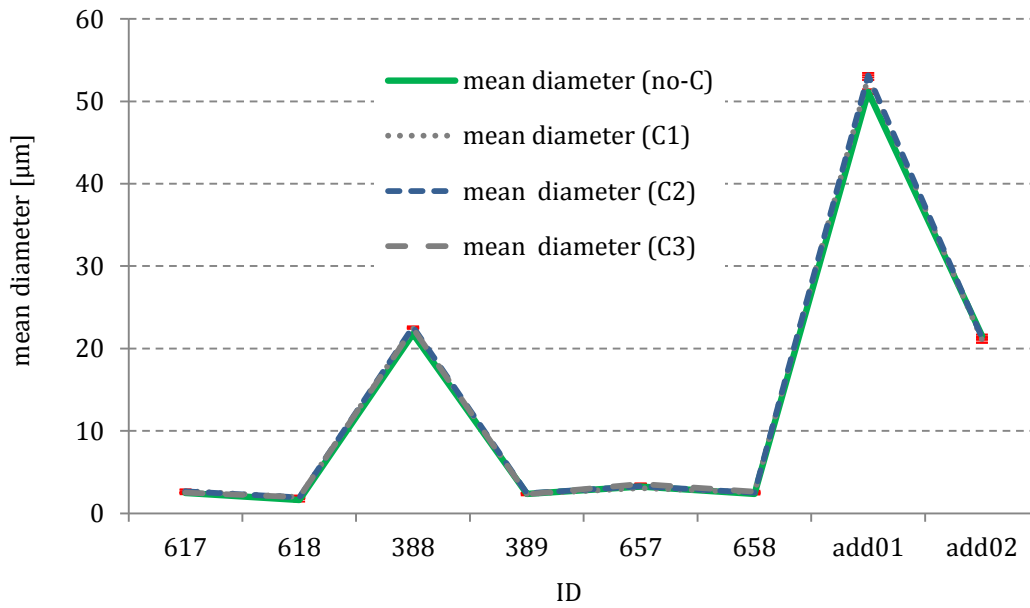


Figure 4.85: Diameter of selected craters before (no-C) and after carbon coating (C1, C2 and C3). There error bars are shown in red and barley visible. No significant changes by carbon coating are discernible.

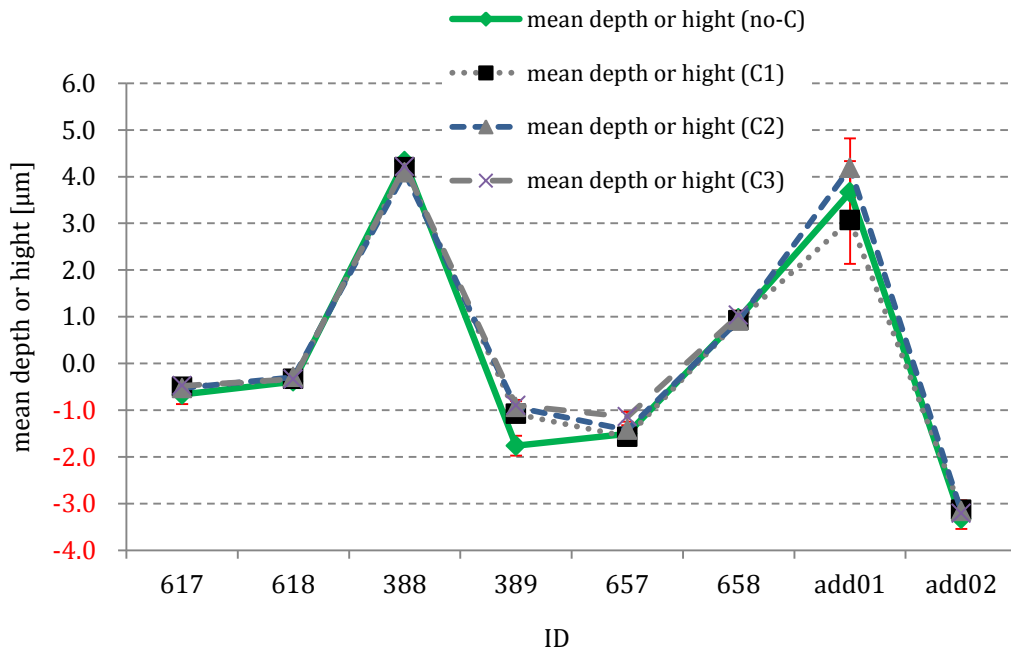


Figure 4.86: Depth of selected craters before (no-C) and after carbon coating (C1, C2 and C3). Error bars are shown in red and are barely visible. No significant changes by carbon coating are discernible, except for 1 feature: Crater ID 389 seems to indicate a depth difference before and after coating. However, it is unclear if coating is the reason or probably alteration by SEM electron beam bombardment, or other procedures involving laboratory handling of the sample.

In general, carbon coating does not alter measurements of diameter and depth or height significantly. From eight simply shaped impact features the average relative error for the diameter is 2.6 % (max. 8.6 %) and for depth or height 1.4 % (max. 11.3 %).

Most values of diameter (Fig. 4.85), depth and height (Fig. 4.86) are indistinguishable before and after carbon coating, most changes if discernible at all are not significant. Only crater ID 389 shows a significant depth reduction. This, however, cannot be safely ascribed to carbon coating, other effects like electron bombardment due to SEM usage and laboratory handling affecting the surface features cannot be ruled out as well.

Carbon coating helps to slightly enhance surface contrast and also works as a smoothening effect on features with reflectivity issues or increases reflectivity of semi-transparent surfaces. It appears that Carbon coating tends to support the visibility of probable shock-effects right beneath the olivine surface (Fig. 4.87). On the other hand fewer details are recognisable, mostly at craters. Lastly, halo effects are blurred out, but in the outskirts of the halo, additional features become visible.

In general, it appears preferable to use uncoated targets for impact feature investigations. Carbon coating after the recording of LSM data can be helpful to find additional shock-effects in the outskirts of halos or resolve uncertainties caused reflexion or transmission issues. In addition, methods like carbon coating pollute a target's surface and make it difficult to distinguish between smaller objects. On this particular Olivine_6 sample, it also seemed that carbon merged with oil residues and caused a phenomenon that looks like a smear film in LSM images.

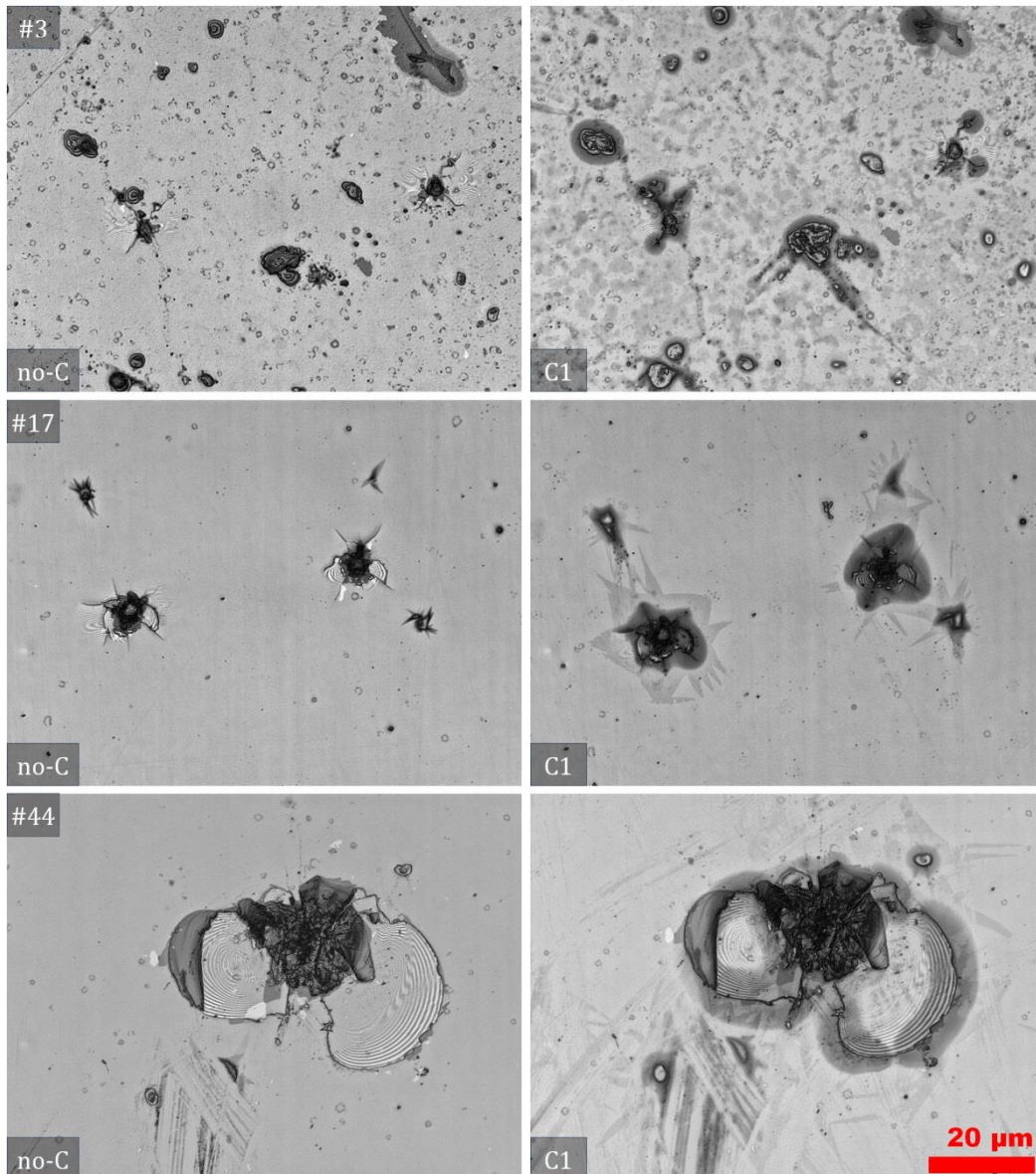


Figure 4.87: These figures show different frames as C-Laser DIC images before carbon coating (no-C) and after (C1).

Frame #3 shows two craters (C type) left and right mid, some sticking particles (A type) upper left area, at the bottom and close to the center, and a mineral defect in top right area (N_1). The sprinkled rings all over the image are dents (D type) and are blurred after carbon coating. All larger features except for the N_1 show a darkening effect surrounding the features.

Frame #17 shows two craters (C type) and two A_2 features, one above the left crater and one below the right crater. All four features show a surrounding darkening effect.

Frame #44 shows a large crater (C type). The shadowing effect occurs on the edges of the crater and the fracture lines of the spallation.

4.10 Shadowing effects after carbon coating

This effect was first observed in LSM after carbon coating was applied. Shadowing effects like in Figure 4.87 (Frame #44) and figure 4.88 surround a feature by aligning to its shape.

Comparative measurements of shadows show a surface levitation of 74 ± 116.3 (1σ) nm – the vertical resolution for our LSM device is 36 nm (3σ) given by the manufacturer. Despite the large uncertainty, this effect tends to be an additive to the surface by its height measurements. For impact features, it is quite possible that shock and stress could levitate proximal areas of a sticking projectile or zones at craters with no spallation or fracture. Reasons for shadowing around defects can be only assumed. It seems reasonable that the mineral structure in the close vicinity of a mineral defect is deficient compared to the surround material. This could cause the weakening of the bindings of an atom layer within the lattice (of an olivine), which might result in a slight elevation of the surface very close to the actual defect. The same would be true for craters. Secondly, and most likely, this might be an effect due to the polishing process, where mineral irregularities or inclusions are torn out and damage the surrounding area. Shadowing effects have no influences on any measurements of any feature's diameter, depth or height.

Shadowing effects were also found around a very large non-Cu particle (laboratory contamination). It might be possible that carbon was not able to hold on to very steep edges of the particle, trickled downward and accumulated next to it. Tests on the surrounding shadowing area showed a surface elevation of maximal ~ 25 nm (Fig. 4.86). However, this elevation is negligible as compared to the vertical precision of 36 nm (3σ) and surface roughness of ~ 10 -20 nm. Although shadowing effects are connected to carbon coating it can be considered an optical artefact and should not be confused with shock/heating effects as described in the chapter before (see chapter 4.9 *The effect of carbon coating in laser microscopy measurements*).

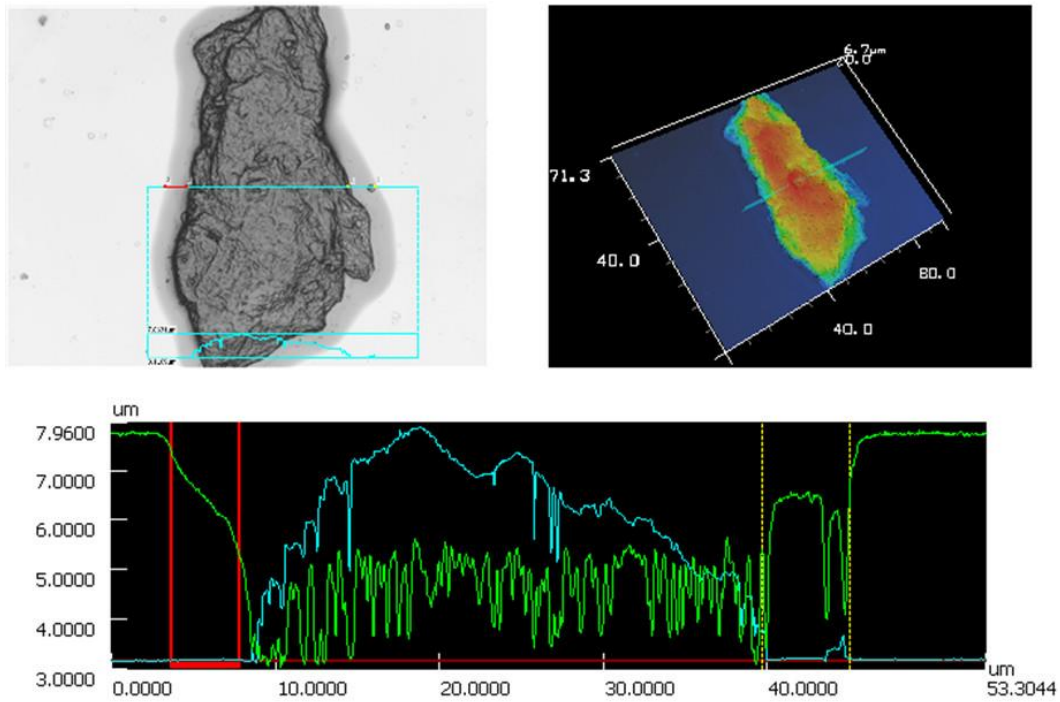


Figure 4.88: (Upper left) The C-Laser-DIC image shows a non-Cu particle lying on top of the olivine surface with a shadowing zone surrounding it. The blue line represents the profile in every picture. (Upper right) The same particle in 3D shows a maximal height of $\sim 6.7 \mu\text{m}$. (Bottom) This illustration shows the topographical profile (blue line) of the non-Cu particle and its reflectivity (green line). Note that the shadowing stretches, which is outlined in the red and yellow borders, showing different reflection intensity, as compared to the regular surface.

5 Discussion

5.1 Interpretation of surface features

During the bombardment of Olivine_6 it was not possible to select a specific particle size and velocity window. Therefore, it is also not possible to correlate a particle size with a certain impact feature sizes. Impact feature sizes are related to the projectile's size and velocity, and to the mechanical properties of the target. For this particular Olivine_6 target, there are impact features and types with varying sizes due to the varying projectile's kinetic energy.

Impact related features:

Stuck projectiles (A types)

Positive impact features are Cu projectiles that did not damage the olivine surface to form craters or dents. It can be shown that A_1 and A_2 types are similar or related features, since they cover the same areas in the $D-d$ and $D/d-D$ diagrams (Chapter 4.7.1 and 4.7.2). Due to reflectivity issues with A_1 features, it is suggested that A_1 is not a really independent subtype. It appears that some projectiles are slightly or moderately compressed and deformed, as seen from their relatively high D/d values.

In LSM optical images, and even in LSM laser images, it is possible to observe a (shining) halo effect surrounding stuck particles (A_3 types). This effect occurs with projectiles of $\sim 4 \mu\text{m}$ diameter and larger. The appearance is either in star-shaped gradations or blurred due to carbon coating. In addition, halos show a slight elevation of several tens of nanometers and are possibly a result of shock effects. Due to the transparent nature of the olivine, these diffraction patterns are assumed to make shock effects visible in LSM optical images.

A reason for occurrence of positive impact features instead of cratering could be low projectile velocities. Similarly, Li *et al.* (2014) argued for absence of craters on aluminum targets due to the lack of sufficient projectile speeds that impacted at less than 1 km/s. NEUKUM *et al.*, (1970) simulated impacts on lunar material and reported the presence of a stuck particle in a hole. Those corresponding projectiles had velocities be-

tween 1 and 2 km/s, and too little kinetic energy to form a real crater. On the other hand, copper melts around 1083°C and forsterite (Fo₉₀) beyond 1700°C (NEUKIRCHEN & RIES, 2016). Considering that Cu melts before Mg-rich olivine, it is likely that projectiles partially melt onto the deformed and cracked target surface upon impact and in the end appear as stuck projectiles. In 2009, KOBUSCH *et al.* found that about 40% of the kinetic energy of an Fe projectile impacting onto a calorimeter converts into heat. They assumed that energy conversion into heat is independent of impact velocity and the target's material and projectile's material combination. On the other hand, melting needs not necessarily be involved, as metals are ductile and can more easily be deformed and compressed than minerals. Whatever caused deformation, it is concluded that A type features are related to mid-range impact energies when compared to dents and craters.

Projectile splattering and cones (B types)

Cones and splash features are considered to be impacts, but with insufficient energy density to cause a crater. Considering energy density, this must be higher for B than for A types, these types reach rather high degrees of compression and flattening, i.e. large D/d ratios of ~ 12–54. For slow projectiles, splattering was previously documented by MANDEVILLE & VEDDER (1974). Since some splattering or splash features (B₁) mostly appear in conjunction with a colorful appearance in LSM optical images, it is possible that their appearance is influenced by oil residues from the vacuum-pump of the dust accelerator that hit the target before an actual particle hit the same location. The cone B₂ type was only observed in the carbon coated Cu-track. Only one example of B₂ type showed slight fracturing. Hence, the B₂ type could be an effect of i) a smoothed out B₁ type, ii) a very rare occurrence of projectile almost molten or compressed into its own early crater stage, or iii) a secondary Cu impact into an already existing crater (although very unlikely). It is not fully clear at which velocities these features appear.

Craters (C type)

The majority of the identified craters are single pits apparently caused by individual projectiles. Hence, our study does not indicate that projectiles have impacted the olivine target as aggregates, which was previously reported by KEARSLEY *et al.* (2008, 2009).

RUDOLPH (1969) found that Fe projectiles penetrating a Cu target surface at 0.5 – 1.5 km/s, produce almost the same diameter of craters as their projectile diameters. Above a value of 1.5 km/s, the projectiles start to deform or break, and above 4 km/s they are vaporised. He also stated that crater depths increase with a projectile's velocity, which would result in decreasing D/d for same projectile diameters. RUDOLPH (1969) also reports that crater diameter is a function of a projectile's velocity, diameter and target material. For a soda lime glass For a soda lime glass target, the data showed that the higher the velocity of projectiles, the deeper the craters would be, as compared to their diameter. Later, it was suggested that crater morphologies depend primarily on particle velocity and the density of the target material (VEDDER & MANDEVILLE, 1974). Plotting the mean D - and mean D_P -values into a diagram together with data of other studies, the connection of crater diameter and projectile diameter can be visualised (Fig. 5.01). It is important to point out that the mean D_P of this study contains all projectiles regardless of what impact feature they produce.

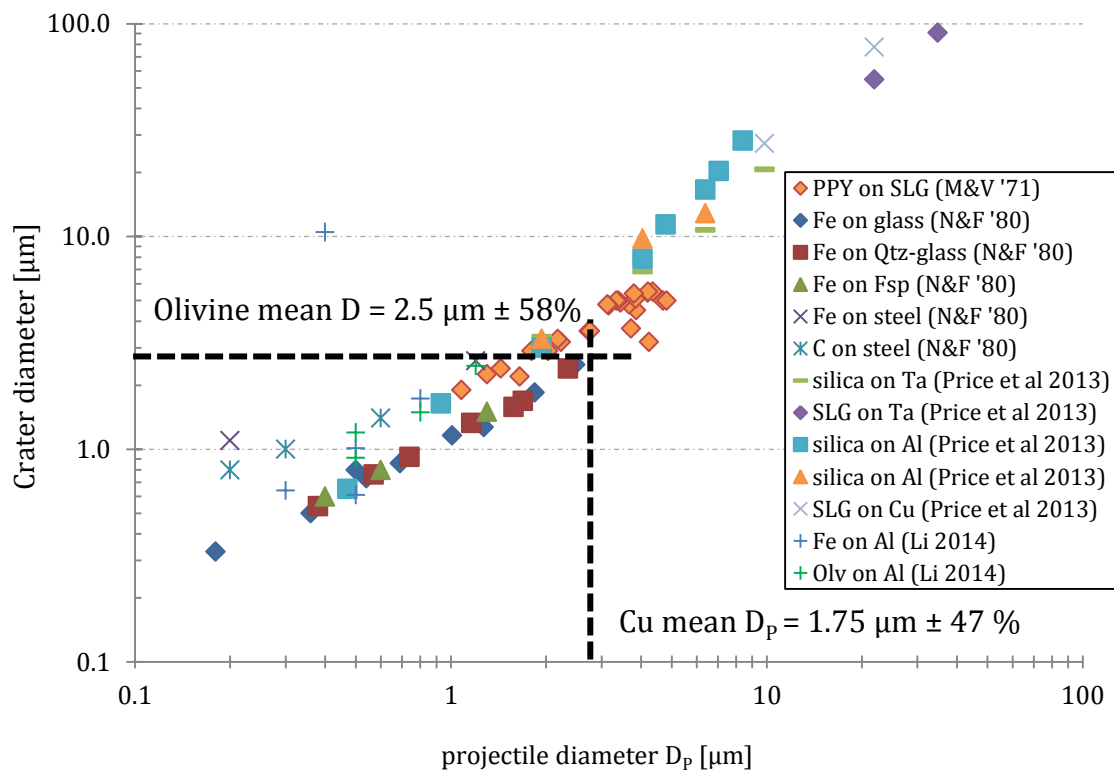


Figure 5.01: By illustrating data from different studies into a Crater diameter to projectile diameter diagram, the relationship between these two parameters becomes visible. Plotting the mean crater diameters and D_p -values of this experiment into the diagram the intersection point is right on the trend line. D -values of PRICE *et al.* 2013 are acquired by lip to lip measurements, which results in slightly larger D/d ratios.

Most dependencies for density- or velocity-to-crater diameter and D/d ratios are consistent for craters with diameters between 1 – 30 μm . Craters with smaller diameters have much deeper crater pits. Larger impacts seem to encounter other influences. A trend was observed that small craters on lunar rock are possibly related to particles of higher density (NAGEL *et al.*, 1976a; MANDEVILLE, 1977). Using dense projectiles, such as Fe, produces bulbous shaped craters in soda lime glass at velocities of 8.8 km/s and beyond, as compared to less denser Al or PS-DVB projectiles (VEDDER & MANDEVILLE, 1974). Such bulbous phenomena could not be observed, due to the static optics of the LSM instrument. Also, the depth to diameter ratio to deduct the initial particle density only works for bowl shaped craters. It was also concluded that irregular internal crater morphologies can be derived from irregular projectiles (KEARSLEY *et al.*, 2007). This might be true for less brittle targets. The depth of a crater is determined by the projectiles velocity and material strength (MERZHIEVSKY, 1997), which is true for spherical particles and

homogenous target surfaces. VEDDER & MANDEVILLE (1974) and MANDEVILLE (1977) stated that acquiring the depth of a crater is accompanied by uncertainties when using SEM, due to the magnification, stage orientation, resolution and irregular crater morphology. They give errors of crater depths $\pm 20\text{--}25\%$ for very shallow craters, deep pits of craters with small diameters and pits containing Fe remnants at the bottom. In this study the depth uncertainty was $\sim 17\%$ (98 craters, ranging from -0.02 to $-2.34\ \mu\text{m}$) using the LSM technique.

Chemical EDS analysis on craters is also complicated (Fig. 5.02). A detailed study on this subject was performed by KEARSLEY *et al.* (2007). Here, side-effects of tilting and crater lips affecting element quantification were shown, and severe analytical problems regarding shadowing (X-ray absorption) for small craters with diameters less than $20\ \mu\text{m}$ were mentioned. At diameters below $10\ \mu\text{m}$ geometrical effects impact conventional EDS strongly, however, FIB assisted TEM can achieve good results at such scales.

Chemical EDS analysis on craters is also complicated (Fig. 5.02). A detailed study on this subject was performed by KEARSLEY *et al.* (2007). Here, side-effects of tilting and crater lips affecting element quantification was shown, and severe analytical problems regarding shadowing (X-ray absorption) for small craters with diameters less than $20\ \mu\text{m}$ were mentioned. At diameters below $10\ \mu\text{m}$ geometrical effects impact conventional EDS strongly, however, FIB assisted TEM can achieve good results at such scales.

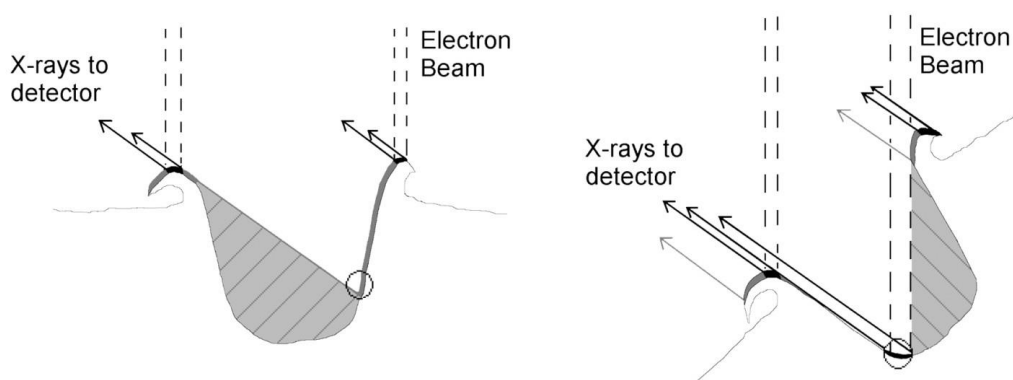


Figure 5.02: Schematic illustration by KEARSLEY *et al.* (2007) showing the X-ray generation for a typical impact crater profile and its collection by an EDS detector in normal (left) and tilted (right) orientation to the beam. Dashed lines represent the electron beam; grey and black areas resemble yield detectable X-rays; cross-hatched areas yield little or no useful X-rays; in circled areas usually the thickest projectile residues are found.

In this study, the chemical SEM analysis conducted on crater sites showed signals of Cu. This indicates projectile residues within the craters. The exact location of residue within a crater could not be determined. The calculation of the crater volume seemed ineffective, since the crater pits show irregular topographies which are generally difficult to acquire.

Additional crater structures, such as lips, are rare, but fractures and spallation effects are frequent. Fractures and spallation tend to share similar preferred directions (Fig. 5.03). Spallation zones primarily occur between 1:30 to 4:30 and 7:30 to 10:30 o'clock. This could be caused by the crystallographic orientation of the olivine target, or be an effect of the polishing process (VEDDER, 1971). On the other hand, the occurrence of displaced fragments (E type) increased, with decreasing spallation.

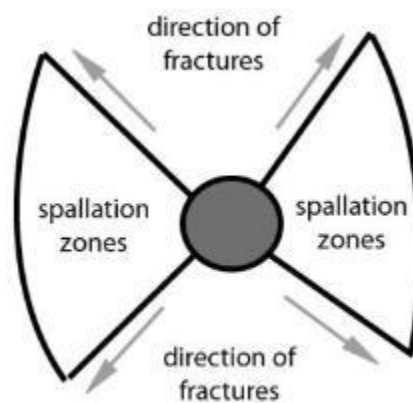


Figure 5.03: The grey circle in the center represents a simplified crater. Arrows show the primary directions of radial fractures. The zones where the majorities of spallation occurred are between 1:30 to 4:30 and 7:30 to 10:30 o'clock. Spallation likely occurs between two fractures.

Though it is not possible to establish a specific projectile diameter or velocity for an individual crater due to the setup of this experiment, the relationship of D to d can give a small insight into the nature of this experiment nevertheless. As stated earlier, the crater depth acquisition with SEM and LSM bears some uncertainties in the d -values. By plotting data of other studies in combination with Cu impacts on olivine, general trends can be observed (Fig. 5.04). It could be shown that Cu impacting on Olivine has variable D/d ratios) and cannot be distinguished from other studies, which is most likely due to lack

of controlled projectile velocities and sizes. Furthermore, if considering the mechanical properties of olivine (Appendix C), they are quite different from FQ, SLG or other target materials.

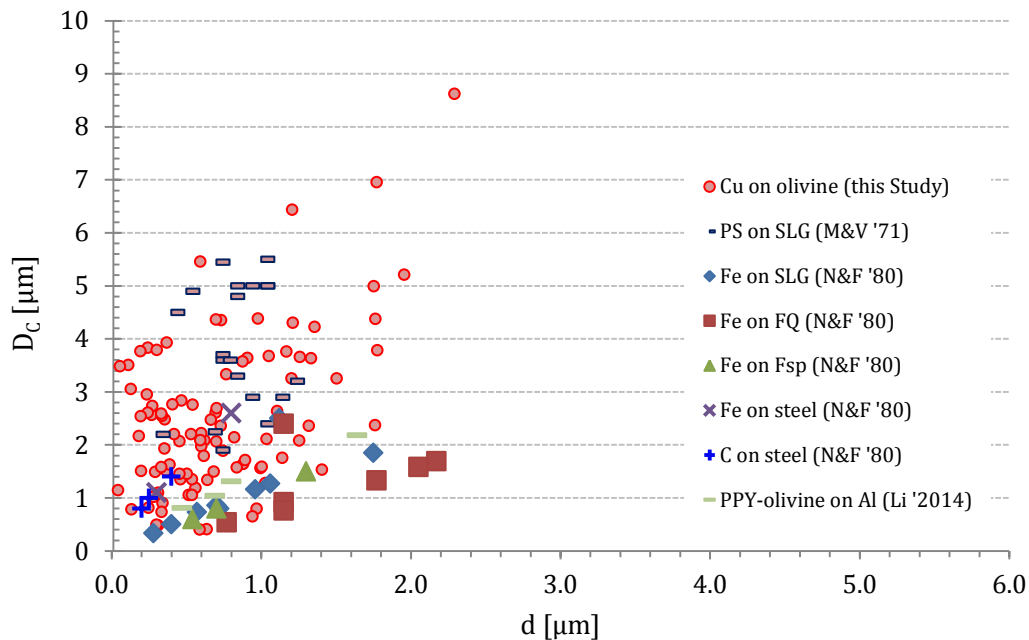


Figure 5.04: D to d values of different impact experiments. MANDEVILLE & VEDDERS (1971) used Polystyrene ($D_p = 1.08 - 4.82 \mu\text{m}$, $v = 2.95 - 14.0 \text{ km/s}$) on soda lime glass; NAGEL & FECHTIG (1980) used iron ($D_p = 0.18 - 2.48 \mu\text{m}$, $v = 2.6 - 14.5 \text{ km/s}$) on soda lime glass; iron ($D_p = 0.38 - 2.35 \mu\text{m}$, $v = 2.5 - 8.5 \text{ km/s}$) on fused quartz; iron ($D_p = 0.4 - 1.3 \mu\text{m}$, $v = 4.8 - 10.8 \text{ km/s}$) on feldspar (bytownite); iron ($D_p = 0.2 - 1.2 \mu\text{m}$, $v = 5.2 - 21.1 \text{ km/s}$) on stainless steel; carbon ($D_p = 0.2 - 0.6 \mu\text{m}$, $v = 7.5 - 20.8 \text{ km/s}$) on stainless steel; Li (2014) used PPY coated olivine ($D_p = 0.5 - 1.2 \mu\text{m}$, $v = 5.0 - 7.0 \text{ km/s}$) on aluminium; iron ($D_p = 0.3 - 0.8 \mu\text{m}$, $v = 3.0 - 7.0 \text{ km/s}$) on aluminium. Data of this study and PS on SLG show rather large scattering.

Cleanly shaped crater pits with lips, such as on metal targets, were rare. In turn, it could not be detected, whether craters on olivine bear central pits. Impact simulations via laser ablation on a Cu target demonstrated e.g. by RUSSO (1995) show smooth and clean crater morphologies with a lined crater pit and lips (Fig. 5.05). However, these are not comparable with particle impacts on a brittle rigid mineral surface with its individual cleavage preference and the tendency to generate fractures and spallation. RUDOLPH (1969) as well stated that crater formation is also dependent on the target material.

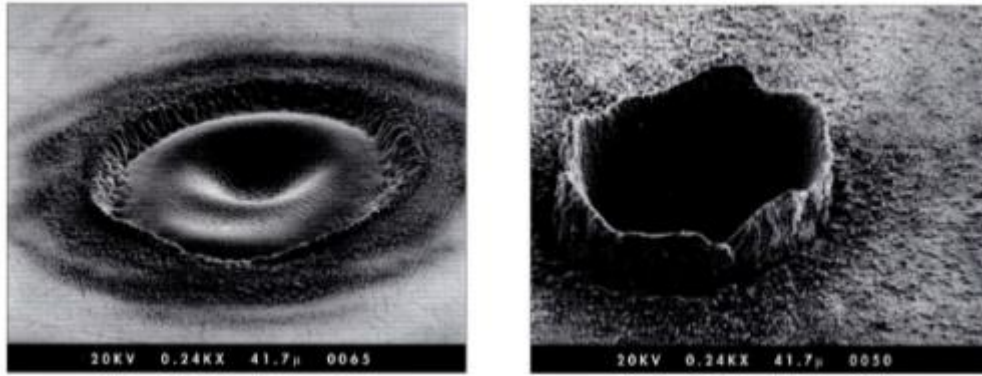


Figure 5.05: SEM images of craters on a Cu target produced by laser ablation (RUSSO (1995)).

Displaced fragments (E type)

Displaced fragments are assumed to be an effect of excavation translation onto the surface in a radial direction away from the impact center. In LSM laser-images it can be observed, that next to most fragments on the turned-away side of the crater, some small bright areas can occur. These areas appear as bright phenomena, cast by the impact explosion, and shielded by the fragments themselves. To understand the displaced of projectile material, knowledge of melting- and vaporization-temperatures generated by impact shock pressures is important. These shock pressures vary by projectile velocity, projectile density and target material strength. For a given shock pressure, less dense projectiles require higher velocities than denser ones. Indicators for high temperatures generated upon impact can be crater lips, ejected melt and the melting of projectiles (VEDDER & MANDEVILLE, 1974). An impacting HV projectile can explode after an abrupt decrease of surface penetration, which evaporates due to heavy compression (MERZHIEVSKY, 1997). I consider that such an explosion could shear off fragments and displace them along the surface.

Impact effects of secondary ejecta and their velocities are still a topic of discussion. Early simulations of micro impacts showed that detectable ejecta particles have very low velocities of less than 100 m/s or do not exceed those of their corresponding impact projectiles (BRASLAU, 1970). AUTODYN simulations are considering these velocities to be rather slow with only a few km/s (PRICE *et al.*, 2012). Ejecta particles with 1 km/s are very rare (LI, 2015). In contrast, low impact velocities and relatively high ejection veloci-

ties (even higher than those for high-velocity impacts) were reported (WAZA et al., 1985). NAGEL *et al.*, (1975) showed ejecta velocities ≥ 3 km/s for impact angles between 35° and 75° , and ejecta velocities ≥ 1 km/s for impact angles between $<20^\circ$.

Dents and precursor craters (D type)

Phenomena, i.e., indentation effects on micron scale, resulting from very low impactor velocities, have been reported by different authors. NEUKUM *et al.* (1970) speaks of flat impacts without rims caused by Fe projectile hitting lunar material with velocities below 1 km/s. VEDDER (1971) also observed this phenomenon with Fe projectiles below 1 km/s on glass. Later, similar features were observed on soda lime glass and fused quartz. Denser projectiles, such as Al and Fe, could produce dents up to 2.5 km/s, but less dense PS-DVB (Polystyrene divinylbenzene) even up to about 4 km/s (VEDDER & MANDEVILLE, 1974). AUTODYN simulations showed that concrete impacting on a copper target at 1 km/s, produces impact features, which do not look like fully evolved craters (LI, 2015). In this study, some of the features described by VEDDER & MANDEVILLE were found. In addition, most of these look like precursor stages of indentations with poorly pronounced morphology, and are only visible in LSM C-Laser-DIC images. Many were detected, but only a few numbers of these fine dents were measurable in detail with the LSM. The features appear as small dark rings on the olivine surface with diameters between ~ 1 and ~ 2.5 μm . Those with greater depths ($d > 80$ nm) are assumed to be precursor craters. D types are suggested to be impact features, being a result of impactors with the lowest velocity in this experiment.

Miscellaneous features:

Surface or mineral defects (N₁ type)

Defects on mineral surfaces can occur due to different reasons. It could be mineral inclusions, cavities from gas inclusions or lattice defects that get uncovered by slicing the targets into pieces and subsequent polishing – anything during the target production can lead to the development of surface weaknesses or expose pre-existing defect areas. It could be shown that surface defects on the non-bombarded olivine target are also occurring on the bombarded counter piece. Their diameters and depth values can overlap

with those of craters. However, N_1 type can be easily distinguished from craters as they tend to have angular shapes. Defects showed a D/d ratio of about -16 to -17.

Undeterminable negative features (N_2 type)

This type includes all negative features that were undeterminable by simple observation. N_2 is an interesting type, as it overlaps with craters in diameters of $\sim 1 \mu\text{m}$ and are more frequent on the bombarded sample than on non-bombarded target (Tab. 5.01). It is highly likely, that N_2 types include submicron craters, which could not be determined with LSM imaging. D/d ratios for this type vary between the bombarded and the non-bombarded target, serving as an additional indicator for P_1 types including impact features. With the method explained in Chapter 4.8 (see chapter 4.8 *The approach to deducting submicron-scaled craters*) another indicator was described, which points to potential small craters.

Surface contamination (P_1 type)

Laboratory situation and sample handling was already described in chapter 2.4.2 *Laboratory situation and sample handling*. Surface or dust contamination occurs at any time, e.g., when the sample was placed under the SEM or when exposed to the laboratory atmosphere in general. Large non-Cu particles were also added via carbon coating, i.e., as large carbon particles. In general, these features are more irregular or angular shaped and are rather rare. With LSM techniques, contamination can be rather easily distinguished from real Cu projectiles, as $\sim 93\%$ of all projectiles are spherical in shape.

Undeterminable positive features (P_2 type)

On both olivine targets these features were found, having the same diameters and height ratios. P_2 can be also considered as the positive counter part of N_2 type, and likely contains some sub-micron sized stuck particles. D/d ratios for this type vary on the bombarded and the non-bombarded target, which is an additional indicator that P_2 type includes impact types.

5.2 General interpretation of the bombarded olivine target

Almost 99 % of all projectiles in this study travelled at velocities of $\sim 0.45\text{--}13$ km/s with D_P of $0.01\text{--}4.9$ μm . With regard to other studies velocities can be separated into two different regimes: low hyper-velocities (LHV: <2.5 km/s), and hyper-velocities (HV: >2.5 km/s). In 1974, VEDDER & MANDEVILLE performed an experiment with projectiles of different densities (e.g. Al, Fe) and used soda lime glass (SLG) and fused quartz (FQ) as targets. They found different types of morphologies at impact sites, depending on impact velocity and projectile material (density). They showed that experiments with Al and Fe projectiles at LHV (<2.5 km/s Fe on FQ, <3.0 km/s Al on FQ <2.1 km/s Al on SLG; not specified lower v Fe on SLG) result in rebounding, dents and projectile splattering. At higher velocities, effects of spallation and projectile residues were found. As outlined in chapter 3.3.1 *Velocities of projectiles*, the experiment of this thesis showed that 80 % of the projectiles had velocities below 2.0 km/s. In order to achieve the same kinetic energy, equal sized Cu and Fe projectiles should have $v_{\text{Cu}} = 1.06 \cdot v_{\text{Fe}}$ (Equation [8], see chapter 3.3.3 *Kinetic energy of projectiles*). Using this relationship and the observations on Fe projectiles by VEDDER & MANDEVILLE (1974), some impact feature types can be ascribed to LHV impacts <2.5 km/s (i.e. stuck projectiles: A types, splattering projectiles: B types, dents: D type), while C type craters are assumed to be HV. The ratio of LHV to HV features is $\sim 75:25$ % (Tab. 5.01 bottom). This ratio agrees with the velocity distribution of this experiment, with 79,7% of all projectiles having velocities $0.45\text{--}2$ km/s and 20.3 % > 2 km/s (Table 3.01; chapter 3.3.1). Considering that Cu projectiles need less velocity than Al or Fe to achieve similar energy in crater formation, the consistency seems even more reasonable within uncertainties.

Table 5.01: All counts for each type on the Olivine_6 (bombarded) and the Olivine_7 (non-bombarded) target and their corresponding diameter and depth ratios. Negative D/d ratios indicate negative surface features. It should be noted that dents (D type) are underrepresented by likely a factor of four.

	Olivine_6				Olivine_7			
	total count	count percentage	mean D_c/d ratio (abs.)	mean d/D_c ratio (abs.)	total count	count percentage	mean D_c/d ratio (abs.)	mean d/D_c ratio (abs.)
<i>A₁-Type</i>	108	12.4%	3.68	0.36				
<i>A₂-Type</i>	84	9.6%	3.53	0.44				
<i>A₃-Type</i>	12	1.4%	3.72	0.33				
A-Type (all)	204	23.4%	3.62	0.39				
<i>B₁-Type</i>	10	1.1%	19.95	0.06				
<i>B₂-Type</i>	6	0.7%	19.10	0.07				
B-Type (all)	16	1.8%	19.63	0.06				
C-Type	98	11.3%	-5.63	-0.36				
D-Type	73	8.4%	-44.85	-0.03				
E-Type	17	2.0%	4.75	0.34				
N₁-Type	9	1.0%	-17.03	-0.18	50	22.6%	-16.01	-0.12
N₂-Type	161	18.5%	-6.93	-0.42	35	15.8%	-11.68	-0.14
P₁-Type	3	0.3%	12.12	0.11	4	1.8%	6.21	0.33
P₂-Type	290	33.3%	5.86	0.53	132	59.7%	17.18	0.17
Total	871				221			

293	74.9%	LHV impact related types (A, B, D)
98	25.1%	HV impact related type (C)

Comparing the miscellaneous types of both olivine targets (Table 5.01), it is obvious that the non-bombarded target (22 analysed frames) has far more N₁ types (surface defects) than the bombarded (43 analysed frames). This is a result of the sampling method. On Olivine_7, frames were selected more randomly, compared to Olivine_6, which were focused in an area of major bombardment with fewer defects. The mean D/d and d/D ratios for N₁ types (Table 5.01) are very similar on both targets. The D/d ratio of N₂ types on Olivine_6 is very different from those on Olivine_7, and more similar to C types on Olivine_6. Similarly, the D/d ratio of P₂ types on Olivine_6 is more similar to A types than P₂ types on Olivine_7. This could indicate that the N₂ and P₂ types on Olivine_6 likely contain very tiny impact features that could not have been identified with LSM images. For P₁ type (contamination particles) it can be stated that contamination from the laboratory environment may potentially occur during handling and storing the samples, but is statistically insignificant with three and four occurrences only. All impact types A, B, C and D show differences in their D/d and d/D ratios and, as such, define their own specific group. Since the majority of projectiles were of LHV, generally more positive, impact

related types could be determined as compared to negative types. However, it should be taken into account, that not every D type (dents) was determinable and there are a lot more features of this type as represented by the numbers. Most likely there are four times more dents, which would shift the LHV: HV ratio to $\sim 82:18$, which coincides even better with the projectile velocity bins of 80:20 (Tab. 3.01).

The maximum velocity of a projectile in this thesis was ~ 13 km/s (within 3σ) and ~ 4.5 % of all particles had velocities above 6 km/s (Table 3.01). The mean D/d ratio for all C types is -5.63. Calculating D/d ratio without outliers (5 % of the most extreme values) the ratio decreases to -4.85. The crater D/d values have a large variation due to different projectile velocities. The data of negative features of this study are plotted as a histogram and show a maximum at $D/d = -3.5$ (Fig. 5.07). A D/d ratio ranging between -3.5 to -4.85, is well comparable to other studies taking in to account different targets. NAGEL *et al.* (1976b) published data on feldspar targets struck by glass and iron projectiles with $v = 4.5 - 11$ km/s, having D/d ratios between -1.4 and -1.9., respectively. In another study, targets impacted by a steel projectile of $2.0 \cdot 10^3 \mu\text{m}$ with $v =$ of 4.7 km/s caused a crater of $3.0 \cdot 10^3 \mu\text{m}$ diameter, a depth of $1.1 \cdot 10^3 \mu\text{m}$, and a D/d ratio of -2.7 ± 0.4 . Stainless steel impacted by a Fe projectile of $1.2 \cdot 10^3 \mu\text{m}$ with $v = 5.2$ km/s caused a crater of $2.6 \cdot 10^3 \mu\text{m}$ diameter, a depth of $0.8 \cdot 10^3 \mu\text{m}$, and a D/d ratio of -3.3 ± 0.5 (NAGEL & FECHTIG, 1980). It appears that the actual cratering process starts at higher mean velocities, as compared to other studies.

SLG and FQ or stainless steel are at first sight no natural materials and have completely different mechanical properties than olivine. As stated before, natural minerals have an individual cleavage preference (e.g. olivine: conchoidal fractures). This may explain the preferential occurrence of spallation effects and missing of crater lips already reported by VEDDER (1971). In this study, crater lips were also very rare, and craters rather showed large fractures and spallation. Considering olivine to be a material with high melting temperatures and general higher material strength as compared to other targets described before (see *Appendix C: Material properties*), cratering might cause more fracturing, spallation and ejection of surface material. This could indicate larger crater diameters, which can be observed by high D/d ratios (Fig. 5.06).

For dents (D type), no comparable values from other studies are available (Fig. 5.07), but it is noticeable that dents show two populations. Some are simple dents with

D/d ratio = -110, others are considered forms of precursor craters with $D/d = -50$.

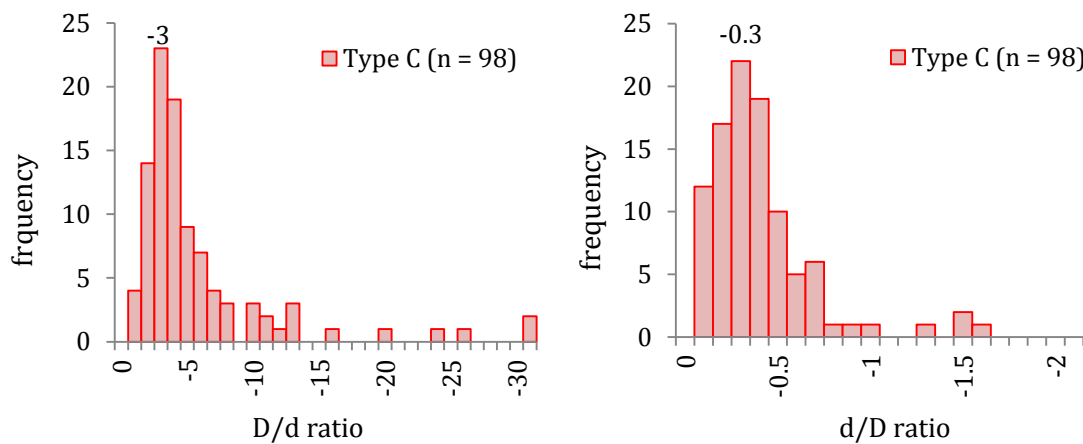


Figure 5.06: Illustration of diameter and depth related ratios of craters (C type).

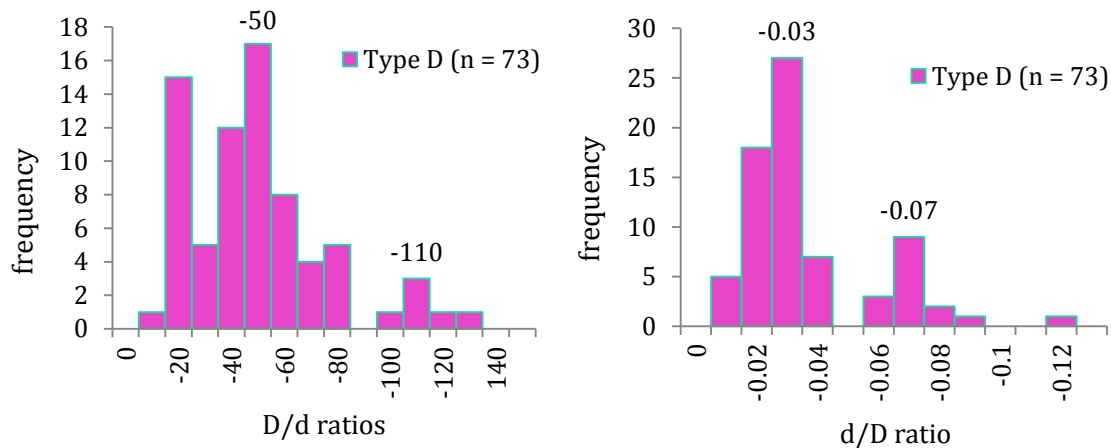


Figure 5.07: Illustration of diameter and depth related ratios of craters (D type). It is noticeable that there are two distinct populations, due to the effect of a simple dent and a precursor stage of a crater structure.

NAGEL & FECHTIG (1980) discussed the dependency of D/d ratios found in several other studies and their own findings. Based on that, it appears that D/d ratios slowly increase with a projectile's diameter, which is also valid for macro-scaled craters (size of kilometres).

The reverse-proportionality of D/d to $v^{2/3}$ is constant at velocities of 4 km/s. Above 4 km/s it remains constant (BLOCH *et al.*, 1971; NEUKUM *et al.*, 1972; NAGEL & FECHTIG, 1980). This would speak for D/d ratios strongly depend on a projectile's velocity.

Assuming a crater D/d ratio of -3 (most frequent value shown in Fig. 5.06) and using the approximation equation of $D/d \sim v^{2/3}$, would yield a projectile velocity of $v = \sim 5.2$ km/s for these craters. VEDDER & MANDEVILLE (1974) calculated cratering velocity thresholds of ~ 2 km/s for Fe projectiles impacting on SLG and FQ, with the latter being considered “weaker” than olivine. Taking also into account that Cu projectiles with the same velocity have a higher kinetic energy (see chapter 3.3.3 *Kinetic energies of projectiles*; Equation [8] $v_{\text{Cu}}(E_{\text{kin}}, m) = 1.06 * v_{\text{Fe}}$) than Fe, cratering for same-sized particles probably start at lower velocities. A 4 μm diameter Cu projectile at 1 km/s has about the same kinetic energy as 1 μm (Fe) diameter projectile at ~ 7 km/s. Such, only looking at a projectile's velocity, size or density would be misleading in this study. It was also reported that the projectile's shape and porosity affects the crater's d/D ratios (KEARSLEY *et al.*, 2008, 2009), and further that D/D_P is close to being a linear function (Fig. 5.01). Studies regarding lunar micro - cratering, from IPD flux values of $D/D_P = 2$ at $D = 6 \mu\text{m}$, and $D/D_P = 3$ at $D \lesssim 6 \mu\text{m}$ were derived (LE SERGEANT D'HENDECOURT & LAMY, 1980; GRÜN *et al.*, 1985).

By plotting D/D_P to areal energy density $D_{E(A)}$ the dependence can be conceived. From studies of MANDEVILLE & VEDDERS (1971), NAGEL & FECHTIG (1980) and LI (2014) the formation of craters could be observed to start at $D_{E(A)} = \sim 13,000$ [J/m^2] and can reach $\sim 220,000$ [J/m^2] for a 0.2 μm diameter Fe projectile at 21.1 km/s. By considering a theoretical cratering threshold of $D_{E(A)} = \sim 13,000$ [J/m^2], then only 16.1 % of Cu projectiles of this study achieved this value. This would result in $\sim 150,000$ possible craters. In 75 frames, that represent $\sim 50.6 \text{ mm}^2$ of the olivine target, from 871 measured features (incl. non-impact types) 25% were identified as craters and linked to $\geq\text{LHV}$. 16.1 % of all Cu projectiles had sufficient $D_{E(A)}$ to cause craters seems realistic regarding the $\geq\text{LHV}$ ratio, considering uncertainties. By Lowering the $D_{E(A)}$ threshold to 7600 [J/m^2], this would include 25% of all Cu projectiles. Revisiting such thresholds for certain impact features, or at least for craters, occurring in a specific material could be useful to yield constraints regarding projectile and target interaction. Finally, knowledge of the porosity or spatial structure of projectiles would allow to calculate the volume related energy density $D_{E(V)}$ which may define a more comprehensive correlation with impact behaviour and cratering threshold, independent of mass and velocity distributions.

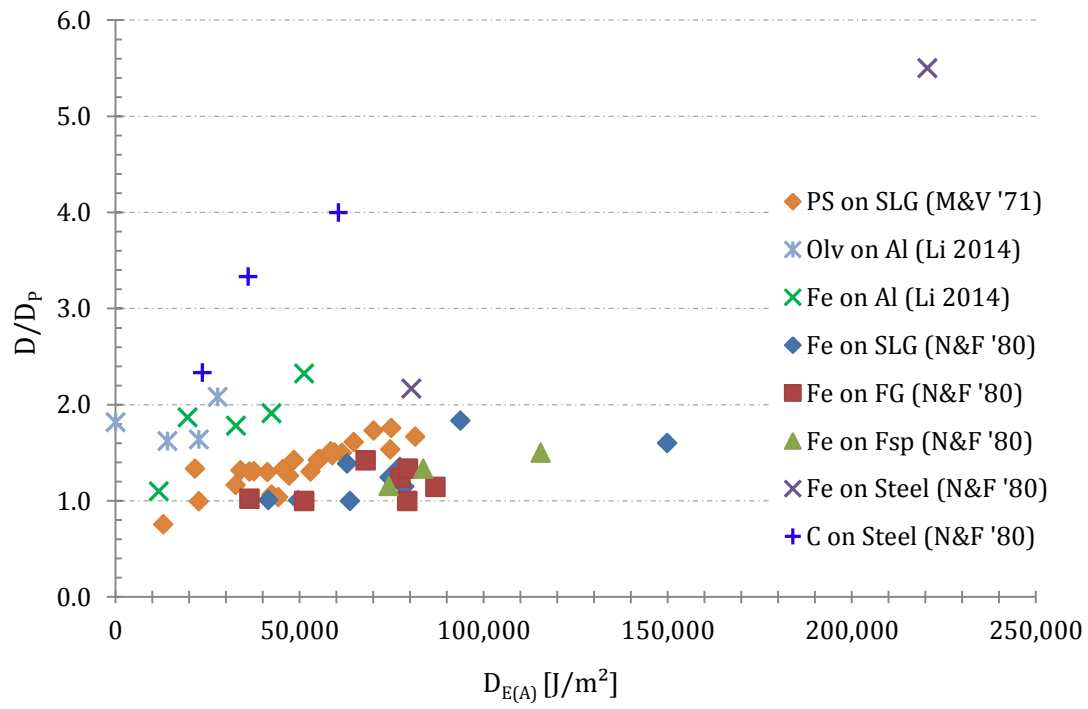


Figure 5.08: Diagram of crater diameter/projectile diameter to energy density $D_{E(A)}$ [J/m^2]. Data are from studies of MANDEVILLE & VEDDERS (1971), NAGEL & FECHTIG (1980) and LI (2014).

Preliminary findings on a diopside target

Preliminary SEM-SE investigations of the test target Diopside_1, bombarded with a mixture of irregular and spherical Cu projectiles, with low flux rates (9 particles/sec; total = 4045), $v = \sim 1 - 49$ km/s and $D_p = \sim 0.05 - 4.2$ μm yielded the identification of very few craters (Fig. 5.09). An overview of projectile bins is illustrated in Table 5.02a and b.

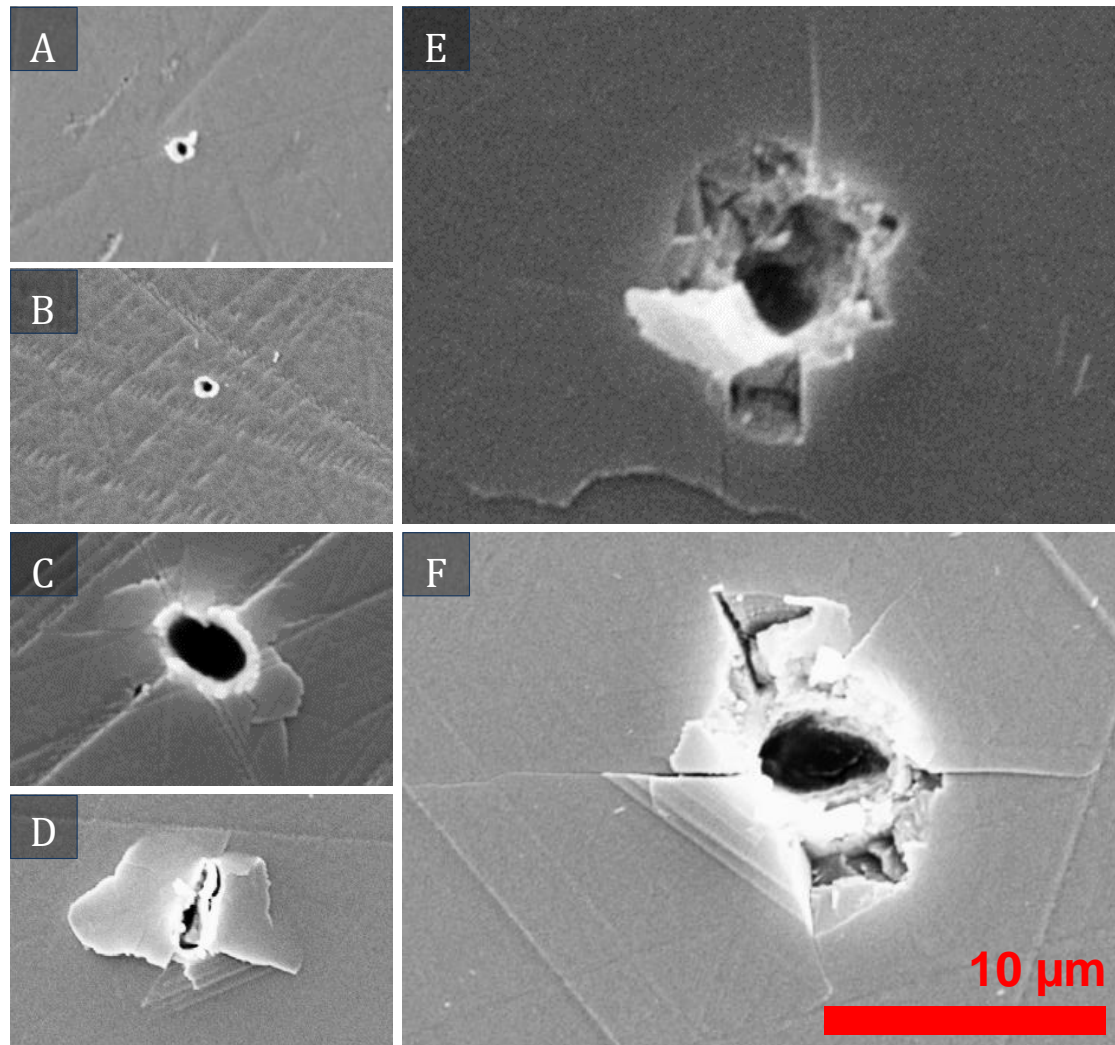


Figure 5.09: Image of SEM-SE images of mixed shaped Cu projectiles, impacting on the test target Diopside_1 ($v = \sim 1 - 49$ km/s, $D_p = \sim 0.05 - 4.15$ μm). The scale applies to all images. Craters on [A] and [B] have crater diameters < 1 μm . At crater diameters beyond 2 μm fracturing and spallation occurs: [C] and [D]. On larger craters [E] and [F] fracturing is much wider and spallation zones tend to be ejected.

On the Diopside_1 SEM-SE images it is noticeable, that the crater bottom is barely visible or completely invisible. Acquiring depth values with the SEM seems problematic for cra-

ters below 5 μm . It is considered that LHV projectiles caused elliptical or irregular shaped craters with fractures and large spallation zones on Diopside_1 (Fig. 5.09: D, E, and F). Craters without spallation or fractures (Fig. 5.09 A & B), with more circular diameters show crater lips and are suggested to be results of faster HV impacts. A transition between those two extremes likely shows less spallation and the beginning of lip formation in circular crater diameters (e.g. Fig. 5.09: C). On the olivine target, almost no craters with complete crater lips were found. In general, crater lips were largely absent, which is likely due to insufficient kinetic energy as compared to the target strength. However, crater lips were easily identified with SEM-SE investigation and are difficult to determine with the LSM. This particular issue will be further investigated with SEM-SE, after the completion of other investigations (e.g. NIR, SIMS), which do not require gold coating.

Table 5.02: Overview of 4045 Cu projectiles (mixed charge; produced inhouse) shot on Diopside_1 target. Table (a) shows velocity bins with PSU limitation of 1–100 km/s (fastest particle: 46.9 km/s). Table (b) shows the particle diameter bins with no PSU limitation set (largest particle: 4.2 μm).

a				b			
v [km/s]	count	percentage		D [μm]	count	percentage	
< 1.0	0	0%		< 0.1	23	1%	
1 - 1.5	1684	42%		0.1 - 0.25	593	15%	
1.5 - 2	471	12%		0.25 - 0.5	977	24%	
2 - 3	409	10%		0.5 - 1	2304	57%	
3 - 4	299	7%		1 - 2	138	3%	
4 - 6	439	11%		2 - 4	8	0%	
6 - 10	427	11%		4 - 5	2	0%	
10 - 20	259	6%		>5	0	0%	
> 20	57	1%					

Only 1434 particles (35 %) of all Cu projectiles that impacted Diopside_1 had $D_{\text{Energy}} > 13,000 \text{ [J/m}^2\text{]}$. This would mean ten times less possible craters compared to Olivine_6.

Noteworthy is that the transformation of energy during impact is an important aspect of crater formation. An impact study on graphite/epoxy (IM7/977-3) at different temperatures showed that the crater diameter increased with the temperature of the target. At lower temperatures, hole sizes were comparable to room temperature, but impact morphologies were more complex (SMITH *et al.*, 2010).

Reconsidering aspects of impact dynamics

It can be stated that impact processes on a natural mineral target are different from those on metal or other synthetically produced targets. At low velocities, or kinetic energy, impact features different from classical craters may occur. These LHV are barely investigated or understood. The cratering on terrestrial diopside and olivine shows morphological similarities to FQ or SLG, even though the olivine has mechanical properties more comparable to steel.

Since diameters and velocities of Olivin_6 projectiles varied widely, and as LSM imaging allowed detection for very small and shallow features compared to SEM, a large variety of impact features could be identified and described in more detail than in previous studies. As this large variety of features may appear somewhat confusing, Fig. 5.10 shows a sequence of impact features or types according to increasing energy density and the associated change of D/d ratios for dents and craters.

As shown in Fig. 5.10, low impact velocities of Cu projectiles just left very shallow – and frequently quite small - dents without projectile residues on the surface. At larger impact energies, particles could stick to the surface (type A features) which are already significantly compressed and flattened. A further increase of energy density results in crater formation, either as simple craters or including fracturing, spallation and displaced fragments, with decreasing amounts of measurable projectile residues. The extremely flattened B type projectile residue maybe classified somewhere in between A and C type.

The experimental conditions in this study covered a wide range of impact velocities which is also typical for the solar system environment, since bodies and particles in space move relative to each other causing collisions with greatly varying impactor velocities. For cometary gas-dust jets DROBYSHEVSKI (2008) suggests ~ 1 km/s. For ISP with masses about $10^{-6.5}$ g velocities of 25–50 km/s were reported (Frisch, 2000). Nano-scale particles driven by solar wind can even reach velocities of ~ 300 Km/s (PRICE *et al.*, 2012). In general, LHUV particles are generally rather accreted, while faster particles would pulverize the surface with an impact area of $\sim 3 \cdot D_p$, including the fractionation and spallation zone. At even faster HV straight penetration with formation of crater lips and no spallation can occur. These features can be expected from experiments with impact angles close to $\theta = 90^\circ$.

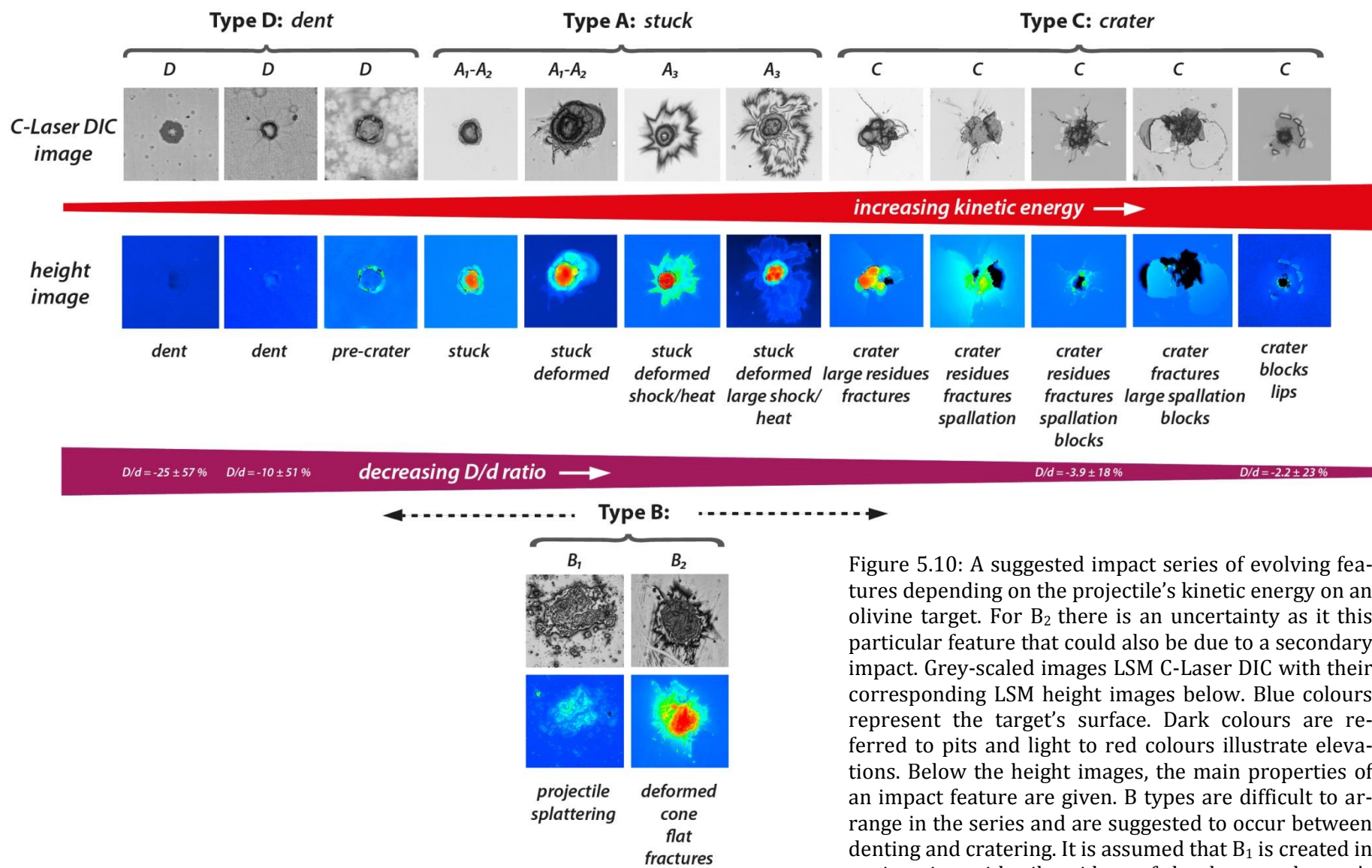


Figure 5.10: A suggested impact series of evolving features depending on the projectile's kinetic energy on an olivine target. For B_2 there is an uncertainty as it is this particular feature that could also be due to a secondary impact. Grey-scaled images LSM C-Laser DIC with their corresponding LSM height images below. Blue colours represent the target's surface. Dark colours are referred to pits and light to red colours illustrate elevations. Below the height images, the main properties of an impact feature are given. B types are difficult to arrange in the series and are suggested to occur between denting and cratering. It is assumed that B_1 is created in conjunction with oil residues of the dust accelerator's vacuum pump. B_2 was rare and could also be a secondary impact feature besides LHV.

4-Profile-Method

To ensure reliable determination of feature shapes, diameters and depths or elevations, 4 profile measurements were applied routinely. Except for the measurement of craters, errors in all measured diameters can be reduced by measuring four diameters instead of only two (Tab 5.03). However, for crater diameters, the difference of 0.1 % is marginal. In general, it can be said that a mean value, using four separate profiles on one feature, yields a slightly more precise mean diameter as compared to the two-profile method. The case is different, however, when comparing depth and height values. Except for very flat features (B type), or very large features (P₁ type), all mean errors show an increase with the application of the 4-profile method. The total mean error for diameters can be improved from 18.2 % to 17.1% of all investigated features. On the other hand the total depth or height mean error for all investigated features increased from 15.3 % to 16.6 %. Two possible arguments can be made regarding this issue: Firstly, height measurements with LSM are less accurate than measurements with lateral resolution (see chapter 2.4.2 *Principles of confocal laser microscopy*). Secondly, a combination of reflectance, along with effects of the aforementioned problem, can result in pixels or pixel areas with signal intensity of zero, which can distort surface interpretation. Still, likely the most important aspect are e.g. asymmetric profiles on craters described in section 2.4.3 *Measuring procedure with a Keyence confocal laser microscope* (Fig. 2.36). The lowest measureable pit had D/d ratio of -0.40 ± 24 %. Finally, the only modest changes of the error achieved by 4 profiles may simply reflect the circumstance that the analysed features are not perfectly symmetrical, but irregular to a certain degree.

However, for very large features (incl. 5 C types, 2 A₂ types and 1 A₃ type) with diameters over 5 μm, the mean error for diameter of 15.3% showed a decrease towards 4.98%, and the mean error for depth or height decreased from 16.6% to 8.15% (values not shown here). Hence, it can be concluded that, for features above a certain size (~5 μm), the 4-profile-method improves the quality of diameter acquisition and also those of depth or height- measurements.

Table 5.03: Comparison of the errors of the mean values derived from two profile and four profile measurements. Green highlighted cells illustrate the improvement for errors; red cells show an increase of the error.

Typ	mean	mean	min.	max.	mean	mean	min. depth	min. depth	counts
	2-diameter error	4-diameter error	diameter value [μm]	diameter value [μm]	2-depth/height error	4-depth/height error	or height value [μm]	or height value [μm]	
A	11.8%	10.9%	0.43	37.65	9.4%	10.4%	0.07	10.94	204
B	9.7%	6.6%	3.67	18.88	6.1%	5.2%	0.18	0.59	16
C	15.1%	15.2%	0.19	9.74	16.7%	16.9%	-0.02	-2.34	98
D	14.3%	13.6%	0.37	4.57	23.3%	26.9%	-0.003	-0.18	73
E	29.8%	29.0%	0.36	5.83	16.7%	17.5%	0.03	0.50	17
N ₁	56.0%	49.9%	0.08	18.36	12.6%	22.6%	-0.02	-4.28	9
N ₂	24.4%	23.4%	0.06	2.88	22.2%	24.0%	-0.01	-0.73	161
P ₁	19.9%	16.2%	1.68	36.46	24.4%	19.8%	0.08	6.10	3
P ₂	19.1%	17.4%	0.07	3.38	12.8%	13.9%	0.02	2.70	290

Additional possibilities with laser scanning microscopy

Laser-scanning microscopy (LSM) is powerful method for the quick and accurate analysis of samples from micrometeorite impact experiments, yielding a large variety and number of excellently useful data. The measurement of diameters is very accurate and the accuracy of depth measurements is statistically improved with respect to SEM. Furthermore, LSM has the potential of conducting automated surface evaluation, which would be an enormous improvement regarding data production and statistical analysis. First attempts to convert raw data from LSM into CSV-files and using those with a scripting language (R-script) are promising. It was possible to create dynamic 3D plots from the height data of the LSM (Fig 5.11 and 5.12). Much more work needs to be done for auto-processing surface data, and even more so with respect to impact features.

Further promising aspects in auto-processing are the collection of large amounts of data and the application of machine learning, e.g., the automated identification of different impact structures. For this, available standard modelling languages (e.g. MathLab, Python, IDL) beside R-Script should be appropriate. The calculation of crater volumes or material transformation would also be a topic of interest, which will greatly benefit using automated LSM evaluation. The source code developed for 3D illustration is explained in *appendix B*.

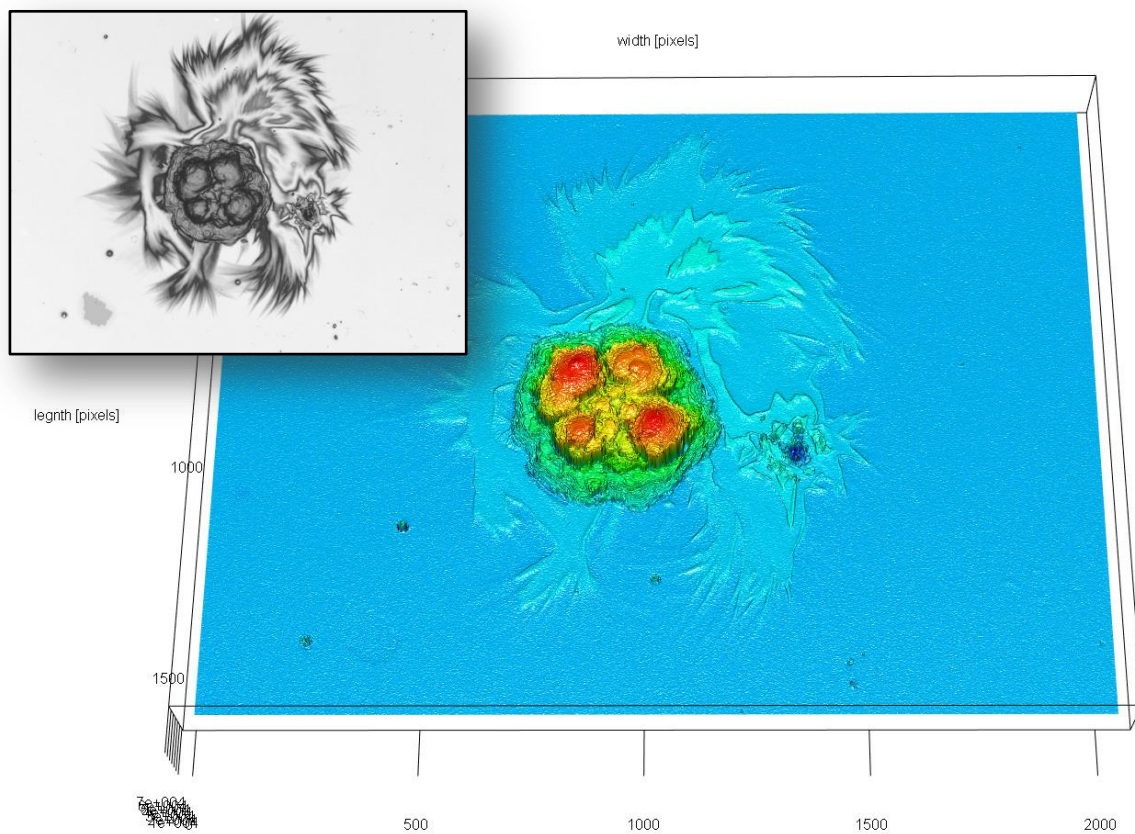


Figure 5.11: 3D plot of height data acquired with the Keyence LSM and laser intensity image on the upper right. The image is slightly tilted and was generated with R-script. The target surface is displayed in blue, with a large stuck-on particle (A_3 type) in the center, showing a shining halo effect and a secondary crater on the left.

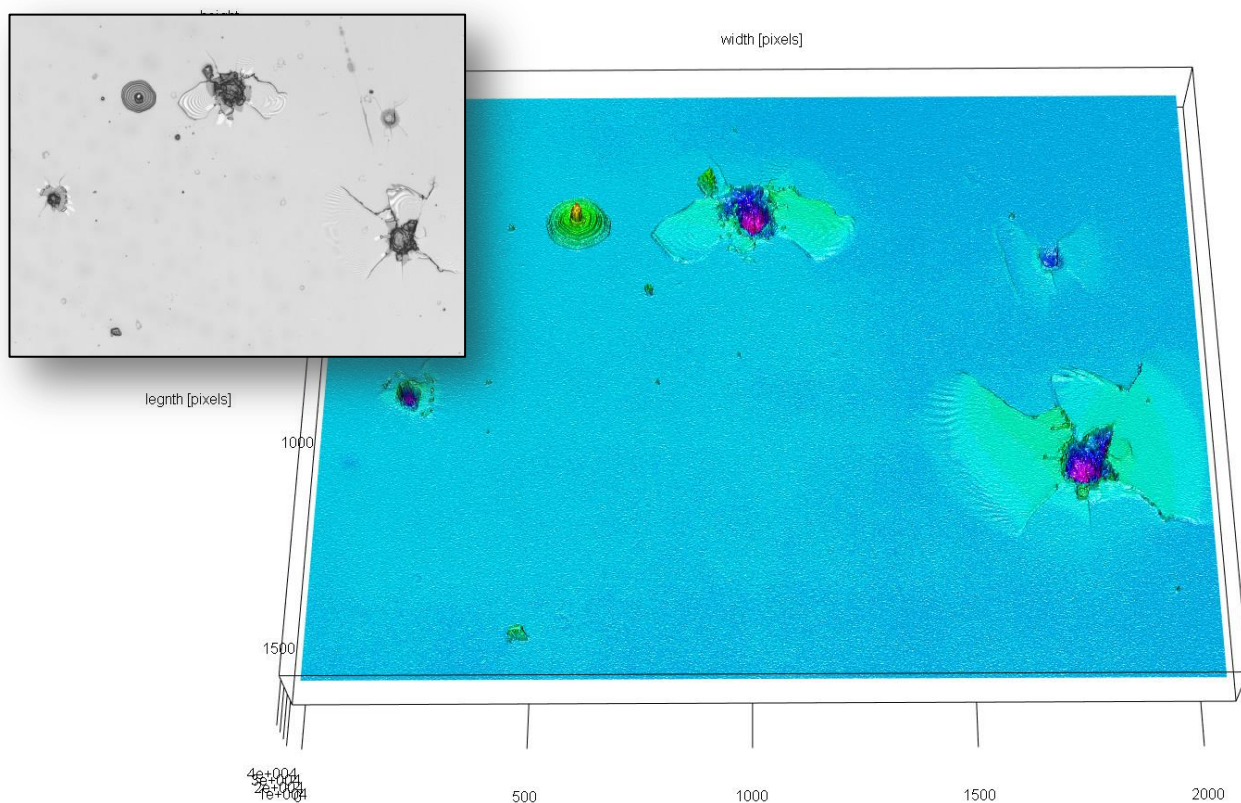


Figure 5.12: 3D plot of height data acquired with the Keyence LSM and laser intensity image on the upper right. The image is slightly tilted and was generated with R-script. The target surface is displayed in light blue showing two larger craters (C type) with fractures, spallation and fragments and two smaller craters with fractures and fragments and a stuck particle (A₁ type).

6 Conclusions

Materials with olivine-like composition are considered to be one of the major building-blocks in our Solar System. High abundances are e.g., found in chondrites, on asteroids and to lesser extent in the lunar regolith. The evolution of olivine on surfaces of atmosphereless bodies in the Solar System can aid the understanding of surface maturing caused by impacts. Micrometeorite impacts are one of the most important aspects in the processes of surface maturation, together with other effects of space weathering like high energy particle irradiation. This study investigated HV impacts on mineral targets with a high resolution confocal laser microscope (LSM) examination of a bombarded and a non-bombarded olivine target. HV impacts on mineral targets with Cu projectiles utilizing LSM technique for analysis are novel to this field of science.

With a modified Van de Graaff accelerator, $\sim 92\%$ spherical Cu projectile ($\sim 99.7\%$: $D_P = 0.01\text{--}4.9\ \mu\text{m}$ and $v = 0.45\text{--}13\ \text{km/s}$) were shot onto homogeneously polished thick sectioned olivine (F_{0.7}). It has been shown that there are not only craters or indentations (negative impact features) as a result of HV impacts, but also stuck or splattered projectiles (positive impact features). In this experiment $\sim 930,000$ spherical Cu projectiles were shot on this particular target and over 50% of all analysed impact features were positive.

As shown in many studies and experiments before, the density of a projectile and its velocity, i.e., the kinetic energy, play a major role in crater formation. Other studies showed that at LHV (e.g. $<2.5\ \text{km/s}$) variations of impact features strongly differ, causing dents and precursor cratering, depending also on the target material and not on projectile properties alone. About 80% of all projectiles impacting on olivine had velocities $<2.0\ \text{km/s}$. This turned out to be the velocity regime for additional positive features, such as stuck or splattered projectiles, besides the observed dents or precursor craters. The appearance of craters in olivine is mainly accompanied by wide radial fractures, spallation, displaced fragments and the lack of crater lips. Similar crater morphologies were found during SEM-SE investigations of a diopside target bombarded with Cu projectiles ($v = \sim 1\text{--}49\ \text{km/s}$ and $D_P = \sim 0.05\text{--}4.2\ \mu\text{m}$). On diopside, also crater lips have been observed at submicron sized craters. It is assumed that fractionation and spallation decrease, when at the same time crater lip occurrences increase. In addition to that,

crater lips seem to appear more likely on smaller craters. Similar effects were observed on lunar microcraters before (HARTUNG *et al.*, 1972). Hence, it is assumed that the development of craters showing crater lips is likely determined by either the mineral's properties (e.g. crystallography, cleavage preference), or nanometer-scaled and fast HV projectiles. It is possible that LSM is not capable of visualizing such morphological aspects properly.

Nevertheless the importance of detailed examination of the targets physical properties in order to get reliable comparisons to other similar studies has been shown. Using mineral targets for impact studies is not common, only few early experiments using lunar regolith or feldspar minerals were conducted. The majority of micro impact studies use metals and alloys (e.g. copper, aluminium, gold, stainless steel, etc.) or ceramics, glass-ceramics and polymers (e.g. fused quartz, soda-lime glass, polystyrene etc.) as a target material. These materials have very different optical, chemical, mineralogical, mechanical and further thermodynamical properties and cannot be reduced to their density or material strength alone. It is very difficult to predict the response of mineral targets by using analogy of metals or ceramics. An important open task for future studies is to determine, what target material properties most strongly influence impact morphology.

Considering crater morphologies showing mostly spallation and torn crater edges, mineral surfaces (e.g. Fo_{90.7}-olivine, diopside) tend to be evaporised at HV. At LHV, assuming velocities <3 km/s, accretion or rebounding of particles occur. Faster HV rather cause penetration with deep craters and lip - formation. With respect to space weathering, surfaces of planetesimals, or other atmosphereless solar system objects, the ubiquitous dust flux does not necessarily cause the removal of surface material, but likely leads to the accumulation of material from LHV particles. Such a deposition effect, for particles with masse in 10⁻⁶ to 10⁻² g range, was stated before (HARTUNG *et al.*, 1972).

In this study, in conjunction with preliminary investigations of other mineral targets, almost 1500 features have been investigated and over 6000 profiles were captured with the LSM technique. It was shown that LSM (lateral error: ±21 nm; vertical error: ±36 nm) for crater analysis, or impact studies in general, is a powerful method to study by imaging structures down to ~ 1 µm and is even more excellent for features above 2 µm. This method can compete with SEM stereographic analysis. However, limits using an instrument such as the Keyence VK-X210 due to its static optics are

apparent. It appears to be difficult to see below crater lips, if a crater is shaped bulbous or beneath an object's shadow, e.g., a spherical projectile.

Primary aspects of confocal laser scanning microscope investigations are:

- Non-destructive
- No prior coating needed
- 3D presentation and high image resolution close to conventional SEM
- Out-of-the-box solutions for impact feature measurements and comparison
- LSM height images give a better impression of crater topography than conventional SEM-SE images
- The minimum accessed D/d ratio (incl. maximal error for D and d) was -0.52 (real value $-0.40 \pm 24\%$) and every discerned crater was measurable
- Combinations of LSM laser and height images can partially visualise shock effects in semi-transparent mineral targets. Although this aspect needs to be confirmed further, it shows to be a great advantage as compared to electron microscopy
- The identification of impact features smaller than $1\ \mu\text{m}$ is difficult. Similar issues also occur with SEM.

Outlook

Most important is an even deeper investigation of the studied olivine targets. Further, secondary ion mass spectrometry (SIMS) measurements can probably determine whether any oxygen fractionation effects have occurred at large craters. First results of variations in oxygen were reported in crater residues of Stardust impacts (SNEAD & MCKEEGAN, 2015; SNEAD *et al.*, 2015). Preliminary findings with near infrared (NIR) of the second sample suit (FIEGE *et al.*, 2017 in prep) showed slight effects of bombardment. In the very end, after all non-destructive methods have been applied, the bombarded olivine target can be coated with gold and SEM-SE investigation can be conducted, which allows for a direct comparison of LSM measurement quality as compared to SEM. Seven other bombarded mineral targets are still on hold and need to undergo the same examinations as the olivine targets in this work. These targets were bombarded with different projectile velocity ranges, and could help to set better impact constraints of Cu projectiles on mineral target, and will most likely allow a refinement of the results obtained for Olivine. Another aim is the investigation of mineral targets mechanical properties in or-

der to examine their additional aspects of the impact process. It will be interesting to evaluate, whether micrometeorite bombardment can cause the shock induced growth of wadsleyite, a transformation of olivine. TSCHAUNER *et al.* (2009) stated that it is not necessary to have long durations of shock phases to cause μm -length crystals to grow within an impact region. It has been shown that LSM can contribute new and additional information of impact features to the already established instrumentation in this field.

Bibliography

- ALTOBELLI, N., POSTBERG, F., FIEGE, K., TRIELOFF, M., KIMURA, H., STERKEN, V. J., HSU, H.-W., HILLIER, J., KHAWAJA, N., MORAGAS-KLOSTERMEYER, G., BLUM, J., BURTON, M., SRAMA, R., KEMPF, S., GRÜN, E. (2016). Flux and composition of interstellar dust at Saturn from Cassini's Cosmic Dust Analyzer. *Science (New York, N.Y.)*, 352(6283), 312–8. <http://doi.org/10.1126/science.aac6397>
- APAI, D., & LAURETTA, D. S. (2010). *Protoplanetary Dust - Astrophysical and Cosmochemical Perspectives* (Cambridge). Cambridge University Press.
- ASAY, J. R., & SHAHINPOOR, M. (1993). *High-Pressure Shock Compression of Solids*. (J. R. Asay & M. Shahinpoor, Eds.). New York, NY: Springer New York. <http://doi.org/10.1007/978-1-4612-0911-9>
- BENNETT, C. J., PIRIM, C., & ORLANDO, T. M. (2013). Space-weathering of solar system bodies: A laboratory perspective. *Chemical Reviews*, 113(12), 9086–9150. <http://doi.org/10.1021/cr400153k>
- BLOCH, M. R.; FECHTIG, H.; GENTNER, W.; NEUKUM, G.; SCHNEIDER, E. (1971). Meteorite impact craters, crater simulations, and the meteoroid flux in the early solar system. *Proceedings of the Lunar Science Conference*, 3, 2639–2652. Retrieved from
- BOGARD, D. D. (2011). K-Ar ages of meteorites: Clues to parent-body thermal histories. *Chemie Der Erde - Geochemistry*, 71(3), 207–226. <http://doi.org/10.1016/j.chemer.2011.03.001>
- BRANDMAIER, C., SPRING, K. R., & DAVIDSON, M. W. (2016). Reflected Light DIC Microscop. Retrieved January 1, 2017, from <https://www.microscopyu.com/techniques/dic/reflected-light-dic-microscopy>
- BRASLAU, D. (1970). Partitioning of energy in hypervelocity impact against loose sand targets. *Journal of Geophysical Research*, 75(20), 3987–3999. <http://doi.org/10.1029/JB075i020p03987>
- BROWNLIE, D. E., HÖRZ, F., VEDDER, J. F., GAULT, D. E., & HARTUNG, J. B. (1973). Some physical parameters of micrometeoroids. *Proceedings of the Lunar Science Conference*, 4th, 3197–3212. Retrieved from <http://adsabs.harvard.edu/full/1973LPSC....4.3197B>

- BURCHELL, M. J., COLE, M. J., McDONNELL, J. A. M., & ZARNECKI, J. C. (1999). Hypervelocity impact studies using the 2 MV Van de Graaff accelerator and two-stage light gas gun of the University of Kent at Canterbury. *Measurement Science and Technology*, 10, 41–50. <http://doi.org/10.1088/0957-0233/10/1/011>
- CHAPMAN, C. R. (2004). Space Weathering of Asteroid Surfaces. *Annual Review of Earth and Planetary Sciences*, 32(1), 539–567.
<http://doi.org/10.1146/annurev.earth.32.101802.120453>
- CHRISTOFFERSEN, R., & BUSECK, P. R. (1986). Mineralogy of interplanetary dust particles from the “olivine” infrared class. *Earth and Planetary Science Letters*, 78(1), 53–66. [http://doi.org/10.1016/0012-821X\(86\)90172-X](http://doi.org/10.1016/0012-821X(86)90172-X)
- CLARK, B. E., HAPKE, B., PIETERS, C., & BRITT, D. (2002). Asteroid Space Weathering and Regolith Evolution. In W. F. BOTTKE, A. CELLINO, P. PAOLICCHI, & R. P. BINZEL (Eds.), *Asteroids III* (pp. 585–599). Tucson: University of Arizona Press. [http://doi.org/10.1016/0273-1177\(91\)90551-T](http://doi.org/10.1016/0273-1177(91)90551-T)
- DEER, W. A., HOWIE, R. A., & ZUSSMAN, J. (1992). *An Introduction to the Rock-Forming Minerals* (2nd ed.). Pennsylvania State University: Longman Scientific & Technical. Retrieved from <http://geoscienceworld.org/content/an-introduction-to-the-rock-forming-minerals>
- DRAINE, B. ~T. T. (2003). Interstellar Dust Grains. *Araa*, 41, 46. <http://doi.org/10.1146/annurev.astro.41.011802.094840>
- DROBYSHEVSKI, E. (2008). Stardust findings favor not only the planetary origin of comets but the underlying close-binary cosmogony of the Solar System as well. *Icarus*, 197(1), 203–210. <http://doi.org/10.1016/j.icarus.2008.03.025>
- FIEGE, K., BENNETT, C. J., GUGLIELMINO, M., ALTOBELLI, N., TRIELOFF, M., & SRAMA, R. (2017). *Space weathering induced via micrometeorite impacts onto meteorite targets*. (in prep).
- FLORES-GUTIÉRREZ, D., URRUTIA-FUCUGAUCHI, J., PÉREZ-CRUZ, L., DÍAZ-HERNÁNDEZ, R., & LINARES-LÓPEZ, C. (2010). Scanning electron microscopy characterization of iron, nickel and sulfur in chondrules from the Allende meteorite - further evidence for between-chondrules major compositional differences. *Revista Mexicana de Ciencias Geológicas*, 27(2), 338–346.

-
- FREEDMAN, D., & DIACONIS, P. (1981). On the histogram as a density estimator: L² theory. *Zeitschrift Für Wahrscheinlichkeitstheorie Und Verwandte Gebiete*, 57(4), 453–476.
<http://doi.org/10.1007/BF01025868>
- FRICHTENICHT, J. F. (1962). Two-Million-Volt Electrostatic Accelerator for Hypervelocity Research. *Review of Scientific Instruments*, 33(2), 209–212.
<http://doi.org/10.1063/1.1746548>
- FRISCH, P. C. (2000). The galactic environment of the sun. *American Scientist*, 88(1), 52–59.
<http://doi.org/10.1511/2000.1.52>
- GOODING, J. L., & KEIL, K. (1981). Relative Abundances of Chondrule Primary Textural Types in Ordinary Chondrites and Their Bearing on Conditions of Chondrule Formation. *Meteoritics*, 16(1), 17–43.
<http://doi.org/10.1111/j.1945-5100.1981.tb00183.x>
- GRÜN, E., ZOOK, H. A., FECHTIG, H., & GIESE, R. H. (1985). Collisional balance of the meteoritic complex. *Icarus*, 62(2), 244–272.
[http://doi.org/10.1016/0019-1035\(85\)90121-6](http://doi.org/10.1016/0019-1035(85)90121-6)
- HAPKE, B. (2001). Space weathering from Mercury to the asteroid belt. *Geology*, 106, 39–73. <http://doi.org/doi:10.1029/2000JE001338>
- HARTMANN, W. K., PHILLIPS, R. J., & TAYLOR, G. J. (1986). *Origin of the Moon*. Lunar and Planetary Institute. Retrieved from <http://adsabs.harvard.edu/abs/1986ormo.conf.....H>
- HARTUNG, J. B., HÖRZ, F. ., & GAULT, D. E. (1972). Lunar microcraters and interplanetary dust. In *Proceedings of the Lunar Science Conference* (Vol. 3, pp. 2735–2753). Houston, TX: The M.I.T. Press. Retrieved from <https://ntrs.nasa.gov/search.jsp?R=19730035064>
- HEIKEN, G. H., VANIMAN, D. T., & FRENCH, B. M. (1991). *Lunar Sourcebook - A User's Guide to the Moon*. Lunar and Planetary Institute.

- HILLIER, J. K., SESTAK, S., GREEN, S. F., POSTBERG, F., SRAMA, R., & TRIELOFF, M. (2009). The production of platinum-coated silicate nanoparticle aggregates for use in hypervelocity impact experiments. *Planetary and Space Science*, 57(14–15), 2081–2086. <http://doi.org/10.1016/j.pss.2009.09.019>
- HOPPE, P. (2009). 4.3.3 Meteorites. In J. E. Trümper (Ed.), *Landolt-Börnstein - Group VI Astronomy and Astrophysics* (pp. 582–602). Springer Verlag. http://doi.org/10.1007/978-3-540-88055-4_30
- HÖRZ, F., BROWNLEE, D. E., FECHTIG, H., HARTUNG, J. B., MORRISON, D. A., NEUKUM, G., SCHEIDER, E., VEDDER, J. G., GAULT, D. E. (1975). Lunar microcraters: Implications for the micrometeoroid complex. *Planetary and Space Science*, 23(1), 151–172. [http://doi.org/10.1016/0032-0633\(75\)90076-8](http://doi.org/10.1016/0032-0633(75)90076-8)
- HSU, H.-W., POSTBERG, F., KEMPF, S., TRIELOFF, M., BURTON, M., ROY, M., MORAGAS-KLOSTERMEYER, G., SRAMA, R. (2011). Stream particles as the probe of the dust-plasma-magnetosphere interaction at Saturn. *Journal of Geophysical Research: Space Physics*, 116(9), 1–23. <http://doi.org/10.1029/2011JA016488>
- KEARSLEY, A. T., GRAHAM, G. A., BURCHELL, M. J., COLE, M. J., DAI, Z. R., TESLICH, N., BRADLEY, J. P., CHATER, R., WOZNIAKIEWICZ, P. A., SPRATT, J., JONES, G. (2007). Analytical scanning and transmission electron microscopy of laboratory impacts on Stardust aluminum foils: Interpreting impact crater morphology and the composition of impact residues. *Meteoritics & Planetary Science*, 42(2), 191–210. <http://doi.org/10.1111/j.1945-5100.2007.tb00227.x>
- KEARSLEY, A. T., GRAHAM, G. A., BURCHELL, M. J., COLE, M. J., WOZNIAKIEWICZ, P. J., TESLICH, N., BRINGA, E., HÖRZ, F., BLUM, J., POPPE, T. (2008). Micro-craters in aluminum foils: Implications for dust particles from comet Wild 2 on NASA's Stardust spacecraft. *International Journal of Impact Engineering*, 35(12), 1616–1624. <http://doi.org/10.1016/j.ijimpeng.2008.07.006>
- KEARSLEY, A. T., BURCHELL, M. J., PRICE, M. C., GRAHAM, G. A., WOZNIAKIEWICZ, P. J., COLE, M. J., FOSTER, N. J., TESLICH, N. (2009). Interpretation of Wild 2 dust fine structure: Comparison of Stardust aluminum foil craters to the three-dimensional shape of experimental impacts by artificial aggregate particles and meteorite powders. *Meteoritics and Planetary Science*, 44(10), 1489–1509. <http://doi.org/10.1111/j.1945-5100.2009.tb01188.x>

-
- KEMPF, S., BECKMANN, U., & SCHMIDT, J. (2010). How the Enceladus dust plume feeds Saturn's E ring. *Icarus*, 206(2), 446–457.
<http://doi.org/10.1016/j.icarus.2009.09.016>
- Keyence. (2011). Keyence VK-X200K/X210 User' s Manual. Keyence Corporation.
- KIMURA, H., MANN, I., & JESSBERGER, E. ~K. (2003). Composition, Structure, and Size Distribution of Dust in the Local Interstellar Cloud. *ApJ*, 583(Leroy 1993), 314–321.
<http://doi.org/10.1086/345102>
- KOBUSCH, M., SARGE, S., BUNTE, K. D., FICHNA, T., HAGEDORN, D., JÄGER, F., & MEEß, R. (2009). Microcalorimeter array for the measurement of kinetic energies of small particles in space. *Thermochimica Acta*, 492(1–2), 89–94.
<http://doi.org/10.1016/j.tca.2009.03.008>
- LE SERGEANT D'HENDECOURT, L. B., & LAMY, P. L. (1980). On the size distribution and physical properties of interplanetary dust grains. *Icarus*, 43(3), 350–372.
[http://doi.org/10.1016/0019-1035\(80\)90180-3](http://doi.org/10.1016/0019-1035(80)90180-3)
- LEXOW, B., WICKERT, M., THOMA, K., SCHÄFER, F., POELCHAU, M. H., & KENKMANN, T. (2013). The extra-large light-gas gun of the Fraunhofer EMI: Applications for impact cratering research. *Meteoritics and Planetary Science*, 48(1), 3–7.
<http://doi.org/10.1111/j.1945-5100.2012.01427.x>
- LI, Y. W., BUGIEL, S., TRIELOFF, M., HILLIER, J. K., POSTBERG, F., PRICE, M. C., SHU, A., FIEGE, K., FIELDING, L. A., ARMES, S. P., WU, Y. Y., GRÜN, E., SRAMA, R. (2014). Morphology of craters generated by hypervelocity impacts of micron-sized polypyrrole-coated olivine particles. *Meteoritics & Planetary Science*, 49(8), 1375–1387.
<http://doi.org/10.1111/maps.12338>
- LI, Y. (2015). *Dissertation: Instrument study of the Lunar Dust eXplorer (LDX) for a lunar lander mission. Advances in Space Research*. Universität Stuttgart. Retrieved from <http://elib.uni-stuttgart.de/handle/11682/8830>
- MANDEVILLE, J. C., & VEDDER, J. F. (1971). Microcraters formed in glass by low density projectiles. *Earth and Planetary Science Letters*, 11(1–5), 297–306.
[http://doi.org/10.1016/0012-821X\(71\)90183-X](http://doi.org/10.1016/0012-821X(71)90183-X)

- MANDEVILLE, J.-C. (1977). Impact microcraters on 12054 rock. *Proceedings of the Lunar Science Conference, 8th, 1*, 883–888. Retrieved from <http://articles.adsabs.harvard.edu/full/1977LPSC....8..883M>
- MARKL, G. (2015). *Minerale und Gesteine*. <http://doi.org/10.1007/978-3-662-44628-7>
- McSWEEN, H. Y. (1977). Carbonaceous chondrites of the Ornans type: A metamorphic sequence. *Geochimica et Cosmochimica Acta*, 41(4), 477–491. [http://doi.org/10.1016/0016-7037\(77\)90286-1](http://doi.org/10.1016/0016-7037(77)90286-1)
- MERZHEVSKY, L. A. (1997). Crater formation in a plastic target under hypervelocity impact. *International Journal of Impact Engineering*, 20(6–10), 557–568. [http://doi.org/10.1016/S0734-743X\(97\)87444-1](http://doi.org/10.1016/S0734-743X(97)87444-1)
- MISAWA, K., YAMAGUCHI, A., & KAIKEN, H. (2005). U-Pb and ²⁰⁷Pb-²⁰⁶Pb ages of zircons from basaltic eucrites: Implications for early basaltic volcanism on the eucrite parent body. *Geochimica et Cosmochimica Acta*, 69(24), 5847–5861. <http://doi.org/10.1016/j.gca.2005.08.009>
- MOCKER, A., BUGIEL, S., AUER, S., BAUST, G., COLETTE, A., DRAKE, K., FIEGE, K., GRÜN, E., HECKMANN, F., HELFER, S., HILLIER, J., KEMPF, S., MATT, G., MELLERT, T., MUNSAT, T., OTTO, K., POSTBERG, F., RÖSER, H-P., SHU, A., STERNOVSKY, Z., SRAMA, R. (2011). A 2 MV Van de Graaff accelerator as a tool for planetary and impact physics research. *Review of Scientific Instruments*, 82(9), 1–8. <http://doi.org/10.1063/1.3637461>
- MOCKER, A. (2015). *Dissertation: Comparison of impact ionisation plasma with laser ionisation*. Ruprecht-Karl Universität Heidelberg, Deutschland.
- NAGEL, K.; NEUKUM, G.; EICHHORN, G.; FECHTIG, H.; MUELLER, O.; SCHNEIDER, E. (1975). Dependencies of microcrater formation on impact parameters. *Proceedings of the Lunar Science Conference, 6th, 3*, 3417–3432. Retrieved from <http://adsabs.harvard.edu/full/1975LPSC....6.3417NNAGEL>, K., NEUKUM, G., FECHTIG, H., & GENTNER, W. (1976a). Density and composition of interplanetary dust particles. *Earth and Planetary Science Letters*, 30(2), 234–240. [http://doi.org/10.1016/0012-821X\(76\)90250-8](http://doi.org/10.1016/0012-821X(76)90250-8)

-
- NAGEL, K., NEUKUM, G., DOHNANYI, J. S., FECHTIG, H., & GENTNER, W. (1976b). Density and chemistry of interplanetary dust particles, derived from measurements of lunar microcraters. *Proceedings of the Lunar Science Conference 7th, 1*, 1021–1029. Retrieved from <http://articles.adsabs.harvard.edu/full/1976LPSC....7.1021N>
- NAGEL, K., & FECHTIG, H. (1980). Diameter to depth dependence of impact craters. *Planetary and Space Science*, 28(6), 567–573.
- NEUKIRCHEN, F., & RIES, G. (2016). *Die Welt der Rohstoffe* (2nd ed.). Berlin, Heidelberg: Springer Berlin Heidelberg. <http://doi.org/10.1007/978-3-642-37739-6>
- NEUKUM, G., MEHL, A., FECHTIG, H., & ZÄHRINGER, J. (1970). Impact phenomena of micrometeorites on lunar surface material. *Earth and Planetary Science Letters*, 8(1), 31–35. [http://doi.org/10.1016/0012-821X\(70\)90095-6](http://doi.org/10.1016/0012-821X(70)90095-6)
- NEUKUM, G., SCHNEIDER, E., MEHL, A., STORZER, D., WAGNER, G. A., FECHTIG, H., & BLOCH, M. R. (1972). Lunar Craters and Exposure Ages Derived From Crater Statistics and Solar Flare Tracks. *Proceedings of the Lunar Science Conference*, 3(January 1972), 2793–2810. Retrieved from http://articles.adsabs.harvard.edu/cgi-bin/nph-article_query?1972LPSC....3.2793N&data_type=PDF_HIGH&whole_paper=YES&type=PRINTER&filetype=.pdf
- NOGUCHI, T., KIMURA, M., HASHIMOTO, T., KONNO, M., NAKAMURA, T., ZOLENSKY, M. E., OKAZAKI, R., TANAKA, M., TSUCHIYAMA, A., NAKATO, A., OGAMI, T., ISHIDA, H., SAGAE, R., TSUJIMOTO, S., MATSUMOTO, T., MATSUNO, J., FUJIMURA, A., ABE, M., YADA, T., MUKAI, T., UENO, M., OKADA, T., SHIRAI, K., ISHIBASHI, Y. (2014). Space weathered rims found on the surfaces of the Itokawa dust particles. *Meteoritics and Planetary Science*, 49(2), 188–214. <http://doi.org/10.1111/maps.12111>
- NOGUCHI, T., NAKAMURA, T., KIMURA, M., ZOLENSKY, M. E., TANAKA, M., HASHIMOTO, T., KONNO, M., NAKATO, A., OGAMI, T., FUJIMURA, A., ABE, M., YADA, T., MUKAI, T., UENO, M., OKADA, T., SHIRAI, K., ISHIBASHI, Y., OKAZAKI, R. (2011). Incipient Space Weathering Observed on the Surface of Itokawa Dust Particles. *Science*, 333(6046), 1121–1125. <http://doi.org/10.1126/science.1207794>
- NORTON, O. R., & CHITWOOD, L. A. (2008). *Field Guide to Meteors and Meteorites*. London: Springer London. <http://doi.org/10.1007/978-1-84800-157-2>

- O'KEEFE, J. A. (1969). Origin of the Moon. *Journal of Geophysical Research*, 74(10), 2758–2767. <http://doi.org/10.1029/JB074i010p02758>
- OKRUSCH, M., & MATTHES, S. (2014). *Mineralogie - Eine Einführung in die spezielle Mineralogie, Petrologie und Lagerstättenkunde*. Journal of Chemical Information and Modeling. Berlin, Heidelberg: Springer Berlin Heidelberg. <http://doi.org/10.1007/978-3-642-34660-6>
- PRICE, M. C., KEARSLEY, A. T., BURCHELL, M. J., HOWARD, L. E., HILLIER, J. K., STARKEY, N. A., WOZNIAKIEWICZ, P. J., COLE, M. J. (2012). Stardust interstellar dust calibration: Hydrocode modeling of impacts on Al-1100 foil at velocities up to 300 km s⁻¹ and validation with experimental data. *Meteoritics & Planetary Science*, 47(4), 684–695. <http://doi.org/10.1111/j.1945-5100.2011.01300.x>
- RAI, V., & DEY, N. (2011). The Basics of Confocal Microscopy. *Laser Scanning, Theory and Applications*, 75–96. <http://doi.org/10.5772/16214>
- REED, S. J. B. (2005). *Electron Microprobe Analysis and Scanning Electron Microscopy in Geology* (2nd ed.). Cambridge University Press.
- RUBIN, A. E. (2005). Relationships among intrinsic properties of ordinary chondrites: Oxidation state, bulk chemistry, oxygen-isotopic composition, petrologic type, and chondrule size. *Geochimica et Cosmochimica Acta*, 69(20), 4907–4918. <http://doi.org/10.1016/j.gca.2005.06.017>
- RUDOLPH, V. (1969). Untersuchungen an Kratern von Mikroprojektilen im Geschwindigkeitsbereich von 0,5 bis 10 km/sec. *Zeitschrift Für Naturforschung A*, 24(3). <http://doi.org/10.1515/zna-1969-0304>
- RUSSO, R. E. (1995). Laser Ablation. *Applied Spectroscopy*, 49(9), 14A–28A. Retrieved from <https://www.osapublishing.org/as/abstract.cfm?uri=as-49-9-14A>
- SMITH, JR., J. G., JEGLEY, D. C., SIOCHI, E. J., & WELLS, B. K. (2010). Hypervelocity Impact Testing of IM7/977-3 with Micron-Sized Particles. *51st AIAA/ASME/ASCE/AHS/ASC Structures, Structural Dynamics, and Materials Conference*, (April), 1–27.
- SNEAD, C. J., & MCKEEGAN, K. D. (2015). New Oxygen Isotope Measurements of stardust impact crater residues show IDP-like compositions. In *78th Annual Meeting of the Meteoritical Society*. Retrieved from <http://www.hou.usra.edu/meetings/metsoc2015/pdf/5253.pdf>

-
- SNEAD, C. J., MCKEEGAN, K. D., BOEHNKE, P., & KEARSLEY, A. T. (2015). Further Oxygen Isotope Measurements for Two Cometary Impact Crater Residues: Still Like Chondrites. *46th Lunar and Planetary Science Conference*, (2621).
- SRAMA, R. (2009). *Cassini-Huygens and Beyond – Tools for Dust Astronomy*. Universität Stuttgart.
- SRAMA, R., AHRENS, T. J., ALTOBELLI, N., AUER, S., BRADLEY, J. G., BURTON, M., DIKAREV, V. V., ECONOMOU, T., FECHTIG, H., GÖRLICH, M., GRANDE, M., GRAPS, A., GRÜN, E., HAVNES, O., HELFERT, S., KEMPF, S., KRIVOV, A. V., KRÜGER, H., MOCKER-AHLREEP, A. MORAGAS-KLOSTERMEYER, G., LAMY, P., LANDGRAF, M., LINKERT, D., LINKERT, G., LURA, F., McDONELL, J. A. M., MÖHLMANN, D., MORFILL, G. E., MÜLLER, M., ROY, M., SCHÄFER, G., SCHLOTZHAUER, G., SCHWEHM, G. H., SPAHN, F., STÜBIG, M., SVESTKA, J., TSCHERNJAWSKI, V., TUZZOLINO, A. J., WÄSCH, R., ZOOK, H. A. (2004). The Cassini Cosmic Dust Analyzer. *Space Science Reviews*, 114(1–4), 465–518. <http://doi.org/10.1007/s11214-004-1435-z>
- SRAMA, R., STEPHAN, T., GRÜN, E., PAILER, N., KEARSLEY, A. T., GRAPS, A., LAUFER, R., EHRENFREUND, P., ALTOBELLI, N., ALTWEGG, K., SIEGFRIED, A., BAGGALEY, J., BURCHELL, M. J., CARPENTER, J., COLANGELI, L., ESPOSITO, F., GREEN, S. F., HENKEL, H., HORANYI, M., JÄCKEL, A., KEMPF, S., MCBRIDE, N., MORAGAS-KLOSTERMEYER, G., KÜRGER, H., PALUNBO, P., SROWIG, A., TRIEFLOFF, M., TSOU, P., STERNOVSKY, Z., ZEILE, O., RÖSER, H.-P. (2008). Sample return of interstellar matter (SARIM). *Experimental Astronomy*, 23(1), 303–328. <http://doi.org/10.1007/s10686-008-9088-7>
- STRADLING, G. L., IDZOREK, G. C., SHAFER, B. P., CURLING, H. L., COLLOPY, M. T., BLOSSOM, A. A. H., & FUERSTENAU, S. (1993). Ultra-high velocity impacts: cratering studies of microscopic impacts from 3 km/s to 30 km/s. *International Journal of Impact Engineering*, 14(1–4), 719–727. [http://doi.org/10.1016/0734-743X\(93\)90066-G](http://doi.org/10.1016/0734-743X(93)90066-G)
- TSCHAUNER, O., ASIMOW, P. D., KOSTANDOVA, N., AHRENS, T. J., MA, C., SINOGEIKIN, S., LIU, Z., FAKRA, S., TAMURA, N. (2009). Ultrafast growth of wadsleyite in shock-produced melts and its implications for early solar system impact processes. *Proceedings of the National Academy of Sciences of the United States of America*, 106(33), 13691–13695. <http://doi.org/10.1073/pnas.0905751106>

- TSUCHIYAMA, A., UESUGI, M., MATSUSHIMA, T., MICHIKAMI, T., KADONO, T., NAKAMURA, T., UESUGI, K., NKANO, T., SANDFORD, S. A., NOGUCHI, R., MATSUMOTO, T., MATSUNO, J., NAGANO, T., IMAI, Y., TAKEUCHI, A., SUZUKI, Y., OGAMI, T., KATAGIRI, J., EBIHARA, M., IRELAND, T. R., KITAJIMA, F., NAGAO, K., NARAOKO, H., NOGUCHI, T., OKAZAKI, R., YURIMOTO, H., ZOLENSKY, M. E., MUKAI, T., ABE, M., YADA, T., FUJIMURA, A., YOSHIKAWA, M., KAWAGUCHI, J. (2011). Three-Dimensional Structure of Hayabusa Samples: Origin and Evolution of Itokawa Regolith. *Science*, 333(6046), 1125–1128. <http://doi.org/10.1126/science.1207807>
- VEDDER, J. F. (1971). Microcraters in glass and minerals. *Earth and Planetary Science Letters*, 11(1–5), 291–296. [http://doi.org/10.1016/0012-821X\(71\)90182-8](http://doi.org/10.1016/0012-821X(71)90182-8)
- VEDDER, J. F., & MANDEVILLE, J.-C. (1974). Microcraters formed in glass by projectiles of various densities. *Journal of Geophysical Research*, 79(23), 3247–3256. <http://doi.org/10.1029/JB079i023p03247>
- VERNAZZA, P., BINZEL, R. P., ROSSI, A, FULCHIGNONI, M., & BIRLAN, M. (2009). Solar wind as the origin of rapid reddening of asteroid surfaces. *Nature*, 458(7241), 993–995. <http://doi.org/10.1038/nature07956>
- WALSH, J. M., STRADLING, G. L., IDZOREK, G. C., SHAFER, B. P., WX-DO, & CURLING, H. L. (1993). Microparticle impacts at ultra-high velocities: Their relation to macroparticle impacts. *International Journal of Impact Engineering*, 14(1–4), 775–784. [http://doi.org/10.1016/0734-743X\(93\)90071-E](http://doi.org/10.1016/0734-743X(93)90071-E)
- WAZA, T., MATSUI, T., & KANI, K. (1985). Laboratory simulation of planetesimal collision: 2. Ejecta velocity distribution. *Journal of Geophysical Research*, 90(B2), 1995. <http://doi.org/10.1029/JB090iB02p01995>
- WEISBERG, M. K., MCCOY, T. J., & KROT, A. N. (2006). Systematics and Evaluation of Meteorite Classification. *Meteorites and the Early Solar System II*, 19–52. Retrieved from <http://eps.mcgill.ca/~courses/c570/Readings/Weisberg06a.pdf>

WESTPHAL, A. J., BECHTEL, H. A., BRENKER, F. E., BUTTERWORTH, A. L., FLYNN, G., FRANK, D. R., GAINSFORTH, Z., HILLIER, J., POSTBERG, F., SIMIONOVICI, A. S., STERKEN, V. J., STROUD, R. M., ALLEN, C., ANDERSON, D., ANSARI, A., BAJT, S., BASTIEN, R. K., BASSIM, N., BORG, J., BRIDGES, J., BROWNLEE, D. E., BURCHELL, M., BURGHAMMER, M., CHANGELA, H., CLOETENS, P., DAVIS, A. M., DOLL, R., FLOSS, C., GRÜN, E., HECK, P. R., HOPPE, P., HUDSON, B., HUTH, J., HVIDE, B., KEARSLEY, A., KING, A., LAI, B., LEITNER, J., LEMELLE, L., LEROUX, H., LEONARD, A., LETTIERI, R., MARCHANT, W., NITTLER, L. R., OGLIORE, R., ONG, W. J., PRICE, M. C., SANDFORD, S. A., TRESSERAS, J-A. S., SCHMITZ, S., SCHOONJANS, T., SILVERSMIT, G., SOLÉ, V. A., SRAMA, RALF, STADERMANN, F., STEPHAN, T., STODOLNA, J., SUTTON, S., TRIELOFF, M., TSOU, P., TSUCHIYAMA, A., TYLISZCZAK, T., VEKEMANS, B., VINCZE, L., KORFF, J. VON, WORDSWORTH, N., ZEVIN, D., ZOLENSKY, M. E. (2014). Final reports of the stardust interstellar preliminary examination. *Meteoritics and Planetary Science*, 49(9), 1720–1733. <http://doi.org/10.1111/maps.12221>

WILHELM, S., GRÖBLER, B., GLUCH, M., & HEINZ, H. (2003). Konfokale Laser Scanning Mikroskopie (CLSM) - Grundlagen. *Mikroskopie von Carl Zeiss*. Jena: Carl Zeiss Jena GmbH. Retrieved from http://www.cai.hhu.de/fileadmin/redaktion/Fakultaeten/Mathematisch-Naturwissenschaftliche_Fakultaet/CAI/Literatur/Die_konfokale_Laser_Scanning_Mikroskopie.pdf

ZOLENSKY, M. E., ZEGA, T. J., YANO, H., WIRICK, S., WESTPHAL, A. J., WEISBERG, M. K., WEBER, I., WARREN, J. L., VELBEL, M. A., TSUCHIYAMA, A., TSOU, P., TOPPANI, A., TOMIOKA, N., TOMEOKA, K., TESLICH, N., TAHERI, M., SUSINI, J., STROUD, R., STEPHAN, T., STADERMANN, F. J., SNEAD, C. J., SIMON, S. B., SIMIONOVICI, A., SEE, T. H., ROBER, F., RIETMEIJER, F. J. M., RAO, W., PERRONET, M. C., PAPANASTASSIOU, D. A., OKUDAIRA, K., OSHUMI, K., OHNISHI, NAKAMURA-MESSENGER, K., NAKAMURA, T., MOSTEFAOUI, S., MIKOUCHI, T.M MEIBOM, A., MATRAJT, G., MARCUS, M. A., LEROUX, H., LEMELLE, L., LE, L., LANZUOTTI, A., LANGENHORST, F., KROT, A. N., KELLER, L. P., KEARSLEY, A. T., JOSWIAK, D., JACOB, D., ISHII, H., HARVEY, R., HAGIYA, K., GROSSMAN, L., GROSSMAN, J. N., GRAHAM, G. A., GOUNELLE, M., GILLET, P., GENGE, M. J., FLYNN, G., TRISTAN, F., FALLON, S., EBEL, D. S., DAI, Z. R., CORDIER, P., CLARK, B., CHI, M., BUTTERWORTH, A. L., BROWNLEE, D. E., BRIDGES, J. C., BRENNAN, S., BREARLEY, A., BRADLEY, J. P., BLEUET, P., BLAND, P. A., BASTIEN, R. (2006). Mineralogy and Petrology of Comet 81P/Wild 2 Nucleus Samples. *Science*, 314(5806), 1735–1739. <http://doi.org/10.1126/science.1135842>

Appendix A: EMP measurements

Table A.01: Forsterite composition of Olivine_6 acquired with EMP.

Mineral	fors	fors	mean	st.dev.	min	max																	
SiO ₂	40.95	41.16	41.50	41.06	40.79	41.01	40.95	40.84	40.97	40.88	41.14	40.87	40.78	40.85	40.86	41.03	40.90	40.80	39.59	40.89	.36	39.59	41.50
TiO ₂	0.02	0.00	0.02	0.00	0.00	0.00	0.00	0.01	0.01	0.00	0.01	0.01	0.01	0.03	0.00	0.00	0.00	0.00	0.00	.01	.01	.00	.03
Al ₂ O ₃	0.00	0.00	0.00	0.00	0.00	0.00	0.01	0.00	0.00	0.01	0.00	0.00	0.00	0.01	0.00	0.00	0.01	0.00	0.00	.00	.00	.00	.01
Cr ₂ O ₃	0.06	0.01	0.01	0.00	0.05	0.00	0.04	0.03	0.02	0.02	0.04	0.00	0.01	0.03	0.03	0.05	0.00	0.00	0.05	.02	.02	.00	.06
Fe ₂ O ₃	0.00	0.00	0.00	0.00	0.00	0.00	0.00	0.00	0.00	0.00	0.00	0.00	0.00	0.00	0.00	0.00	0.00	0.00	0.00	.00	.00	.00	.00
FeO	9.08	9.04	6.42	8.55	9.26	8.80	8.92	8.98	9.00	9.19	8.81	9.03	9.09	8.89	9.06	8.57	8.73	8.92	8.57	8.78	.61	6.42	9.26
MnO	0.13	0.15	0.14	0.19	0.16	0.16	0.16	0.16	0.16	0.13	0.12	0.17	0.12	0.14	0.19	0.10	0.13	0.12	0.16	.15	.02	.10	.19
NiO	0.39	0.31	0.39	0.31	0.37	0.40	0.39	0.41	0.36	0.31	0.38	0.42	0.34	0.37	0.33	0.36	0.32	0.34	0.31	.36	.04	.31	.42
MgO	50.58	50.53	52.71	51.01	50.40	50.60	50.51	50.51	50.44	50.36	50.38	50.24	50.42	50.46	50.25	50.57	50.35	50.15	48.44	50.47	.73	48.44	52.71
CaO	0.00	0.00	0.00	0.01	0.00	0.00	0.00	0.01	0.00	0.01	0.00	0.00	0.01	0.00	0.00	0.00	0.00	0.02	0.02	.00	.01	.00	.02
Na ₂ O	0.01	0.00	0.00	0.02	0.01	0.02	0.00	0.02	0.00	0.01	0.00	0.04	0.01	0.00	0.00	0.00	0.01	0.01	0.03	.01	.01	.00	.04
K ₂ O	0.00	0.01	0.02	0.00	0.01	0.01	0.00	0.01	0.00	0.00	0.00	0.01	0.00	0.00	0.00	0.00	0.00	0.00	0.00	.00	.01	.00	.02
Σ oxides	101.21	101.21	101.21	101.14	101.05	101.01	100.98	100.97	100.96	100.92	100.88	100.79	100.79	100.79	100.73	100.69	100.46	100.35	97.17	100.70	.89	97.17	101.21
Si	0.990	0.994	0.991	0.991	0.989	0.992	0.992	0.990	0.993	0.991	0.996	0.992	0.990	0.991	0.993	0.994	0.994	0.994	0.996	.99	.00	.99	1.00
Ti	0.000	0.000	0.000	0.000	0.000	0.000	0.000	0.000	0.000	0.000	0.000	0.000	0.000	0.001	0.000	0.000	0.000	0.000	0.000	.00	.00	.00	.00
Al	0.000	0.000	0.000	0.000	0.000	0.000	0.000	0.000	0.000	0.000	0.000	0.000	0.000	0.000	0.000	0.000	0.000	0.000	0.000	.00	.00	.00	.00
Cr	0.001	0.000	0.000	0.000	0.001	0.000	0.001	0.001	0.000	0.000	0.001	0.000	0.000	0.001	0.001	0.001	0.000	0.000	0.001	.00	.00	.00	.00
Fe ³⁺	0.000	0.000	0.000	0.000	0.000	0.000	0.000	0.000	0.000	0.000	0.000	0.000	0.000	0.000	0.000	0.000	0.000	0.000	0.000	.00	.00	.00	.00
Fe ²⁺	0.184	0.183	0.128	0.173	0.188	0.178	0.181	0.182	0.182	0.186	0.178	0.183	0.185	0.180	0.184	0.174	0.177	0.182	0.180	.18	.01	.13	.19
Mn	0.003	0.003	0.003	0.004	0.003	0.003	0.003	0.003	0.003	0.003	0.002	0.003	0.003	0.003	0.004	0.002	0.003	0.002	0.003	.00	.00	.00	.00
Ni	0.008	0.006	0.008	0.006	0.007	0.008	0.008	0.008	0.007	0.006	0.007	0.008	0.007	0.007	0.006	0.007	0.006	0.007	0.006	.01	.00	.01	.01
Mg	1.823	1.819	1.877	1.835	1.822	1.825	1.823	1.825	1.821	1.821	1.818	1.819	1.825	1.825	1.820	1.827	1.825	1.821	1.816	1.83	.01	1.82	1.88
Ca	0.000	0.000	0.000	0.000	0.000	0.000	0.000	0.000	0.000	0.000	0.000	0.000	0.000	0.000	0.000	0.000	0.000	0.000	0.000	.00	.00	.00	.00
Na	0.000	0.000	0.000	0.001	0.000	0.001	0.000	0.001	0.000	0.000	0.000	0.002	0.000	0.000	0.000	0.000	0.000	0.001	0.001	.00	.00	.00	.00
K	0.000	0.000	0.001	0.000	0.000	0.000	0.000	0.000	0.000	0.000	0.000	0.000	0.000	0.000	0.000	0.000	0.000	0.000	0.000	.00	.00	.00	.00
Σ octa	3.009	3.006	3.008	3.010	3.011	3.008	3.008	3.010	3.007	3.009	3.003	3.009	3.010	3.008	3.007	3.005	3.006	3.007	3.004	3.01	.00	3.00	3.01
Mg-Value	90.9	90.9	93.6	91.4	90.7	91.1	91.0	90.9	90.9	90.7	91.1	90.8	90.8	91.0	90.8	91.3	91.1	90.9	91.0	91.10	.63	90.66	93.60
Mg#	90.9	90.9	93.6	91.4	90.7	91.1	91.0	90.9	90.9	90.7	91.1	90.8	90.8	91.0	90.8	91.3	91.1	90.9	91.0	91.10	.63	90.66	93.60
Fo	90.7	90.7	93.5	91.2	90.5	91.0	90.8	90.8	90.8	90.6	91.0	90.7	90.7	90.9	90.6	91.2	91.0	90.8	90.8	90.96	.64	90.51	93.47

Table A.02: Magnetite composition of Olivine_6 acquired with EMP.

Mineral	Magnetite	Magnetite	Magnetite	Magnetite	Magnetite	mean	st.dev	min	max
SiO₂	0.10	0.09	0.08	0.06	0.03	.07	.03	.03	.10
TiO₂	0.04	0.00	0.02	0.01	0.04	.02	.02	.00	.04
Al₂O₃	0.00	0.00	0.00	0.02	0.00	.00	.01	.00	.02
Cr₂O₃	0.16	0.18	0.13	0.21	0.05	.15	.06	.05	.21
Fe₂O₃	70.19	75.55	69.23	68.11	63.60	69.34	4.29	63.60	75.55
FeO	30.04	16.54	29.47	29.00	26.99	26.41	5.63	16.54	30.04
MnO	0.04	0.02	0.08	0.04	0.05	.05	.02	.02	.08
NiO	0.59	0.60	0.68	0.61	0.59	.61	.04	.59	.68
MgO	0.64	9.54	0.70	0.70	0.60	2.44	3.97	.60	9.54
CaO	0.00	0.00	0.00	0.00	0.01	.00	.00	.00	.01
Na₂O	0.02	0.03	0.00	0.01	0.01	.01	.01	.00	.03
K₂O	0.01	0.00	0.00	0.01	0.01	.01	.01	.00	.01
Σ oxides	101.84	102.54	100.39	98.76	91.99	99.10	4.23	91.99	102.54
Si	0.004	0.003	0.003	0.002	0.001	.00	.00	.00	.00
Ti	0.001	0.000	0.001	0.000	0.001	.00	.00	.00	.00
Al	0.000	0.000	0.000	0.001	0.000	.00	.00	.00	.00
Cr	0.005	0.005	0.004	0.006	0.002	.00	.00	.00	.01
Fe³⁺	1.988	1.991	1.989	1.988	1.995	1.99	.00	1.99	2.00
Fe²⁺	0.945	0.484	0.941	0.941	0.941	.85	.20	.48	.95
Mn	0.001	0.001	0.002	0.001	0.002	.00	.00	.00	.00
Ni	0.018	0.017	0.021	0.019	0.020	.02	.00	.02	.02
Mg	0.036	0.498	0.040	0.040	0.037	.13	.21	.04	.50
Ca	0.000	0.000	0.000	0.000	0.000	.00	.00	.00	.00
Na	0.002	0.002	0.000	0.000	0.001	.00	.00	.00	.00
K	0.001	0.000	0.000	0.000	0.001	.00	.00	.00	.00
Σ octa	3.000	3.000	3.000	3.000	3.000	3.00	.00	3.00	3.00

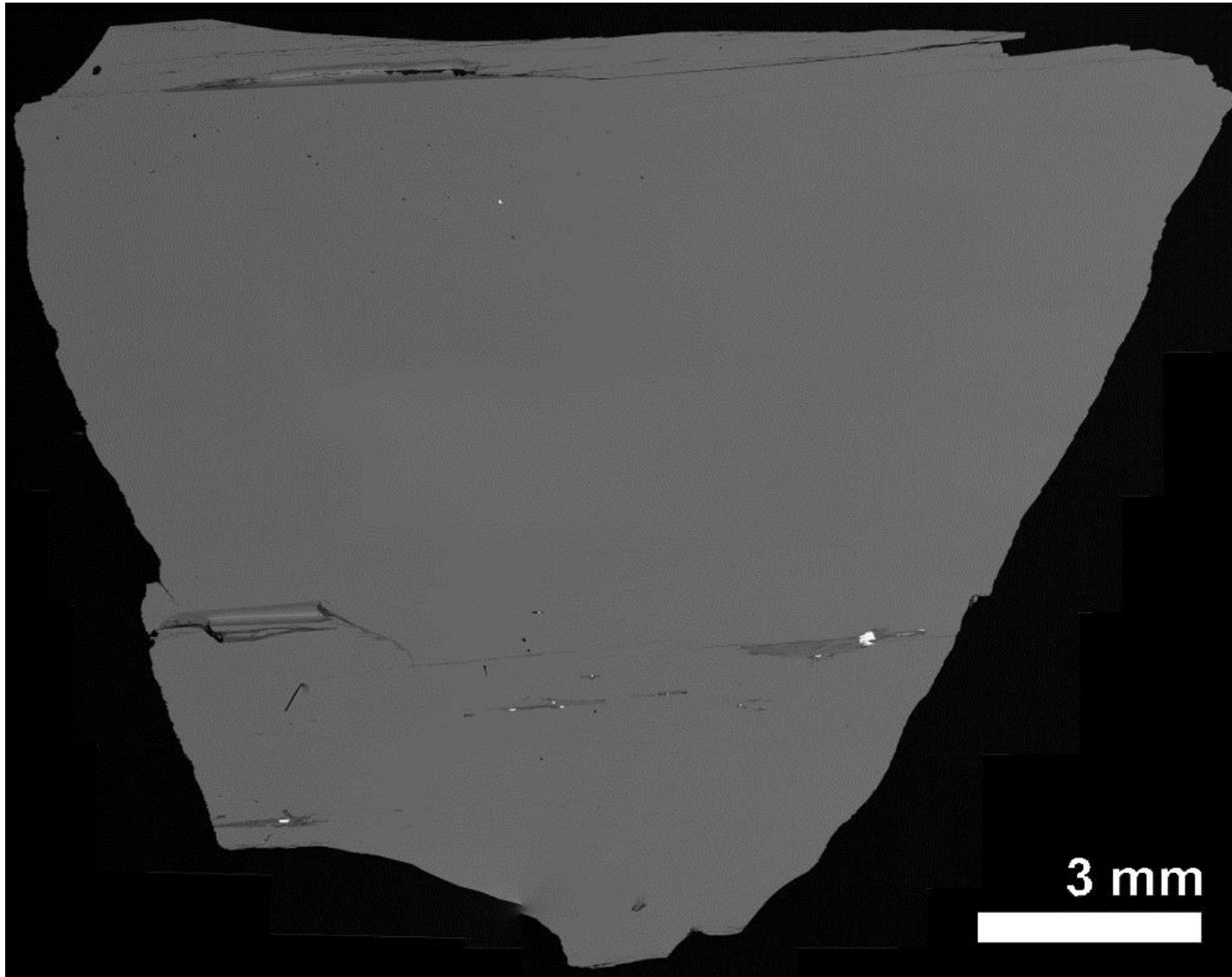


Figure A.01: SEM-BSD stitched panorama image of Enstatite_3, which is remarkably homogeneous.

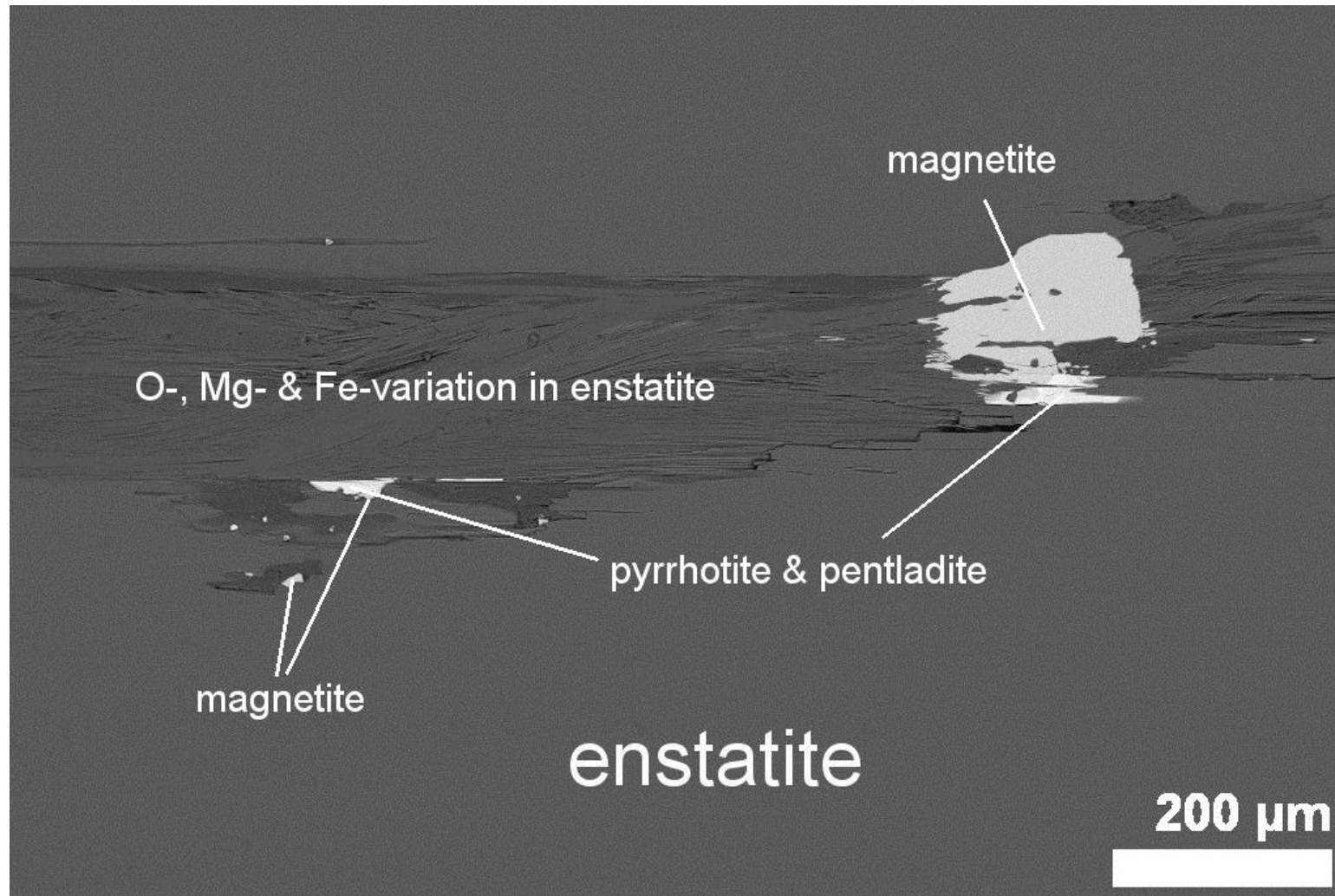


Figure A.02: SEM-BSD image of a heterogeneous zone of Enstatite_3, showing inclusions of magnetite and the intergrowing sulphide pyrrhotite and pentlandite.

Table A.03: Enstatite composition of Enstatite_6 acquired with EMP.

Mineral	enst	mean	st.dev.	min	max																					
SiO2	57.46	57.49	57.63	57.47	57.51	57.43	57.63	57.47	57.61	57.33	57.37	57.43	57.31	57.52	57.37	57.33	57.77	57.09	57.41	57.61	57.39	57.46	0.15	57.09	57.77	
TiO2	.04	.05	.06	.04	.04	.03	.02	.03	.03	.05	.03	.04	.02	.04	.06	.03	.02	.05	.05	.04	.01	0.04	0.01	0.01	0.06	
Al2O3	.24	.25	.23	.24	.22	.23	.23	.22	.23	.22	.23	.23	.23	.24	.23	.23	.07	.23	.23	.21	.21	0.22	0.04	0.07	0.25	
Cr2O3	.01	.08	.06	.04	.04	.08	.04	.06	.04	.06	.02	.03	.07	.06	.03	.04	.01	.06	.01	.05	.06	0.05	0.02	0.01	0.08	
Fe2O3	1.42	1.19	.78	1.17	.91	1.14	.47	.79	.53	1.23	1.13	.99	1.28	.56	.83	.92	.10	1.50	.37	.00	.41	0.84	0.42	0.00	1.50	
FeO	8.64	8.71	9.02	8.71	8.87	8.58	9.16	8.99	9.04	8.61	8.60	8.66	8.37	8.98	8.81	8.81	9.19	8.34	9.32	9.19	9.08	8.84	0.27	8.34	9.32	
MnO	.28	.26	.27	.21	.22	.24	.27	.29	.23	.25	.25	.22	.22	.24	.30	.30	.25	.28	.30	.25	.21	0.26	0.03	0.21	0.30	
NiO	.07	.07	.08	.08	.09	.06	.02	.04	.06	.01	.08	.10	.12	.04	.04	.03	.07	.07	.04	.04	.05	0.06	0.03	0.01	0.12	
MgO	33.31	33.28	33.21	33.32	33.21	33.28	33.16	33.15	33.20	33.30	33.29	33.23	33.31	33.17	33.17	33.11	33.26	33.15	32.91	33.13	33.02	33.20	0.10	32.91	33.32	
CaO	.26	.26	.24	.26	.25	.28	.26	.27	.26	.25	.25	.26	.28	.26	.27	.26	.21	.27	.27	.27	.27	0.26	0.02	0.21	0.28	
Na2O	.01	.01	.02	.00	.02	.02	.00	.00	.01	.01	.00	.02	.02	.02	.02	.00	.02	.01	.04	.00	.00	.02	0.01	0.01	0.00	0.04
K2O	.00	.00	.00	.00	.01	.01	.01	.00	.00	.00	.01	.03	.01	.01	.01	.01	.01	.00	.01	.00	.00	.00	0.01	0.01	0.00	0.03
H2O	.00	.00	.00	.00	.00	.00	.00	.00	.00	.00	.00	.00	.00	.00	.00	.00	.00	.00	.00	.00	.00	0.00	0.00	0.00	0.00	
Σ ox	101.75	101.67	101.58	101.55	101.38	101.36	101.29	101.30	101.25	101.32	101.26	101.22	101.23	101.12	101.11	101.08	100.97	101.09	100.91	100.79	100.74	101.24	0.27	100.74	101.75	
Si	1.976	1.978	1.984	1.979	1.983	1.980	1.988	1.984	1.988	1.978	1.980	1.982	1.978	1.987	1.983	1.983	1.997	1.975	1.989	1.994	1.990	1.98	0.01	1.97	2.00	
Al(IV)	0.010	0.010	0.009	0.010	0.009	0.009	0.009	0.009	0.009	0.009	0.009	0.009	0.009	0.010	0.009	0.009	0.003	0.009	0.009	0.006	0.009	0.01	0.00	0.00	0.01	
Fe3+	0.015	0.012	0.007	0.012	0.008	0.011	0.002	0.008	0.003	0.013	0.011	0.008	0.013	0.004	0.008	0.008	0.000	0.016	0.001	0.000	0.002	0.01	0.00	0.00	0.02	
Σ tet	2.000	2.000	2.000	2.000	2.000	2.000	2.000	2.000	2.000	2.000	2.000	2.000	2.000	2.000	2.000	2.000	2.000	2.000	2.000	2.000	2.000	2.00	0.00	2.00	2.00	
Al(VI)	0.000	0.000	0.000	0.000	0.000	0.000	0.000	0.000	0.000	0.000	0.000	0.000	0.000	0.000	0.000	0.000	0.000	0.000	0.000	0.003	0.000	0.00	0.00	0.00	0.00	
Fe3+	0.022	0.019	0.013	0.019	0.016	0.019	0.010	0.013	0.011	0.019	0.019	0.017	0.021	0.011	0.014	0.016	0.002	0.023	0.008	0.000	0.009	0.01	0.01	0.00	0.02	
Ti	0.001	0.001	0.002	0.001	0.001	0.001	0.001	0.001	0.001	0.001	0.001	0.001	0.000	0.001	0.002	0.001	0.001	0.001	0.001	0.001	0.000	0.00	0.00	0.00	0.00	
Cr	0.000	0.002	0.002	0.001	0.001	0.002	0.001	0.002	0.001	0.002	0.000	0.001	0.002	0.002	0.001	0.001	0.000	0.002	0.000	0.001	0.002	0.00	0.00	0.00	0.00	
Mg	1.707	1.707	1.704	1.710	1.707	1.710	1.705	1.706	1.707	1.713	1.713	1.710	1.714	1.708	1.709	1.707	1.714	1.710	1.700	1.710	1.707	1.71	0.00	1.70	1.71	
Ni	0.002	0.002	0.002	0.002	0.002	0.002	0.001	0.001	0.002	0.000	0.002	0.003	0.003	0.001	0.001	0.001	0.002	0.002	0.001	0.001	0.001	0.00	0.00	0.00	0.00	
Fe2+	0.248	0.251	0.260	0.251	0.256	0.247	0.264	0.259	0.261	0.248	0.248	0.250	0.242	0.259	0.255	0.255	0.265	0.241	0.270	0.266	0.263	0.26	0.01	0.24	0.27	
Mn	0.008	0.007	0.008	0.006	0.006	0.007	0.008	0.009	0.007	0.007	0.007	0.006	0.007	0.007	0.009	0.009	0.007	0.008	0.009	0.007	0.006	0.01	0.00	0.01	0.01	
Ca	0.009	0.010	0.009	0.010	0.009	0.010	0.010	0.010	0.010	0.009	0.009	0.010	0.010	0.010	0.010	0.010	0.008	0.010	0.010	0.010	0.010	0.01	0.00	0.01	0.01	
Na	0.001	0.001	0.002	0.000	0.001	0.002	0.000	0.000	0.001	0.000	0.000	0.001	0.001	0.001	0.000	0.001	0.000	0.003	0.000	0.000	0.001	0.00	0.00	0.00	0.00	
K	0.000	0.000	0.000	0.000	0.001	0.000	0.000	0.000	0.000	0.000	0.000	0.001	0.000	0.000	0.001	0.000	0.000	0.000	0.000	0.000	0.000	0.00	0.00	0.00	0.00	
Σ oct	2.000	2.000	2.000	2.000	2.000	2.000	2.000	2.000	2.000	2.000	2.000	2.000	2.000	2.000	2.000	2.000	2.000	2.000	2.000	2.000	2.000	2.00	0.00	2.00	2.00	
Σ	4.000	4.000	4.000	4.000	4.000	4.000	4.000	4.000	4.000	4.000	4.000	4.000	4.000	4.000	4.000	4.000	4.000	4.000	4.000	4.000	4.000	4.00	0.00	4.00	4.00	
Si + Al	1.985	1.988	1.993	1.988	1.992	1.989	1.998	1.992	1.997	1.987	1.989	1.992	1.987	1.996	1.992	1.992	2.000	1.984	1.999	2.000	1.998	1.99	0.00	1.98	2.00	
Al(VI)/Al(IV)	0.00	0.00	0.00	0.00	0.00	0.00	0.00	0.00	0.00	0.00	0.00	0.00	0.00	0.00	0.00	0.00	0.00	0.00	0.00	0.53	0.00	0.03	0.11	0.00	0.53	
Fe ²⁺ /(Fe ²⁺ +Fe ³⁺)	0.87	0.89	0.93	0.89	0.92	0.89	0.96	0.93	0.95	0.89	0.89	0.91	0.88	0.95	0.92	0.91	0.99	0.86	0.97	1.00	0.96	0.92	0.04	0.86	1.00	

Enstatite (En₈₆) composition can be expressed as: (Ca_{0.01} Mn_{0.01} Fe³⁺_{0.01} Fe²⁺_{0.26} Mg_{1.71})_{Σ=2.00} (Al_{0.01} Fe³⁺_{0.01} Si_{1.98})_{Σ=2.00} O₆.

Table A.04: Sulphidic composition of Enstatite_6 inclusions acquired with EMP.

Mineral	Pentladite	Pyrrhotite	Pyrrhotite	Pyrrhotite
Na	0.46	0.00	0.00	0.00
Mg	0.00	0.00	0.00	0.00
S	33.32	39.34	40.12	39.41
Cl	0.03	0.00	0.00	0.00
K	0.00	0.01	0.00	0.02
Ca	0.00	0.00	0.00	0.00
Ti	0.01	0.00	0.01	0.00
Cr	0.02	0.00	0.00	0.00
Mn	0.03	0.03	0.02	0.00
Fe	38.54	59.58	57.70	58.96
Ni	23.12	1.90	3.35	2.84
Cu	0.06	0.00	0.00	0.00
Zn	0.05	0.00	0.00	0.00
Total	95.63	100.85	101.20	101.23

Enstatite_6 occurs to be very homogeneous. There is magnetite (Tab. A.05) and sulphidic inclusions (Tab. A.04), identified as pyrrhotite and pentladite. They are known to accompany orthopyroxenes and the found sulphides tend to occur in intergrowth (Markl, 2015). EMP analysis show sometimes slight mixtures of these sulphides with magnetite.

Ideal structural formula of pentladite: $(\text{Fe}, \text{Ni})_9\text{S}_8$

Ideal structural formula of pyrrhotite: Fe_{1-x}S

Table A.05: Composition magnetite inclusions of Enstatite_6 acquired with EMP.

Mineral	magn	mean	st.dev.	min	max										
SiO ₂	.02	.00	.01	.00	.03	.02	.06	.03	.02	.01	.01	.02	.02	.00	.06
TiO ₂	.03	.06	.08	.07	.07	.06	.03	.12	.00	.07	.04	.06	.03	.00	.12
Al ₂ O ₃	.00	.00	.00	.00	.00	.00	.00	.02	.00	.00	.00	.00	.00	.00	.02
Cr ₂ O ₃	1.89	.68	1.11	.51	.53	.50	.09	6.50	.54	1.89	1.81	1.46	1.79	.09	6.50
Fe ₂ O ₃	69.41	70.32	69.79	70.55	70.46	70.32	70.84	63.64	69.89	68.24	67.78	69.20	2.08	63.64	70.84
FeO	30.46	30.53	30.38	29.61	29.31	29.66	29.29	28.43	30.09	29.98	29.88	29.78	.62	28.43	30.53
MnO	.11	.06	.04	.11	.06	.13	.03	.13	.07	.06	.05	.08	.04	.03	.13
NiO	.15	.09	.07	.04	.19	.08	.05	.43	.08	.09	.08	.12	.11	.04	.43
MgO	.84	.73	.76	1.18	1.34	1.20	1.44	1.63	.68	.81	.77	1.04	.33	.68	1.63
CaO	.00	.02	.01	.02	.03	.02	.01	.04	.01	.01	.01	.02	.01	.00	.04
Na ₂ O	.00	.00	.03	.04	.03	.00	.02	.00	.05	.02	.00	.02	.02	.00	.05
K ₂ O	.00	.01	.02	.00	.00	.00	.00	.02	.00	.00	.01	.01	.01	.00	.02
Σ oxides	102.93	102.51	102.29	102.14	102.04	101.98	101.87	100.98	101.42	101.19	100.45	101.80	.72	100.45	102.93
Si	0.001	0.000	0.000	0.000	0.001	0.001	0.002	0.001	0.001	0.000	0.000	.00	.00	.00	.00
Ti	0.001	0.002	0.002	0.002	0.002	0.002	0.001	0.003	0.000	0.002	0.001	.00	.00	.00	.00
Al	0.000	0.000	0.000	0.000	0.000	0.000	0.000	0.001	0.000	0.000	0.000	.00	.00	.00	.00
Cr	0.056	0.020	0.033	0.015	0.016	0.015	0.003	0.193	0.016	0.057	0.054	.04	.05	.00	.19
Fe ³⁺	1.941	1.977	1.965	1.983	1.981	1.981	1.993	1.798	1.986	1.941	1.943	1.95	.05	1.80	1.99
Fe ²⁺	0.947	0.954	0.951	0.925	0.915	0.928	0.916	0.893	0.950	0.948	0.952	.93	.02	.89	.95
Mn	0.004	0.002	0.001	0.004	0.002	0.004	0.001	0.004	0.002	0.002	0.002	.00	.00	.00	.00
Ni	0.005	0.003	0.002	0.001	0.006	0.002	0.002	0.013	0.002	0.003	0.003	.00	.00	.00	.01
Mg	0.046	0.041	0.043	0.066	0.074	0.067	0.080	0.091	0.038	0.046	0.044	.06	.02	.04	.09
Ca	0.000	0.001	0.001	0.001	0.001	0.001	0.001	0.001	0.000	0.001	0.001	.00	.00	.00	.00
Na	0.000	0.000	0.002	0.003	0.002	0.000	0.002	0.000	0.004	0.002	0.000	.00	.00	.00	.00
K	0.000	0.001	0.001	0.000	0.000	0.000	0.000	0.001	0.000	0.000	0.001	.00	.00	.00	.00
Σ octa	3.000	3.000	3.000	3.000	3.000	3.000	3.000	3.000	3.000	3.000	3.000	3.00	.00	3.00	3.00

The structural formula of the magnetite (spinel group) inclusions can be expressed as: $(\text{Fe}^{2+}_{0.93}\text{Mg}_{0.05})_{\Sigma=0.98}(\text{Fe}^{3+}_{1.95}\text{Cr}_{0.04}\text{Mg}_{0.01})_{\Sigma=2.00}\text{O}_4$

Table A.05: Composition the f inclusions of Enstatite_6 acquired with EMP.

Mineral	diopside	diopside	mean	st.dev	min	max																			
SiO ₂	55.28	55.20	55.59	55.06	55.31	55.35	55.42	55.04	55.29	55.37	55.25	55.40	55.28	55.26	55.37	55.35	55.28	55.29	55.40	54.90	55.28	.15	54.90	55.59	
TiO ₂	.21	.21	.25	.25	.24	.24	.21	.28	.22	.20	.26	.23	.24	.26	.23	.19	.22	.23	.23	.18	.18	.23	.02	.18	.28
Al ₂ O ₃	.08	.08	.08	.10	.08	.09	.10	.06	.09	.09	.08	.08	.06	.12	.08	.09	.09	.09	.08	.09	.08	.01	.06	.12	
Cr ₂ O ₃	.12	.18	.16	.12	.11	.11	.13	.12	.12	.11	.11	.10	.10	.15	.15	.12	.10	.12	.11	.11	.12	.02	.10	.18	
Fe ₂ O ₃	.46	.43	.00	.77	.28	.03	.00	.54	.20	.41	.22	.08	.20	.40	.10	.00	.08	.07	.20	.27	.24	.21	.00	.77	
FeO	1.37	1.39	1.89	1.08	1.53	1.68	1.68	1.28	1.54	1.45	1.60	1.75	1.59	1.49	1.66	1.80	1.65	1.76	1.59	1.69	1.57	.19	1.08	1.89	
MnO	.07	.03	.05	.01	.01	.06	.04	.07	.02	.06	.00	.08	.05	.07	.04	.01	.04	.05	.05	.07	.04	.02	.00	.08	
NiO	.03	.00	.00	.00	.00	.02	.00	.02	.01	.00	.07	.00	.00	.00	.02	.05	.07	.00	.02	.04	.02	.02	.00	.07	
MgO	17.61	17.74	17.76	17.91	17.67	17.74	17.75	17.74	17.82	17.85	17.82	17.76	17.74	17.93	17.73	17.71	17.83	17.72	17.80	17.39	17.75	.11	17.39	17.93	
CaO	25.78	25.71	25.70	25.69	25.64	25.62	25.61	25.59	25.59	25.57	25.57	25.56	25.56	25.56	25.55	25.55	25.54	25.48	25.46	25.42	25.59	.09	25.42	25.78	
Na ₂ O	.08	.05	.03	.03	.10	.04	.03	.05	.04	.06	.02	.04	.07	.00	.07	.02	.01	.06	.10	.07	.05	.03	.00	.10	
K ₂ O	.01	.00	.00	.00	.00	.00	.00	.01	.00	.00	.00	.00	.00	.01	.01	.01	.00	.00	.01	.03	.01	.01	.00	.03	
Σ oxides	101.10	101.01	101.49	101.02	100.97	100.99	100.97	100.78	100.93	101.18	100.99	101.09	100.90	101.25	101.01	100.89	100.89	100.86	101.03	100.27					
Si	1.988	1.986	1.991	1.980	1.990	1.991	1.993	1.984	1.989	1.988	1.988	1.991	1.990	1.983	1.991	1.993	1.990	1.991	1.991	1.991	1.99	.00	1.98	1.99	
Al ^(IV)	.003	.003	.003	.004	.003	.004	.004	.003	.004	.004	.003	.004	.003	.005	.004	.004	.004	.004	.003	.004	.00	.00	.00	.01	
Fe ³⁺	.009	.011	.000	.016	.007	.000	.000	.013	.000	.009	.000	.000	.000	.000	.000	.000	.000	.000	.005	.005	.00	.01	.00	.02	
Σ tet	2.000	2.000	1.994	2.000	2.000	1.995	1.997	2.000	1.993	2.000	1.991	1.995	1.993	1.988	1.995	1.997	1.994	1.995	2.000	2.000	2.00	.00	1.99	2.00	
Al ^(VI)	0.000	0.000	0.000	0.000	0.000	0.000	0.000	0.000	0.000	0.000	0.000	0.000	0.000	0.000	0.000	0.000	0.000	0.000	0.000	0.000	.00	.00	.00	.00	
Fe ³⁺	0.004	0.001	0.000	0.005	0.001	0.001	0.000	0.002	0.006	0.002	0.006	0.002	0.005	0.011	0.003	0.000	0.002	0.002	0.000	0.003	.00	.00	.00	.01	
Ti	0.006	0.006	0.007	0.007	0.007	0.007	0.006	0.007	0.006	0.005	0.007	0.006	0.006	0.007	0.006	0.005	0.006	0.006	0.006	0.005	.01	.00	.00	.01	
Cr	0.003	0.005	0.004	0.003	0.003	0.003	0.004	0.003	0.003	0.003	0.003	0.003	0.003	0.004	0.004	0.003	0.003	0.004	0.003	0.003	.00	.00	.00	.01	
Fe ²⁺	0.041	0.042	0.057	0.033	0.046	0.051	0.051	0.038	0.046	0.044	0.048	0.053	0.048	0.045	0.050	0.054	0.050	0.053	0.048	0.051	.05	.01	.03	.06	
Mn	0.002	0.001	0.001	0.000	0.000	0.002	0.001	0.002	0.001	0.002	0.000	0.003	0.002	0.002	0.001	0.000	0.001	0.001	0.001	0.002	.00	.00	.00	.00	
Ni	0.001	0.000	0.000	0.000	0.000	0.000	0.000	0.001	0.000	0.000	0.002	0.000	0.000	0.000	0.001	0.002	0.002	0.000	0.000	0.001	.00	.00	.00	.00	
Mg	0.944	0.952	0.948	0.960	0.948	0.951	0.952	0.954	0.956	0.955	0.956	0.952	0.952	0.959	0.950	0.951	0.957	0.952	0.954	0.940	.95	.00	.94	.96	
Ca	0.993	0.991	0.986	0.990	0.988	0.987	0.987	0.989	0.986	0.984	0.986	0.984	0.986	0.983	0.985	0.986	0.985	0.983	0.980	0.988	.99	.00	.98	.99	
Na	0.006	0.003	0.002	0.002	0.007	0.003	0.002	0.004	0.003	0.004	0.001	0.003	0.005	0.000	0.005	0.001	0.001	0.004	0.007	0.005	.00	.00	.00	.01	
K	0.000	0.000	0.000	0.000	0.000	0.000	0.000	0.001	0.000	0.000	0.000	0.000	0.000	0.000	0.001	0.001	0.000	0.000	0.000	0.001	.00	.00	.00	.00	
Σ octa	2.000	2.000	2.005	2.000	2.000	2.005	2.002	2.000	2.007	2.000	2.009	2.005	2.007	2.012	2.005	2.002	2.006	2.005	2.000	2.000	2.00	.00	2.00	2.01	
Σ	4.000	4.000	3.999	4.000	4.000	4.000	3.999	4.000	3.999	4.000	4.000	4.000	4.000	4.00	.00	4.00	4.00								
Si + Al	1.99	1.99	1.99	1.98	1.99	1.99	2.00	1.99	1.99	1.99	1.99	1.99	1.99	1.99	1.99	2.00	1.99	2.00	1.99	2.00					
Al ^(VI) /Al ^(IV)	0.00	0.00	0.00	0.00	0.00	0.00	0.00	0.00	0.00	0.00	0.00	0.00	0.00	0.00	0.00	0.00	0.00	0.00	0.00	0.00					
Fe ²⁺ /(Fe ²⁺ +Fe ³⁺)	0.77	0.78	1.00	0.61	0.86	0.98	1.00	0.72	0.89	0.80	0.89	0.96	0.90	0.80	0.95	1.00	0.96	0.96	0.90	0.88					

The structural formula of the diopside can be expressed as: Ca_{1.00}(Mg_{0.95}Fe²⁺_{0.05})_{Σ=1.00}(Si_{0.99}Fe³⁺_{0.01})_{Σ=1.00}O₆

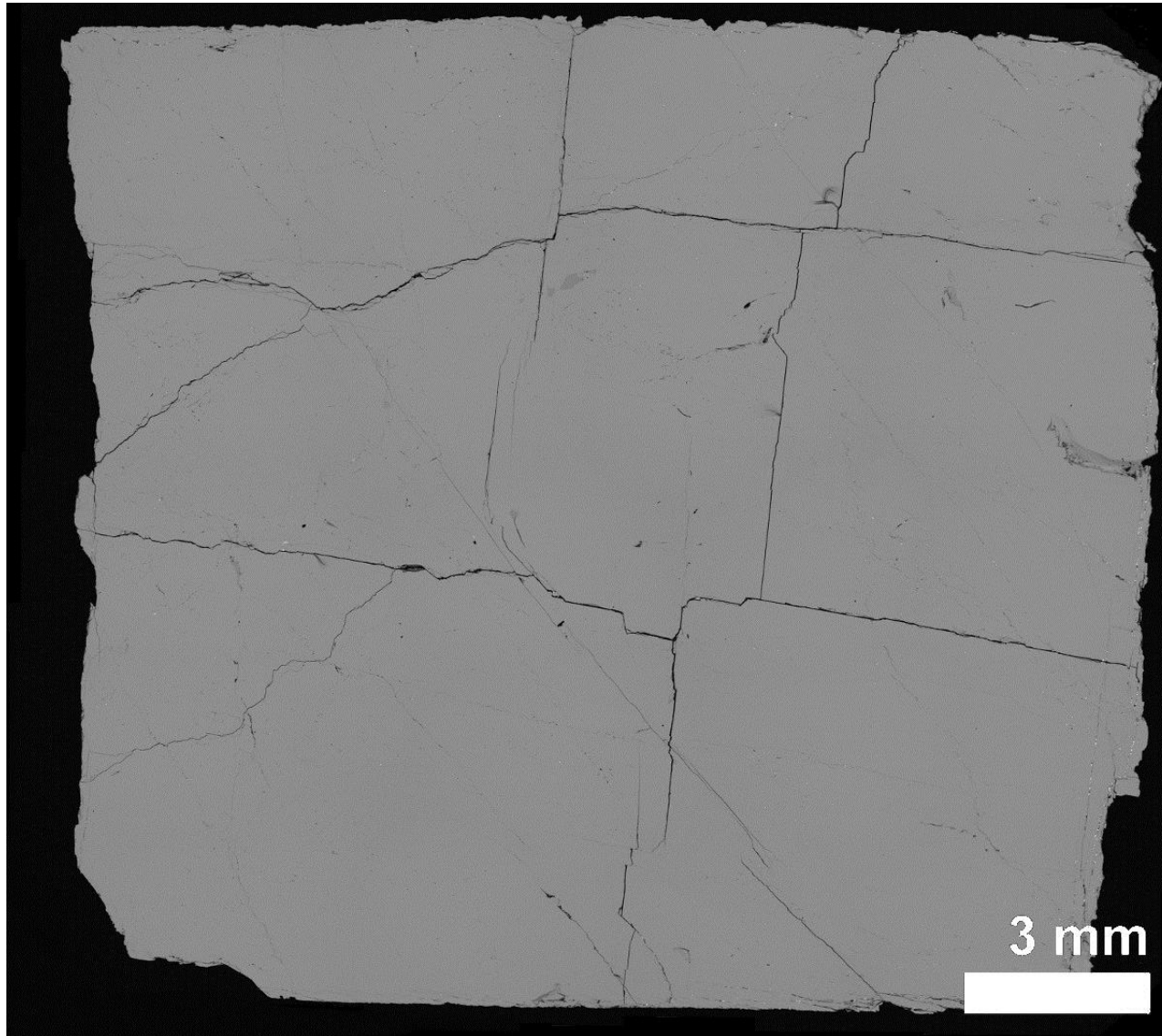


Figure A.03: SEM-BSD stitched panorama image of Diopside_7.

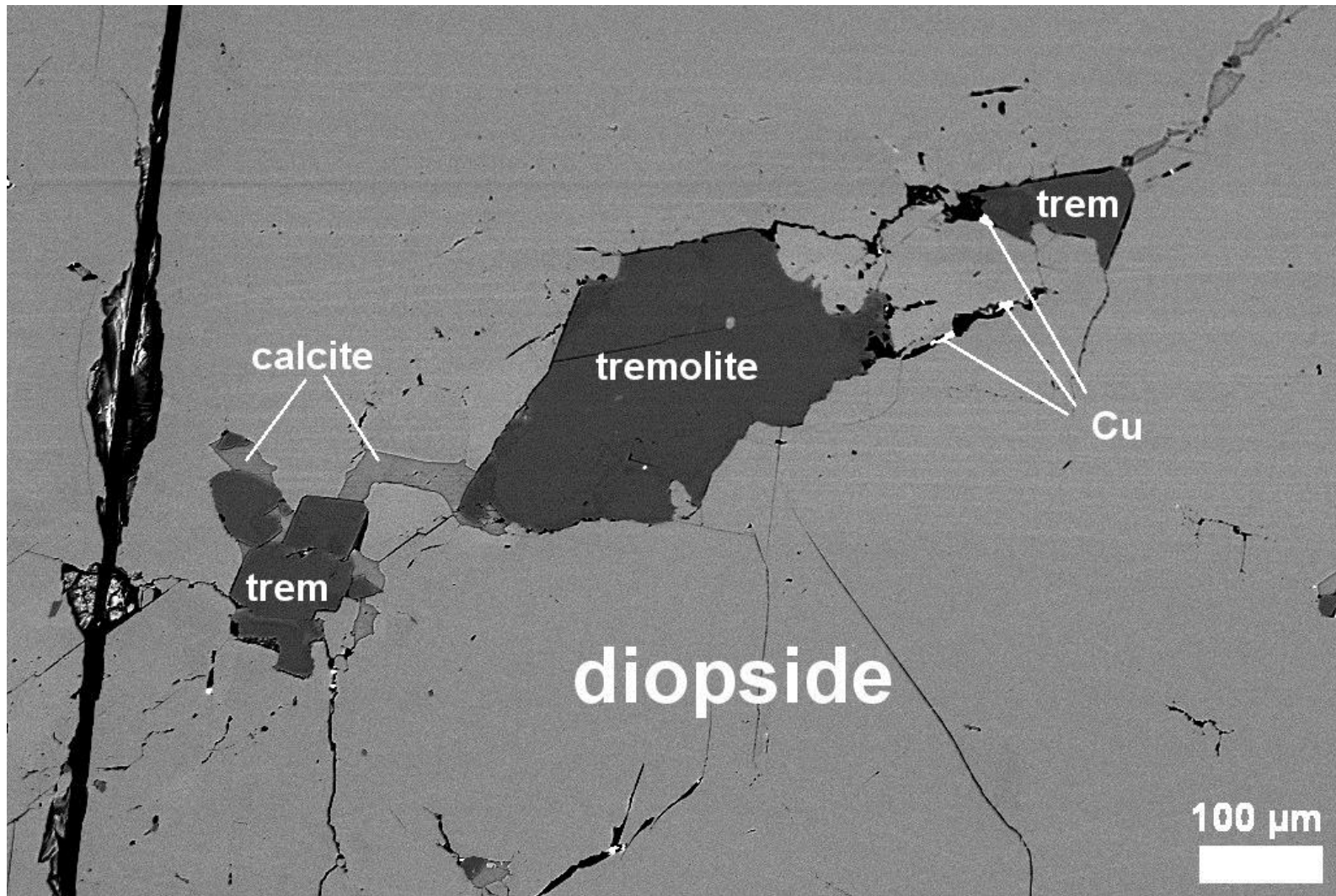


Figure A.04: SEM-BSD image of a heterogeneous zone of Diopside_7, showing tremolite phases and inclusions of calcite and metallic Cu.

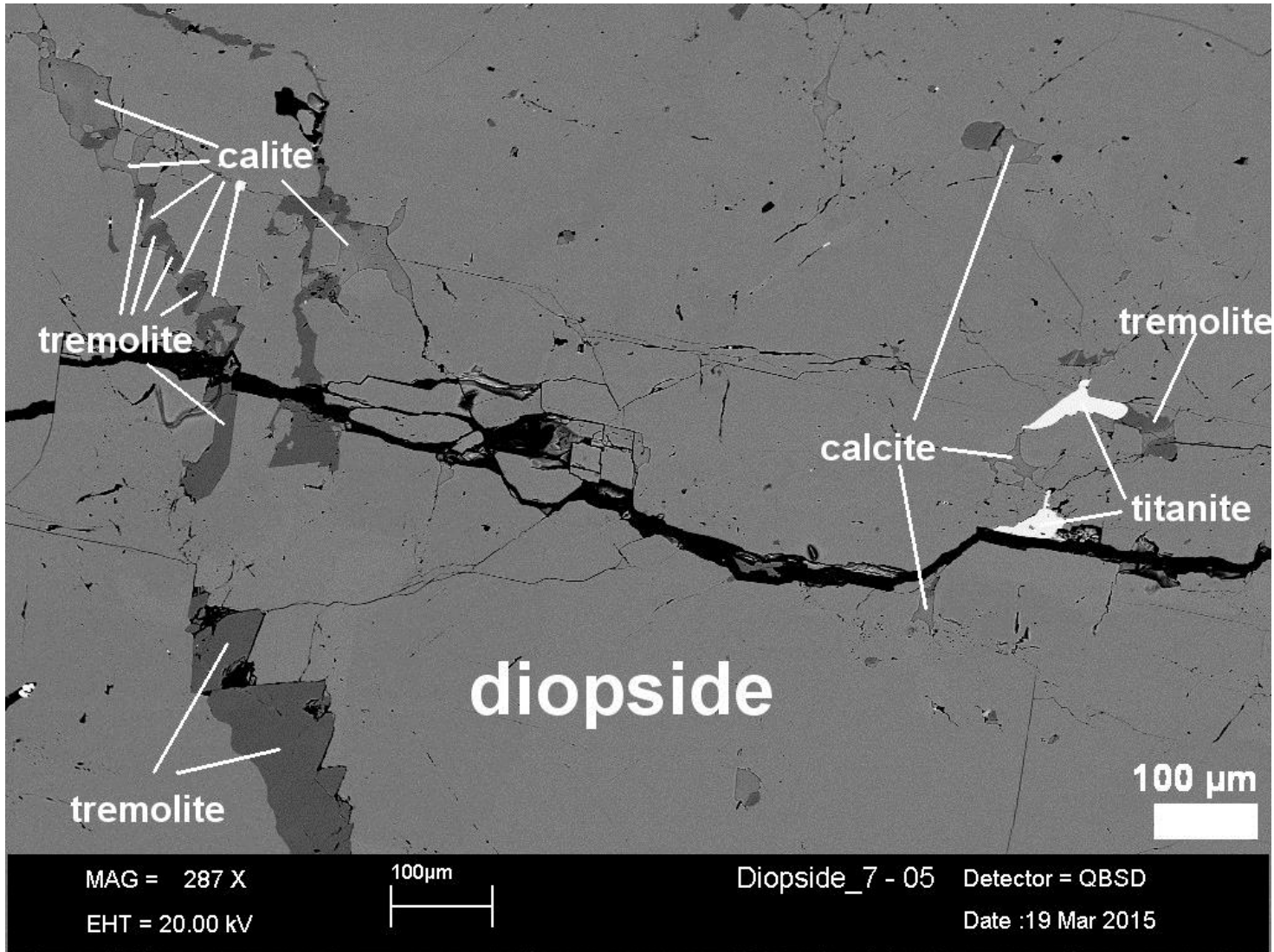


Figure A.02: SEM-BSD image of a heterogeneous zone of Diopside_7, showing tremolite phases and inclusions of calcite and titanite.

Table A.06: Composition the tremolite inclusions of Diopside_7 target acquired with EMP.

Mineral	tremolite	mean	st.dev.	min	max									
SiO₂	58.48	58.00	58.40	57.96	57.94	57.93	58.13	57.78	57.73	57.52	57.99	0.29	57.52	58.48
TiO₂	.03	.04	.05	.06	.02	.07	.19	.09	.12	.23	0.09	0.07	0.02	0.23
Al₂O₃	.06	.09	.13	.11	.11	.17	.07	.22	.24	.14	0.13	0.06	0.06	0.24
Cr₂O₃	.02	.05	.12	.06	.09	.01	.00	.03	.04	.00	0.04	0.04	0.00	0.12
Fe₂O₃	.00	.00	.00	.00	.00	.00	.00	.00	.00	.00	0.00	0.00	0.00	0.00
FeO	2.77	2.78	2.79	2.69	2.65	2.75	2.67	2.59	2.73	2.57	2.70	0.08	2.57	2.79
MnO	.02	.06	.01	.04	.05	.03	.02	.03	.03	.10	0.04	0.03	0.01	0.10
NiO	.00	.00	.05	.00	.06	.05	.00	.02	.05	.02	0.03	0.02	0.00	0.06
MgO	22.67	22.64	22.73	22.63	22.53	22.41	22.70	22.69	22.54	22.51	22.60	0.10	22.41	22.73
CaO	13.01	12.50	12.45	12.32	12.05	10.97	9.85	9.57	9.53	9.51	11.18	1.44	9.51	13.01
Na₂O	.40	.70	.65	.75	.69	1.35	2.19	2.03	2.30	2.37	1.34	0.80	0.40	2.37
K₂O	.59	1.04	1.01	1.06	1.08	2.12	2.56	2.78	2.82	3.06	1.81	0.94	0.59	3.06
H₂O	2.29	2.28	2.29	2.27	2.27	2.27	2.28	2.26	2.27	2.26	2.27	0.01	2.26	2.29
Σ oxides	100.34	100.18	100.67	99.95	99.55	100.12	100.65	100.09	100.38	100.30	100.22	0.33	99.55	100.67
Si	7.660	7.635	7.643	7.640	7.661	7.656	7.655	7.651	7.637	7.628	7.65	0.01	7.63	7.66
Ti	0.003	0.004	0.005	0.006	0.002	0.007	0.019	0.009	0.012	0.023	0.01	0.01	0.00	0.02
Al	0.009	0.013	0.019	0.018	0.017	0.026	0.010	0.034	0.038	0.023	0.02	0.01	0.01	0.04
Cr	0.002	0.005	0.013	0.006	0.010	0.001	0.000	0.003	0.004	0.000	0.00	0.00	0.00	0.01
Fe³⁺	0.000	0.000	0.000	0.000	0.000	0.000	0.000	0.000	0.000	0.000	0.00	0.00	0.00	0.00
Fe²⁺	0.304	0.306	0.305	0.297	0.293	0.304	0.294	0.287	0.302	0.285	0.30	0.01	0.29	0.31
Mn	0.002	0.007	0.001	0.004	0.005	0.003	0.002	0.003	0.003	0.011	0.00	0.00	0.00	0.01
Ni	0.000	0.000	0.005	0.000	0.006	0.005	0.000	0.002	0.005	0.002	0.00	0.00	0.00	0.01
Mg	4.427	4.442	4.435	4.447	4.441	4.415	4.457	4.478	4.445	4.450	4.44	0.02	4.41	4.48
Ca	1.825	1.763	1.746	1.740	1.707	1.554	1.390	1.357	1.350	1.352	1.58	0.20	1.35	1.82
Na	0.102	0.178	0.164	0.192	0.176	0.346	0.559	0.522	0.589	0.610	0.34	0.21	0.10	0.61
K	0.098	0.174	0.169	0.178	0.183	0.357	0.430	0.470	0.475	0.518	0.31	0.16	0.10	0.52
OH	2.000	2.000	2.000	2.000	2.000	2.000	2.000	2.000	2.000	2.000	2.00	0.00	2.00	2.00
Σ octa	14.431	14.528	14.503	14.527	14.503	14.675	14.816	14.817	14.862	14.902	14.66	0.18	14.43	14.90

Tremolite was calculated with 2 OH groups given from the ideal structural formula: $\square\text{Ca}_2(\text{Mg}_{5.0-4.5}\text{Fe}^{2+}_{0.0-0.5})\text{Si}_8\text{O}_{22}(\text{OH})_2$

Table A.06: (Left) Composition of titanite inclusions of Diopside_7 target acquired with EMP, without detecting for REE and flour.

Table A.07: (Right) Composition of calcite inclusions of Diopside_7 target acquired with EMP, without detecting for carbon.

Mineral	titanite	titanite	titanite	mean	st.dev.	min	max	Mineral	Calcite	Calcite	Calcite	Calcite	Calcite	Calcite	mean	st.dev.	min	max
SiO₂	29.90	29.76	29.38	29.68	.27	29.38	29.90	SiO₂	.05	.02	.07	.03	.02	.01	.03	.02	.01	.07
TiO₂	37.57	38.73	37.82	38.04	.61	37.57	38.73	TiO₂	.00	.00	.08	.00	.01	.00	.02	.03	.00	.08
Al₂O₃	.00	.00	.00	.00	.00	.00	.00	Al₂O₃	.00	.00	.01	.01	.00	.00	.00	.00	.00	.01
Cr₂O₃	1.70	.54	.93	1.06	.59	.54	1.70	Cr₂O₃	.02	.02	.00	.02	.00	.00	.01	.01	.00	.02
Fe₂O₃	.68	.79	.64	.71	.08	.64	.79	Fe₂O₃	.11	.02	.22	.12	.12	.03	.10	.07	.02	.22
FeO	.00	.00	.00	.00	.00	.00	.00	FeO	.00	.00	.00	.00	.00	.00	.00	.00	.00	.00
MnO	.00	.00	.00	.00	.00	.00	.00	MnO	.09	.04	.06	.00	.07	.07	.05	.03	.00	.09
NiO	.02	.07	.02	.03	.03	.02	.07	NiO	.03	.00	.02	.01	.02	.00	.01	.01	.00	.03
MgO	.00	.00	.00	.00	.00	.00	.00	MgO	.08	.13	.39	1.24	.11	.00	.32	.47	.00	1.24
CaO	28.08	27.75	27.41	27.74	.33	27.41	28.08	CaO	56.72	55.80	55.45	53.94	53.68	52.78	54.73	1.49	52.78	56.72
Na₂O	.01	.04	.05	.03	.02	.01	.05	Na₂O	.04	.00	.01	.02	.02	.02	.02	.01	.00	.04
K₂O	.00	.00	.01	.00	.00	.00	.01	K₂O	.00	.00	.01	.02	.00	.00	.01	.01	.00	.02
Σ oxides	97.96	97.68	96.26	97.30	.91	96.26	97.96	Σ oxides	57.13	56.01	56.30	55.41	54.05	52.91	55.30	1.56	52.91	57.13
Si	1.002	0.998	1.000	1.00	.00	1.00	1.00	Si	0.002	0.001	0.003	0.002	0.001	0.001	.00	.00	.00	.00
Ti	0.947	0.977	0.968	.96	.02	.95	.98	Ti	0.000	0.000	0.003	0.000	0.001	0.000	.00	.00	.00	.00
Al	0.000	0.000	0.000	.00	.00	.00	.00	Al	0.000	0.000	0.000	0.000	0.000	0.000	.00	.00	.00	.00
Cr	0.045	0.014	0.025	.03	.02	.01	.05	Cr	0.001	0.001	0.000	0.001	0.000	0.000	.00	.00	.00	.00
Fe³⁺	0.017	0.020	0.016	.02	.00	.02	.02	Fe³⁺	0.004	0.001	0.008	0.004	0.005	0.001	.00	.00	.00	.01
Fe²⁺	0.000	0.000	0.000	.00	.00	.00	.00	Fe²⁺	0.000	0.000	0.000	0.000	0.000	0.000	.00	.00	.00	.00
Mn	0.000	0.000	0.000	.00	.00	.00	.00	Mn	0.004	0.002	0.003	0.000	0.003	0.003	.00	.00	.00	.00
Ni	0.000	0.002	0.001	.00	.00	.00	.00	Ni	0.001	0.000	0.001	0.000	0.001	0.000	.00	.00	.00	.00
Mg	0.000	0.000	0.000	.00	.00	.00	.00	Mg	0.006	0.009	0.028	0.093	0.009	0.000	.02	.03	.00	.09
Ca	1.008	0.997	0.999	1.00	.01	1.00	1.01	Ca	2.976	2.985	2.943	2.893	2.977	2.993	2.96	.04	2.89	2.99
Na	0.000	0.003	0.003	.00	.00	.00	.00	Na	0.003	0.000	0.001	0.001	0.002	0.002	.00	.00	.00	.00
K	0.000	0.000	0.000	.00	.00	.00	.00	K	0.000	0.000	0.000	0.001	0.000	0.000	.00	.00	.00	.00
Σ octa	3.020	3.010	3.013	3.01	.01	3.01	3.02	Σ octa	2.997	2.999	2.990	2.997	2.998	2.999	3.00	.00	2.99	3.00

Beside inclusion of metallic Copper (Cu, Si, O, Fe: detected with SEM-BSD) and calcite, there is also titanite and can be expressed in structural formula: $\text{Ca}_{1.00}(\text{Ti}_{0.96} \text{Cr}_{0.3} \text{Fe}^{3+}_{0.1})_{\Sigma=1.00} \text{Si}_{1.00} \text{O}_5$ (neglecting possible REE and F) .

Table A.08: Composition of other indeterminable phases measured in Diopside_7 target acquired with EMP.

Mineral	Other A	Other B	Other C	Other C
SiO₂	22.83	43.09	39.71	35.49
TiO₂	.02	.39	.09	.14
Al₂O₃	.01	10.64	.05	.03
Cr₂O₃	.09	.03	.11	.11
Fe₂O₃	.00	.00	.00	.00
FeO	.83	5.76	1.55	1.30
MnO	.04	.03	.07	.13
NiO	.00	.02	.03	.00
MgO	3.55	25.31	3.33	3.06
CaO	8.85	.15	19.11	15.78
Na₂O	.32	.04	.00	.41
K₂O	.04	10.20	.03	.09
Σ oxides	36.57	95.65	64.09	56.55

Appendix B: R-script

The R-script source code for 3D presentation of the exported height values from VK-Analyzer.

```
library(rgl)
setwd("c:/R")

hight_data_variable <- read.csv2(file="FILENAME.csv",head=FALSE,sep=";",skip=52)

all_data <- as.matrix(hight_data_variable)

z <- all_data
x<-c(1:dim(z)[1])
y<-c(1:dim(z)[2])

nbc0l = 50
color = rev(rainbow(nbc0l, start = 0, end = 0.7))
zcol = cut(z, nbc0l)

persp3d(x, y, z,zlab="height", xlab="legnth [pixels]", ylab="width [pixels]", col=color[zcol], aspect
= c(9,12,1)
```

```
library(rgl)
```

```
# Calls the library rgl, that provides functions for 3D interactive graphics.
```

```
setwd("c:/R")
```

```
# Sets the working directory.
```

```
hight_data_variable <- read.csv2(file="FILENAME.csv",head=FALSE,sep=";",skip=52)
```

Opens the *.csv-file exported from the VK-Analyzer, and skip all rows until 52, and puts all values into a variable named *hight_data_variable*. The *.csv-file stores absolute height values per pixel in spreadsheet that has 2048 columns and 1536 rows (resolution of the image). The first 52 row are information of about measurement conditions and of no use for 3D plotting.

```
all_data <- as.matrix(hight_data_variable)
```

```
# Transforms the imported data into a matrix named all_data.
```

```
z <- all_data
```

```
x<-c(1:dim(z)[1])
```

```
y<-c(1:dim(z)[2])
```

```
# Data of matrix is assigned to xyz-coordinates, with variables named x, y and z.
```

```
nbcol = 50
color = rev(rainbow(nbcol, start = 0, end = 0.7))
zcol = cut(z, nbcol)
# Defines a colour scheme in dependency of z-values for the 3d plotting. It uses
rainbow colours divided into 50 steps, starting a colour no. 0 and end at 70%.

persp3d(x, y, z, zlab="height", xlab="length [pixels]", ylab="width [pixels]", col=color[zcol],
aspect = c(9,12,1)
# Uses the function persp3d() from the rgl library, to plot the variables x, y and z,
labels all axis, by using the defined colouration and the set display aspect ratio
(x : y : z = 9 : 12 : 1).
```

Appendix C: Material properties

In a LGG experiment with aluminium spheres shot in to dry quartz sand BRASLAU (1970) computed energy conversion and stated that 53 % is absorbed by the ejecta, 26% into target heating, 20% or less to compaction and 10–20 % to pulverisation, depending on the target material. Although partitioning of these constraints in a solid material is different, to understand the conversion of impact energy is important. In a different study MERZHIEVSKY (1997) stated that 30 % of the projectiles kinetic energy is transformed into evaporation. And hence material properties and deformation behaviour needs to be understood.

In Table C.01 some values that might influence a target's impact behaviour are listed: Density ρ [g/cm³], Vicker hardness HK, Poisson's ratio ν , bulk modulus K , shear modulus G , Young's modulus E , ultimate tensile strength R_{UTS} and thermal expansion α . Ductility, melting points and other temperature thresholds are not listed due to lack of information at that point.

Table C.01: Not every physical property could be found in scientific publication or industry's material specifications, which are mainly due to lack missing tests. These related cells are left blank. For some missing values of ν , K , G and E the conversion formulas were used for transformation if necessary. Concerning stainless steel, values of five different stainless steel alloys (UNS-J92701, UNS-J93000; UNS-S20161; UNS-S30400; UNS-S35315) have been abstracted to one average value.

Target-material	Abbreviation	mean ρ [g/cm ³]	mean HK	mean ν	mean K [Mpa]	mean G [Mpa]	mean E [Mpa]	mean R_{UTS} [Mpa]	mean α [10 ⁻⁶ /K]
Fused quartz	FQ	2.20	655	0.23	37.0	30.0	72.4	50.0	0.5
Soda lime glass	SLG	2.51	570	0.17	43.0	29.8	72.0	110.5	8.9
Borosilicate Glass	Boros	2.40	510	0.21	43.0	31.0	74.5	280.0	4.2
Aluminum Plates	AlMg3	2.68	60	0.33	71.0	27.0	71.0	270.0	24.0
Aluminum 1100	A91100	2.76	45	0.33	93.9	26.0	82.9	128.0	23.8
α Olv-Forsterite (Mg)	Fo	3.31	1100	0.24	126.5	78.2	194.0		26.5
β Olv-Wadsleyite	Wads	3.84		0.23	168.0	110.1	264.0		
Plagioclase (Albit)	Albit	2.62		0.25	59.0	34.5	81.5		18.5
Feldspar (Bytonite)	Byto	2.73	560	0.29	80.0	36.0	93.3		
Copper (99,95%)	Cu	8.95	209	0.34	126.0	44.0	115.0	315.0	16.8
Iron	Fe	7.87	647	0.29	170.0	82.0	211.0	275.0	11.8
Stainless Steel (average)	StSt	7.85	232.80	0.28	156.8	80.5	205.4	673.5	14.6
Epoxy	Epox	1.30		0.4	4.3	0.9	2.4	67.0	72.5
Polystyrene divinylbenzene	PS-DVB	1.03	32	0.4	5.5	1.2	3.3	38.0	89.0

The parameters in Table C.01 are derived from different source .

Books & publications:

- BAOSHENG, LI; LIEBERMANN, ROBERT C. & WEIDNER, DONALD J. 1998. *Elastic Moduli of Wadsleyite (β -Mg₂SiO₄) to 7 Gigapascals and 873 Kelvin*. Science, Vol. 281, Issue 5377, pp 675–677
- BOUHFID, M. A., ANDRAULT, D. FIQUET, G. & RICHTER, P. 1996. *Thermal expansion of forsterite up to the melting point*. Geophysical Research Letters, Vol. 23, No. 10, pp 1143–1146.
- COLLINS, M. D. & BROWN, J. M. 1998. *Elasticity of upper mantle clinopyroxene*. Physics and Chemistry of Minerals, Vol. 26, Issue 1, pp 7–13.
- KRAR STEVE & GILL ARTHUR. 2003. *Exploring advanced manufacturing technologies*. Industrial Press, 448 p.
- PABST, WILLI; GREGOROVA, EVA; RAMBALDI, ELISA & BIGNOZZI, MARIA CHIARA. 2015. *Effective elastic constants of plagioclase feldspar aggregates in dependence of the anorthite content – A concise review*. Ceramics-Silikáty, issue 59(4), pp 326–330
- REICHMANN, HANS J.; SINOGEIKIN, STANISLAV V.; BASS, JAY D. & GASPARIK TIBOR. 2002. *Elastic Moduli of Jadeit-Enstatite Majorite*. Geophysical Research Letters, vol. 29, issue 19, pp 42-1–42-4.
- STEWART, D. B. & VON LIMBACH, DORA. 1967. *Thermal expansion of low and high Albite*. American Mineralogist, Vol. 52, pp 389–413.

Websites for material sciences and parameters and documents:

- *Mineral Standards* (PDF) on https://dawn.jpl.nasa.gov/DawnClassrooms/3_instrument/ (accessed on 2017-02-24)
- <http://www.matweb.com/> (accessed on 2017-02-24)
- <http://www.makeitfrom.com> (accessed on 2017-02-24)
- <http://ruby.colorado.edu/~smyth/min/minerals.html> (accessed on 2017-02-24)

Appendix D: Data

Table D.01: Spreadsheet of all measurements acquired by random sampling on the non-bombarded Olivine_7 target.

ID	type	Feature	D ₁	D ₂	D ₃	D ₄	mean D	d ₁	d ₂	d ₃	d ₄	mean d
1	N ₂	pit	0.256	0.207	0.197	0.177	0.209	-0.047	-0.048	-0.051	-0.032	-0.045
2	P ₁	dust	1.262	1.522	1.050	1.381	1.304	0.612	0.654	0.551	0.762	0.645
3	N ₂	pit	0.354	0.559	0.495	0.480	0.472	-0.031	-0.029	-0.031	-0.026	-0.029
4	N ₂	pit	0.333	0.367	0.495	0.322	0.379	-0.035	-0.031	-0.034	-0.039	-0.035
5	N ₂	pit	0.229	0.217	0.273	0.373	0.273	-0.008	-0.008	-0.015	-0.010	-0.010
6	N ₂	pit	0.281	0.171	0.294	0.220	0.242	-0.009	-0.009	-0.007	-0.015	-0.010
7	N ₂	pit	0.254	0.484	0.468	0.459	0.416	-0.022	-0.021	-0.027	-0.025	-0.024
8	P ₁	dust	1.074	2.054	1.914	1.167	1.552	0.886	0.943	0.871	1.019	0.930
9	P ₂	rough	0.903	1.382	0.673	0.634	0.898	0.014	0.023	0.021	0.024	0.021
10	N ₂	pit	0.170	0.134	0.160	0.179	0.161	-0.040	-0.034	-0.033	-0.027	-0.034
11	N ₂	pit	0.175	0.169	0.146	0.175	0.166	-0.021	-0.012	-0.014	-0.016	-0.016
12	P ₂	peak	0.473	0.711	0.492	0.396	0.518	0.278	0.369	0.364	0.373	0.346
13	N ₂	pit	0.124	0.158	0.158	0.137	0.144	-0.069	-0.054	-0.036	-0.045	-0.051
14	P ₂	rough	1.442	1.208	1.488	1.122	1.315	0.415	0.338	0.603	0.430	0.447
15	P ₂	rough	0.646	0.675	0.638	0.589	0.637	0.540	0.501	0.486	0.468	0.499
16	P ₂	rough	1.165	1.068	1.142	1.165	1.135	0.226	0.200	0.185	0.231	0.210
17	P ₂	rough	0.358	0.286	0.224	0.256	0.281	0.558	0.554	0.537	0.553	0.551
18	N ₂	pit	0.161	0.167	0.188	0.091	0.152	-0.013	-0.017	-0.015	-0.010	-0.014
19	P ₂	peak	0.319	0.252	0.215	0.286	0.268	-0.191	-0.182	-0.153	-0.170	-0.174
20	P ₂	peak	0.905	0.382	0.527	0.425	0.560	0.073	0.068	0.063	0.079	0.071
21	P ₂	peak	0.427	0.849	0.641	0.722	0.660	0.146	0.183	0.168	0.118	0.154
22	P ₂	peak	0.403	0.556	0.705	0.467	0.533	0.042	0.044	0.030	0.034	0.038
23	P ₂	peak	0.705	0.684	0.662	0.637	0.672	0.056	0.049	0.038	0.039	0.045
24	P ₂	rough	0.758	0.510	0.710	0.748	0.681	0.046	0.030	0.041	0.061	0.045
25	P ₂	rough	0.977	0.724	0.743	0.467	0.728	0.032	0.032	0.029	0.038	0.033
26	P ₂	rough	0.531	0.632	0.680	0.701	0.636	0.032	0.031	0.023	0.031	0.029
27	P ₂	rough	0.679	0.556	0.822	0.785	0.711	0.023	0.020	0.025	0.031	0.025
28	P ₂	peak	0.297	0.495	0.645	0.666	0.526	0.025	0.036	0.045	0.031	0.034
29	P ₂	peak	0.382	0.387	0.297	0.295	0.340	0.019	0.029	0.018	0.025	0.023
30	P ₂	rough	1.154	2.866	1.889	1.422	1.833	0.043	0.056	0.043	0.055	0.049
31	P ₂	peak	0.573	0.662	0.722	0.639	0.649	0.070	0.065	0.086	0.092	0.078
32	P ₂	peak	0.807	0.688	0.464	0.641	0.650	0.024	0.024	0.022	0.026	0.024
33	P ₂	peak	0.616	0.925	0.556	0.598	0.674	0.042	0.032	0.026	0.032	0.033
34	P ₂	peak	0.403	0.624	0.754	0.833	0.654	0.029	0.034	0.041	0.033	0.034
35	P ₂	rough	1.019	0.977	1.146	1.104	1.061	0.030	0.038	0.037	0.031	0.034
36	P ₂	rough	0.637	0.620	0.946	0.455	0.664	0.022	0.027	0.024	0.020	0.023
37	P ₂	peak	0.402	0.368	0.530	0.363	0.416	0.021	0.017	0.018	0.028	0.021
38	P ₂	peak	0.297	0.701	0.637	0.427	0.515	0.028	0.039	0.032	0.031	0.033
39	P ₂	peak	0.553	0.405	0.512	0.630	0.525	0.017	0.031	0.018	0.032	0.024
40	P ₂	peak	0.585	0.553	0.457	0.621	0.554	0.017	0.028	0.024	0.022	0.023
41	P ₂	rough	1.052	0.589	0.645	0.779	0.766	0.028	0.019	0.034	0.028	0.027
42	P ₂	peak	0.252	0.274	0.453	0.393	0.343	0.026	0.025	0.032	0.022	0.026
43	P ₂	rough	0.612	0.439	0.497	0.658	0.552	0.034	0.024	0.019	0.034	0.028
44	P ₂	peak	0.245	0.439	0.464	0.278	0.357	0.034	0.027	0.034	0.030	0.031
45	P ₂	rough	0.470	0.662	0.645	0.727	0.626	0.017	0.026	0.022	0.017	0.020

46	P ₂ peak	0.505	0.475	0.239	0.311	0.383	0.026	0.025	0.022	0.032	0.026
47	N ₁ defect	7.834	2.833	3.633	4.828	4.782	-4.741	-3.822	-4.529	-4.582	-4.418
48	N ₁ defect	26.631	14.801	34.509	18.526	23.617	-6.400	-5.793	-7.211	-5.962	-6.341
49	P ₂ peak	0.475	0.442	0.553	0.490	0.490	0.034	0.041	0.027	0.034	0.034
50	P ₂ peak	0.313	0.366	0.420	0.457	0.389	0.030	0.027	0.022	0.027	0.026
51	P ₂ peak	0.493	0.700	0.575	0.405	0.543	0.032	0.032	0.047	0.038	0.037
52	P ₂ rough	0.882	1.226	0.989	0.866	0.991	0.044	0.022	0.024	0.039	0.032
53	P ₂ rough	0.919	0.855	0.849	0.849	0.868	0.024	0.021	0.025	0.024	0.023
54	P ₂ rough	0.457	0.339	0.424	0.567	0.447	0.025	0.020	0.014	0.018	0.019
55	P ₂ rough	0.420	0.718	0.530	0.548	0.554	0.025	0.021	0.031	0.035	0.028
56	P ₂ rough	1.023	0.501	0.891	0.939	0.839	0.023	0.031	0.033	0.023	0.028
57	P ₂ rough	0.737	0.558	0.635	0.571	0.625	0.022	0.022	0.024	0.025	0.023
58	P ₂ rough	0.768	0.658	0.859	0.816	0.775	0.036	0.036	0.021	0.029	0.030
59	P ₂ rough	0.585	0.355	0.755	0.617	0.578	0.018	0.016	0.021	0.021	0.019
60	P ₂ rough	0.987	0.921	0.774	0.969	0.912	0.020	0.015	0.027	0.025	0.022
61	P ₂ rough	0.931	0.987	1.197	1.133	1.062	0.027	0.024	0.029	0.032	0.028
62	P ₂ rough	0.932	1.088	0.987	1.042	1.012	0.025	0.023	0.023	0.032	0.026
63	P ₂ rough	1.169	0.928	1.068	1.123	1.072	0.029	0.027	0.027	0.019	0.025
64	P ₂ rough	0.512	0.774	0.829	0.774	0.722	0.027	0.038	0.033	0.027	0.031
65	P ₂ rough	0.749	1.087	0.658	0.671	0.791	0.025	0.025	0.027	0.020	0.024
66	P ₂ rough	0.724	0.829	0.786	1.071	0.852	0.033	0.027	0.026	0.020	0.026
67	P ₂ rough	1.005	0.914	0.810	0.804	0.883	0.023	0.028	0.028	0.030	0.027
68	P ₂ rough	0.946	1.087	1.499	1.115	1.162	0.026	0.019	0.019	0.020	0.021
69	P ₂ rough	0.804	1.076	1.188	1.188	1.064	0.024	0.025	0.031	0.018	0.025
70	P ₂ rough	0.987	0.618	1.386	0.883	0.968	0.013	0.014	0.012	0.010	0.012
71	P ₂ rough	0.548	0.768	0.806	0.791	0.728	0.013	0.014	0.014	0.011	0.013
72	N ₂ rough, pit	0.430	0.977	1.466	0.495	0.842	-0.044	-0.037	-0.024	-0.032	-0.034
73	N ₂ rough, pit	0.488	0.437	0.297	0.517	0.435	-0.032	-0.029	-0.034	-0.023	-0.029
74	N ₂ rough, pit	0.166	0.284	0.666	0.252	0.342	-0.019	-0.019	-0.025	-0.028	-0.023
75	N ₁ defect	1.133	0.602	1.199	0.934	0.967	-0.065	-0.074	-0.070	-0.072	-0.070
76	N ₁ defect	0.898	1.125	1.154	0.769	0.986	-0.066	-0.066	-0.069	-0.058	-0.065
77	N ₁ defect	1.400	0.786	0.786	1.271	1.061	-0.138	-0.085	-0.104	-0.107	-0.108
78	N ₁ defect	0.774	0.987	1.002	0.902	0.916	-0.225	-0.218	-0.188	-0.183	-0.203
79	N ₂ rough, pit	1.078	1.216	1.261	1.097	1.163	-0.054	-0.053	-0.059	-0.060	-0.056
80	P ₂ peak	0.261	0.628	0.583	0.526	0.499	0.031	0.027	0.032	0.036	0.031
81	N ₁ defect	2.023	0.976	1.455	1.316	1.442	-0.111	-0.055	-0.063	-0.075	-0.076
82	N ₁ defect	1.577	0.645	0.950	0.603	0.944	-0.042	-0.041	-0.037	-0.037	-0.039
83	N ₁ defect	2.118	1.087	1.005	1.676	1.471	-0.114	-0.177	-0.249	-0.180	-0.180
84	N ₁ defect	1.197	0.792	0.700	0.852	0.885	-0.036	-0.043	-0.038	-0.047	-0.041
85	N ₁ defect	1.225	0.368	0.932	0.676	0.800	-0.044	-0.020	-0.021	-0.032	-0.029
86	N ₁ defect	1.308	0.909	1.050	0.731	0.999	-0.137	-0.074	-0.118	-0.062	-0.098
87	N ₁ defect	0.911	1.063	1.154	0.835	0.991	-0.081	-0.065	-0.058	-0.071	-0.069
88	N ₂ rough, pit	0.395	0.782	0.631	0.337	0.536	-0.031	-0.026	-0.029	-0.022	-0.027
89	N ₂ pit	0.323	0.266	0.188	0.207	0.246	-0.025	-0.020	-0.020	-0.016	-0.020
90	N ₁ defect	1.613	1.210	1.380	1.453	1.414	-0.100	-0.093	-0.099	-0.101	-0.098
91	N ₁ defect	1.553	0.727	0.950	0.571	0.950	-0.052	-0.033	-0.033	-0.037	-0.039
92	N ₁ defect	1.050	1.133	1.736	1.042	1.240	-0.136	-0.141	-0.133	-0.150	-0.140
93	N ₁ defect	1.197	1.484	1.352	1.308	1.335	-0.096	-0.080	-0.086	-0.093	-0.089
94	N ₁ defect	1.132	0.567	0.737	0.621	0.764	-0.037	-0.031	-0.041	-0.026	-0.034
95	P ₂ peak	0.460	0.361	0.234	0.334	0.347	0.038	0.031	0.025	0.026	0.030

96	P ₂ rough	0.531	0.471	0.451	0.368	0.455	0.051	0.054	0.044	0.050	0.050
97	N ₁ defect	1.364	0.759	1.108	1.169	1.100	-0.091	-0.078	-0.080	-0.089	-0.085
98	N ₁ defect	0.843	1.036	0.919	0.835	0.908	-0.085	-0.081	-0.073	-0.067	-0.076
99	N ₂ pit	0.197	0.182	0.196	0.152	0.182	-0.027	-0.018	-0.026	-0.026	-0.024
100	N ₁ defect	0.744	1.226	0.751	0.698	0.855	-0.043	-0.032	-0.034	-0.025	-0.034
101	N ₁ defect	2.818	1.677	1.239	2.607	2.085	-0.258	-0.200	-0.043	-0.239	-0.185
102	N ₁ defect	27.419	15.583	24.819	17.938	21.440	-0.550	-0.617	-0.719	-0.615	-0.626
103	N ₁ defect	5.385	2.672	3.588	3.128	3.693	-0.389	-0.767	-0.624	-0.469	-0.562
104	N ₂ pit	0.169	0.127	0.120	0.122	0.134	-0.021	-0.027	-0.020	-0.029	-0.024
105	N ₁ defect	6.224	5.072	6.954	5.711	5.990	-0.415	-0.491	-0.606	-0.329	-0.460
106	N ₁ defect	5.369	3.275	3.494	3.932	4.018	-0.334	-0.325	-0.333	-0.383	-0.344
107	P ₂ rough	1.044	0.995	0.950	1.076	1.016	0.068	0.069	0.058	0.055	0.063
108	P ₂ rough	0.987	0.828	1.206	1.060	1.020	0.078	0.064	0.060	0.080	0.071
109	P ₂ rough	1.097	1.123	1.115	1.188	1.131	0.109	0.116	0.114	0.108	0.112
110	P ₂ rough	1.076	0.700	1.031	1.050	0.964	0.041	0.046	0.051	0.061	0.050
111	P ₂ rough	0.589	0.505	0.516	0.653	0.566	0.024	0.025	0.027	0.027	0.026
112	P ₂ rough	0.744	0.829	0.841	0.914	0.832	0.069	0.058	0.058	0.071	0.064
113	P ₂ rough	0.402	0.368	0.402	0.445	0.404	0.035	0.035	0.035	0.035	0.035
114	N ₁ defect	4.616	2.536	2.563	3.674	3.347	-0.336	-0.310	-0.285	-0.440	-0.343
115	N ₁ defect	7.355	4.879	4.936	5.300	5.617	-0.212	-0.565	-0.514	-0.416	-0.427
116	N ₁ defect	8.265	4.879	4.413	6.650	6.052	-0.429	-0.444	-0.422	-0.436	-0.433
117	P ₂ peak	0.644	0.690	0.620	0.592	0.636	0.057	0.075	0.078	0.089	0.075
118	N ₁ defect	1.913	1.237	1.594	1.349	1.523	-0.144	-0.187	-0.166	-0.188	-0.171
119	P ₂ peak	0.186	0.199	0.299	0.158	0.210	0.045	0.026	0.024	0.021	0.029
120	P ₂ peak	0.380	0.486	0.471	0.425	0.440	0.458	0.439	0.453	0.431	0.445
121	N ₁ Defect	2.823	2.244	2.590	2.436	2.523	-0.288	-0.611	-0.721	-0.604	-0.556
122	P ₂ rough	1.169	1.456	1.287	1.230	1.285	0.240	0.235	0.217	0.235	0.232
123	N ₁ defect	1.701	1.427	1.427	1.549	1.526	-0.354	-0.731	-0.543	-0.652	-0.570
124	P ₂ rough	0.974	0.531	0.829	0.653	0.747	0.069	0.041	0.050	0.043	0.051
125	P ₂ rough	0.865	0.790	1.002	0.873	0.882	0.128	0.122	0.117	0.115	0.121
126	P ₂ rough	0.410	0.598	0.638	0.582	0.557	0.038	0.049	0.047	0.033	0.042
127	P ₁ dust	63.779	29.048	24.707	27.830	36.341	5.422	4.987	5.114	5.176	5.175
128	N ₁ defect	34.304	11.656	32.736	31.318	27.504	-0.656	-0.622	-0.698	-0.628	-0.651
129	P ₂ peak	0.613	0.796	0.889	0.668	0.741	0.033	0.050	0.047	0.038	0.042
130	P ₂ peak	2.136	1.700	2.044	1.984	1.966	0.158	0.185	0.193	0.176	0.178
131	P ₂ peak	0.858	0.812	1.180	0.797	0.912	0.071	0.074	0.069	0.082	0.074
132	P ₂ peak	1.073	0.978	1.184	1.119	1.088	0.181	0.134	0.155	0.158	0.157
133	P ₂ peak	1.078	1.226	1.032	1.151	1.122	0.185	0.146	0.135	0.170	0.159
134	P ₂ peak	0.552	0.638	0.711	0.820	0.680	0.050	0.035	0.041	0.048	0.043
135	P ₂ rough	0.364	0.444	0.582	0.587	0.494	0.027	0.033	0.030	0.036	0.031
136	P ₂ peak	0.790	0.926	0.904	0.835	0.864	0.071	0.089	0.070	0.078	0.077
137	P ₂ rough	0.774	0.628	0.873	0.516	0.698	0.033	0.033	0.038	0.028	0.033
138	P ₂ rough	0.665	0.911	0.766	0.843	0.796	0.051	0.053	0.047	0.044	0.049
139	P ₂ rough	0.737	0.782	0.812	0.659	0.747	0.070	0.055	0.045	0.049	0.055
140	P ₂ rough	1.245	1.272	1.318	1.134	1.242	0.232	0.194	0.211	0.183	0.205
141	P ₂ peak	1.042	0.911	0.896	1.154	1.001	0.127	0.126	0.119	0.112	0.121
142	P ₂ rough	0.547	0.820	0.835	0.729	0.733	0.043	0.038	0.032	0.034	0.037
143	P ₂ peak	1.002	1.052	1.169	1.128	1.088	0.154	0.167	0.158	0.166	0.161
144	P ₂ peak	1.516	1.473	1.503	1.609	1.525	0.183	0.210	0.187	0.205	0.196
145	P ₂ peak	1.335	1.458	1.412	1.655	1.465	0.225	0.199	0.212	0.223	0.215
146	P ₂ peak	1.502	1.503	1.578	1.531	1.529	0.212	0.196	0.228	0.205	0.210
147	P ₂ rough	0.766	0.650	0.774	0.758	0.737	0.039	0.023	0.038	0.026	0.031

148	P ₂ peak	1.036	1.088	1.119	1.032	1.069	0.151	0.157	0.153	0.150	0.153
149	P ₂ rough	0.744	0.744	0.486	0.805	0.695	0.037	0.042	0.027	0.038	0.036
150	P ₂ peak	2.116	2.099	2.044	2.120	2.095	0.256	0.236	0.245	0.247	0.246
151	N ₁ defect	43.016	27.866	31.705	30.559	33.287	-0.697	-0.060	-0.465	-0.690	-0.478
152	N ₁ defect	7.060	3.437	3.172	4.464	4.533	-0.454	-0.444	-0.442	-0.380	-0.430
153	P ₂ peak	0.425	0.607	0.471	0.665	0.542	0.157	0.167	0.146	0.169	0.160
154	P ₂ rough	1.119	0.582	0.456	0.562	0.680	0.035	0.034	0.030	0.030	0.032
155	N ₂ rough, pit	0.847	1.050	1.097	0.822	0.954	-0.074	-0.081	-0.086	-0.082	-0.081
156	P ₂ peak	0.536	0.387	0.714	0.759	0.599	0.057	0.031	0.045	0.042	0.044
157	P ₂ peak	0.368	0.273	0.304	0.376	0.330	0.418	0.426	0.383	0.406	0.408
158	P ₂ peak	0.598	0.490	0.588	0.511	0.547	0.077	0.077	0.071	0.067	0.073
159	N ₂ pit	0.658	0.731	0.798	0.804	0.748	-0.062	-0.062	-0.075	-0.083	-0.070
160	P ₂ peak	0.804	0.841	0.658	0.713	0.754	0.092	0.080	0.074	0.080	0.082
161	P ₂ peak	0.768	0.658	0.884	0.841	0.788	0.208	0.218	0.217	0.195	0.209
162	P ₂ peak	0.534	0.424	0.548	0.696	0.550	0.370	0.385	0.359	0.243	0.339
163	P ₂ peak	0.364	0.217	0.402	0.356	0.335	0.346	0.296	0.219	0.312	0.293
164	N ₁ defect	1.915	0.854	0.785	0.859	1.103	-0.231	-0.306	-0.313	-0.341	-0.298
165	P ₂ rough	1.230	0.810	1.108	0.729	0.969	0.160	0.161	0.164	0.151	0.159
166	P ₂ peak	0.304	0.383	0.340	0.337	0.341	0.464	0.428	0.437	0.435	0.441
167	N ₁ defect	4.484	3.517	3.543	4.235	3.945	-0.711	-0.331	-0.557	-0.505	-0.526
168	N ₁ defect	1.510	0.859	1.133	1.179	1.170	-0.159	-0.065	-0.069	-0.090	-0.096
169	N ₁ defect	1.828	1.590	1.271	1.578	1.567	-0.351	-0.273	-0.379	-0.337	-0.335
170	N ₂ pit	0.847	0.798	0.884	0.689	0.805	-0.053	-0.051	-0.059	-0.052	-0.054
171	N ₂ rough, pit	0.990	0.928	0.873	0.812	0.901	-0.012	-0.118	-0.113	-0.098	-0.085
172	N ₂ rough, pit	0.810	1.261	1.151	0.631	0.963	-0.391	-0.289	-0.355	-0.232	-0.317
173	N ₂ rough, pit	1.837	1.032	1.379	1.073	1.330	-0.372	-0.299	-0.334	-0.261	-0.317
174	N ₂ rough, pit	0.759	0.797	1.048	0.552	0.789	-0.059	-0.076	-0.068	-0.070	-0.068
175	P ₂ peak	0.795	0.680	0.705	0.705	0.721	0.047	0.038	0.048	0.029	0.040
176	N ₂ pit	0.722	0.544	0.587	0.722	0.644	-0.088	-0.097	-0.103	-0.078	-0.091
177	N ₁ defect	16.777	13.791	14.408	15.988	15.241	-1.599	-1.985	-1.678	-1.786	-1.762
178	N ₁ defect	1.809	1.389	1.553	1.572	1.581	-0.193	-0.267	-0.317	-0.148	-0.231
179	N ₁ defect	1.676	0.921	0.969	0.847	1.103	-0.328	-0.307	-0.290	-0.288	-0.303
180	N ₁ defect	9.292	5.830	8.955	7.654	7.933	-0.631	-0.559	-0.911	-0.523	-0.656
181	N ₁ defect	6.613	1.773	3.354	1.612	3.338	-0.659	-0.621	-0.669	-0.641	-0.648
182	N ₂ pit	0.847	1.216	0.841	0.984	0.972	-0.067	-0.085	-0.085	-0.079	-0.079
183	N ₁ defect	4.646	3.494	4.256	3.462	3.964	-0.594	-0.445	-0.550	-0.452	-0.510
184	N ₁ defect	2.500	2.717	2.866	2.543	2.656	-0.721	-0.614	-0.744	-0.075	-0.539
185	P ₂ peak	1.397	1.078	1.197	0.850	1.131	0.105	0.100	0.095	0.100	0.100
186	P ₂ peak	1.134	0.805	0.851	0.820	0.902	0.055	0.028	0.073	0.041	0.049
187	P ₂ peak	0.406	0.567	0.475	0.410	0.464	0.042	0.053	0.045	0.042	0.045
188	P ₂ rough	1.473	0.650	1.057	1.078	1.064	0.435	0.392	0.431	0.377	0.409
189	P ₂ rough	0.623	0.484	0.634	0.668	0.602	0.030	0.031	0.041	0.044	0.037
190	N ₂ rough, pit	0.987	0.919	1.011	1.088	1.001	-0.088	-0.089	-0.088	-0.076	-0.085
191	P ₂ rough	0.592	0.835	0.644	0.820	0.723	0.025	0.040	0.035	0.035	0.034
192	P ₂ rough	0.607	0.572	0.547	0.562	0.572	0.030	0.031	0.025	0.032	0.030
193	P ₂ rough	0.972	0.744	0.912	1.160	0.947	0.037	0.034	0.036	0.032	0.035
194	P ₂ rough	0.628	0.707	0.632	0.736	0.676	0.033	0.027	0.025	0.040	0.031
195	P ₂ rough	1.093	0.704	0.398	0.782	0.745	0.020	0.026	0.023	0.022	0.023
196	P ₂ rough	0.572	0.572	0.790	0.444	0.595	0.019	0.029	0.023	0.018	0.022
197	P ₂ rough	0.850	0.471	0.661	0.715	0.674	0.020	0.018	0.023	0.020	0.020

198	N ₁ defect	3.216	3.259	3.794	3.198	3.367	-0.440	-0.525	-0.398	-0.499	-0.466
199	N ₁ defect	3.181	2.500	2.229	2.885	2.699	-0.342	-0.163	-0.302	-0.232	-0.260
200	P ₂ rough	0.851	1.088	0.841	0.749	0.882	0.050	0.056	0.039	0.042	0.047
201	P ₂ rough	1.546	0.598	0.782	0.850	0.944	0.061	0.025	0.051	0.027	0.041
202	N ₂ rough, pit	2.505	1.316	1.639	1.480	1.735	-0.093	-0.104	-0.106	-0.116	-0.105
203	N ₁ defect	51.113	33.222	13.619	8.419	26.593	-0.215	-0.190	-0.251	-0.298	-0.239
204	N ₁ defect	16.584	8.229	7.837	10.396	10.761	-2.881	-2.318	-2.322	-2.272	-2.448
205	P ₂ rough	1.553	1.535	1.480	1.553	1.531	0.095	0.085	0.075	0.072	0.082
206	P ₂ peak	1.027	0.607	0.705	0.790	0.782	0.120	0.107	0.095	0.105	0.107
207	N ₂ rough, pit	0.720	0.588	0.484	0.501	0.573	-0.031	-0.041	-0.033	-0.034	-0.035
208	P ₂ peak	0.301	0.322	0.276	0.356	0.314	0.387	0.377	0.360	0.377	0.375
209	P ₂ peak	0.531	0.486	0.547	0.501	0.516	-0.137	-0.129	-0.136	-0.149	-0.138
210	N ₂ rough, pit	0.935	0.868	1.195	0.990	0.997	-0.150	-0.146	-0.102	0.095	-0.076
211	N ₂ rough, pit	1.180	0.797	0.843	0.935	0.939	-0.181	-0.146	-0.154	-0.145	-0.156
212	N ₂ rough, pit	0.950	1.410	1.093	0.941	1.099	-0.214	-0.166	-0.246	-0.199	-0.206
213	P ₂ rough	1.215	0.820	0.628	0.850	0.878	0.067	0.059	0.064	0.055	0.061
214	P ₂ peak	0.364	0.322	0.402	0.364	0.363	0.459	0.458	0.457	0.429	0.451
215	P ₂ peak	0.429	0.398	0.390	0.402	0.405	0.440	0.458	0.465	0.432	0.449
216	P ₂ peak	0.319	0.598	0.536	0.319	0.443	0.020	0.026	0.025	0.017	0.022
217	P ₂ peak	0.398	0.449	0.429	0.464	0.435	0.411	0.416	0.387	0.414	0.407
218	P ₁ dust	4.379	1.248	1.702	1.639	2.242	0.161	0.163	0.149	0.162	0.159
219	P ₂ rough	1.225	0.976	1.023	1.133	1.089	0.224	0.213	0.229	0.212	0.220
220	P ₂ rough	1.683	1.133	1.316	1.216	1.337	0.153	0.125	0.144	0.155	0.144
221	P ₂ rough	0.607	0.690	0.598	0.607	0.626	0.049	0.031	0.036	0.038	0.039

Table D.02: Spreadsheet of all measurements acquired by random sampling on the bombarded Olivine_6 target in the region of major bombardment.

ID	type	Feature	D ₁	D ₂	D ₃	D ₄	mean D	d ₁	d ₂	d ₃	d ₄	mean d
1	D	dent	2.001	1.495	1.761	1.281	1.635	-0.031	-0.030	-0.034	-0.028	-0.031
2	A ₂	stuck	1.880	2.041	1.692	2.175	1.947	1.669	1.888	1.899	1.900	1.839
3	A ₂	stuck	0.742	0.744	0.755	0.644	0.721	0.296	0.238	0.268	0.246	0.262
4	N ₁	pit	0.489	0.179	0.223	0.449	0.335	-0.021	-0.023	-0.015	-0.021	-0.020
5	P ₂	peak	0.626	0.790	0.688	0.677	0.695	0.343	0.368	0.393	0.337	0.360
6	N ₁	pit	0.269	0.243	0.333	0.345	0.297	-0.023	-0.022	-0.021	-0.022	-0.022
7	A ₂	stuck	0.779	0.682	0.823	0.563	0.712	0.306	0.273	0.305	0.273	0.289
8	P ₂	peak	0.423	0.434	0.487	0.372	0.429	0.363	0.389	0.383	0.371	0.377
9	N ₁	pit	0.349	0.240	0.210	0.190	0.247	-0.015	-0.020	-0.015	-0.014	-0.016
10	C	crater	0.471	0.471	0.471	0.492	0.476	-0.253	-0.334	-0.329	-0.334	-0.312
11	N ₁	pit	0.183	0.256	0.139	0.241	0.205	-0.017	-0.010	-0.015	-0.010	-0.013
12	N ₁	pit	0.324	0.297	0.225	0.153	0.250	-0.022	-0.015	-0.021	-0.031	-0.022
13	P ₂	peak	0.452	0.380	0.421	0.380	0.408	0.342	0.376	0.374	0.399	0.373
14	N ₁	pit	0.240	0.363	0.299	0.262	0.291	-0.056	-0.045	-0.051	-0.058	-0.052
15	N ₁	pit	0.214	0.263	0.313	0.318	0.277	-0.043	-0.066	-0.054	-0.057	-0.055
16	N ₁	pit	0.661	0.243	0.796	0.304	0.501	-0.218	-0.096	-0.080	-0.088	-0.120
17	N ₁	pit	0.156	0.280	0.296	0.165	0.224	-0.320	-0.129	-0.107	-0.203	-0.190
18	N ₁	pit	0.126	0.132	0.137	0.499	0.223	-0.169	-0.181	-0.226	-0.038	-0.153
19	N ₁	pit	0.253	0.264	0.292	0.276	0.271	-0.030	-0.025	-0.035	-0.025	-0.029
20	N ₁	pit	0.226	0.276	0.261	0.197	0.240	-0.034	-0.022	-0.029	-0.019	-0.026
21	N ₁	pit	0.351	0.236	0.225	0.318	0.282	-0.026	-0.033	-0.025	-0.020	-0.026
22	P ₂	peak	0.448	0.493	0.499	0.408	0.462	0.375	0.414	0.439	0.373	0.400
23	P ₂	peak	0.473	0.780	0.506	0.664	0.606	0.249	0.425	0.308	0.235	0.304
24	N ₁	pit	0.363	0.232	0.283	0.314	0.298	-0.028	-0.058	-0.027	-0.047	-0.040
25	N ₁	pit	0.274	0.366	0.689	0.436	0.441	-0.182	0.000	-0.051	-0.052	-0.071
26	P ₂	peak	0.806	0.738	0.945	0.746	0.809	0.273	0.347	0.272	0.252	0.286
27	P ₂	peak	0.407	0.666	0.443	0.452	0.492	0.375	0.319	0.371	0.365	0.358
28	P ₂	peak	0.344	0.360	0.378	0.344	0.357	0.268	0.259	0.256	0.250	0.258
29	P ₂	peak	0.404	0.433	0.378	0.417	0.408	0.346	0.340	0.295	0.328	0.327
30	P ₂	peak	0.640	0.776	0.669	0.631	0.679	0.272	0.328	0.276	0.302	0.295
31	P ₂	peak	0.496	0.514	0.493	0.607	0.528	0.345	0.309	0.334	0.322	0.327
32	P ₂	peak	0.489	0.479	0.527	0.609	0.526	0.307	0.348	0.366	0.372	0.348
33	P ₂	peak	0.677	0.876	0.687	0.770	0.752	0.235	0.243	0.243	0.218	0.235
34	P ₂	peak	0.638	0.478	0.469	0.523	0.527	0.350	0.333	0.335	0.340	0.339
35	A ₂	stuck	1.846	1.250	1.476	1.575	1.536	0.444	0.447	0.482	0.460	0.458
36	P ₂	peak	0.473	0.631	0.585	0.510	0.550	0.403	0.396	0.383	0.380	0.390
37	P ₂	peak	0.326	0.609	0.497	0.465	0.474	0.257	0.335	0.338	0.353	0.320
38	C	crater	3.228	4.767	3.927	3.141	3.766	-0.183	-0.190	-0.201	-0.202	-0.194
39	N ₁	pit	0.228	0.338	0.147	0.304	0.254	-0.043	-0.026	-0.030	-0.052	-0.038
40	P ₂	peak	0.410	0.562	0.475	0.536	0.496	0.352	0.379	0.347	0.334	0.353
41	P ₂	peak	0.322	0.340	0.352	0.322	0.334	0.343	0.336	0.339	0.349	0.342
42	P ₂	peak	0.340	0.366	0.235	0.357	0.325	0.463	0.415	0.445	0.456	0.444
43	P ₂	peak	0.713	0.475	0.475	0.626	0.572	0.412	0.388	0.424	0.420	0.411
44	P ₂	peak	0.261	0.226	0.194	0.289	0.242	0.289	0.315	0.245	0.319	0.292
45	P ₂	peak	0.291	0.277	0.278	0.387	0.308	0.503	0.455	0.481	0.469	0.477

46	C	crater, spallation/fracture	4.570	4.928	4.341	3.374	4.303	-0.162	-1.999	-1.029	-1.661	-1.213
47	P ₂	peak	1.157	1.198	1.158	1.298	1.203	0.478	0.392	0.391	0.353	0.404
48	A ₁	con. ring	2.986	2.632	3.163	2.733	2.878	0.402	0.401	0.413	0.391	0.402
49	P ₂	peak	0.582	0.633	0.557	0.683	0.614	0.375	0.376	0.350	0.363	0.366
50	P ₂	peak	0.793	0.828	1.020	1.480	1.030	0.090	0.086	0.081	0.092	0.087
51	P ₂	peak	0.549	0.666	0.607	0.576	0.600	0.337	0.382	0.407	0.339	0.366
52	P ₂	peak	0.592	0.799	0.801	0.727	0.730	0.286	0.303	0.318	0.307	0.303
53	P ₂	peak	1.350	1.260	1.253	0.855	1.179	0.169	0.159	0.186	0.140	0.163
54	P ₂	peak	1.184	0.843	0.965	1.333	1.081	0.076	0.077	0.075	0.090	0.080
55	A ₁	con. ring	5.303	4.583	5.487	5.010	5.096	1.154	1.077	1.101	1.089	1.105
56	A ₂	stuck	11.505	9.402	9.402	9.838	10.037	3.484	3.683	3.652	3.505	3.581
57	C	crater, spallation/fracture	2.295	2.697	2.511	2.659	2.540	-0.348	-0.337	-0.331	-0.331	-0.337
58	A ₁	con. ring	2.889	3.093	3.521	2.849	3.088	0.541	0.574	0.571	0.492	0.544
59	A ₂	stuck	2.461	1.999	2.175	2.099	2.183	0.174	0.193	0.184	0.214	0.191
60	C	crater, spallation/fracture	9.741	8.803	8.468	7.468	8.620	-2.278	-2.291	-2.259	-2.343	-2.293
61	C	crater, fragm.	1.426	1.860	1.590	1.674	1.637	-0.724	-0.928	-0.976	-0.898	-0.881
62	P ₂	peak	0.602	0.577	0.545	0.642	0.591	0.328	0.334	0.340	0.336	0.334
63	A ₁	con. ring	4.979	5.265	5.708	5.580	5.383	1.872	1.859	1.895	1.819	1.861
64	C	crater, spallation/fracture	3.293	4.061	4.225	3.114	3.673	-1.240	-0.758	-0.985	-1.221	-1.051
65	P ₂	peak	0.480	0.531	0.584	0.551	0.536	0.331	0.329	0.315	0.341	0.329
66	A ₁	con. ring	3.862	3.010	3.748	3.213	3.458	0.887	0.897	0.934	0.847	0.891
67	A ₁	con. ring	3.438	3.856	3.646	3.835	3.694	1.010	1.663	0.964	1.048	1.171
68	D	dust	1.681	2.276	2.124	1.830	1.978	0.102	0.118	0.124	0.080	0.106
69	A ₁	con. ring	2.881	3.479	3.119	3.146	3.156	0.554	0.592	0.573	0.579	0.575
70	C	crater	2.876	2.342	2.093	3.099	2.602	-0.622	-0.735	-0.719	-0.709	-0.696
71	A ₂	stuck	5.537	2.405	3.216	3.104	3.566	0.549	0.497	0.465	0.591	0.526
72	A ₁	con. ring	7.251	4.615	4.038	6.076	5.495	0.981	0.855	0.898	1.117	0.963
73	A ₁	con. ring	3.097	3.319	3.319	3.203	3.234	0.561	0.492	0.553	0.551	0.539
74	A ₂	stuck	1.616	1.886	2.179	1.347	1.757	0.475	0.411	0.606	0.629	0.530
75	C	crater	1.998	1.293	2.194	2.233	1.930	-0.447	-0.378	-0.301	-0.290	-0.354
76	A ₂	stuck	1.108	1.859	1.540	1.558	1.516	0.364	0.333	0.278	0.477	0.363
77	A ₁	con. ring	7.717	8.166	5.854	6.032	6.942	1.120	1.171	1.110	1.097	1.125
78	A ₁	con. ring	2.246	1.646	2.000	1.855	1.937	0.413	0.502	0.572	0.482	0.492
79	A ₁	con. ring	2.564	1.778	2.399	2.688	2.357	0.438	0.302	0.362	0.466	0.392
80	A ₁	con. ring	3.148	2.906	2.954	3.075	3.021	0.543	0.469	0.485	0.445	0.485
81	A ₁	con. ring	1.432	1.867	1.356	1.586	1.560	0.203	0.211	0.189	0.189	0.198
82	A ₁	con. ring	1.292	2.921	3.154	2.352	2.430	0.157	0.244	0.230	0.301	0.233
83	N ₁	defect	1.937	3.659	1.660	1.291	2.137	-0.520	-0.632	-0.653	-0.390	-0.549
84	A ₁	con. ring	2.626	2.482	3.123	1.716	2.487	0.536	0.456	0.508	0.530	0.508
85	N ₁	pit	0.202	0.192	0.261	0.261	0.229	-0.359	-0.334	-0.206	-0.291	-0.298
86	P ₂	peak	0.820	0.820	0.771	0.710	0.781	0.187	0.180	0.171	0.164	0.176
87	P ₂	peak	0.563	0.563	0.551	0.467	0.536	0.191	0.133	0.215	0.186	0.181
88	P ₂	peak	0.814	0.726	0.747	0.627	0.728	0.203	0.186	0.178	0.203	0.192
89	N ₁	pit	0.245	0.212	0.114	0.560	0.283	-0.114	-0.382	-0.158	-0.202	-0.214
90	P ₂	peak	0.698	0.663	0.747	0.833	0.735	0.221	0.220	0.192	0.196	0.207
91	N ₁	pit	0.125	0.204	0.236	0.163	0.182	-0.145	-0.288	-0.189	-0.074	-0.174
92	P ₂	rough	0.626	0.966	0.776	0.639	0.752	0.237	0.289	0.233	0.281	0.260
93	N ₁	pit	0.920	0.987	0.914	0.907	0.932	-0.230	-0.262	-0.260	-0.201	-0.238
94	P ₂	peak	0.554	0.473	0.529	0.490	0.511	0.186	0.190	0.204	0.197	0.194
95	P ₂	rough	0.722	0.840	0.847	0.888	0.824	0.565	0.552	0.553	0.534	0.551

96	P ₂ peak	1.333	1.188	1.452	1.040	1.253	0.131	0.106	0.140	0.123	0.125
97	P ₂ rough	0.852	0.911	1.043	0.952	0.940	0.515	0.586	0.504	0.313	0.479
98	P ₂ rough	0.907	0.840	0.747	1.000	0.873	0.528	0.551	0.508	0.514	0.525
99	P ₂ rough	0.923	0.736	0.836	0.838	0.833	0.597	0.628	0.570	0.557	0.588
100	P ₂ rough	1.657	0.876	1.143	0.958	1.158	0.047	0.055	0.056	0.052	0.053
101	P ₂ peak	0.664	0.624	0.531	0.581	0.600	0.051	0.055	0.071	0.055	0.058
102	P ₂ peak	0.216	0.681	0.730	0.807	0.608	0.031	0.036	0.036	0.036	0.035
103	P ₂ rough	0.294	0.523	0.388	0.422	0.407	0.374	0.398	0.376	0.352	0.375
104	P ₂ peak	0.755	0.681	1.156	0.847	0.859	0.136	0.122	0.134	0.127	0.130
105	P ₂ peak	0.640	0.549	0.653	0.612	0.613	0.345	0.326	0.313	0.273	0.314
106	N ₁ pit	0.706	0.131	0.813	0.722	0.593	-0.226	-0.168	-0.254	-0.251	-0.225
107	P ₂ peak	0.617	0.600	0.574	0.617	0.602	0.370	0.361	0.364	0.349	0.361
108	P ₂ rough	1.629	1.526	1.509	0.911	1.393	0.427	0.291	0.334	0.410	0.365
109	P ₂ peak	0.547	0.653	0.666	0.597	0.616	0.405	0.393	0.403	0.383	0.396
110	P ₂ peak	0.441	0.531	0.590	0.498	0.515	0.372	0.385	0.358	0.346	0.365
111	P ₂ rough	0.797	0.847	0.564	0.548	0.689	0.323	0.348	0.337	0.323	0.333
112	E peak	0.389	0.583	0.481	0.652	0.526	0.376	0.369	0.339	0.344	0.357
113	N ₁ pit	0.265	0.212	0.248	0.248	0.243	-0.224	-0.255	-0.344	-0.172	-0.249
114	P ₂ peak	0.602	0.676	0.763	0.632	0.668	0.351	0.349	0.343	0.323	0.342
115	P ₂ peak	0.540	0.940	0.522	0.749	0.688	0.319	0.283	0.306	0.307	0.304
116	P ₂ peak	0.848	0.620	0.703	0.786	0.739	0.150	0.128	0.116	0.105	0.125
117	N ₁ pit	0.147	0.147	0.170	0.165	0.157	-0.262	-0.076	-0.274	-0.320	-0.233
118	N ₁ pit	0.216	0.133	0.131	0.131	0.152	-0.050	-0.110	-0.093	-0.106	-0.089
119	P ₂ rough	1.649	1.212	1.417	1.437	1.429	0.145	0.163	0.128	0.138	0.143
120	P ₂ peak	0.538	0.642	0.582	0.872	0.659	0.163	0.162	0.179	0.167	0.168
121	E peak	0.829	0.557	0.661	0.674	0.680	0.223	0.217	0.228	0.193	0.215
122	P ₂ rough	0.648	0.518	0.596	0.673	0.609	0.321	0.319	0.295	0.290	0.306
123	P ₂ rough	0.355	0.698	0.687	0.673	0.603	0.394	0.398	0.126	0.348	0.317
124	P ₂ rough	0.634	0.622	0.774	0.373	0.601	0.375	0.355	0.309	0.331	0.342
125	P ₂ rough	0.812	0.427	0.816	0.508	0.641	0.398	0.289	0.380	0.368	0.359
126	P ₂ peak	0.402	0.376	0.436	0.531	0.436	0.396	0.359	0.370	0.347	0.368
127	A ₁ con. ring	1.848	1.708	2.117	1.612	1.821	0.395	0.334	0.469	0.246	0.361
128	P ₂ rough	0.639	0.624	0.546	0.634	0.611	0.224	0.360	0.310	0.253	0.287
129	P ₂ rough	1.523	1.351	1.351	1.427	1.413	0.422	0.417	0.426	0.437	0.426
130	P ₂ rough	1.787	1.753	1.735	1.821	1.774	0.463	0.373	0.352	0.430	0.404
131	P ₂ peak	0.509	0.480	0.436	0.523	0.487	0.375	0.393	0.392	0.375	0.383
132	P ₂ rough	0.753	0.949	0.844	0.799	0.836	0.052	0.055	0.046	0.049	0.051
133	P ₂ rough	0.698	0.651	0.710	0.884	0.736	0.042	0.040	0.057	0.068	0.052
134	P ₂ rough	0.803	0.863	0.730	1.325	0.930	0.105	0.105	0.090	0.128	0.107
135	P ₂ rough	1.335	0.728	0.930	1.146	1.035	0.139	0.179	0.122	0.170	0.153
136	P ₂ rough	0.582	0.733	0.779	0.547	0.660	0.058	0.049	0.051	0.052	0.052
137	P ₂ rough	0.482	0.472	0.675	0.785	0.604	0.043	0.045	0.049	0.050	0.047
138	P ₂ peak	0.546	0.339	0.471	0.546	0.476	0.038	0.039	0.041	0.045	0.040
139	P ₂ rough	0.742	0.798	0.594	0.668	0.701	0.048	0.042	0.036	0.039	0.041
140	P ₂ rough	1.397	0.790	1.175	0.696	1.014	0.078	0.084	0.080	0.072	0.078
141	P ₂ peak	0.648	0.496	0.486	0.607	0.559	0.035	0.035	0.036	0.037	0.036
142	P ₂ peak	0.634	0.405	0.489	0.330	0.465	0.027	0.024	0.033	0.027	0.028
143	E peak	1.100	0.753	0.806	0.568	0.807	0.090	0.104	0.099	0.072	0.091
144	E peak	0.557	0.718	0.854	0.483	0.653	0.061	0.050	0.066	0.033	0.053
145	E peak	0.998	0.371	0.650	0.877	0.724	0.221	0.500	0.221	0.299	0.310
146	P ₂ rough	1.500	0.680	1.653	1.670	1.376	0.294	0.089	0.261	0.154	0.199
147	P ₂ rough	1.366	1.640	1.458	1.549	1.503	0.179	0.163	0.160	0.166	0.167

148	P ₂ rough	1.230	1.093	1.078	1.442	1.211	0.196	0.186	0.158	0.197	0.184
149	E peak	0.680	0.557	0.755	0.384	0.594	0.388	0.329	0.318	0.323	0.340
150	P ₂ rough	0.926	0.668	0.742	0.926	0.816	0.291	0.290	0.236	0.302	0.279
151	P ₂ rough	1.308	0.634	0.753	0.972	0.917	0.055	0.046	0.050	0.042	0.048
152	N ₁ pit	0.164	0.164	0.313	0.164	0.201	-0.023	-0.016	-0.168	-0.008	-0.054
153	N ₁ pit	0.252	0.194	0.234	0.247	0.232	-0.385	-0.517	-0.322	-0.259	-0.371
154	P ₂ rough	0.657	0.634	0.817	0.657	0.691	0.344	0.342	0.319	0.302	0.327
155	A ₁ con. ring	4.738	4.185	3.873	4.322	4.279	1.663	1.405	1.423	1.483	1.493
156	N ₁ pit	0.161	0.164	0.179	0.209	0.178	-0.277	-0.417	-0.250	-0.225	-0.292
157	P ₂ rough	0.796	0.620	0.785	0.702	0.726	0.336	0.283	0.309	0.265	0.298
158	P ₂ rough	1.708	1.378	1.392	1.212	1.422	0.208	0.240	0.237	0.215	0.225
159	N ₁ pit	0.154	0.154	0.138	0.208	0.163	-0.431	-0.312	-0.212	-0.089	-0.261
160	P ₂ peak	0.650	0.918	1.166	0.776	0.878	0.058	0.062	0.060	0.051	0.058
161	P ₂ rough	0.863	0.793	0.840	1.074	0.893	0.070	0.061	0.061	0.061	0.063
162	P ₂ rough	0.565	0.923	0.848	0.754	0.772	0.071	0.050	0.048	0.038	0.052
163	N ₁ pit	1.434	0.817	1.262	1.147	1.165	-0.449	-0.240	-0.448	-0.335	-0.368
164	A ₃ shining halo	21.185	20.262	17.958	22.724	20.532	3.871	3.914	4.504	4.439	4.182
165	P ₂ peak	0.238	0.736	0.563	0.520	0.514	0.315	0.323	0.325	0.306	0.317
166	A ₁ con. ring	3.203	2.151	2.402	3.103	2.715	0.507	0.663	0.499	0.496	0.541
167	P ₂ peak	0.160	0.289	0.240	0.294	0.246	0.537	0.234	0.451	0.521	0.436
168	A ₁ con. ring	2.918	2.755	2.455	2.836	2.741	0.708	0.757	0.679	2.836	1.245
169	A ₂ stuck	1.733	1.596	1.670	1.243	1.561	1.080	1.016	1.067	1.103	1.066
170	C crater	0.683	0.783	0.658	0.987	0.778	-0.166	-0.098	-0.155	-0.113	-0.133
171	C crater	4.753	3.589	3.363	3.621	3.832	-0.234	-0.269	-0.225	-0.246	-0.243
172	P ₂ peak	0.750	0.621	0.629	0.846	0.712	0.091	0.065	0.071	0.067	0.073
173	P ₂ peak	0.496	0.837	0.725	0.630	0.672	0.064	0.057	0.070	0.059	0.062
174	P ₂ peak	0.421	0.470	0.445	0.408	0.436	0.104	0.094	0.089	0.093	0.095
175	P ₂ peak	0.511	0.511	0.551	0.655	0.557	0.087	0.043	0.062	0.061	0.063
176	C crater, fragm.	1.491	1.385	1.491	1.740	1.527	-1.639	-1.318	-1.029	-1.638	-1.406
177	C crater, spallation/fracture	1.955	2.029	2.128	2.227	2.085	-0.640	-0.542	-0.711	-0.597	-0.623
178	C crater, spallation/fracture	3.356	4.131	4.088	4.131	3.926	-0.414	-0.327	-0.384	-0.348	-0.368
179	P ₂ peak	0.787	1.089	1.029	0.787	0.923	0.574	0.543	0.527	0.441	0.521
180	P ₂ peak	0.368	0.484	0.500	0.565	0.479	0.406	0.370	0.408	0.378	0.390
181	P ₂ peak	0.353	0.250	0.445	0.445	0.373	0.513	0.503	0.477	0.434	0.482
182	P ₂ peak	0.568	0.712	0.568	0.610	0.614	0.305	0.420	0.375	0.337	0.359
183	A ₁ con. ring	5.286	5.547	4.142	5.263	5.059	1.421	1.454	1.352	1.552	1.445
184	A ₂ stuck	2.895	3.075	3.247	2.796	3.003	0.388	0.401	0.572	0.388	0.437
185	A ₁ con. ring	4.671	5.055	4.782	5.405	4.978	1.422	1.019	1.197	1.138	1.194
186	A ₂ stuck	2.412	2.227	1.963	2.116	2.179	0.350	0.260	0.241	0.322	0.293
187	A ₂ stuck	4.898	5.559	5.370	4.936	5.191	1.735	1.704	1.388	1.371	1.550
188	A ₂ stuck	3.327	2.520	3.058	2.651	2.889	0.636	0.665	0.692	0.488	0.620
189	A ₂ stuck	1.653	1.468	1.724	1.706	1.638	0.685	0.670	0.677	0.681	0.678
190	P ₂ rough	2.106	2.677	2.619	2.871	2.568	0.806	1.058	0.812	0.653	0.832
191	C crater, stuck	3.206	2.164	3.045	2.632	2.762	-0.434	-0.663	-0.112	-0.424	-0.408
192	C crater, stuck	3.464	3.655	3.627	3.873	3.655	0.755	0.727	0.808	0.752	0.760
193	P ₂ rough	3.153	3.382	2.988	2.851	3.093	0.216	0.194	0.201	0.371	0.246
194	D dent	1.355	1.501	1.350	1.113	1.330	-0.098	-0.072	-0.064	-0.058	-0.073
195	N ₁ pit	0.602	0.450	0.550	0.338	0.485	-0.089	-0.094	-0.075	-0.079	-0.084
196	N ₁ pit	0.425	0.536	0.356	0.602	0.480	-0.073	-0.051	-0.042	-0.045	-0.053
197	N ₁ pit	0.368	0.518	0.300	0.472	0.415	-0.067	-0.062	-0.044	-0.061	-0.059
198	D dent	1.164	1.086	1.029	0.750	1.007	-0.044	-0.021	-0.019	-0.021	-0.026
199	D dent	1.119	0.632	0.837	1.052	0.910	-0.039	-0.020	-0.019	-0.018	-0.024

200	N ₁ pit	0.675	0.586	0.854	0.648	0.691	-0.078	-0.103	-0.095	-0.088	-0.091
201	D dent	0.916	0.928	0.984	1.076	0.976	-0.026	-0.016	-0.012	-0.027	-0.020
202	N ₁ pit	0.354	0.520	0.585	0.482	0.485	-0.668	-0.263	-0.609	-0.523	-0.516
203	N ₁ pit	0.608	0.681	0.479	0.621	0.597	-0.090	-0.096	-0.094	-0.086	-0.092
204	N ₁ rough, pit	1.279	1.060	1.068	1.151	1.140	-0.062	-0.065	-0.071	-0.076	-0.068
205	N ₁ pit	0.812	0.414	0.789	0.790	0.701	-0.351	-0.438	-0.394	-0.489	-0.418
206	N ₁ pit	0.870	0.460	0.433	0.674	0.609	-0.053	-0.094	-0.081	-0.062	-0.073
207	P ₂ peak	0.486	0.364	0.364	0.567	0.445	0.256	0.437	0.368	0.389	0.363
208	N ₁ pit	0.281	0.562	0.332	0.371	0.387	-0.101	-0.069	-0.085	-0.087	-0.086
209	N ₁ defect	1.721	0.876	1.068	0.998	1.166	-0.034	-0.028	-0.022	-0.035	-0.030
210	N ₁ pit	0.442	0.493	0.321	0.292	0.387	-0.072	-0.069	-0.065	-0.062	-0.067
211	D dent	4.572	0.636	0.919	1.959	2.021	-0.030	-0.025	-0.027	-0.022	-0.026
212	P ₂ rough	2.315	1.518	2.317	1.984	2.033	0.115	0.077	0.042	0.269	0.126
213	D dent	1.382	1.685	1.334	1.473	1.468	-0.031	-0.032	-0.033	-0.035	-0.033
214	D dent	0.987	0.919	0.926	0.941	0.943	-0.033	-0.031	-0.052	-0.030	-0.036
215	N ₁ rough, pit	0.714	0.918	0.758	0.789	0.794	-0.037	-0.026	-0.032	-0.034	-0.032
216	D dent	1.180	0.668	0.805	1.165	0.954	-0.044	-0.021	-0.035	-0.038	-0.034
217	P ₂ rough	2.165	1.429	1.139	1.254	1.497	0.085	0.049	0.081	0.051	0.067
218	P ₂ peak	0.768	0.475	0.779	0.626	0.662	0.264	0.441	0.387	0.406	0.374
219	P ₂ peak	0.759	0.547	0.486	0.644	0.609	0.073	0.065	0.047	0.081	0.067
220	P ₂ rough	0.820	0.440	0.714	0.504	0.619	0.375	0.323	0.325	0.448	0.368
221	N ₁ pit	0.493	0.366	0.377	0.366	0.400	-0.035	-0.053	-0.055	-0.048	-0.047
222	N ₁ pit	1.625	0.387	0.505	0.337	0.713	-0.056	-0.048	-0.044	-0.047	-0.048
223	D dent	1.241	0.957	1.119	0.950	1.067	-0.042	-0.014	-0.012	-0.016	-0.021
224	N ₁ pit	0.484	0.928	0.611	0.547	0.642	-0.051	-0.051	-0.043	-0.040	-0.046
225	P ₂ rough	0.444	0.603	0.537	0.457	0.510	0.036	0.031	0.029	0.028	0.031
226	D dent	1.011	1.149	1.379	1.245	1.196	-0.025	-0.020	-0.019	-0.029	-0.023
227	P ₂ rough	0.790	0.429	0.611	0.766	0.649	0.056	0.058	0.045	0.040	0.050
228	P ₂ peak	0.567	0.332	0.483	0.493	0.468	0.399	0.389	0.416	0.695	0.475
229	P ₂ peak	0.521	0.471	0.380	0.516	0.472	0.027	0.019	0.041	0.038	0.031
230	D dent	0.921	1.042	0.932	0.939	0.958	-0.024	-0.018	-0.020	-0.019	-0.020
231	D dent	0.926	0.805	0.668	0.981	0.845	-0.035	-0.016	-0.019	-0.039	-0.028
232	D dent	0.932	0.731	0.884	0.902	0.862	-0.019	-0.012	-0.014	-0.020	-0.016
233	P ₂ peak	0.366	0.311	0.332	0.311	0.330	0.486	0.425	0.413	0.457	0.445
234	P ₂ peak	0.319	0.319	0.352	0.291	0.320	0.439	0.448	0.456	0.489	0.458
235	P ₂ peak	0.368	0.380	0.398	0.383	0.382	0.041	0.033	0.042	0.042	0.039
236	P ₂ peak	0.417	0.304	0.258	0.471	0.362	0.371	0.103	0.228	0.390	0.273
237	N ₁ pit	0.506	0.456	0.322	0.531	0.454	-0.076	-0.051	-0.038	-0.042	-0.052
238	N ₁ pit	0.368	0.626	0.411	0.378	0.446	-0.211	-0.331	-0.315	-0.346	-0.301
239	P ₂ peak	0.552	0.349	0.506	0.471	0.469	0.370	0.285	0.322	0.329	0.327
240	P ₂ peak	0.501	0.501	0.273	0.349	0.406	0.033	0.031	0.034	0.039	0.034
241	P ₂ rough	1.260	0.751	1.473	1.078	1.141	0.345	0.281	0.174	0.365	0.291
242	P ₂ rough	0.562	0.919	0.812	0.828	0.780	0.038	0.063	0.032	0.046	0.045
243	P ₂ peak	0.276	0.501	0.376	0.319	0.368	0.056	0.033	0.041	0.034	0.041
244	N ₁ pit	0.445	0.281	0.408	0.532	0.417	-0.100	-0.082	-0.156	-0.082	-0.105
245	D dent	0.959	1.027	0.904	0.897	0.947	-0.028	-0.022	-0.020	-0.021	-0.023
246	N ₁ pit	0.289	0.410	0.334	0.383	0.354	-0.022	-0.119	-0.119	-0.131	-0.098
247	P ₂ rough	1.093	1.032	1.098	0.957	1.045	0.294	0.140	0.140	0.199	0.193
248	P ₂ rough	0.829	0.661	1.126	0.569	0.796	0.239	0.206	0.231	0.167	0.211
249	P ₂ rough	1.137	0.891	0.916	1.027	0.993	0.317	0.241	0.226	0.222	0.252
250	P ₂ rough	0.673	0.239	0.378	0.718	0.502	0.698	0.569	0.595	0.051	0.478
251	P ₂ peak	0.379	0.493	0.458	0.388	0.430	0.068	0.062	0.065	0.061	0.064

252	N ₁	rough, pit	2.050	0.598	2.053	1.977	1.669	-0.424	-0.237	-0.226	-0.103	-0.247
253	N ₁	rough, pit	0.972	0.738	1.032	0.820	0.890	-0.208	-0.141	-0.074	-0.314	-0.184
254	N ₁	rough, pit	1.274	0.905	1.076	1.151	1.102	-0.052	-0.046	-0.083	-0.065	-0.061
255	N ₁	rough, pit	0.483	0.297	0.272	0.253	0.326	-0.065	-0.049	-0.056	-0.049	-0.055
256	N ₁	rough, pit	0.738	0.496	0.650	0.801	0.671	-0.096	-0.358	-0.294	-0.211	-0.240
257	N ₁	rough, pit	1.199	0.844	0.854	1.262	1.040	-0.318	-0.187	-0.414	-0.272	-0.298
258	N ₁	rough, pit	0.269	0.735	0.453	0.795	0.563	-0.405	-0.127	-0.050	-0.225	-0.202
259	N ₁	rough, pit	0.575	0.477	0.563	0.742	0.589	-0.048	-0.060	-0.053	-0.063	-0.056
260	N ₁	rough, pit	0.406	0.428	0.430	0.465	0.432	-0.090	-0.081	-0.087	-0.088	-0.086
261	N ₁	rough, pit	0.391	0.359	0.557	0.375	0.421	-0.037	-0.089	-0.050	-0.071	-0.062
262	N ₁	rough, pit	0.453	0.868	0.594	0.404	0.580	-0.374	-0.121	-0.313	-0.369	-0.294
263	N ₁	rough, pit	0.978	0.977	0.978	1.173	1.027	-0.048	-0.045	-0.054	-0.047	-0.049
264	N ₁	rough, pit	0.404	0.599	0.657	0.379	0.510	-0.069	-0.080	-0.073	-0.089	-0.078
265	N ₁	rough, pit	0.391	0.599	0.343	0.440	0.443	-0.127	-0.118	-0.123	-0.110	-0.120
266	N ₁	rough, pit	0.274	0.430	0.436	0.306	0.361	-0.134	-0.166	-0.145	-0.130	-0.144
267	N ₁	rough, pit	0.288	0.567	0.306	0.378	0.385	-0.084	-0.080	-0.080	-0.079	-0.081
268	N ₁	rough, pit	0.325	0.668	0.402	0.343	0.435	-0.083	-0.071	-0.048	-0.060	-0.065
269	P ₂	rough	2.581	1.564	1.320	1.898	1.841	0.496	0.482	0.547	0.560	0.521
270	N ₁	rough, pit	0.445	0.366	0.278	0.486	0.394	-0.092	-0.105	-0.099	-0.116	-0.103
271	P ₂	rough	0.512	0.713	0.795	0.558	0.644	0.232	0.276	0.173	0.225	0.227
272	N ₁	pit	0.223	0.320	0.399	0.292	0.308	-0.071	-0.060	-0.064	-0.061	-0.064
273	N ₁	pit	0.373	0.476	0.252	0.439	0.385	-0.035	-0.026	-0.028	-0.029	-0.030
274	N ₁	pit	0.265	0.378	0.369	0.296	0.327	-0.064	-0.070	-0.077	-0.049	-0.065
275	N ₁	pit	0.220	0.625	0.384	0.247	0.369	-0.129	-0.111	-0.109	-0.114	-0.116
276	N ₁	rough, pit	0.393	0.381	0.347	0.302	0.356	-0.047	-0.039	-0.042	-0.040	-0.042
277	N ₁	rough, pit	0.128	0.319	0.172	0.175	0.198	-0.051	-0.057	-0.040	-0.042	-0.047
278	N ₁	rough, pit	0.274	0.457	0.356	0.338	0.356	-0.104	-0.087	-0.091	-0.095	-0.094
279	N ₁	rough, pit	0.256	0.383	0.405	0.302	0.336	-0.059	-0.054	-0.100	-0.050	-0.066
280	N ₁	rough, pit	0.311	0.247	0.257	0.270	0.271	-0.047	-0.043	-0.034	-0.043	-0.042
281	N ₁	rough, pit	0.251	0.349	0.274	0.275	0.287	-0.039	-0.032	-0.039	-0.036	-0.037
282	N ₁	rough, pit	0.228	0.612	0.373	0.380	0.399	-0.065	-0.057	-0.047	-0.067	-0.059
283	P ₂	rough	0.254	0.139	0.273	0.260	0.232	0.296	0.394	0.477	0.469	0.409
284	P ₂	rough	0.292	0.165	0.329	0.279	0.266	0.462	0.486	0.461	0.502	0.478
285	P ₂	rough	0.334	0.232	0.360	0.189	0.279	0.424	0.410	0.416	0.449	0.424
286	P ₂	peak	0.320	0.243	0.223	0.320	0.276	0.477	0.422	0.445	0.512	0.464
287	P ₂	rough	0.965	0.742	1.002	0.832	0.885	0.700	0.517	0.583	0.533	0.583
288	P ₂	rough	0.538	0.452	0.815	0.265	0.517	0.141	0.090	0.205	0.155	0.148
289	P ₂	rough	0.457	0.380	0.356	0.685	0.470	0.507	0.267	0.174	0.276	0.306
290	P ₂	peak	0.265	0.225	0.275	0.247	0.253	0.429	0.383	0.429	0.405	0.411
291	N ₁	pit	0.234	0.565	0.311	0.241	0.338	-0.073	-0.072	-0.096	-0.069	-0.077
292	N ₁	rough, pit	0.264	0.256	0.402	0.356	0.320	-0.065	-0.059	-0.060	-0.055	-0.060
293	N ₁	rough, pit	0.320	0.306	0.367	0.371	0.341	-0.060	-0.050	-0.060	-0.049	-0.055
294	P ₂	rough	0.807	0.854	0.909	0.770	0.835	0.267	0.208	0.189	0.190	0.213
295	P ₂	rough	0.576	0.594	0.687	0.677	0.633	0.265	0.236	0.283	0.280	0.266
296	N ₁	pit	0.251	0.390	0.213	0.301	0.289	-0.115	-0.109	-0.129	-0.123	-0.119
297	P ₂	peak	0.486	0.402	0.530	0.440	0.464	0.101	0.294	0.118	0.281	0.199
298	P ₂	rough	0.978	0.658	0.566	1.270	0.868	0.189	0.145	0.248	0.263	0.212
299	P ₂	peak	0.201	0.402	0.356	0.430	0.347	0.226	0.221	0.244	0.130	0.205

300	P ₂ rough	0.475	0.464	0.375	0.974	0.572	0.189	0.238	0.250	0.212	0.222
301	P ₂ rough	0.539	0.950	0.687	0.661	0.709	0.108	0.112	0.081	0.096	0.099
302	N ₁ pit	0.311	0.471	0.436	0.330	0.387	-0.102	-0.094	-0.084	-0.090	-0.093
303	N ₁ pit	0.292	0.475	0.292	0.337	0.349	-0.098	-0.090	-0.087	-0.091	-0.091
304	N ₁ pit	0.247	0.265	0.288	0.270	0.267	-0.051	-0.055	-0.044	-0.060	-0.053
305	P ₂ rough	0.464	0.594	0.868	0.585	0.628	0.263	0.335	0.252	0.308	0.289
306	N ₁ rough, pit	0.265	0.622	0.306	0.380	0.393	-0.057	-0.049	-0.054	-0.047	-0.051
307	N ₁ rough, pit	0.302	0.480	0.399	0.353	0.383	-0.302	-0.085	-0.068	-0.063	-0.129
308	N ₁ pit	0.270	0.315	0.420	0.343	0.337	-0.080	-0.068	-0.076	-0.074	-0.074
309	N ₁ pit	0.269	0.292	0.315	0.292	0.292	-0.078	-0.072	-0.071	-0.072	-0.073
310	N ₁ pit	0.493	0.510	0.396	0.366	0.441	-0.064	-0.091	-0.093	-0.092	-0.085
311	P ₂ rough	0.695	0.603	0.770	0.798	0.716	0.189	0.359	0.259	0.298	0.276
312	P ₂ rough	0.366	0.230	0.339	0.251	0.296	0.414	0.462	0.403	0.354	0.408
313	N ₁ pit	0.247	0.408	0.306	0.324	0.321	-0.089	-0.089	-0.075	-0.078	-0.083
314	N ₁ pit	0.207	0.396	0.266	0.448	0.329	-0.060	-0.064	-0.054	-0.058	-0.059
315	P ₂ peak	0.302	0.247	0.439	0.503	0.372	0.374	0.295	0.343	0.343	0.339
316	N ₁ pit	0.548	0.455	0.278	0.334	0.404	-0.149	-0.098	-0.104	-0.117	-0.117
317	P ₂ peak	0.786	0.716	0.804	0.863	0.792	0.270	0.380	0.279	0.244	0.293
318	N ₁ pit	0.329	0.493	0.349	0.510	0.420	-0.089	-0.084	-0.099	-0.063	-0.084
319	N ₁ pit	0.369	0.510	0.402	0.475	0.439	-0.087	-0.088	-0.086	-0.085	-0.086
320	N ₁ rough, pit	0.355	0.355	0.636	0.532	0.469	-0.069	-0.076	-0.105	-0.064	-0.079
321	N ₁ rough, pit	0.520	0.428	0.544	0.575	0.517	-0.065	-0.047	-0.063	-0.053	-0.057
322	N ₁ rough, pit	0.281	0.245	0.445	0.334	0.326	-0.034	-0.038	-0.033	-0.031	-0.034
323	N ₁ pit	0.246	0.492	0.411	0.346	0.374	-0.100	-0.105	-0.099	-0.083	-0.097
324	P ₂ rough	0.795	0.538	0.795	0.749	0.719	0.197	0.182	0.203	0.225	0.202
325	N ₁ pit	0.251	0.356	0.329	0.329	0.316	-0.107	-0.112	-0.103	-0.099	-0.106
326	N ₁ pit	0.288	0.330	0.275	0.342	0.308	-0.101	-0.097	-0.088	-0.096	-0.095
327	N ₁ pit	0.343	0.330	0.322	0.384	0.344	-0.028	-0.030	-0.027	-0.029	-0.028
328	N ₁ pit	0.297	0.405	0.260	0.418	0.345	-0.077	-0.071	-0.073	-0.709	-0.232
329	N ₁ pit	0.493	0.540	0.445	0.631	0.527	-0.114	-0.094	-0.098	-0.100	-0.101
330	N ₁ pit	0.228	0.443	0.512	0.297	0.370	-0.043	-0.037	-0.039	-0.039	-0.040
331	P ₂ rough	0.488	0.641	0.445	0.485	0.515	0.065	0.037	0.041	0.051	0.048
332	N ₁ pit	0.266	0.360	0.316	0.302	0.311	-0.055	-0.042	-0.045	-0.046	-0.047
333	N ₁ pit	0.343	0.664	0.556	0.288	0.463	-0.060	-0.058	-0.055	-0.052	-0.056
334	N ₁ pit	0.292	0.320	0.302	0.287	0.300	-0.071	-0.062	-0.076	-0.055	-0.066
335	P ₂ rough	0.269	0.685	0.563	0.472	0.497	0.035	0.043	0.042	0.031	0.038
336	P ₂ rough	0.783	0.697	0.484	0.508	0.618	0.028	0.040	0.051	0.047	0.042
337	N ₁ pit	0.283	0.343	0.329	0.338	0.323	-0.023	-0.022	-0.024	-0.019	-0.022
338	N ₁ pit	0.260	0.510	0.277	0.241	0.322	-0.036	-0.017	-0.030	-0.025	-0.027
339	N ₁ pit	0.213	0.333	0.279	0.274	0.275	-0.038	-0.027	-0.027	-0.031	-0.031
340	P ₂ rough	0.786	0.612	1.318	0.532	0.812	0.051	0.038	0.041	0.047	0.044
341	N ₁ pit	0.213	0.398	0.243	0.320	0.293	-0.028	-0.024	-0.027	-0.026	-0.026
342	N ₁ pit	0.411	0.238	0.373	0.362	0.346	-0.387	-0.495	-0.406	-0.441	-0.432
343	N ₁ pit	0.380	0.430	0.338	0.349	0.374	-0.085	-0.086	-0.081	-0.083	-0.084
344	D dent	1.040	0.881	1.294	1.125	1.085	-0.033	-0.021	-0.022	-0.024	-0.025
345	P ₂ rough	0.288	0.445	0.377	0.232	0.336	0.022	0.024	0.022	0.022	0.023
346	N ₁ pit	0.251	0.270	0.223	0.360	0.276	-0.026	-0.025	-0.028	-0.025	-0.026
347	P ₂ rough	0.408	0.393	0.384	0.320	0.376	0.029	0.019	0.021	0.027	0.024

348	P ₂ rough	0.288	0.462	0.349	0.384	0.370	0.039	0.018	0.044	0.026	0.032
349	N ₁ pit	0.288	0.292	0.283	0.287	0.288	-0.027	-0.021	-0.019	-0.023	-0.022
350	P ₂ rough	0.274	0.557	0.288	0.330	0.362	0.031	0.030	0.031	0.034	0.032
351	P ₂ rough	0.219	0.292	0.260	0.248	0.255	0.027	0.021	0.018	0.024	0.022
352	P ₂ rough	0.390	0.640	0.405	0.512	0.487	0.043	0.050	0.055	0.044	0.048
353	D dent	1.014	1.248	1.235	1.199	1.174	-0.034	-0.021	-0.030	-0.028	-0.028
354	A ₂ stuck	3.528	2.431	1.758	4.487	3.051	2.200	2.264	2.130	1.043	1.909
355	A ₁ con. ring	1.832	1.502	1.510	1.772	1.654	0.572	0.332	0.436	0.442	0.446
356	A ₂ stuck	1.577	1.098	1.217	1.291	1.296	0.248	0.224	0.269	0.261	0.250
357	P ₂ peak	0.840	0.516	0.597	0.612	0.641	0.248	0.267	0.203	0.298	0.254
358	P ₂ peak	0.983	0.658	0.940	1.103	0.921	1.208	1.186	1.169	1.227	1.198
359	P ₂ peak	0.270	0.300	0.276	0.289	0.284	0.481	0.518	0.390	0.401	0.447
360	P ₂ peak	0.460	0.410	0.628	0.425	0.481	0.273	0.294	0.296	0.256	0.280
361	D dent	1.197	1.480	1.773	1.407	1.464	-0.014	-0.011	-0.021	-0.018	-0.016
362	P ₂ peak	0.489	0.587	0.356	0.372	0.451	0.058	0.049	0.046	0.054	0.052
363	N ₁ pit	0.235	0.363	0.191	0.387	0.294	-0.035	-0.040	-0.030	-0.026	-0.033
364	N ₁ pit	0.296	0.233	0.218	0.298	0.261	-0.036	-0.025	-0.027	-0.023	-0.028
365	P ₂ rough	1.115	1.480	1.499	0.859	1.238	0.085	0.089	0.090	0.075	0.085
366	A ₂ stuck	0.734	0.827	0.661	0.783	0.751	0.632	0.709	0.640	0.668	0.662
367	P ₂ peak	0.369	0.291	0.391	0.349	0.350	0.514	0.477	0.487	0.480	0.489
368	P ₂ peak	0.270	0.252	0.272	0.318	0.278	0.355	0.394	0.393	0.409	0.388
369	P ₂ peak	0.374	0.351	0.354	0.368	0.362	0.426	0.456	0.458	0.461	0.450
370	P ₂ peak	0.272	0.326	0.344	0.256	0.299	0.437	0.395	0.406	0.422	0.415
371	P ₂ peak	0.398	0.254	0.326	0.398	0.344	0.509	0.486	0.496	0.469	0.490
372	P ₂ peak	0.471	0.326	0.435	0.365	0.399	0.444	0.433	0.449	0.434	0.440
373	D dent	1.111	1.133	1.004	0.946	1.049	-0.004	-0.013	-0.014	-0.003	-0.009
374	P ₂ rough	0.869	0.616	0.779	0.924	0.797	0.042	0.048	0.040	0.033	0.041
375	P ₂ rough	0.730	0.906	0.797	0.566	0.750	0.027	0.030	0.030	0.030	0.029
376	P ₂ rough	0.543	0.670	0.616	0.557	0.597	0.034	0.043	0.035	0.203	0.078
377	P ₂ rough	0.924	0.797	0.748	0.811	0.820	0.049	0.050	0.044	0.046	0.047
378	P ₂ rough	0.634	1.001	0.803	0.657	0.774	0.037	0.035	0.036	0.023	0.033
379	D dent	0.839	1.838	0.977	1.422	1.269	-0.035	-0.029	-0.043	-0.041	-0.037
380	N ₁ defect	3.150	1.794	1.772	2.056	2.193	-0.038	-0.032	-0.034	-0.041	-0.036
381	P ₂ peak	0.884	0.699	0.626	0.820	0.757	0.037	0.034	0.029	0.036	0.034
382	D dent	1.432	0.934	1.170	1.370	1.227	-0.025	-0.024	-0.029	-0.028	-0.027
383	D dent	1.262	1.296	1.388	1.466	1.353	-0.029	-0.021	-0.013	-0.011	-0.019
384	D dent	1.059	0.913	0.436	1.059	0.867	-0.019	-0.024	-0.022	-0.025	-0.022
385	D dent	1.751	0.828	0.881	1.223	1.171	-0.025	-0.022	-0.029	-0.022	-0.025
386	P ₂ peak	0.423	0.504	0.355	0.426	0.427	0.031	0.031	0.034	0.031	0.032
387	N ₁ pit	0.218	0.556	0.360	0.360	0.374	-0.023	-0.040	-0.020	-0.024	-0.027
388	A ₃ shining halo	22.078	21.296	21.841	21.961	21.794	4.283	4.032	4.636	4.355	4.327
389	C crater, fragm.	2.559	2.277	2.309	2.323	2.367	-1.862	-1.266	-1.765	-2.156	-1.762
390	A ₂ stuck	1.330	1.863	1.327	1.302	1.455	1.226	1.092	1.408	1.314	1.260
391	A ₂ stuck	0.706	0.680	0.790	0.790	0.741	0.420	0.519	0.503	0.603	0.512
392	P ₂ peak	0.345	0.304	0.388	0.456	0.373	0.380	0.375	0.367	0.385	0.377
393	P ₂ peak	0.329	0.313	0.384	0.274	0.325	0.511	0.472	0.483	0.459	0.481
394	A ₂ stuck	1.139	1.139	1.063	1.234	1.144	1.211	0.818	1.039	0.971	1.010
395	A ₂ stuck	1.181	1.081	1.039	1.156	1.114	0.832	0.690	0.759	0.861	0.786
396	N ₁ pit	0.128	0.172	0.106	0.214	0.155	-0.280	-0.327	-0.283	-0.261	-0.288
397	N ₁ pit	0.347	0.585	0.700	0.384	0.504	-0.462	-0.284	-0.403	-0.508	-0.414
398	A ₂ stuck	0.534	0.950	0.928	0.804	0.804	0.480	0.528	0.114	0.427	0.387
399	P ₂ peak	0.366	0.332	0.311	0.368	0.344	0.512	0.382	0.485	0.493	0.468
400	P ₂ peak	0.146	0.204	0.219	0.276	0.211	0.349	0.368	0.305	0.338	0.340

401	P ₂ peak	0.456	0.456	0.440	0.451	0.451	0.469	0.550	0.447	0.396	0.465
402	P ₂ peak	0.332	0.387	0.353	0.408	0.370	0.474	0.462	0.437	0.462	0.459
403	N ₁ pit	0.671	0.274	0.571	0.313	0.457	-0.250	-0.369	-0.325	-0.391	-0.334
404	P ₂ peak	0.442	0.366	0.350	0.460	0.404	0.414	0.426	0.387	0.401	0.407
405	N ₁ pit	0.506	0.334	0.346	0.567	0.438	-0.068	-0.060	-0.052	-0.052	-0.058
406	N ₁ pit	0.349	0.215	0.245	0.169	0.244	-0.039	-0.080	-0.063	-0.050	-0.058
407	N ₁ pit	0.232	0.158	0.349	0.228	0.242	-0.045	-0.095	-0.051	-0.061	-0.063
408	N ₁ rough, pit	0.954	0.486	0.584	0.318	0.586	-0.041	-0.026	-0.026	-0.038	-0.033
409	D dent	0.368	1.078	1.316	1.105	0.967	-0.035	-0.021	-0.034	-0.020	-0.028
410	C crater, fragm.	1.555	2.046	1.609	1.800	1.752	-1.348	-1.099	-1.267	-0.850	-1.141
411	C crater, fragm.	1.173	1.167	2.018	1.883	1.560	-1.268	-0.885	-0.545	-1.282	-0.995
412	C crater, flat	2.342	3.045	2.777	2.242	2.601	-0.181	-0.200	-0.403	-0.184	-0.242
413	C crater, flat	1.167	0.881	1.119	1.394	1.140	-0.052	-0.051	-0.044	-0.033	-0.045
414	N ₁ pit	0.291	0.263	0.273	0.243	0.268	-0.023	-0.023	-0.417	-0.667	-0.282
415	P ₂ peak	0.243	0.215	0.258	0.213	0.232	0.367	0.361	0.353	0.349	0.357
416	N ₁ pit	0.215	0.123	0.155	0.167	0.165	-0.325	-0.114	-0.161	-0.312	-0.228
417	P ₂ peak	0.536	0.471	0.425	0.429	0.465	0.405	0.448	0.399	0.414	0.417
418	N ₁ rough, pit	0.695	0.658	0.676	0.713	0.685	-0.053	-0.059	-0.040	-0.047	-0.050
419	P ₂ rough	1.316	1.060	0.877	1.415	1.167	0.058	0.053	0.052	0.064	0.057
420	P ₂ rough	0.731	0.896	0.877	0.896	0.850	0.043	0.061	0.059	0.049	0.053
421	P ₂ peak	0.289	0.383	0.337	0.352	0.340	0.490	0.487	0.457	0.476	0.478
422	C crater, stuck	0.658	0.513	1.061	0.701	0.733	-0.279	-0.330	-0.367	-0.366	-0.335
423	P ₂ rough	0.582	1.761	0.881	0.592	0.954	0.054	0.050	0.047	0.043	0.048
424	N ₁ rough, pit	0.577	1.367	0.790	0.759	0.873	-0.019	-0.022	-0.013	-0.022	-0.019
425	P ₂ rough	0.623	0.380	0.501	0.414	0.479	0.045	0.032	0.028	0.024	0.032
426	A ₂ stuck	0.429	0.473	0.641	0.473	0.504	0.356	0.340	0.405	0.403	0.376
427	P ₂ rough	0.429	0.476	0.612	0.576	0.523	0.031	0.033	0.041	0.048	0.038
428	P ₂ rough	0.562	0.516	0.699	0.545	0.580	0.038	0.028	0.026	0.021	0.028
429	D dent	0.766	0.811	0.937	0.878	0.848	-0.029	-0.022	-0.019	-0.024	-0.023
430	N ₁ pit	0.442	0.268	0.283	0.270	0.316	-0.020	-0.042	-0.022	-0.015	-0.025
431	N ₁ pit	0.251	0.210	0.221	0.251	0.233	-0.033	-0.026	-0.030	-0.026	-0.029
432	D dent	0.958	0.727	0.983	1.047	0.929	-0.029	-0.024	-0.017	-0.022	-0.023
433	N ₁ pit	0.223	0.195	0.251	0.192	0.215	-0.021	-0.032	-0.020	-0.020	-0.023
434	N ₁ pit	0.139	0.122	0.162	0.249	0.168	-0.017	-0.023	-0.018	-0.031	-0.022
435	N ₁ pit	0.225	0.223	0.236	0.177	0.215	-0.019	-0.035	-0.023	-0.020	-0.024
436	N ₁ pit	0.221	0.223	0.225	0.223	0.223	-0.017	-0.025	-0.024	-0.021	-0.022
437	P ₂ rough	0.976	0.621	0.585	0.563	0.686	0.037	0.037	0.038	0.038	0.037
438	N ₁ pit	0.164	0.251	0.174	0.253	0.210	-0.045	-0.041	-0.024	-0.023	-0.033
439	D dent	0.956	0.854	1.167	1.351	1.082	-0.030	-0.021	-0.018	-0.022	-0.023
440	P ₂ peak	0.373	0.347	0.268	0.286	0.318	0.431	0.444	0.417	0.435	0.432
441	D dent	1.480	1.279	1.476	1.399	1.408	-0.019	-0.029	-0.024	-0.022	-0.024
442	A ₁ con. ring	1.730	1.709	1.709	1.878	1.757	0.522	0.610	0.560	0.518	0.552
443	N ₁ pit	0.183	0.211	0.332	0.222	0.237	-0.025	-0.033	-0.021	-0.043	-0.030
444	P ₂ peak	0.453	0.396	0.408	0.408	0.416	0.469	0.470	0.448	0.442	0.457
445	A ₂ stuck	1.317	1.097	1.245	1.274	1.233	0.498	0.737	0.709	0.716	0.665
446	P ₂ peak	0.166	0.181	0.274	0.257	0.219	0.314	0.232	0.284	0.289	0.280
447	P ₂ rough	0.867	0.641	0.418	0.545	0.618	0.027	0.032	0.033	0.020	0.028
448	P ₂ rough	0.418	0.509	0.275	0.476	0.419	0.043	0.041	0.020	0.026	0.032
449	P ₂ rough	0.751	0.879	0.613	0.716	0.740	0.080	0.100	0.077	0.071	0.082
450	D dent	0.864	0.841	0.828	0.828	0.840	-0.022	-0.026	-0.021	-0.020	-0.022
451	P ₂ peak	0.320	0.333	0.344	0.333	0.333	0.422	0.439	0.393	0.404	0.415
452	P ₂ rough	1.143	0.911	1.127	1.110	1.073	0.066	0.074	0.080	0.069	0.072

453	A ₂	stuck	1.302	1.640	1.442	1.292	1.419	0.547	0.659	0.458	0.591	0.564
454	N ₁	pit	0.250	0.196	0.317	0.352	0.279	-0.035	-0.038	-0.028	-0.029	-0.032
455	P ₂	peak	0.308	0.370	0.392	0.459	0.382	0.041	0.029	0.033	0.032	0.034
456	D	dent	1.768	1.956	1.653	1.780	1.789	-0.039	-0.016	-0.035	-0.029	-0.030
457	P ₂	peak	0.412	0.377	0.350	0.408	0.387	0.439	0.416	0.407	0.461	0.431
458	P ₂	peak	0.359	0.335	0.362	0.389	0.361	0.052	0.059	0.055	0.072	0.059
459	A ₂	stuck, spallation/fracture	7.834	9.170	6.513	8.320	7.960	1.324	1.462	1.132	1.904	1.456
460	C	crater, spallation/fracture, fragm.	2.378	2.462	3.014	2.897	2.688	-0.657	-0.709	-0.733	-0.711	-0.703
461	C	crater, spallation/fracture, fragm.	2.123	2.250	2.208	2.215	2.199	-0.541	-0.581	-0.494	-0.515	-0.533
462	C	crater, spallation/fracture	2.250	2.802	2.692	2.607	2.588	-0.356	-0.291	-0.314	-0.372	-0.333
463	A ₂	stuck	1.252	1.139	1.380	1.175	1.237	1.467	1.293	1.244	1.175	1.295
464	P ₂	rough	1.750	0.774	1.326	0.896	1.186	0.466	0.194	0.204	0.246	0.277
465	N ₁	pit	0.106	0.122	0.124	0.120	0.118	-0.334	-0.327	-0.309	-0.215	-0.296
466	P ₂	peak	0.490	0.557	0.531	0.665	0.561	0.040	0.045	0.035	0.044	0.041
467	N ₁	pit	0.137	0.091	0.122	0.169	0.129	-0.314	-0.073	-0.141	-0.275	-0.201
468	N ₁	pit	0.213	0.213	0.213	0.261	0.225	-0.410	-0.328	-0.407	-0.391	-0.384
469	P ₂	rough	0.774	0.935	0.941	0.820	0.867	0.098	0.089	0.093	0.106	0.096
470	N ₁	pit	0.198	0.148	0.169	0.261	0.194	-0.443	-0.359	-0.412	-0.412	-0.407
471	N ₁	pit	0.213	0.140	0.213	0.151	0.179	-0.409	-0.204	-0.400	-0.434	-0.362
472	P ₂	rough	0.655	0.960	0.807	0.755	0.794	0.303	0.235	0.263	0.292	0.273
473	P ₂	rough	0.574	0.396	0.589	0.609	0.542	0.038	0.040	0.044	0.050	0.043
474	P ₂	rough	1.072	1.227	1.227	1.080	1.151	0.271	0.185	0.210	0.205	0.218
475	P ₂	rough	0.392	0.619	0.558	0.564	0.533	0.061	0.050	0.058	0.050	0.054
476	P ₂	rough	0.679	0.649	0.548	0.533	0.602	0.044	0.062	0.040	0.052	0.049
477	P ₂	rough	0.507	0.801	0.594	0.491	0.598	0.037	0.043	0.034	0.034	0.037
478	P ₂	rough	0.792	1.072	1.162	0.589	0.904	0.247	0.304	0.300	0.213	0.266
479	P ₂	rough	0.381	0.762	0.625	0.664	0.608	0.045	0.062	0.058	0.045	0.053
480	P ₂	rough	1.199	0.970	1.017	1.025	1.053	0.150	0.161	0.142	0.368	0.205
481	P ₂	peak	0.259	0.354	0.381	0.259	0.313	0.470	0.444	0.450	0.482	0.461
482	P ₂	peak	0.335	0.320	0.350	0.310	0.329	0.527	0.454	0.477	0.501	0.490
483	P ₂	peak	0.287	0.259	0.350	0.335	0.308	0.445	0.457	0.427	0.440	0.442
484	P ₂	peak	0.487	0.400	0.483	0.411	0.445	0.055	0.033	0.041	0.041	0.042
485	N ₁	pit	0.106	0.060	0.091	0.076	0.083	-0.214	-0.257	-0.052	-0.389	-0.228
486	P ₂	peak	0.418	0.476	0.654	0.577	0.531	0.060	0.063	0.050	0.052	0.056
487	P ₂	rough	0.513	0.618	0.527	0.763	0.605	0.087	0.088	0.089	0.084	0.087
488	N ₁	pit	0.106	0.107	0.091	0.106	0.102	-0.311	-0.049	-0.240	-0.135	-0.184
489	P ₂	rough	0.461	0.418	0.465	0.472	0.454	0.033	0.030	0.035	0.030	0.032
490	P ₂	peak	0.458	0.472	0.527	0.545	0.500	0.030	0.039	0.025	0.027	0.030
491	P ₂	peak	0.408	0.528	0.615	0.584	0.534	0.063	0.054	0.029	0.055	0.050
492	N ₁	pit	0.306	0.095	0.164	0.179	0.186	-0.195	-0.175	-0.310	-0.419	-0.275
493	P ₂	peak	0.287	0.229	0.289	0.242	0.262	0.466	0.464	0.447	0.484	0.465
494	P ₂	peak	0.242	0.226	0.272	0.226	0.241	0.419	0.412	0.384	0.422	0.409
495	D	dent	1.190	0.919	1.007	1.054	1.042	-0.040	-0.047	-0.036	-0.037	-0.040
496	P ₂	peak	0.641	0.618	0.418	0.531	0.552	0.061	0.093	0.064	0.057	0.069
497	D	dent	1.179	1.429	1.419	1.119	1.286	-0.034	-0.041	-0.048	-0.039	-0.041
498	P ₂	peak	0.284	0.287	0.335	0.289	0.299	0.483	0.502	0.481	0.493	0.489
499	D	dent	0.921	1.222	1.011	1.192	1.087	-0.026	-0.034	-0.024	-0.023	-0.027
500	N ₁	pit	0.122	0.137	0.138	0.121	0.129	-0.122	-0.348	-0.361	-0.369	-0.300
501	P ₂	peak	0.604	0.622	0.517	0.654	0.599	0.063	0.067	0.053	0.089	0.068
502	P ₂	rough	0.427	0.262	0.350	0.659	0.424	0.039	0.035	0.030	0.034	0.035

503	P ₂	rough	0.622	0.581	0.418	0.703	0.581	0.051	0.045	0.039	0.037	0.043
504	P ₂	rough	0.520	0.382	0.345	0.472	0.430	0.043	0.040	0.035	0.041	0.040
505	C	crater, spallation/fracture	4.008	5.101	4.709	3.705	4.381	-0.973	-0.870	-0.990	-1.079	-0.978
506	C	crater, spallation/fracture, fragm.	3.273	3.709	3.609	4.036	3.657	-1.295	-1.151	-1.323	-1.272	-1.260
507	A ₁	con. ring	3.818	3.405	3.131	3.767	3.530	0.981	0.955	0.923	0.948	0.952
508	A ₁	con. ring	4.473	2.836	3.627	3.709	3.661	1.013	1.042	0.920	0.924	0.975
509	A ₃	spallation/fracture	2.043	2.213	2.140	1.932	2.082	-0.519	-0.446	-0.695	-0.718	-0.595
510	A ₃	spallation/fracture	2.271	1.847	2.080	1.337	1.884	-0.770	-0.705	-0.649	-0.856	-0.745
511	A ₂	stuck	3.423	3.022	3.095	3.253	3.198	1.285	1.658	1.529	1.399	1.468
512	A ₁	con. ring	4.309	4.636	4.827	3.736	4.377	0.836	0.773	0.810	0.876	0.824
513	C	crater	3.371	3.492	2.581	2.746	3.047	-0.127	-0.131	-0.142	-0.118	-0.130
514	C	crater	0.608	0.876	0.632	1.119	0.809	-0.356	-0.159	-0.224	-0.249	-0.247
515	C	crater, spallation/fracture	4.033	3.216	3.821	4.089	3.790	-0.331	-0.260	-0.326	-0.295	-0.303
516	C	crater, spallation/fracture	2.126	1.787	2.412	2.115	2.110	-1.123	-0.825	-0.925	-1.275	-1.037
517	A ₂	stuck	2.201	2.059	1.953	2.116	2.082	2.180	2.261	2.418	2.206	2.266
518	A ₁	con. ring	3.168	2.873	2.906	2.851	2.949	0.621	0.669	0.548	0.646	0.621
519	A ₁	con. ring	4.302	5.827	4.737	4.039	4.726	1.970	2.406	2.313	2.555	2.311
520	A ₁	con. ring	4.889	4.576	4.555	4.676	4.674	2.038	2.240	2.778	2.599	2.414
521	C	crater, fragm.	1.517	1.272	1.211	1.397	1.349	-0.557	-0.489	-0.554	-0.557	-0.539
522	C	crater, destroyed	6.940	7.109	6.603	7.144	6.949	-2.080	-1.318	-1.584	-2.108	-1.772
523	C	crater, spallation/fracture	1.087	1.712	1.466	1.125	1.348	-0.444	-0.476	-0.476	-0.449	-0.461
524	C	crater, spallation/fracture	4.479	4.058	4.499	4.369	4.351	-0.776	-0.707	-0.760	-0.691	-0.734
525	A ₁	con. ring	3.620	3.474	4.037	3.376	3.627	1.035	1.044	1.033	1.073	1.046
526	A ₁	con. ring	3.522	4.232	3.865	3.253	3.718	0.981	0.914	0.903	0.819	0.904
527	A ₁	con. ring	4.133	4.936	5.673	4.298	4.760	1.023	1.043	1.044	1.043	1.038
528	A ₁	con. ring	3.440	3.872	2.505	3.312	3.282	1.063	0.809	1.060	1.061	0.998
529	A ₁	con. ring	2.376	2.449	2.760	2.099	2.421	0.576	0.551	0.534	0.527	0.547
530	A ₁	con. ring	3.869	4.330	4.013	4.110	4.080	1.019	0.906	0.867	0.954	0.937
531	A ₁	con. ring	2.673	2.209	2.948	2.046	2.469	1.620	1.623	1.652	1.585	1.620
532	A ₁	con. ring	16.083	14.338	12.557	16.918	14.974	2.416	2.544	2.764	2.945	2.667
533	C	crater, destroyed, spallation/fracture	2.462	2.951	2.784	2.713	2.727	-0.396	-0.222	-0.269	-0.209	-0.274
534	A ₁	con. ring	8.610	9.972	8.415	8.924	8.980	2.964	3.131	2.902	3.182	3.045
535	A ₁	con. ring	3.870	4.183	3.551	4.819	4.106	1.091	1.117	1.077	1.069	1.089
536	A ₁	con. ring	4.402	3.927	4.055	4.381	4.191	0.674	0.635	0.647	0.688	0.661
537	A ₂	stuck	2.166	1.755	1.608	1.741	1.817	1.074	0.742	1.188	0.860	0.966
538	B ₁	splash	15.624	12.438	12.248	17.952	14.565	0.847	0.809	0.838	0.740	0.808
539	A ₁	con. ring	5.229	4.149	4.099	3.761	4.309	1.446	1.396	1.625	1.543	1.503
540	A ₁	con. ring	5.921	5.236	5.154	4.911	5.305	0.638	0.512	0.570	0.581	0.575
541	A ₁	con. ring	6.506	7.018	7.815	7.027	7.092	1.485	1.369	1.424	1.248	1.382
542	C	crater, spallation/fracture, fragm.	1.656	1.658	0.928	1.547	1.447	-0.625	-0.337	-0.474	-0.387	-0.456
543	C	crater, destroyed	1.199	1.397	1.160	0.990	1.186	-0.699	-0.406	-0.575	-0.566	-0.561
544	A ₁	con. ring	3.010	2.965	3.210	3.029	3.053	0.508	0.409	0.544	0.590	0.513
545	C	crater, spallation/fracture, fragm.	6.705	7.350	6.896	4.774	6.431	-1.148	-1.212	-1.156	-1.318	-1.208
546	C	crater, spallation/fracture, fragm.	1.359	1.741	1.282	1.592	1.493	-0.650	-0.718	-0.568	-0.801	-0.684
547	A ₂	stuck	4.991	4.574	4.391	5.346	4.825	2.608	2.689	2.711	2.939	2.737
548	A ₂	stuck	2.968	3.611	3.503	3.184	3.317	2.135	2.384	2.619	2.242	2.345

549	C	crater	1.125	1.235	0.795	1.052	1.052	-0.274	-0.245	-0.319	-0.347	-0.296
550	A ₂	stuck	3.474	3.405	3.381	3.571	3.458	2.695	2.520	2.580	2.473	2.567
551	A ₂	stuck	4.550	4.036	3.743	3.745	4.018	2.577	2.510	2.510	2.986	2.646
552	A ₂	stuck	3.138	3.399	2.760	3.155	3.113	1.817	2.135	2.062	1.961	1.994
553	A ₁	con. ring	4.167	3.528	3.269	3.991	3.739	0.817	0.834	0.754	0.743	0.787
554	A ₁	con. ring	4.076	3.829	3.927	4.113	3.986	0.789	0.767	0.750	0.771	0.769
555	A ₂	stuck	3.036	3.174	3.271	3.092	3.143	1.722	1.799	1.763	1.802	1.772
556	A ₁	con. ring	1.553	1.695	1.814	1.460	1.630	0.724	0.644	0.621	0.653	0.661
557	A ₁	con. ring	3.633	3.715	4.203	2.993	3.636	0.541	0.481	0.495	0.494	0.503
558	P ₂	rough	2.193	2.157	2.115	2.211	2.169	0.200	0.192	0.176	0.162	0.183
559	P ₂	rough	0.730	1.287	0.991	1.138	1.036	0.090	0.103	0.083	0.320	0.149
560	A ₁	con. ring	1.174	0.866	1.151	1.248	1.110	1.034	0.743	0.704	0.746	0.807
561	D	dent	2.292	1.808	2.236	2.798	2.283	-0.043	-0.041	-0.038	-0.035	-0.039
562	D	dent	2.602	2.006	1.957	1.859	2.106	-0.034	-0.047	-0.047	-0.041	-0.042
563	C	crater, fragm.	0.521	0.744	0.683	0.638	0.646	-1.052	-0.808	-0.722	-1.190	-0.943
564	A ₃	shining halo, stuck	16.735	17.968	18.543	18.238	17.871	10.604	10.771	10.523	10.936	10.708
565	B ₁	splash	10.560	8.911	10.856	10.669	10.249	1.743	1.875	1.632	1.360	1.653
566	A ₂	stuck	1.076	1.040	0.976	1.113	1.051	0.517	0.593	0.552	0.584	0.562
567	A ₂	stuck	0.954	1.064	0.917	0.832	0.942	0.803	0.851	0.755	0.835	0.811
568	C	crater, spallation/fracture, fragm.	5.056	5.375	4.797	4.721	4.987	-1.895	-1.728	-1.515	-1.877	-1.753
569	C	crater, spallation/fracture, fragm.	2.182	1.991	2.046	2.100	2.080	-1.041	-1.243	-1.397	-1.342	-1.256
570	C	crater, spallation/fracture, fragm.	5.300	6.605	3.850	5.072	5.206	-2.027	-2.070	-1.774	-1.954	-1.956
571	A ₁	con. ring	7.064	6.689	6.882	6.663	6.824	1.786	1.942	1.823	1.837	1.847
572	C	crater, spallation/fracture	2.092	2.397	2.140	2.176	2.201	-0.396	-0.498	-0.376	-0.403	-0.418
573	N ₁	rough, pit	0.771	0.489	0.856	0.758	0.719	-0.407	-0.402	-0.415	-0.370	-0.399
574	P ₂	rough	0.730	0.795	0.758	0.599	0.721	0.571	0.492	0.442	0.429	0.483
575	A ₁	con. ring	1.126	1.529	1.407	1.431	1.373	0.644	0.737	0.636	0.970	0.747
576	N ₁	pit	0.364	0.349	0.276	0.258	0.312	-0.027	-0.028	-0.024	-0.024	-0.026
577	P ₂	peak	0.711	0.471	0.547	0.613	0.585	0.383	0.382	0.334	0.371	0.367
578	D	dent	0.954	1.248	1.113	1.138	1.113	-0.019	-0.022	-0.015	-0.015	-0.018
579	N ₁	pit	0.506	0.490	0.521	0.541	0.515	-0.375	-0.607	-0.363	-0.399	-0.436
580	P ₂	peak	0.486	0.340	0.511	0.492	0.457	0.439	0.468	0.450	0.465	0.455
581	N ₁	pit	0.245	0.213	0.301	0.181	0.235	-0.054	-0.037	-0.025	-0.026	-0.035
582	N ₁	pit	0.234	0.213	0.134	0.394	0.244	-0.046	-0.025	-0.027	-0.016	-0.028
583	P ₂	rough	0.623	0.414	0.380	0.587	0.501	0.435	0.396	0.442	0.392	0.416
584	P ₂	peak	0.261	0.273	0.301	0.322	0.289	0.474	0.473	0.445	0.494	0.471
585	P ₂	peak	0.364	0.261	0.356	0.373	0.338	0.383	0.335	0.339	0.368	0.356
586	P ₂	peak	0.421	0.338	0.359	0.367	0.371	0.458	0.479	0.444	0.441	0.456
587	P ₂	peak	0.075	0.097	0.121	0.167	0.115	0.275	0.206	0.248	0.134	0.215
588	P ₂	peak	0.391	0.421	0.382	0.363	0.389	0.467	0.470	0.473	0.447	0.464
589	P ₂	rough	1.957	1.458	2.023	2.099	1.884	0.673	0.625	0.631	0.687	0.654
590	P ₂	rough	0.460	0.444	0.638	0.577	0.530	0.034	0.028	0.030	0.028	0.030
591	D	dent	1.002	0.926	0.991	0.917	0.959	-0.032	-0.022	-0.027	-0.023	-0.026
592	C	crater, spallation/fracture	2.018	1.964	2.018	1.882	1.970	-0.622	-0.619	-0.612	-0.548	-0.600
593	A ₁	con. ring	2.760	3.312	2.717	2.632	2.855	0.823	0.757	0.798	0.791	0.792
594	P ₂	peak	0.416	0.367	0.322	0.354	0.365	0.407	0.366	0.383	0.370	0.382
595	P ₂	rough	0.805	0.607	0.720	0.653	0.696	0.041	0.053	0.042	0.038	0.043
596	P ₂	rough	0.766	0.720	1.027	0.531	0.761	0.107	0.313	0.279	0.265	0.241
597	P ₂	peak	0.304	0.380	0.418	0.356	0.364	0.338	0.418	0.389	0.385	0.382

598	P ₂ peak	0.150	0.075	0.104	0.124	0.113	0.168	0.248	0.236	0.125	0.194
599	P ₂ rough	0.850	0.510	0.572	0.440	0.593	0.335	0.301	0.327	0.332	0.324
600	P ₂ rough	0.472	0.536	0.490	0.523	0.506	0.335	0.337	0.330	0.365	0.342
601	N ₁ pit	0.265	0.152	0.182	0.213	0.203	-0.020	-0.024	-0.021	-0.019	-0.021
602	N ₁ pit	0.213	0.228	0.247	0.247	0.234	-0.029	-0.032	-0.025	-0.021	-0.027
603	N ₁ pit	0.164	0.199	0.199	0.276	0.210	-0.016	-0.021	-0.026	-0.023	-0.021
604	N ₁ pit	0.407	0.406	0.410	0.395	0.405	-0.342	-0.341	-0.344	-0.336	-0.341
605	P ₂ peak	0.258	0.184	0.217	0.241	0.225	0.258	0.345	0.340	0.337	0.320
606	D dent	1.239	1.504	1.423	1.310	1.369	-0.014	-0.021	-0.022	-0.022	-0.020
607	A ₃ shining halo	4.952	6.104	4.880	5.323	5.315	1.521	1.426	1.506	1.588	1.510
608	A ₁ con. ring	3.818	3.683	3.669	3.575	3.686	0.959	0.881	0.939	0.905	0.921
609	C crater, spallation/fracture	7.653	4.433	4.565	5.162	5.454	-0.533	-0.670	-0.561	-0.609	-0.593
610	A ₃ shining halo	4.440	3.911	3.678	4.151	4.045	2.117	2.095	2.012	1.818	2.010
611	A ₃ shining halo	4.512	4.715	3.678	3.546	4.113	0.428	0.569	0.844	0.559	0.600
612	C crater, fragm.	0.445	0.552	0.613	0.359	0.492	-0.423	-0.210	-0.021	-0.546	-0.300
613	P ₂ peak	0.486	0.588	0.588	0.516	0.544	0.292	0.299	0.295	0.314	0.300
614	P ₂ rough	1.594	1.042	1.336	0.957	1.232	0.330	0.175	0.370	0.457	0.333
615	N ₁ pit	0.764	0.998	1.061	1.004	0.957	-0.106	-0.102	-0.111	-0.104	-0.106
616	P ₂ rough	5.830	0.790	1.098	0.950	2.167	0.190	0.195	0.184	0.197	0.192
617	C crater, spallation/fracture, fragm.	2.127	2.455	3.000	2.291	2.468	-0.835	-0.519	-0.597	-0.710	-0.665
618	C crater, spallation/fracture	1.231	1.995	1.847	1.432	1.626	-0.424	-0.353	-0.397	-0.382	-0.389
619	A ₁ con. ring	2.992	3.312	3.057	3.163	3.131	1.467	1.355	1.358	1.204	1.346
620	N ₁ pit	0.383	0.368	0.355	0.372	0.369	-0.686	-0.408	-0.491	-0.636	-0.555
621	D dent	1.314	1.067	1.376	1.382	1.285	-0.035	-0.022	-0.031	-0.022	-0.028
622	P ₂ peak	0.449	0.376	0.456	0.391	0.418	0.402	0.375	0.663	0.371	0.453
623	P ₂ rough	1.023	0.797	0.835	0.896	0.888	0.471	0.585	0.665	0.495	0.554
624	P ₂ peak	0.265	0.286	0.325	0.331	0.302	0.509	0.488	0.487	0.476	0.490
625	D dent	1.116	0.996	1.002	1.053	1.042	-0.013	-0.030	-0.011	-0.013	-0.017
626	N ₁ rough, pit	2.784	2.024	2.882	2.249	2.485	-0.027	-0.024	-0.027	-0.030	-0.027
627	D dent	0.935	1.199	1.321	1.057	1.128	-0.033	-0.034	-0.026	-0.032	-0.031
628	P ₂ peak	0.526	0.418	0.640	0.486	0.517	0.092	0.097	0.092	0.077	0.089
629	C crater, spallation/fracture, fragm.	3.569	3.831	3.448	3.670	3.630	-1.479	-1.323	-1.143	-1.393	-1.334
630	C crater, spallation/fracture, fragm.	1.304	1.645	1.231	1.613	1.448	-0.485	-0.526	-0.558	-0.448	-0.504
631	N ₁ defect	10.201	5.452	7.154	6.616	7.356	-2.150	-2.715	-2.447	-1.962	-2.318
632	C crater, spallation/fracture, fragm.	1.316	1.420	1.539	2.051	1.581	-0.565	-1.420	-0.977	-1.061	-1.006
633	C crater, spallation/fracture	1.871	2.415	2.187	2.187	2.165	-0.194	-0.164	-0.194	-0.184	-0.184
634	N ₁ defect	10.512	7.625	9.343	8.876	9.089	-0.867	-1.049	-0.821	-1.283	-1.005
635	A ₁ con. ring	2.449	2.358	2.431	2.415	2.413	0.713	0.679	0.691	0.662	0.686
636	C crater, fragm.	1.032	1.032	1.027	0.972	1.016	-0.219	-0.257	-0.276	-0.377	-0.282
637	C crater, spallation/fracture, fragm.	2.535	2.264	2.221	2.400	2.355	-1.469	-1.471	-0.991	-1.348	-1.319
638	A ₁ con. ring	2.528	1.655	2.038	2.050	2.068	0.779	0.670	0.640	0.718	0.702
639	A ₁ con. ring	1.260	1.250	1.299	1.225	1.258	0.507	0.521	0.542	0.444	0.503
640	A ₁ con. ring	0.725	0.638	0.577	0.613	0.638	0.159	0.424	0.365	0.240	0.297
641	D dent	1.716	1.579	1.792	2.050	1.784	-0.035	-0.037	-0.045	-0.036	-0.038
642	P ₂ peak	0.744	0.398	0.464	0.490	0.524	0.417	0.325	0.346	0.383	0.368
644	A ₁ con. ring	2.101	2.547	2.271	3.098	2.505	0.846	0.635	0.677	0.608	0.691
645	A ₂ stuck	1.609	1.336	1.928	1.792	1.666	1.144	1.239	1.159	1.037	1.145

646	A ₁	con. ring	2.431	2.394	2.376	2.531	2.433	0.517	0.606	0.561	0.599	0.571
647	A ₁	con. ring	0.957	0.919	1.017	1.180	1.018	0.518	0.522	0.506	0.500	0.512
648	D	dent	1.154	1.260	1.230	1.367	1.253	-0.023	-0.033	-0.021	-0.026	-0.026
649	A ₁	con. ring	0.928	0.850	0.910	0.873	0.890	0.690	0.668	0.613	0.679	0.662
650	D	dent	1.518	1.518	1.427	0.797	1.315	-0.023	-0.033	-0.025	-0.016	-0.024
651	P ₂	peak	0.547	0.714	0.683	0.638	0.645	0.614	0.654	0.608	0.617	0.623
652	P ₂	rough	1.488	1.048	1.291	1.280	1.276	0.443	0.459	0.428	0.458	0.447
653	P ₂	rough	2.412	1.608	2.063	1.823	1.977	0.713	0.372	0.623	0.782	0.622
654	A ₁	con. ring	1.303	1.234	1.165	1.414	1.279	0.601	0.836	0.711	0.365	0.628
655	P ₂	rough	0.766	0.410	0.456	0.567	0.550	0.450	0.262	0.346	0.287	0.336
656	P ₂	peak	0.459	0.372	0.351	0.441	0.406	0.427	0.436	0.405	0.439	0.427
657	C	crater stuck, spalla- tion/fracture, fragm.	3.518	3.022	3.241	3.229	3.252	-1.442	-1.533	-1.546	-1.498	-1.505
658	A ₂	stuck	2.450	2.018	2.549	2.422	2.360	0.854	1.136	1.003	0.863	0.964
659	A ₃	shining halo, con. ring	2.658	3.419	2.187	2.760	2.756	0.650	0.650	0.650	0.650	0.650
660	A ₂	stuck	0.865	0.950	0.919	0.759	0.874	0.826	0.910	0.821	0.831	0.847
661	A ₃	shining halo, con. ring	2.308	3.184	3.169	3.248	2.977	0.475	0.527	0.563	0.650	0.554
662	A ₁	con. ring	1.108	0.835	1.036	0.897	0.969	0.637	0.516	0.545	0.609	0.577
663	D	dent	1.260	1.257	1.211	1.088	1.204	-0.021	-0.011	-0.021	-0.019	-0.018
664	P ₂	rough	0.828	0.881	0.820	0.987	0.879	0.317	0.138	0.244	0.112	0.203
665	P ₂	peak	0.758	0.395	0.380	0.444	0.494	0.442	0.403	0.415	0.413	0.418
666	D	dent	0.940	1.064	1.125	1.255	1.096	-0.030	-0.027	-0.028	-0.023	-0.027
667	P ₂	rough	0.410	0.797	0.552	0.552	0.577	0.035	0.060	0.052	0.042	0.047
668	P ₂	rough	0.606	0.384	0.563	0.445	0.499	0.467	0.420	0.398	0.371	0.414
669	A ₁	con. ring	0.759	0.850	1.023	0.969	0.900	0.580	0.559	0.651	0.461	0.563
670	A ₂	stuck	0.668	0.843	0.832	0.850	0.798	0.304	0.264	0.327	0.265	0.290
671	A ₁	con. ring	3.425	4.231	3.527	4.599	3.945	1.694	1.664	1.798	1.645	1.700
672	A ₁	con. ring	3.672	3.141	3.842	2.970	3.407	1.310	1.384	1.306	1.255	1.314
673	A ₂	stuck	7.325	6.190	6.397	6.290	6.550	2.625	3.131	2.803	2.645	2.801
674	A ₂	stuck	3.648	3.346	3.351	3.400	3.436	1.586	1.326	1.330	1.398	1.410
675	A ₁	con. ring	3.326	2.652	2.486	2.723	2.797	0.781	1.152	0.803	0.947	0.921
676	A ₁	con. ring	1.050	0.709	0.941	0.985	0.921	0.661	0.547	0.576	0.522	0.577
677	D	dent	1.627	1.809	1.864	1.608	1.727	-0.036	-0.034	-0.031	-0.038	-0.035
678	A ₁	con. ring	1.786	1.216	1.455	1.547	1.501	0.540	0.490	0.449	0.481	0.490
679	A ₂	stuck	3.372	1.719	1.677	1.541	2.077	1.039	0.947	0.878	0.940	0.951
680	A ₂	stuck	1.710	2.038	1.487	1.613	1.712	0.690	0.606	0.692	0.912	0.725
681	C	crater, spalla- tion/fracture, fragm.	3.290	3.277	3.168	3.568	3.326	-0.876	-0.781	-0.926	-0.483	-0.767
682	C	crater, spalla- tion/fracture, fragm.	2.460	3.054	2.820	2.684	2.754	-0.592	-0.390	-0.558	-0.627	-0.542
683	A ₂	stuck	1.864	1.608	1.736	1.959	1.792	0.663	0.698	0.663	0.747	0.693
684	P ₂	rough	1.418	0.784	1.046	1.208	1.114	0.509	0.516	0.519	0.513	0.514
685	P ₂	rough	1.510	1.584	1.462	1.444	1.500	0.193	0.254	0.260	0.220	0.232
686	D	dent	1.215	1.191	1.379	1.287	1.268	-0.027	-0.021	-0.031	-0.022	-0.025
687	P ₂	rough	0.577	0.787	0.763	0.765	0.723	0.161	0.170	0.129	0.143	0.151
688	C	crater, spalla- tion/fracture, fragm.	1.718	1.892	1.864	1.691	1.791	-0.545	-0.638	-0.661	-0.627	-0.618
689	A ₁	con. ring	3.573	4.173	4.688	3.300	3.933	1.251	1.248	1.214	1.277	1.247
690	A ₁	con. ring	0.930	1.003	0.965	0.990	0.972	0.469	0.569	0.554	0.541	0.533
691	A ₁	con. ring	0.982	0.832	0.832	0.710	0.839	0.685	0.673	0.627	0.571	0.639
692	P ₂	rough	1.768	0.707	1.608	1.694	1.444	0.370	0.126	0.368	0.409	0.318
693	A ₂	stuck	5.346	4.936	4.578	5.018	4.970	1.257	1.285	1.328	1.245	1.278

694	A ₁	con. ring	1.296	1.432	1.334	1.350	1.353	0.259	0.253	0.253	0.240	0.251
695	P ₂	rough	1.173	0.999	0.900	1.118	1.047	0.532	0.556	0.501	0.522	0.528
696	P ₂	rough	1.200	0.941	1.009	1.006	1.039	0.398	0.200	0.434	0.346	0.344
697	A ₁	con. ring	3.517	3.290	3.518	3.600	3.481	1.629	1.719	1.793	1.794	1.734
698	A ₁	con. ring	1.367	1.199	1.191	0.987	1.186	0.321	0.512	0.754	0.732	0.580
699	A ₁	con. ring	2.285	2.302	2.245	2.302	2.283	0.719	0.494	0.565	0.741	0.630
700	C	crater, spallation/fracture	3.605	1.020	2.202	1.420	2.061	-0.583	-0.827	-0.749	-0.648	-0.702
701	A ₁	con. ring	0.812	0.668	0.790	0.812	0.770	0.374	0.439	0.392	0.384	0.397
702	P ₂	rough	1.093	0.759	0.945	0.981	0.944	0.320	0.279	0.329	0.375	0.326
703	A ₃	shining halo, stuck	9.046	8.909	9.383	7.743	8.771	2.392	2.166	2.337	2.351	2.311
704	A ₁	con. ring	5.466	3.739	4.333	4.504	4.510	1.646	1.545	1.543	1.634	1.592
705	C	crater, fragm.	0.872	0.657	1.003	0.636	0.792	-1.129	-0.964	-0.780	-1.007	-0.970
706	P ₂	rough	1.565	1.160	1.225	1.298	1.312	0.420	0.682	0.526	1.298	0.731
707	A ₁	con. ring	1.492	1.013	1.115	1.170	1.197	0.842	0.816	0.804	0.822	0.821
708	A ₁	con. ring	1.048	1.032	1.098	1.108	1.072	0.992	0.865	0.875	0.891	0.906
709	C	crater, micro	0.905	0.192	0.252	0.243	0.398	-0.609	-0.525	-0.678	-0.550	-0.590
710	D	dent	1.584	1.476	1.571	1.464	1.524	-0.016	-0.013	-0.011	-0.019	-0.015
711	C	crater, flat	4.074	3.289	3.735	2.813	3.478	-0.047	-0.052	-0.070	-0.055	-0.056
712	A ₂	stuck	8.563	6.559	6.945	6.741	7.202	0.900	0.869	0.963	0.848	0.895
713	A ₂	stuck	4.424	4.385	4.306	4.582	4.424	3.584	3.684	3.701	3.606	3.644
714	C	crater	0.439	0.460	0.387	0.331	0.404	-0.772	-0.682	-0.651	-0.441	-0.636
715	C	crater	0.751	1.230	0.820	0.797	0.899	-0.409	-0.261	-0.323	-0.370	-0.340
716	A ₁	con. ring	4.232	2.870	3.916	3.229	3.562	1.455	1.520	1.470	1.458	1.476
717	D	dent	1.577	1.195	1.740	1.526	1.509	-0.019	-0.016	-0.179	-0.018	-0.058
718	A ₁	con. ring	0.987	0.705	0.881	0.881	0.863	0.094	0.366	0.081	0.266	0.202
719	N ₁	pit	0.307	0.410	0.304	0.398	0.355	-0.733	-0.545	-0.577	-0.501	-0.589
720	D	dent	1.870	1.716	1.913	1.854	1.838	-0.021	-0.010	-0.011	-0.019	-0.015
721	C	crater, spallation/fracture, fragm.	3.172	5.400	4.102	2.461	3.784	-2.305	-1.711	-1.600	-1.489	-1.777
722	A ₂	stuck	3.736	2.318	2.550	2.700	2.826	1.718	1.499	2.246	1.828	1.823
723	A ₁	con. ring	1.170	1.133	1.133	1.151	1.147	0.692	0.734	0.704	0.727	0.714
724	A ₂	stuck	37.326	34.165	29.228	37.653	34.593	9.104	8.999	8.433	9.150	8.921
725	A ₂	stuck	1.571	2.714	1.741	2.356	2.095	2.191	2.177	2.310	2.084	2.190
726	A ₁	con. ring	2.320	1.901	1.952	2.118	2.073	0.936	0.919	0.939	0.968	0.941
727	N ₁	pit	0.402	0.406	0.440	0.504	0.438	-0.434	-0.550	-0.375	-0.451	-0.453
728	C	crater	2.318	2.822	2.576	2.520	2.559	-0.273	-0.252	-0.256	-0.295	-0.269
729	A ₁	con. ring	1.755	1.964	2.155	2.209	2.020	1.874	1.739	1.720	1.828	1.790
730	A ₁	con. ring	1.381	1.418	1.480	1.565	1.461	0.938	0.895	0.894	0.886	0.903
731	A ₁	con. ring	1.814	1.678	2.116	1.707	1.829	1.200	1.226	1.278	1.132	1.209
732	P ₂	rough	1.539	2.116	1.571	1.848	1.768	0.082	0.079	0.084	0.073	0.079
733	P ₂	rough	1.083	0.429	0.531	0.659	0.675	0.458	0.330	0.281	0.319	0.347
734	N ₁	defect	10.142	6.835	10.616	11.462	9.764	-1.839	-1.721	-1.494	-1.448	-1.626
735	N ₁	defect	11.223	0.865	0.826	0.677	3.398	-0.594	-0.598	-0.287	-0.347	-0.456
736	C	crater, spallation/fracture, fragm.	4.066	2.772	3.781	3.922	3.635	-1.265	-0.501	-0.959	-0.909	-0.909
737	P ₂	rough	0.918	1.067	1.124	1.017	1.031	0.369	0.284	0.319	0.266	0.309
738	P ₂	peak	0.774	0.774	0.790	0.714	0.763	0.348	0.135	0.169	0.368	0.255
739	A ₁	con. ring	4.221	3.752	4.433	4.251	4.164	2.089	2.061	2.220	2.065	2.109
740	A ₁	con. ring	4.881	3.887	4.485	4.413	4.416	1.784	1.770	1.829	1.763	1.786
741	A ₂	stuck	3.038	3.449	3.454	3.082	3.256	1.241	1.345	1.301	1.608	1.373
742	A ₁	con. ring	2.735	2.925	3.014	2.696	2.843	2.006	2.449	2.447	1.999	2.225
743	A ₁	con. ring	2.960	2.994	3.210	2.967	3.033	1.373	1.403	1.329	1.186	1.323

744	C	crater, fragm.	1.346	1.218	1.295	1.239	1.275	-1.149	-0.714	-1.328	-0.921	-1.028
745	N ₁	defect, rough	2.972	0.506	0.756	0.076	1.077	0.722	0.447	0.465	0.579	0.553
746	P ₂	rough	2.258	2.778	2.420	2.229	2.421	2.003	2.124	1.940	2.701	2.192
747	D	dent	1.383	1.377	1.604	1.755	1.530	-0.026	-0.021	-0.019	-0.017	-0.021
748	P ₂	rough	1.485	0.903	1.199	1.144	1.183	0.549	0.462	0.453	0.467	0.483
749	C	crater, spallation/fracture, fragm.	4.426	4.947	4.293	3.210	4.219	-1.702	-1.431	-0.705	-1.590	-1.357
750	C	crater, fragm.	1.528	1.527	1.517	1.710	1.571	-1.027	-0.878	-0.694	-0.750	-0.837
751	P ₂	rough	1.503	0.720	0.935	1.073	1.058	0.298	0.243	0.268	0.246	0.264
752	D	dent	1.561	1.809	1.580	2.220	1.793	-0.012	-0.016	-0.020	-0.021	-0.017
753	P ₂	rough	0.537	0.596	0.505	0.537	0.544	0.330	0.338	0.331	0.332	0.333
754	P ₂	rough	0.791	0.372	0.627	0.477	0.567	0.399	0.320	0.358	0.364	0.360
755	C	crater, spallation/fracture	2.921	2.864	2.782	2.755	2.830	-0.552	-0.399	-0.450	-0.473	-0.468
756	C	crater, spallation/fracture	2.691	2.991	2.943	3.156	2.945	-0.238	-0.233	-0.225	-0.247	-0.236
757	A ₁	con. ring	1.456	1.609	1.563	1.549	1.544	0.492	0.356	0.521	0.544	0.478
758	C	crater	1.868	1.274	1.355	1.528	1.506	-0.139	-0.214	-0.230	-0.206	-0.197
759	N ₁	defect	9.047	1.453	3.253	1.810	3.891	-0.216	-0.161	-0.158	-0.174	-0.177
760	P ₂	rough	1.371	1.133	1.197	1.462	1.291	0.772	0.797	0.754	0.785	0.777
761	P ₂	rough	0.493	0.420	0.585	0.548	0.512	0.444	0.444	0.444	0.444	0.444
762	P ₂	rough	2.486	0.973	1.261	1.261	1.495	0.449	0.374	0.388	0.444	0.414
763	A ₃	shining halo, con. ring	4.359	3.982	4.359	3.955	4.163	1.576	1.498	1.406	1.580	1.515
764	A ₃	shining halo, con. ring	5.019	5.420	4.985	4.952	5.094	2.860	2.758	2.873	2.873	2.841
765	A ₁	con. ring	6.458	4.985	7.227	4.589	5.815	1.057	0.796	0.951	0.737	0.885
766	P ₂	rough	1.427	1.017	1.144	0.950	1.135	0.555	0.167	0.345	0.377	0.361
767	P ₂	rough	1.226	0.759	0.782	0.935	0.925	0.318	0.275	0.313	0.296	0.300
768	P ₂	rough	1.592	1.090	1.359	1.231	1.318	0.095	0.096	0.108	0.104	0.101
769	A ₂	stuck	2.094	1.484	2.030	1.592	1.800	0.879	0.704	0.726	0.721	0.758
770	A ₁	con. ring	2.314	2.823	2.547	2.441	2.531	0.663	0.556	0.578	0.575	0.593
771	A ₁	con. ring	2.769	2.755	3.327	3.180	3.008	2.718	2.807	3.231	2.798	2.888
772	C	crater, spallation/fracture	2.944	1.974	2.285	1.666	2.217	-0.537	-0.715	-0.696	-0.458	-0.601
773	A ₁	con. ring	4.167	3.000	2.893	3.114	3.293	0.634	0.851	0.703	0.698	0.722
774	A ₁	con. ring	3.184	2.222	2.628	2.030	2.516	0.626	0.611	0.856	0.708	0.700
775	P ₂	rough	1.608	0.977	1.468	1.223	1.319	0.312	0.245	0.295	0.288	0.285
776	P ₂	rough	1.602	1.188	1.142	1.350	1.320	0.087	0.092	0.087	0.100	0.092
777	D	dent	1.582	1.749	1.722	1.810	1.716	-0.017	-0.019	-0.020	-0.012	-0.017
778	P ₂	rough	0.641	0.573	0.600	0.641	0.614	0.349	0.364	0.346	0.347	0.351
779	P ₂	rough	0.529	0.689	0.696	0.524	0.609	0.203	0.490	0.404	0.471	0.392
780	C	crater, spallation/fracture, fragm.	3.562	3.680	3.750	3.279	3.568	-0.921	-0.826	-0.886	-0.873	-0.877
781	A ₂	stuck	1.910	1.828	1.974	1.974	1.921	1.843	1.731	1.993	1.750	1.829
782	C	crater, spallation/fracture	5.337	2.876	4.697	4.532	4.361	-0.663	-0.938	-0.594	-0.602	-0.699
783	A ₁	con. ring	0.737	0.921	1.044	0.859	0.890	0.738	0.699	0.648	0.686	0.693
784	A ₁	con. ring	0.976	1.016	0.859	0.835	0.921	0.310	0.070	0.119	0.339	0.209
785	A ₁	con. ring	2.104	2.067	1.786	2.348	2.076	1.330	1.521	1.597	1.520	1.492
786	A ₁	con. ring	2.836	1.681	2.227	2.044	2.197	0.931	0.938	1.021	0.948	0.959
787	P ₂	rough	0.647	0.577	0.556	0.572	0.588	0.071	0.111	0.269	0.310	0.190
788	A ₁	con. ring	3.056	3.097	2.935	2.797	2.971	0.885	0.803	0.793	0.758	0.809
789	A ₂	stuck	1.170	1.060	1.068	1.225	1.131	0.996	1.033	0.991	1.052	1.018
790	C	crater, spallation/fracture, fragm.	3.264	3.244	3.630	2.871	3.252	-1.266	-0.999	-1.454	-1.095	-1.204
791	C	crater, spallation/fracture,	2.199	2.722	2.822	2.789	2.633	-1.041	-1.086	-1.116	-1.190	-1.108

		fragm.										
792	C	crater, spallation/fracture, fragm.	3.423	5.802	4.971	3.303	4.375	-1.856	-2.222	-1.589	-1.387	-1.763
793	A ₁	con. ring	0.932	0.994	0.997	1.050	0.993	0.248	0.282	0.298	0.279	0.277
794	A ₃	shining halo	7.537	6.128	6.445	6.544	6.663	2.591	2.535	2.416	2.403	2.486
795	P ₂	rough	2.345	1.104	1.859	1.321	1.657	1.616	1.097	1.423	1.813	1.487
796	A ₁	con. ring	0.950	0.843	0.904	0.896	0.898	0.446	0.447	0.178	0.412	0.371
797	D	dent	1.555	1.868	1.670	1.839	1.733	-0.022	-0.021	-0.013	-0.032	-0.022
798	P ₁	dust	22.941	22.205	22.536	18.038	21.430	2.844	6.097	4.489	4.706	4.534
799	B ₂	splash	9.844	8.127	8.509	8.476	8.739	0.594	0.575	0.589	0.587	0.586
800	C	crater	2.083	2.074	2.108	2.008	2.068	-0.433	-0.443	-0.437	-0.503	-0.454
801	C	crater, flat	1.974	2.918	1.769	1.893	2.139	-0.807	-0.895	-0.823	-0.754	-0.820
802	C	crater, fragm.	1.056	1.798	1.651	1.526	1.508	-0.312	-0.440	-0.370	-0.342	-0.366
803	A ₂	stuck	1.889	1.507	1.645	1.656	1.674	0.273	0.230	0.253	0.239	0.249
804	A ₂	stuck	2.083	1.336	1.718	1.555	1.673	0.197	0.233	0.246	0.243	0.230
805	B ₂	splash	3.674	3.915	3.714	3.763	3.766	0.184	0.197	0.188	0.194	0.190
806	C	crater, spallation/fracture	2.422	2.779	2.285	2.422	2.477	-0.442	-0.372	-0.381	-0.234	-0.357
807	A ₂	stuck	2.291	2.318	2.094	2.646	2.337	0.646	0.677	0.739	0.520	0.646
808	A ₁	con. ring	8.062	6.741	7.333	7.082	7.305	0.554	0.610	0.530	0.564	0.564
809	B ₂	splash	7.015	6.554	6.696	6.671	6.734	0.428	0.450	0.453	0.437	0.442
810	A ₂	stuck	1.991	2.001	1.991	2.018	2.000	0.513	0.460	0.452	0.454	0.470
811	A ₂	stuck	1.691	1.636	1.800	1.837	1.741	0.377	0.405	0.358	0.368	0.377
812	A ₂	stuck	1.800	1.800	1.773	1.609	1.745	0.357	0.502	0.369	0.513	0.435
813	B ₂	cone	18.764	16.201	18.883	16.669	17.630	0.344	0.344	0.311	0.317	0.329
814	B ₂	cone	6.534	7.151	6.745	7.493	6.981	0.246	0.314	0.283	0.288	0.283
815	C	crater	1.362	1.473	1.192	1.313	1.335	-0.725	-0.692	-0.544	-0.603	-0.641
816	C	crater	1.261	0.939	1.031	0.969	1.050	-0.501	-0.539	-0.615	-0.415	-0.517
817	B ₂	splash	5.035	5.712	5.375	5.275	5.349	0.369	0.383	0.378	0.353	0.371
818	B ₂	splash	5.755	7.330	6.039	5.956	6.270	0.549	0.512	0.544	0.498	0.526
819	D	dent	1.090	1.175	1.047	1.083	1.099	-0.064	-0.121	-0.047	-0.054	-0.071
820	D	dent	0.977	0.769	0.919	0.839	0.876	-0.081	-0.025	-0.099	-0.069	-0.069
821	D	dent	1.125	1.329	1.019	1.274	1.187	-0.080	-0.087	-0.091	-0.049	-0.076
822	D	dent	1.256	1.252	1.097	1.154	1.190	-0.072	-0.076	-0.083	-0.093	-0.081
823	D	dent	3.263	3.158	3.309	3.026	3.189	-0.090	-0.071	-0.052	-0.121	-0.084
824	B ₂	splash	3.708	4.691	4.139	4.255	4.198	0.214	0.249	0.237	0.197	0.224
825	B ₂	splash	5.120	5.826	5.775	5.753	5.618	0.419	0.382	0.377	0.376	0.388
826	D	dent	1.463	1.352	1.248	1.282	1.336	-0.074	-0.121	-0.102	-0.063	-0.090
827	D	dent	1.710	1.677	1.550	1.656	1.648	-0.095	-0.104	-0.060	-0.129	-0.097
828	D	dent	1.160	1.352	1.115	1.309	1.234	-0.184	-0.052	-0.044	-0.045	-0.081
829	D	dent	2.775	1.828	2.187	1.922	2.178	-0.074	-0.073	-0.061	-0.096	-0.076
830	D	dent	1.667	2.080	1.635	1.721	1.776	-0.096	-0.119	-0.112	-0.103	-0.107
831	D	dent	1.225	1.052	1.215	1.197	1.172	-0.114	-0.074	-0.122	-0.068	-0.095
832	D	dent	1.510	1.547	1.252	1.271	1.395	-0.070	-0.083	-0.143	-0.118	-0.103
833	P ₁	Dust	36.462	21.600	24.300	25.436	26.949	1.985	2.330	2.204	1.790	2.077
834	B ₂	splash	5.145	4.755	5.265	5.299	5.116	0.450	0.400	0.463	0.430	0.436
835	C	crater, spallation/fracture	1.133	1.372	2.566	1.238	1.577	-0.358	-0.284	-0.451	-0.235	-0.332
836	C	crater, spallation/fracture	2.866	2.145	2.677	2.450	2.535	-0.205	-0.204	-0.202	-0.173	-0.196
837	D	dent	1.528	1.097	1.571	1.189	1.346	-0.086	-0.081	-0.074	-0.136	-0.094
838	D	dent	1.154	1.104	1.087	1.125	1.117	-0.124	-0.137	-0.116	-0.118	-0.124
839	D	dent	1.363	1.418	1.517	1.835	1.533	-0.106	-0.069	-0.078	-0.098	-0.088
840	D	dent	1.243	1.197	1.143	1.142	1.181	-0.085	-0.061	-0.070	-0.092	-0.077
841	C	crater, spallation/fracture	1.601	1.787	1.570	1.887	1.711	-0.945	-0.842	-0.869	-0.917	-0.893
842	C	crater	1.026	1.019	1.506	0.833	1.096	-0.388	-0.276	-0.248	-0.336	-0.312
843	C	crater, spallation/fracture, fragm.	3.821	3.014	4.732	3.450	3.754	-1.075	-1.247	-1.046	-1.311	-1.170
844	C	crater, fragm.	1.192	1.028	0.930	1.052	1.050	-0.526	-0.563	-0.532	-0.530	-0.538

845	C	crater, flat	3.153	4.112	3.712	3.042	3.505	-0.099	-0.144	-0.114	-0.096	-0.113
846	C	crater, spallation/fracture, fragm.	2.258	2.888	1.937	2.348	2.358	-0.957	-0.627	-0.641	-0.698	-0.731
847	C	crater, fragm.	1.364	1.636	1.433	1.508	1.485	-0.269	-0.276	-0.336	-0.287	-0.292
848	B ₁	splash	8.831	5.820	7.512	8.317	7.620	0.475	0.238	0.280	0.428	0.355
849	A ₂	stuck	2.976	2.933	2.646	3.218	2.943	0.685	0.758	0.751	0.738	0.733
850	B ₁	splash	11.687	10.250	11.085	8.502	10.381	0.521	0.473	0.533	0.441	0.492
851	B ₁	splash	4.898	2.099	3.145	3.588	3.432	0.333	0.356	0.304	0.278	0.318
852	A ₂	stuck	1.422	1.528	1.444	1.592	1.496	0.239	0.265	0.270	0.263	0.259
853	B ₁	splash	12.396	9.194	11.053	10.628	10.818	0.217	0.323	0.282	0.348	0.292
854	A ₂	stuck	2.277	2.267	2.133	2.548	2.306	0.629	0.415	0.579	0.616	0.560
855	A ₂	stuck	5.073	2.824	3.982	4.664	4.135	0.470	0.424	0.437	0.468	0.450
856	A ₂	stuck	2.820	2.258	2.288	2.419	2.446	0.512	0.498	0.535	0.590	0.534
857	A ₂	stuck	6.156	7.481	7.481	6.260	6.845	0.463	0.447	0.500	0.425	0.459
858	A ₁	con. ring	4.565	4.249	4.417	4.283	4.378	0.656	0.651	0.621	0.721	0.662
859	A ₂	stuck	2.581	2.951	2.484	2.457	2.618	0.316	0.385	0.334	0.356	0.348
860	A ₂	stuck	3.963	3.058	4.135	2.838	3.498	0.322	0.156	0.304	0.242	0.256
861	A ₂	stuck	3.463	3.340	3.522	3.264	3.397	0.530	0.565	0.596	0.509	0.550
862	D	dent	0.755	1.160	1.142	0.928	0.996	-0.099	-0.106	-0.035	-0.032	-0.068
863	A ₂	stuck	1.850	1.720	1.677	1.762	1.752	0.460	0.457	0.307	0.473	0.424
864	A ₂	stuck	1.297	1.677	1.068	1.432	1.368	0.342	0.284	0.312	0.271	0.302
865	A ₂	stuck	1.183	1.517	1.380	1.368	1.362	0.306	0.296	0.411	0.295	0.327
866	A ₂	stuck	2.123	2.271	2.116	2.271	2.195	0.707	0.726	0.658	0.705	0.699
867	A ₂	stuck	4.781	4.002	4.606	5.655	4.761	0.903	0.801	0.897	0.815	0.854
868	A ₂	stuck	2.144	2.338	2.080	2.108	2.168	1.259	1.301	1.439	1.236	1.309
869	A ₂	stuck	3.027	3.572	3.317	3.169	3.271	0.914	0.910	0.918	0.906	0.912
870	A ₂	stuck	2.984	2.213	2.564	2.524	2.571	0.626	0.733	0.735	0.721	0.704
871	A ₂	stuck	3.495	4.130	4.035	3.218	3.720	1.149	1.149	1.117	1.148	1.140

Acknowledgements

I am overwhelmingly thankful to my Prof. Dr. Mario Trieloff for making this thesis possible, for his discussions, ideas, help and guidance. He encouraged me consciously and unconsciously to keep up my work even at the difficult times with his kindness and open mind.

I want to thank Dr. Ralf Srama for welcoming me in to the Cosmic Dust Group, for his discussions and advices regarding the dust accelerator and willing to be my second referee.

I'm in debt to my friend and colleagues Katherina Fiege and Nozair Khawaja. Thank you Katherina for the conception of our space weathering experiment, the planning, inspiration and the great discussions we had. Thank you Nozair for your advices, discussions and the time you offered. And thank you both for being a friend.

Great thanks to Anne Hildebrand and Gregor Austermann for your priceless advices and your discussions.

A special thank goes to Ilona Fin and Oliver Wienand for producing our high quality mineral targets and to Sebastian Bugiel for spending days at the dust accelerator.

I want to thank my colleagues from the University of Heidelberg Alexander Varychew, Jens Hopp, Johannes Grimm, Frank Postberg, Michael Burchard, Petra Fuchs, René Reviol and Winfried Schwarz for their advices, discussions and technical expertise.

I also want to thank my colleagues and Members from the Cosmic Dust Group (IRS, MPIK, University of Kent) Anna Mocker, Eberhard Grün, Jon Hillier and Yanwei Li, for their expertise on the dust accelerator, the advices and the great collaboration.

I want to thank my family and my friends who been so interested in my work and encouraged me keep on.

All those who are mentioned, here please be sure that I really appreciate all your efforts, support, help, advices, encouragement and time you gave to me.

Finally I would like to thank my wife Angelika, who was with me all the time in every way possible and put so much faith in me. This work is dedicated to you.